ELECTRON ACCELERATION IN A PLASMA WAVE ABOVE A LASER IRRADIATED GRATING

By

MICHEL LABERGE

B.Sc., Université Laval 1983
M.Sc., Université Laval 1985

A THESIS SUBMITTED IN PARTIAL FULFILLMENT OF
THE REQUIREMENTS FOR THE DEGREE OF
DOCTOR OF PHILOSOPHY
in
THE FACULTY OF GRADUATE STUDIES
DEPARTMENT OF PHYSICS

We accept this thesis as conforming
to the required standard

THE UNIVERSITY OF BRITISH COLUMBIA
August 1990

Department of PHYSICS

The University of British Columbia
Vancouver, Canada

Date 17/8/90

ABSTRACT

The acceleration of electrons in a laser produced plasma wave was studied experimentally. A plasma with a modulated density was produced by illuminating a grating with a ruby laser at an intensity of 10^{10} W/cm^2. The plasma expanding above the surface of the grating was diagnosed using interferometry, shadowgraphy and Raman-Nath scattering. The plasma density was found to be modulated with an amplitude of $\tilde{n}/n=8\%$ for grating spacings ranging from 6 to 35 μm. A CO_2 laser of intensity 7×10^{11} W/cm^2 then irradiated this modulated plasma and generated plasma waves. The phase speeds of the plasma waves are $v_{ph} = \pm\omega_0/k_g$, where k_g is the wavenumber of the grating and ω_0 is the frequency of the CO_2 laser. Electrons were injected at an energy of 25 keV in one of the plasma waves. In order for the phase speed of the wave to synchronize with the accelerating electrons, a grating with constantly increasing line spacing was used.

No conclusive evidence of electron acceleration was obtained, even after the injection energy was increased to 92 keV. This lack of evidence was the result of a large electric field perpendicular to the surface of the grating, which deflected the electrons onto the grating. This detrimental electric field is produced when fast electrons are emitted by the plasma and leave it positively charged. At the low laser intensity used in this experiment, the origin of these electrons could not be identified. Some techniques to remedy this difficulty are proposed.

TABLE OF CONTENTS

LIST OF TABLES

LIST OF FIGURES

LIST OF ACRONYMS

TEM:	Transverse electromagnetic
EM:	Electromagnetic
UCLA:	University of California at Los Angeles
INRS:	Institut National de la Recherche Scientifique
OTSI:	Oscillating two stream instability
FWHM:	Full width at half maximum
SCR:	Silicon current rectifier
HP:	Hewlett Packard
M1, M2:	Mirror 1, 2
S1, S2:	Beam splitter 1, 2
RL:	Relay lens
MO1, MO2:	Microscope objective 1, 2
L1, L2:	Lens 1, 2
FTP:	Fourier transform plane
HV:	High voltage
OMA:	Optical multichannel analyzer
DC:	Direct current
AC:	Alternating current

ACKNOWLEDGEMENTS

My special thanks are extended to the following people: my supervisor, Dr. Jochen Meyer, for his constant encouragement and many useful suggestions; my girlfriend, Vivien Johnston, for the monumental task of correcting my English and typing the final thesis; Steve Leffler, for his help during the summer of 1989, and to Hubert Houtman and Al Cheuck, for teaching me technical skills and providing technical support during the experimental process. I would also like to thank Hiroshi Kato, from Electrical Engineering, for the preparation of the lithographic gratings. Finally, thanks to my fellow students Abdul Elezzabi, Ross McKenna and Peter Zhu for many hours of interesting discussion.

INTRODUCTION

The search to find the fundamental constituents of matter gathered momentum in the early 20th century. It was then that Rutherford first used high energy particles to explore the constituents of atoms. Since then, our knowledge of matter has expanded hand-in-hand with the increase in the energy of the particles used as a probe, so that each time a new generation of accelerators is used, new particles are discovered. This increase in energy has led to the development of the large present day machines. These accelerators, many kilometers in length or diameter, and worth a few billion dollars, produce beams of charged particles with an energy of several hundred GeV. The machines have reached the limit of present day technology. However, because physicists demand still higher energy, a new technology capable of producing high voltage gradients for acceleration is necessary, so that very high energies can be achieved over a reasonable distance.

In 1961, K. Shimoda [1] proposed using a laser to accelerate electric charges. He recognized the possibilities this invention offered in producing very high electric fields for acceleration. In fact, the laser is capable, by focusing its radiation, of generating electric fields enormously more intense than had been previously possible.

In this thesis, we examine experimentally the laser acceleration of electrons. In Chapter 1 we look at a variety of methods, proposed by different authors for accelerating charged particles using these large, laser-produced, electric fields and discuss some of the problems associated with these methods. In Chapter 2 we introduce an acceleration scheme proposed by Katsouleas et al. [2] (hereafter referred to as, the oscillating plasma grating accelerator), demonstrating, by means of a number of calculations, the basic principles and expected capability of this technique. We describe the laser system and the vacuum chamber used in these experiments in Chapter 3. This acceleration technique needs a preformed plasma with a modulated density and we see in Chapter 4 that the plasma expanding above a laser irradiated grating partially satisfies this condition. The calculations in Chapter 2 help explain how an electromagnetic wave interacts with the modulated plasma to produce a plasma wave, but these calculations do not explain how the plasma wave can accelerate injected electrons. In Chapter 5, we study theoretically the trapping and acceleration of electrons injected into a plasma wave which has a phase speed that increases along the length of the plasma. In Chapter 6, the core of this thesis, we describe two experiments that should have demonstrated electron acceleration using the oscillating plasma grating accelerator. These experiments were unsuccessful. The presence of strong transverse electric fields in the plasma explains the inconclusive evidence. These electric fields deflect the electron beam and disrupt the acceleration process. In the conclusion, we propose some solutions for this problem.

CHAPTER 1

REVIEW OF METHODS PREVIOUSLY PROPOSED

In this chapter we look at the operation of existing accelerators and their limitations. Some simple arguments show the advantages of using shorter wavelengths for acceleration. After examining the difficulties involved in adapting the traditional technique to very short wavelengths, we will review the solutions proposed by various authors for solving this problem.

1.1 The Existing Accelerators

Most of the existing high energy accelerators (synchrocyclotron, linear accelerator, etc.) use electromagnetic waves to accelerate charged particles. These waves are, unfortunately, transverse electromagnetic (TEM) in free propagation. In other words the electric and magnetic fields are perpendicular to the direction of propagation. If a charged particle meets a wave of this type, it will oscillate in the electric field without overall acceleration. If one uses a waveguide it is possible to obtain a component of the electric field in the direction of propagation. The phase speed of the waves in a guide is always greater than the speed of light (Figure 1.1a) and it is impossible to keep a particle in the accelerating phase for a long time. Sooner or later, the particle will be overtaken by the wave and will slow down. If we introduce a periodic perturbation into the guide, for example some irises, the dispersion relation of the wave guide is modified (Figure 1.1b) and any phase speed is possible.

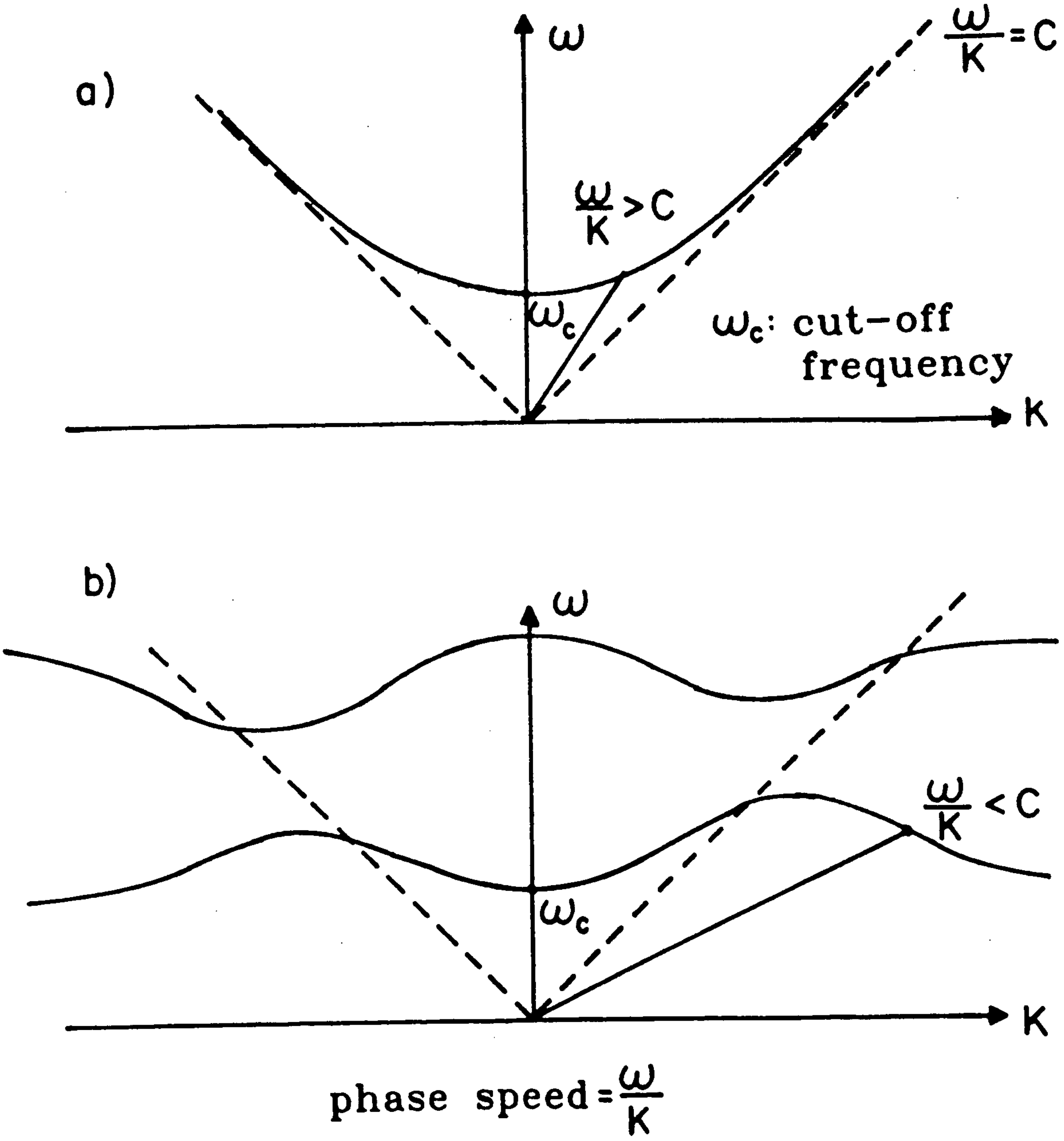

FIGURE 1.1

Dispersion relation for a uniform a) and periodic b) waveguide.

In modifying the parameters of this periodic guide one can adjust the phase speed to the speed of the particle, in such a way that the acceleration can be maintained over a long distance. This is the principle under which the existing linear accelerators operate.

These accelerators operate with a wavelength of about 10 cm. The wavelength is a simple technological choice. To obtain large accelerating electric fields one must have a very powerful source of radiation. The best source available, at the time of the design of these machines, was the klystron with a frequency of several gigahertz. The acceleration obtained at this wavelength is, for example, 17 MeV/m for the Stanford linear accelerator.

1.2 Towards Shorter Wavelengths

These days, with lasers, we are able to produce very powerful sources of radiation with wavelengths as small as 250 nm corresponding to the ultraviolet end of the spectrum. The technological limitations are reduced and we can select any wavelength. The advantages of a shorter wavelength are as follows. The minimum area on which it is possible to concentrate electromagnetic energy is about λ^2, where λ is the wavelength of the electromagnetic radiation. Therefore the power P needed to obtain a given electric field E over this area is:

$$P \propto E^2 \lambda^2$$

A short wavelength allows us to obtain a very high electric field for acceleration with a reasonable amount of power. For example, one can produce the same electric field with a laser Nd:YAG ($\lambda = 1\ \mu$m) of 100 mW as with a klystron ($\lambda = 10$ cm) of a GW. It is also easily possible with a Nd:YAG laser to produce pulses of a GW. This would generate a field equivalent to a klystron producing 10^{10} GW, which would be totally impossible. The maximum gain of the electric field that one can obtain by replacing a klystron by a laser is in the order of 10^5. This permits, in theory, a one centimeter accelerator to produce the same energy as an existing machine of one kilometer.

Electric breakdown is produced when the electrons inside the matter attain sufficient energy in one cycle of the electromagnetic (EM) wave to ionize the atoms. This produces still more free electrons, an avalanche is created and the dielectric properties of the material break down. For the same value of electric field amplitude, but with a higher frequency, the electrons gain less energy before changing direction of motion when the frequency is higher. Therefore materials offer a greater resistance to breakdown at a shorter wavelength. This is very important for all the accelerators where some materials are exposed to strong fields, for example in the traditional accelerator cavities.

The problem of transferring energy from the wave to the particle is still present and is even more complicated at shorter wavelengths. We could use the technique of the periodic wave guides for wavelengths down to one centimeter, but certainly not below this. It would be technically impossible to construct such a small wave guide with the required precision.

An accelerator fed by a free electron laser with $\lambda=1$ cm should have an accelerating gradient about 10 times greater than the existing machines. This is good but not revolutionary. What we would like would be an accelerator using 1 μm! For these short wavelengths we must find new techniques. Let us look at what has already been proposed by various authors.

1.3 Different Accelerating Techniques

We will not present an exhaustive list of the many methods which have been proposed. We will, however, describe the most promising and the most representative of the different types of accelerators.

The techniques proposed to couple the EM waves to the charged particles can be divided into three main categories [3].

1. **Near Field Accelerator.** The accelerating EM field is in a vacuum but is supported by a conductive or dielectric structure. The field only exists in a region very close to the structure (over a distance of about a wavelength).

2. **Far Field Accelerator.** The acceleration is produced in a vacuum, far from any material.

3. **Media Accelerator.** The particles are accelerated within either a gas or a plasma.

1.3.1 Near Field Accelerator

The classic accelerating cavities are of this category. However, for wavelengths below $\lambda=1$ cm, we saw that such a periodic guide is not practical. R.B. Palmer [4] showed that when "unrolling" a structure of this type one obtains a grating (Figure 1.2) which can easily be made with a periodicity of less than a micron. Well designed, a grating of this type is able to carry surface waves with a large longitudinal component of the electric field. The phase speed can be adjusted to that of the accelerated particles. This grating can also have, like a microwave cavity, a gain coefficient $Q>1$. In other words the surface wave can have a much greater amplitude than that of the incident wave which drives it.

An accelerator can thus be made by sending a beam of charged particles a fraction of a wavelength above a grating which is correctly illuminated by a laser. The acceleration obtained by this method is limited to about 1 GeV/m by the destruction of the grating at too high an intensity [4].

If one imagines an expendable grating, for example ripples on a mercury surface, it is acceptable to destroy it with each laser shot. In this case, the particles must be accelerated before the grating becomes inefficient due to

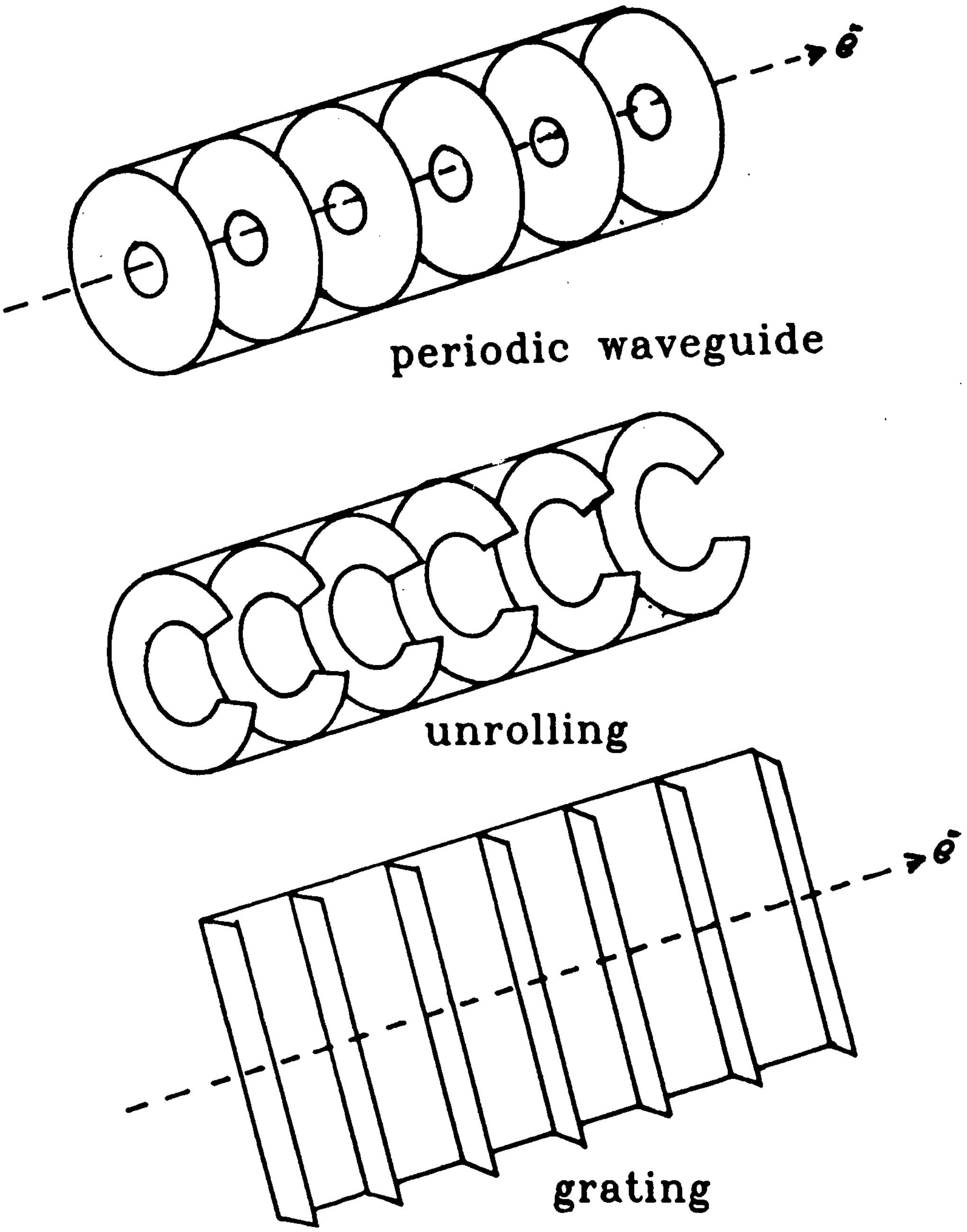

FIGURE 1.2
Transformation of a periodic waveguide to a grating

the ablated plasma which develops on its surface. In these conditions, the accelerating gradient can be as high as 20 GeV/m, 1000 times that of the Stanford linear accelerator [4].

In another proposal by S.A. Kheifets [5], an evanescent wave at the surface of a dielectric guide is used to accelerate the particles (Figure 1.3).

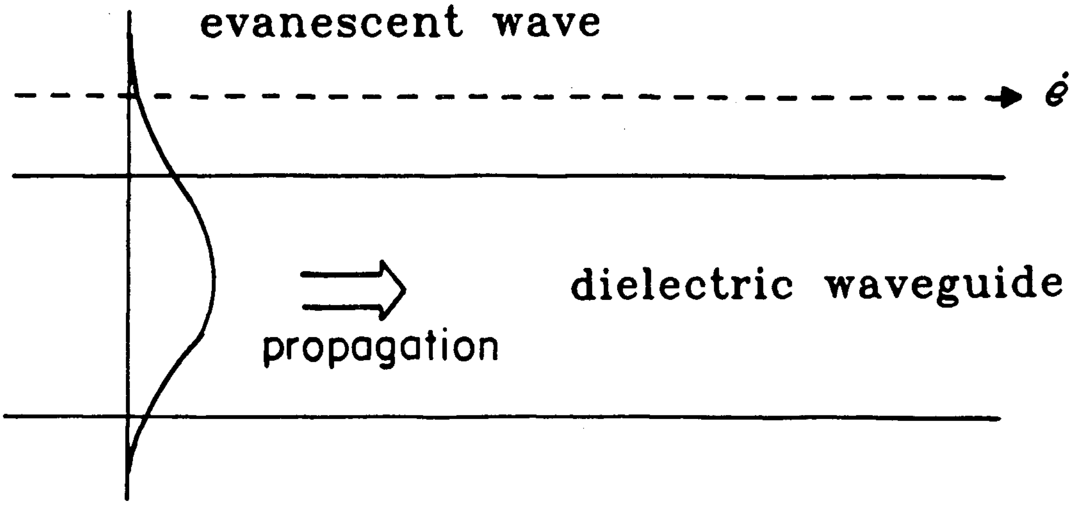

FIGURE 1.3
Evanescent wave accelerator

With the correct choice for the index of refraction and for the dimensions of the guide, it is possible to obtain the correct phase speed and the desired longitudinal polarization of the EM field. The maximum gradient is about 100 MeV/m, limited by the breakdown of the dielectric [5].

Many other methods use the longitudinal component of a EM field in a vacuum. But, as was demonstrated by R.B. Palmer in one of his publications [4], the phase speed of this component is always greater than the speed of light. Eventually, the particle is overtaken by the EM wave and slows down.

To avoid this deceleration one places a mirror pierced with a small hole where the field begins to slow down the particles. On the other side of the mirror the field is adjusted to accelerate the particles as far as another mirror, and so on. Thus a beam of particles can pass through the holes and constantly gain energy. Once again, the problem is the destruction of the mirrors by the intense light which exists on the trajectory of the particles. Paul L.Csonka [6] proposed a method in which he uses an interesting technique to protect the mirrors. If one uses a very thin mirror (with a thickness in the order of 50 nm) and one places it at the position of a node of a standing wave, it is only exposed to a very small fraction ($\approx 10^{-3}$) of the maximum electric field. Gradients of about 5 GeV/m appear to be possible with this method. But building mirrors of this thickness and positioning them at the node of the standing wave with sufficient precision represents a formidable technical challenge.

1.3.2 Far Field Accelerator

In the previous acceleration schemes, the particle is supposed to follow a perfectly linear trajectory. An EM wave, having a longitudinal component of the electric field and a synchronized phase speed, accelerates the particle continuously. A wave of this type cannot exist in a vacuum far from any material support. Thus the far field accelerators cannot work with this method.

It is however possible to superimpose a lateral oscillation on the trajectory of the particle to obtain a helix or a sinusoid. If the transverse component of the electric field of an EM wave is in phase with this oscillation, an effective coupling can be produced.

In the near field accelerators, the mass, or the energy of the accelerated particle does not influence the accelerating gradient. In the far field accelerators however, it is difficult to make heavy or high energy particles oscillate. Also, an oscillating electric charge, loses energy by synchrotron radiation. Because of these limitations, this type of machine accelerates only electrons and cannot attain a very high energy (TeV).

The inverse free electron laser [7] is an accelerator of this type. A relativistic beam of electrons oscillates as it passes through an undulator made of a series of magnets of alternating polarities. A laser beam is then sent on the same axis as the electrons (Figure 1.4).

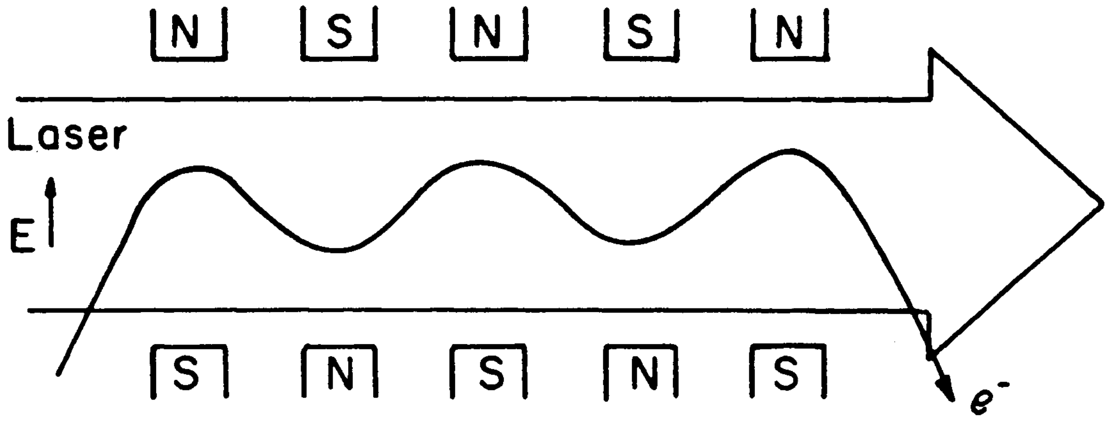

FIGURE 1.4
Inverse free electron laser

The frequency of the laser beam in the electrons' frame of reference, greatly diminished by the Doppler effect, should be equal to the frequency of oscillation of the magnetic field in the same frame of reference. If we use realistic numbers for the power of the laser and the intensity of the undulator magnetic field, a gradient of about 600 MeV/m for electrons of 1 GeV is obtained. This gradient diminishes as the cubic root of the electron energy. It is only 60 MeV/m for an energy of 1 TeV.

In the two wave accelerator [8] the undulator is replaced by a micro-wave cavity adjusted to have a phase speed much less than c. It is the micro-wave field that makes the electrons oscillate. The frequency of the second wave, the laser, diminished by the Doppler effect, should be equal to the frequency of the micro-waves seen by the electrons. The performance of this method is similar to that of the inverse free electron laser, with less loss in synchrotron emission. This slightly increases the gradient at high energy.

1.3.3. Media Accelerator

If a particle moves faster than the speed of light in a given material, it will emit Cherenkov radiation. The process can be reversed by sending the light on a particle which is thus accelerated. This is the idea behind the inverse Cherenkov accelerator [9].

We can understand this method by considering an EM wave which cuts the trajectory of an electric charge with an angle θ (Figure 1.5).

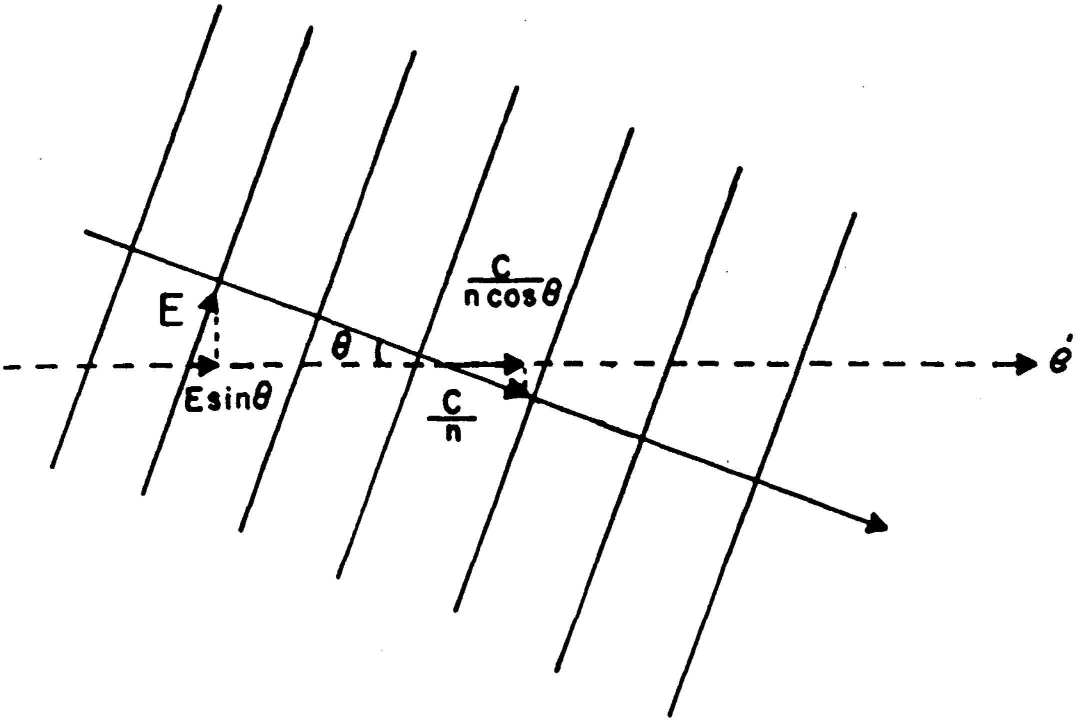

FIGURE 1.5
Inverse Cherenkov accelerator

We can adjust θ so that the projection of the phase speed on the trajectory of the particle is equal to the speed of the particle.

$$v = c/\eta\cos\theta$$

Where v is the speed of the particle, c is the speed of light and η is the index of refraction of the material.

In these conditions, the longitudinal component of the electric field, proportional to sin θ, can accelerate the charge continuously. We must use a low density material, e.g. a gas at one atmosphere pressure, in order to avoid too much diffusion of the particle beam due to collisions. Thus $\eta - 1 \approx 10^{-4}$ and if $v \approx c$, $\theta \approx 15$ milliradians, sin $\theta \approx 1.5 \times 10^{-2}$. We only use 1.5% of the electric field which is still limited by the breakdown of the gas. The maximum gradient is about 100 MeV/m. If we use a geometry such that there is no transverse field on the axis, and there is only a longitudinal field, one is able to increase the gradient to 500 MeV/m. This can be accomplished by focusing with an axicon a radially polarized laser beam, where the electric field direction is always radial. Because of symmetry, the transverse field will vanish on the axis and there will only be a longitudinal field [10]. The scattering of the charged beam by the atoms in the gas, limits the length of an accelerator of this type to about 50 m, for a maximum energy of around 25 GeV.

In many of these methods, the accelerating gradient is limited by the electrical break down of material exposed to high laser intensity. One promising way of solving this problem is to use an already ionized material, a plasma, that cannot breakdown anymore. A plasma can support an electrostatic wave having a longitudinal electric field and any desired phase speed. A wave of this type, an electron plasma wave, is ideal to accelerate charged particles. Many different ways of exciting such a wave have been considered.

In the beat wave accelerator [11], the most studied technique, two collinear laser beams with frequencies of $\omega_1 >> \omega_p$ and $\omega_2 >> \omega_p$ are sent into a uniform plasma, having a plasma frequency $\omega_p = \omega_1 - \omega_2$. The two waves can thus propagate without being reflected, and beat at the resonant frequency of the plasma (Figure 1.6).

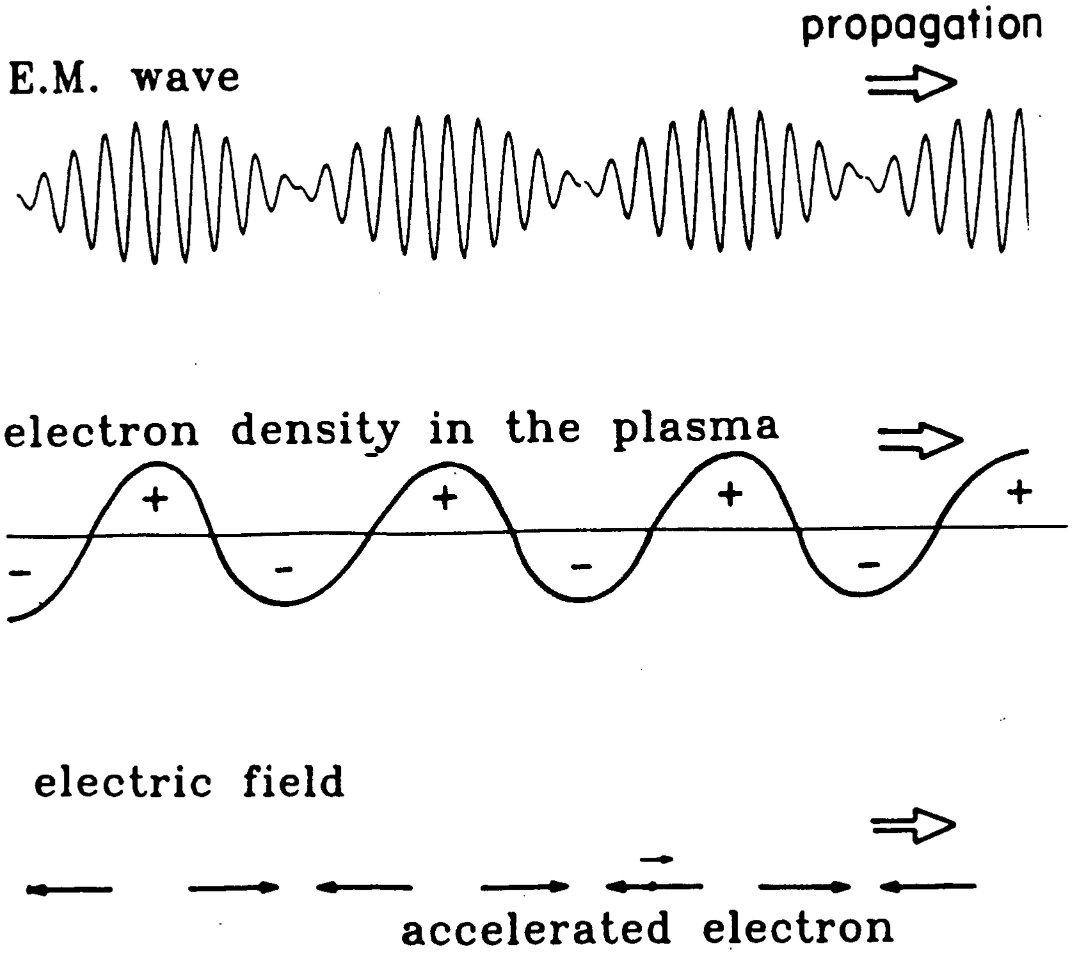

FIGURE 1.6
Beat wave accelerator

The ponderomotive force $f=-q^2\nabla E^2/4m_e\omega^2$, where q and m_e are the charge and mass of the electrons, E is the total electric field of the beating light waves and $\omega=(\omega_1\omega_2)^{1/2}$, pushes the free electrons in the plasma out of the regions with strong EM fields and concentrates them near the nodes of the beat wave. An intense longitudinal electrostatic field is thus created between the regions of strong and weak electron concentrations. This plasma wave moves with the two EM waves which generate it at a phase speed of $v_{ph}\approx c[1-(\omega_p/\omega)^2/2]$ [11]. For $\omega>>\omega_p$ this phase speed is slightly less than the speed of light and relativistic charged particles can be accelerated by the plasma wave. The wave breaking limit for the accelerating electric field is $qE_{max}(eV/m)\approx n_e^{1/2}(cm^{-3})$, giving 30 GeV/m for $\lambda_1=10.6$ μm, $\lambda_2=9.6$ μm and $n=10^{17}$ cm^{-3} for example. This very large gradient is the cause of great interest in this method. However, different saturation mechanisms will prevent the wave from growing to this wave breaking limit. The plasma wave can couple with other plasma waves of frequencies $\omega=n\omega_p$ (n is an integer) and electromagnetic waves of frequencies $\omega=\omega_1\pm n\omega_p$ and in this way loose its energy. Also for large amplitudes the electron can oscillate fast enough to experience a relativistic mass increase. This changes ω_p so $\omega_1-\omega_2$ no longer equals the plasma resonant frequency. This relativistic detuning limits the acceleration field to $E=E_{max}(16\alpha_1\alpha_2/3)^{1/3}$ where $\alpha_{1,2}=qE_{1,2}/m_ec\omega_{1,2}$, $E_{1,2}$ is the electric field of each laser beam. For a reasonable value of 0.1 for α_1 and α_2 and $n=10^{17}$ cm^{-3}, the relativistic detuning limits the accelerating field to 11 GeV/m.

However, because the phase speed of the plasma wave is less than c, the accelerated particles will outrun the wave and begin to be decelerated. This limits the useful length of the accelerator to $L_{max}=\gamma^2\lambda_p/2$ where λ_p is the wavelength of the plasma wave and γ is the relativistic factor of the accelerated electrons [11]. The energy gain ΔW_{max} in this length is $\Delta W_{max}=2\gamma^2 m_e c^2$. Therefore, the maximum length of the acceleration is $L_{max}=2$ cm and the maximum energy gain is $\Delta W_{max}=400$ MeV, given the previous parameters and an injected electron energy of 10 MeV. Many of these accelerating sections can be used in series with a proper phase relationship between each stage to create a very high energy accelerator.

Alternatively a very short duration, very intense laser pulse can be used to drive the plasma wave. The ponderomotive force, due to the strong intensity gradient at the leading and trailing edges of this pulse, pushes the plasma electrons away. Just after the pulse has passed the electrons rush back to fill the area of low electron density, but they overshoot and oscillate for a few cycles (Figure 1.7). This type of wake field accelerator [11] performs in a similar way as the beat wave accelerator. The phase speed of the plasma wave is equal to the group velocity of the laser pulse $v_g=c(1-\omega_p^2/\omega_{laser}^2)^{1/2}$. So for $\omega_{laser}>>\omega_p$, v_g is slightly smaller than c. Once again, multiple stages with the correct phasing must be used to avoid deceleration of the accelerated particles.

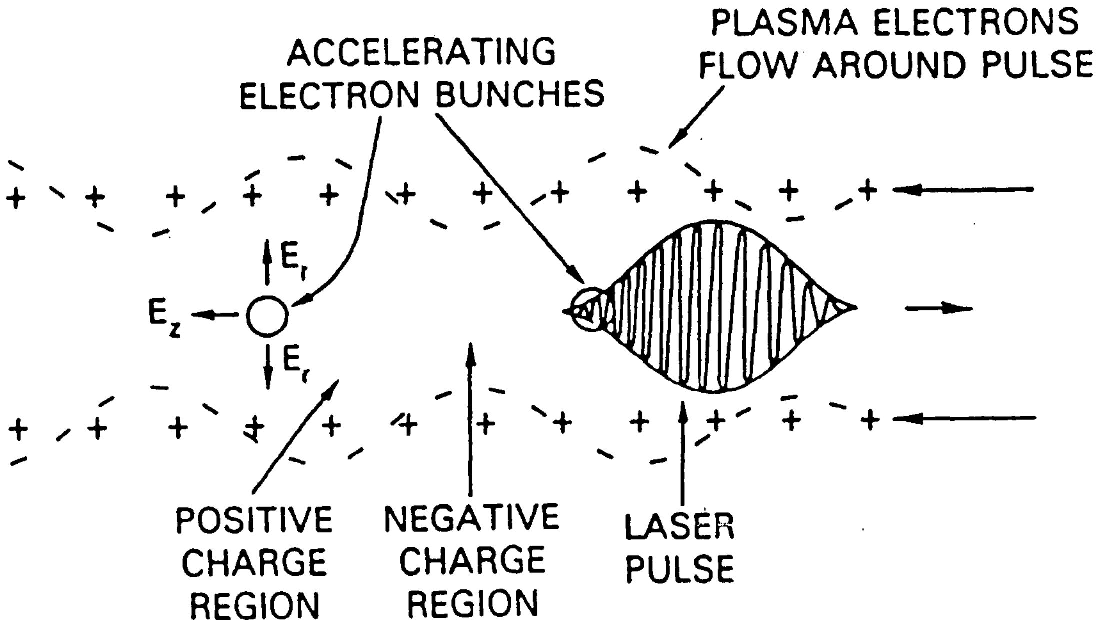

FIGURE 1.7
Laser wake field accelerator

This is a non resonant technique, so the plasma does not have to be as uniform as in the beat wave accelerator, but the laser intensity must be much greater to produce the same plasma wave amplitude. This is because the short pulse pushes only once on the electrons, whereas in the beat wave accelerator the laser oscillates the electrons over many periods and can slowly build up a large amplitude wave.

The wake field can also be produced by a short pulse of relativistic electrons [12]. Although not a laser acceleration, this method can produce very strong accelerating electric fields. In this case it is the electrostatic field of the relativistic electron bunch that pushes the plasma electrons instead of the ponderomotive force. Once again a plasma wave is created in the wake of the bunch which can accelerate injected particles.

1.4 Experimental Results

Many more methods have been proposed and theoretically analyzed than have been experimentally tested. However, a proof of principle experiment for the inverse Cherenkov accelerator was successful [13]. In this experiment a 102 MeV electron bunch gained 200 keV in 7 cm while crossing a 30 MW Nd:YAG laser beam at an angle of 18 mrad in 1.28 atm of H_2. This is a rather weak 3 MeV/m gradient. However, an improved experiment using a radially polarized light cone is in progress and much higher gradients should be demonstrated [10].

For the more promising plasma accelerator a few experimental results have been obtained. Plasma waves driven by the beating of two CO_2 lasers at a frequency of 9.6 μm and 10.6 μm have been observed by the U.C.L.A. group using Thomson scattering of probe laser radiation [14]. A gradient between 0.3 and 1 GeV/m is inferred. Experiments to inject and accelerate electrons in these waves are in progress. Another group, at I.N.R.S. in Quebec [15], have injected laser produced electrons of an energy between 200 keV and 1 MeV into a beat wave driven by one CO_2 laser operating at two frequencies. A claimed energy gain of 1.5 MeV over the Rayleigh length of the focused beam (1.5 mm) demonstrates a 1 GeV/m gradient. Finally, in an impressive experiment at Argonne National Laboratory [16], the plasma wave produced in the wake of an intense electron bunch has been measured by an additional electron group. The additional group of electrons gain or lose energy depending on the time at which they are injected after the driving bunch. A measured acceleration of 150 MeV/m over 27 cm is produced in this experiment.

More experiments are needed to validate the many proposed acceleration concepts and to discover possible technical difficulties. The methods discussed here form a very small fraction of all the proposed acceleration techniques. Few of these proposals have been explored experimentally. In this thesis we will attempt to demonstrate experimentally the oscillating plasma grating accelerator.

CHAPTER 2

THEORY OF THE OSCILLATING PLASMA GRATING ACCELERATOR

In Chapter 2 we introduce the method of Katsouleas et al. to accelerate charged particles with lasers in a plasma. We first discuss some of the shortcomings of the methods proposed in the previous chapter and see how the oscillating plasma grating accelerator solves these shortcomings. The expected acceleration is estimated and a method of producing a promising plasma is described.

2.1 Problems with Other Methods

Let us examine some of the problems that affect most of the acceleration methods described thus far.

2.1.1 Relativistic Mass Increase

In the far-field schemes, some form of transverse oscillation must be superimposed on the electron trajectory to couple it to the laser field. But at a higher energy the particle mass increases and so the oscillation amplitude decreases. It is therefore difficult to couple the laser with the electron beam efficiently and the maximum energy is limited to the GeV range. These methods can be considered for intermediate energy accelerators but not for a multi TeV machine.

2.1.2 Electric Breakdown

As we have seen previously, all of the near field methods are ultimately limited by the problem of electric breakdown. Shorter wavelengths improve the maximum field allowable. but even at laser wavelength ($\lambda = 1$ μm), the maximum possible gradient is only a few hundred MeV/m. This is very good, but physicists want still more acceleration. This is possible only if we allow the material to break down and become a plasma.

2.1.3 Phase Speed Control

In the plasma method, the phase speed of the accelerating wave is determined by the propagation speed of an electron bunch, or laser pulse, in the plasma. This is always very close to, but slightly slower than, the speed of light. Because the speed of the accelerated particles increases and tends towards c, the particles will eventually outrun the wave. For a large accelerator there must be many accelerating sections with the proper phase relationship between them. Each section would begin in phase with the particle beam and stop when phase mismatch begins. This phase matching would be difficult to achieve experimentally.

Because the phase speed is so close to c these methods can only accelerate relativistic beams of particles. The machines to produce such a beam, even for electrons, are large, complex and expensive. So any experiments to demonstrate these accelerating techniques must be well funded.

2.1.4 Pump Depletion

In the two plasma methods discussed in Chapter 1, the source of accelerating power traveled longitudinally with the accelerated beam. Some energy is lost by the pump beam (electron bunch or laser beam) and transferred to the accelerated particles. After a certain length of acceleration there is no longer enough power left in the pump beam to continue the acceleration process. A fresh pump beam must then be re-injected at the correct phase. So, again (see phase speed problem), the accelerator must be broken into many sections. Even if the acceleration within a section is large, the distance between sections must also be taken into account when calculating the average acceleration of the complete accelerator. For example, the following arrangements have been proposed for the beat wave accelerator (Figure 2.1) [3].

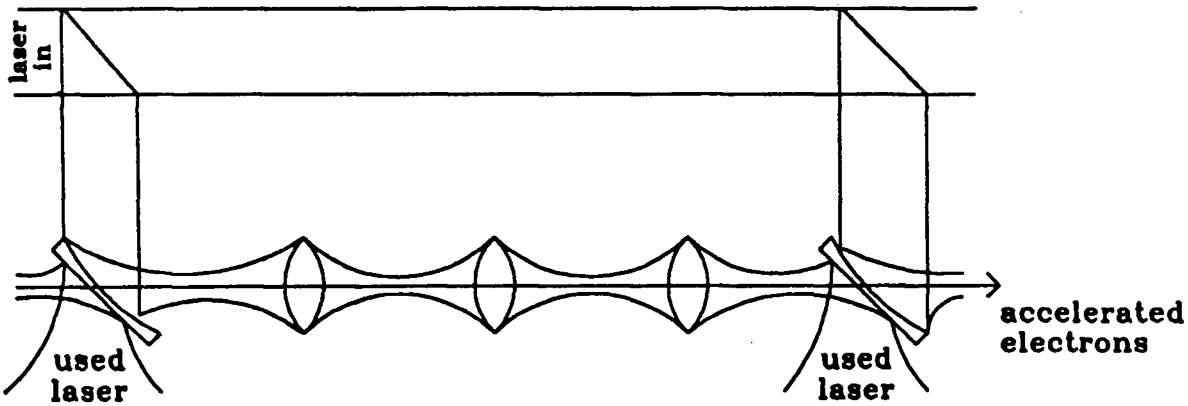

Figure 2.1
Multistage accelerator

The intensity needed for the beat wave accelerator is around 10^{14} W/cm^2 and this intensity will only be available close to the focal region of the lens and mirrors. But these optical components cannot support intensities greater than 10^9 W/cm^2. The components must therefore be sufficiently spaced for the laser beam to expand enough between the focal region and the next optical component. The fraction of the accelerator that will effectively accelerate is only $(I_{max}/I_{lens})^{1/2}=3x10^{-3}$. Where I_{max} is the laser intensity at the focus and I_{lens} is the allowable intensity on the lens or mirror. Such a factor reduces the average accelerating gradient well below the impressive multi GeV/m peak gradient theoretically achievable by this method.

2.2 The Oscillating Plasma Grating Accelerator

Katsouleas et al. [2] proposed a technique where a side injected laser beam falls on a modulated plasma and produces accelerating plasma waves. The geometry is shown in Figure 2.2.

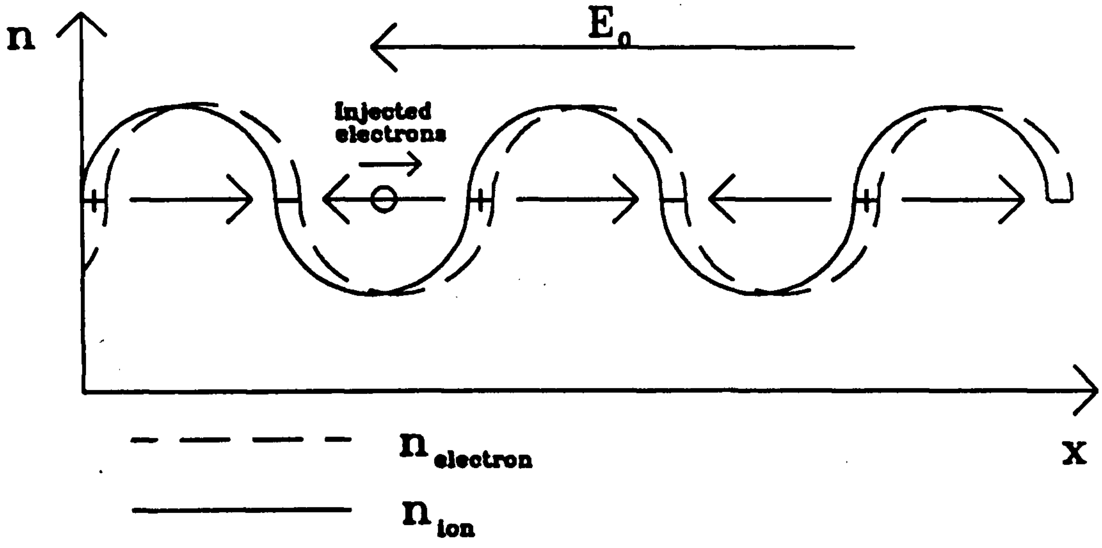

FIGURE 2.2
Oscillating plasma grating accelerator

The laser field E_0 makes the electrons oscillate. The ions do not have time to respond to the rapidly oscillating field. A charge separation occurs, generating a space charge field. This field tends to bring the electrons back to their equilibrium position. If the frequency of the laser ω_0 equals the natural frequency of the plasma oscillation ω_p, very large amplitude plasma waves can be generated. Electrons injected at $v=\omega_0/k_g$, where k_g is the wave vector of the modulation, can be accelerated. Since this is a plasma method, the accelerating field is not limited by electric breakdown. The phase speed is controlled by the periodicity of the modulated plasma and the frequency of the laser. It can be adjusted to any desired value, above or below the speed of light, solving the phase matching problem of the beat wave accelerator. This method can also accelerate non relativistic particles. Also because the laser is injected perpendicularly to the electron trajectory it is very easy to feed more power without large interruptions in the acceleration, (see Figure 2.3 for example). For the above reasons we decided to study this method in more detail.

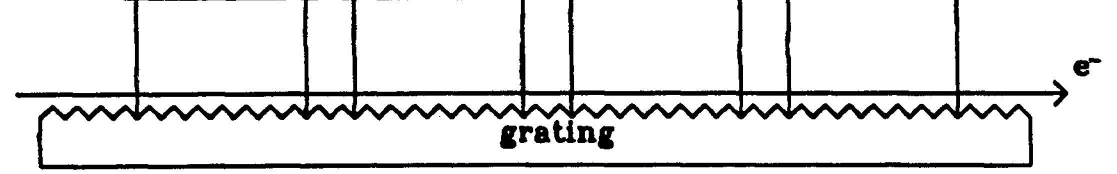

FIGURE 2.3
Multistage plasma grating accelerator

A laser of frequency ω_0 and electric field E_0 falls on a modulated plasma of density $n_e = n_0 + n_1 sin\ k_g x$. Whe can first ignore the motion of the ions due to their large mass. The one dimension fluid equations for the electrons are:

$$\frac{\partial n_e}{\partial t} + v_e \frac{\partial n_e}{\partial x} + n_e \frac{\partial v_e}{\partial x} = 0 \qquad (2.1a)$$

$$\frac{\partial v_e}{\partial t} + v_e \frac{\partial v_e}{\partial x} = -\frac{c_e^2}{n_e}\frac{\partial n_e}{\partial x} - \frac{e}{m_e}(E + E_0 sin\omega_0 t) - v_e \nu_e \qquad (2.1b)$$

$$\frac{\partial E}{\partial x} = \frac{e}{\epsilon_0}(Z^* n_i - n_e) \qquad (2.1c)$$

Where n_e is the electron density, v_e is the electron speed, $c_e^2 = k_B T_e/m_e$ is the electron thermal velocity, k_B is the Boltzman constant, T_e is the electron temperature, m_e is the electron mass, ν_e is the collision frequency, E is the space charge induced electric field, Z^* is the average degree of ionization and ϵ_0 is the permitivity of free space.

We try a solution of the form:

$$n_e = n_0 + n_1 sin\ k_g x + \tilde{n}_e(x,t)$$

$$v_e = v_0 + \tilde{v}_e(x,t)$$

Here, $v_0 = (eE_0/m_e\omega_0)cos\omega_0 t \equiv v_{os} cos\omega_0 t$ is the component of the electron velocity caused by the laser field.

For $\alpha << 1$ $(\alpha = v_{os}/v_{ph},\ v_{ph} = \omega_0/k_g)$, $\tilde{n}_e/n_0 << 1$ and $n_1/n_0 << 1$, we can keep only the lowest order terms and we obtain, after some manipulations, the electron wave equation:

$$\frac{\partial^2 \tilde{n}_e}{\partial t^2} + \nu_e \frac{\partial \tilde{n}_e}{\partial t} - c_e^2 \frac{\partial^2 \tilde{n}_e}{\partial x^2} + \omega_{pe}^2 \tilde{n}_e = \alpha \omega_0^2 n_1 sin\ \omega_0 t\ sin\ k_g x$$
$$-\alpha \omega_0 \nu_e n_1 cos\ \omega_0 t\ sin\ k_g x - c_e^2 k_g^2 n_1 sin\ k_g x \qquad (2.2)$$

Where $\omega_{pe}^2 = n_0 e^2 / m_e \epsilon_0$ is the electron plasma frequency.

The first two terms on the right hand side of this equation drive a standing plasma wave. (The quadrature excitation comes from the collision term in the fluid equation). This standing wave can be decomposed in two counterpropagating waves. The phase speeds of these waves are $v_{ph} = \pm k_g/\omega_0$. Because the k_g vector of the modulation and the frequency ω_0 of the laser can be independently chosen, any phase speed is possible. It is thus possible to accelerate charged particles of any speed using one of these two plasma waves. The electric field of the other wave will be seen as a high frequency perturbation by the accelerated particle and will not affect its trajectory significantly. The third term on the right hand side of the wave equation represents the static ripple in $\tilde{n}_e$ due to the modulated plasma gradient and finite electron temperature.

We can now calculate the amplitude of the excited plasma wave.

Trying a solution to the wave Equation (2.2) of the form:

$$\tilde{n}_e = A sin\ \omega_0 t\ sin\ k_g x + B cos\ \omega_0 t\ sin\ k_g x + C sin\ k_g x$$

We find:

$$A = \frac{\alpha n_1 \omega_0^2 \left\{(\omega_r^2 - \omega_0^2) - \nu_e^2\right\}}{(\omega_r^2 - \omega_0^2)^2 + \nu_e^2 \omega_0^2}$$

$$B = \frac{-\alpha n_1 \omega_0 \nu_e \omega_r^2}{(\omega_r^2 - \omega_0^2)^2 + \nu_e^2 \omega_0^2}$$

$$C = \frac{-c_e^2 k_g^2 n_1}{\omega_r}$$

Where $\omega_r^2 = \omega_{pe}^2 + c_e^2 k^2$

So:

$$\tilde{n}_e = \frac{\alpha n_1 \omega_0 \sqrt{\omega_0^2 + \nu_e^2}}{\sqrt{(\omega_r^2 - \omega_0^2)^2 + \nu_e^2 \omega_0^2}} sin(\omega_0 t + \phi) sin\ k_g x + \frac{-c_e^2 k_g^2 n_1}{\omega_r} sin\ k_g x \qquad (2.3)$$

$$tan(\phi) = \frac{-\nu_e \omega_r^2}{\omega_0 \left((\omega_r^2 - \omega_0^2) - \nu_e^2\right)}$$

From Poisson's equation this charge distribution will create an electric field of:

$$E = \frac{\sqrt{-\omega_0^2 + \nu_e^2}}{\sqrt{(\omega_r^2 - \omega_0^2)^2 + \nu_e^2 \omega_0^2}} \frac{n_1}{n_0} \frac{\omega_{pe}^2}{\omega_0} E_0 sin(\omega_0 t + \phi) cos\ k_g x$$

$$- \frac{e}{\epsilon_0} \frac{c_e^2 k_g^2 n_1}{\omega_r} cos\ k_g x \quad (2.4)$$

For maximum amplitude we need $(\omega_r^2 - \omega_0^2) = 0$. We then have a resonantly driven oscillator. The amplitude of the plasma wave grows linearly with time:

$$\frac{\tilde{n}_e}{n_0} = \alpha \frac{n_1}{n_0} \omega_0 t$$

The amplitude of the wave will saturate at:

$$\frac{\tilde{n}_e}{n_0} = \alpha \frac{n_1}{n_0} \frac{\sqrt{\omega_0^2 + \nu_e^2}}{\nu_e} \qquad (2.5)$$

For a low collision frequency and an intense laser field, $\tilde{n}_e/n_0$ can be extremely large. However, the wave can saturate before this value of $\tilde{n}_e/n_0$ if the background plasma electrons are trapped in the wave . This happens when the kinetic energy of the electrons in the reference frame moving with the wave is equal to the wave potential energy $e\phi$:

$$(\gamma'_{th} - 1) m_e c^2 = e\phi$$

Using the relation between ϕ and $\frac{\tilde{n}_e}{n_0}$ from Poisson's equation, we can rewrite this equation as:

$$\frac{\tilde{n}_e}{n_0} = \frac{\omega_0^2}{\omega_{pe}^2} \frac{(\gamma'_{th} - 1)}{\beta_{ph}^2} \qquad (2.6)$$

Where $\beta_{ph} = v_{ph}/c$, $\gamma'_{th} = 1/\sqrt{1 - \beta'^2_{th}}$, $\beta'_{th} = (\beta_{th} - \beta_{ph})/(1 - \beta_{th}\beta_{ph})$ and $\beta_{th} = c_e/c$. γ'_{th} is the relativistic gamma factor of the thermal electrons in a reference system which moves with the plasma wave at a speed v_{ph}.

Another saturation mechanism that can play a role for very small ν_e is the relativistic detuning. In an analogy with the beat wave accelerator, the following saturation amplitude can be found [17]:

$$\frac{\tilde{n}_e}{n_0} = \left(\frac{16}{3} \frac{n_1}{n_0} \alpha \right)^{1/3} \qquad (2.7)$$

Finally, if none of these saturation mechanisms prevents $\tilde{n}_e/n_0$ from getting close to one, the approximation $\tilde{n}_e << n_0$ is no longer valid and the linear theory collapses. We will not attempt to derive a non linear theory here. But it can be seen that non linear terms (like $v\frac{\partial v}{\partial x}$) in the fluid equation will couple an infinite number of plasma waves with frequencies $n\omega$ and wave vector mk (n and m integer). Only the waves with $n = m$ will have the correct phase speed to accelerate the particles. However, much of the available energy will cascade onto the other waves so the accelerating waves will saturate at a smaller value.

This linear theory is valid only for $n_1/n_0 << 1$, but we will see in Chapter 4 that we can produce a plasma modulated by up to 8%. This is a rather large value and we must examine the effect of such a n_1/n_0 on the production of the plasma wave.

For very small plasma modulation, the resonant condition $\omega_0 = \omega_r$ is satisfied simultaneously everywhere in the plasma. However, for larger n_1/n_0, ω_r is a function of x and the resonant condition is fulfilled only at the position where $\omega_r(x) = \omega_0$. Therefore, the plasma wave will be excited locally (Figure 2.4).

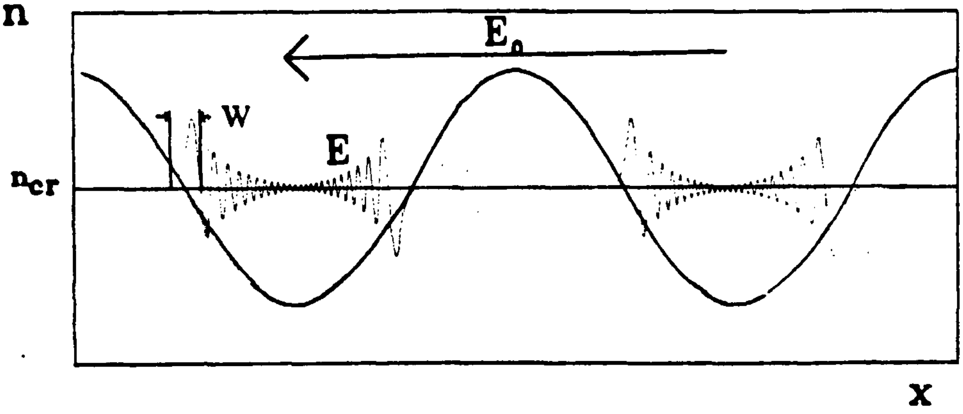

FIGURE 2.4
Localisation of the electric field for large $\tilde{n}/n$

Such a series of localized plasma waves may still be effective to accelerate electrons if the waves are coherent across the total length of the accelerator. But for strong localisation, each small resonant field separated by large zero field regions can oscillate separately with no coherence. Such a strong localization of the plasma wave should be avoided. We must therefore compare the width W of the region where the plasma waves are excited to the wavelength of the plasma modulation. For $Wk_g > 1$, the sinusoid plasma wave approximation is valid, but if $Wk_g < 1$ localization can be a problem.

The degree of localization could be found using the fluid Equations (2.1) without the approximation $n_1/n_0 << 1$, but no analytical solution exists to this problem. However, W can be estimated by considering a laser beam of frequency ω_0 and electric field E_0 illuminating a plasma with a linear density profile (Figure 2.5). This arrangement approximates the

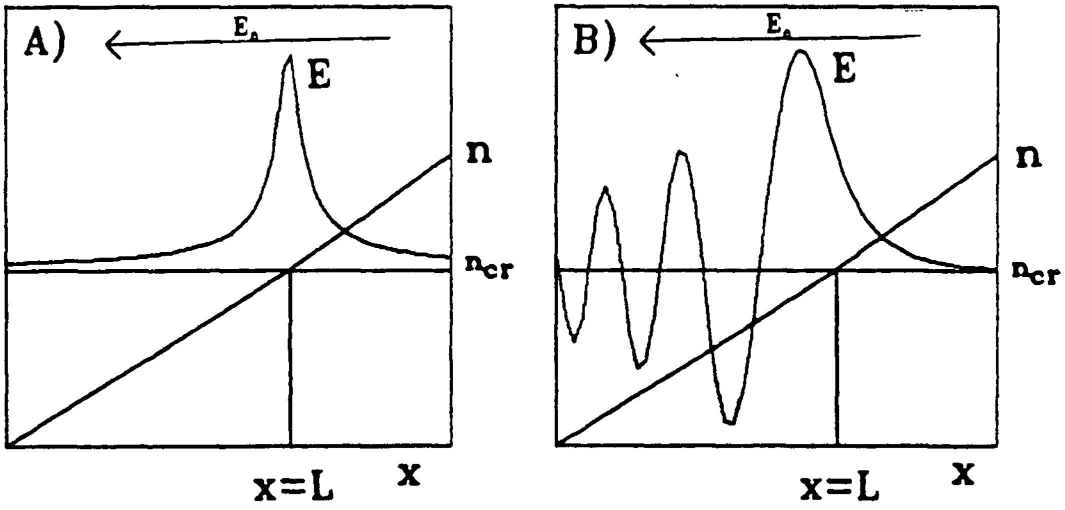

FIGURE 2.5
Electric field of the excited plasma wave for a linear density profile

situation around the critical density point where the waves are excited and it is the geometry for resonant absorbtion. Even for this simpler situation, an analytical solution cannot be found if both the collision term and the thermal term are kept in the fluid equations. A solution can be found for a cold and lossy or for a hot collisionless plasma.

After dropping the thermal term (cold plasma) in Equation 2.1b, a solution of the form:

$$n_e = n_{cr}\frac{x}{L} + \tilde{n}(x,t)$$

$$v_e = v_0 + \tilde{v}(x,t)$$

is introduced in the fluid equations. Here n_{cr} is the critical density where $\omega_{pe} = \omega_0$, $L = n_e/\nabla n_e$ is the scale length of the plasma and $v_0 = v_{os} cos\ \omega_0 t$. The well known solution for the electric field is [18]:

$$E(x,t) = \frac{C}{\sqrt{\left(1-\frac{x}{L}\right)^2 + \frac{\nu^2 x^2}{\omega_{pe}^2 L^2}}} sin(\omega_{pe} + \phi)$$

Where C is a constant. This field is shown on Figure 2.5a at a fixed time. The width W_{cold} at half maximum for the cold plasma approximation is therefore:

$$W_{cold} \approx 2\sqrt{3}L\frac{\nu_e}{\omega_{pe}} \qquad (2.8)$$

For a hot collisionless plasma, the collision term is dropped and the same form of solution is inserted in the fluid equation. The solution for the electric field is [19]:

$$E(x,t) = C\ Ai(u) sin\ \omega_{pe} t$$

With:

$$u = \left(\frac{\omega_{pe}^2}{c_e^2 L}\right)^{1/3} (x - L)$$

Here, Ai is the Airy function [20]. This is plotted at a fixed time on Figure 2.5b. The width W_{th} of the Airy function is about 4 (in the dimensionless unit u). Therefore:

$$W_{th} \approx 4 \left(\frac{\omega_{pe}^2}{c_e^2 L}\right)^{-1/3} = 4 \left(3\lambda_D^2 L\right)^{1/3} \qquad (2.9)$$

Where λ_D is the Deby length. If both collision and temperature terms are present W will be the larger of Equation (2.8) or (2.9).

In our experiment we have an electron temperature of about T_e=100 eV, the effective degree of ionization is $Z^* \approx 6$ and $c_e = 2.1 \times 10^4$ m/s (see Chapter 4). The collision frequency is given by [21]:

$$\nu_e = 3 \times 10^{-6} \frac{n_e Z^*}{T_e^{3/2}} ln\Lambda$$

Here, n_e is in cm^{-3}, T_e is in eV and $\Lambda \approx (c_e/c)^3 \lambda_{laser}^3 n_e$. So for a plasma at the critical density for the CO_2 laser we have:

$$\frac{\nu_e}{\omega_{pe}} = .01$$

The scale length at n_{cr} due the modulated plasma is:

$$L = \frac{n_e}{\nabla n_e} = \frac{n_0}{n_1 k_g}$$

Inserting these numbers we find that the thermal effect produces the larger W. In order to accelerate electrons we must use $\lambda_g < 10.6\ \mu m$. In fact we will see in Chapter 5 that we use $3\mu m < \lambda_g < 7\mu m$. For this modulation wavelength we find that $1 < W_{th}k_g = 4(3\lambda_D k_g n_0/n_1)^{1/3} < 1.6$. This is of the order of 1 and the sinusoidal field approximation is just valid for our experimental parameters. The electric field will be almost sinusoidal with some distortion. This is not damaging to the acceleration process because for such low localisation, the electric field will be coherent over the length of the accelerator

This calculation shows that the approximation $n_1/n_0 << 1$ is valid with the experimental value of $n_1/n_0 = 8\%$. However, we must also check the other approximations made in the linear theory, $v_{os}/v_{ph} << 1$ and $\tilde{n}_e/n_0 << 1$. For the CO_2 laser intensity used during the experiment, $I < 7 \times 10^{11} W/cm^2$, we have $v_{os}/v_{ph} < .006$, which is a small enough value. Finally, we have to verify that the saturation amplitude $\tilde{n}_e/n_0 << 1$. We find that the relevant saturation mechanism for our intensity and collision frequency is collisional damping (Equation (2.5)) and that $\tilde{n}_e/n_0$ is limited to .05. Therefore, the linear theory is sufficient to describe the oscilating plasma grating accelerator with our experimental value of n_1/n_0 and v_{os}/v_{ph}. However, for future experiments with larger plasma density modulation or larger electric fields, a more complete model using computer simulation will be needed.

2.3 Instabilities

So far we have neglected ion motion. If we include this motion, we must consider another set of fluid equations for the ions which are coupled with the electron fluid equation. Solutions to these equations have been found for uniform or linear density change but not for a rippled plasma. For a plasma density around the critical density, two instabilities can be excited [22]. The oscillating two stream instability (OTSI) and the ion-accoustic decay instability (IADI). Both instabilities can produce large amplitude plasma waves at various wavelengths that can destroy the coherence of the plasma wave excited by the oscillating plasma grating accelerator and therefore be damaging to the acceleration process. But these instabilities are only excited above a certain threshold. From reference 22 the threshold for the OTSI in a inhomogeneous plasma with a scale length of L is:

$$\frac{v_{os}^2}{v_e^2} > 2\left(1+\frac{T_i}{T_e}\right)(kL)^{-1} + 4\left(1+\frac{T_i}{T_e}\right)\frac{\nu_e}{\omega_0}$$

Only plasma waves with a phase speed close to the speed of the injected particles are dangerous. The accelerated particles see any other waves as a very high frequency that does not affect their trajectory significantly. We therefore calculate the threshold for $k \approx k_g$. For the few nanoseconds laser pulse used in the experiment we have $T_i < T_e$. Neglecting the gradient due to the modulation, the scale length of the plasma is $L \approx$

$150\mu m$ (see chapter 4) and $\nu_e/\omega_0 = .01$. We find a threshold of:

$$I = 1.6 \times 10^{11} W/cm^2$$

The IADI is convective in the presence of a gradient [22]. The threshold for an amplification of e^A is:

$$\frac{v_{os}^2}{v_e^2} > \frac{1.6A}{kL}\left(1+\frac{3T_i}{T_e}\right)\left(\frac{\nu_i}{\omega_i}\right) + 3.2\frac{\nu_i}{\omega_i}\frac{\nu_e}{\omega_0}$$

Where ω_i and ν_i are the frequency and damping coefficient of the ion-accoustic wave produced. Setting $A = 5$, $k \approx k_g$ and $\nu_i/\omega_i \approx .1$ [22,23] we find:

$$I = 8 \times 10^{10} W/cm^2$$

These threshold intensities are smaller than the intensity used for the experiment ($I \approx 3 - 7 \times 10^{11} W/cm^2$). However the density modulation may change these thresholds and it is not clear if the instability will be excited or not. Even if the instabilities are excited, it is possible that they produce plasma waves at exactly $k = k_g$ because of the large plasma and ion-accoustic waves already present (produced by the imposed modulation) that can act as a seed to start the growth of the instability. The instability would then actually help the acceleration process. Only the exact solution of the fluid equation in presence of a density modulation could determine the effect of these instabilities. However, this is a difficult theoretical problem which has not been discussed in the literature. Though an attempt to derive a satisfactory theory may present a challenge, it is well outside the scope of the present estimates concerning the feasability of the planned acceleration scheme.

2.4 Proof of Principle Experiment

In order to use this method we first need to produce a modulated plasma of controllable wavelength. By irradiating a grating with intense laser radiation one can produce such a plasma. We will explore this technique in more detail in Chapter 4.

We can now design a proof of principle experiment to demonstrate this acceleration scheme, (Figure 2.6).

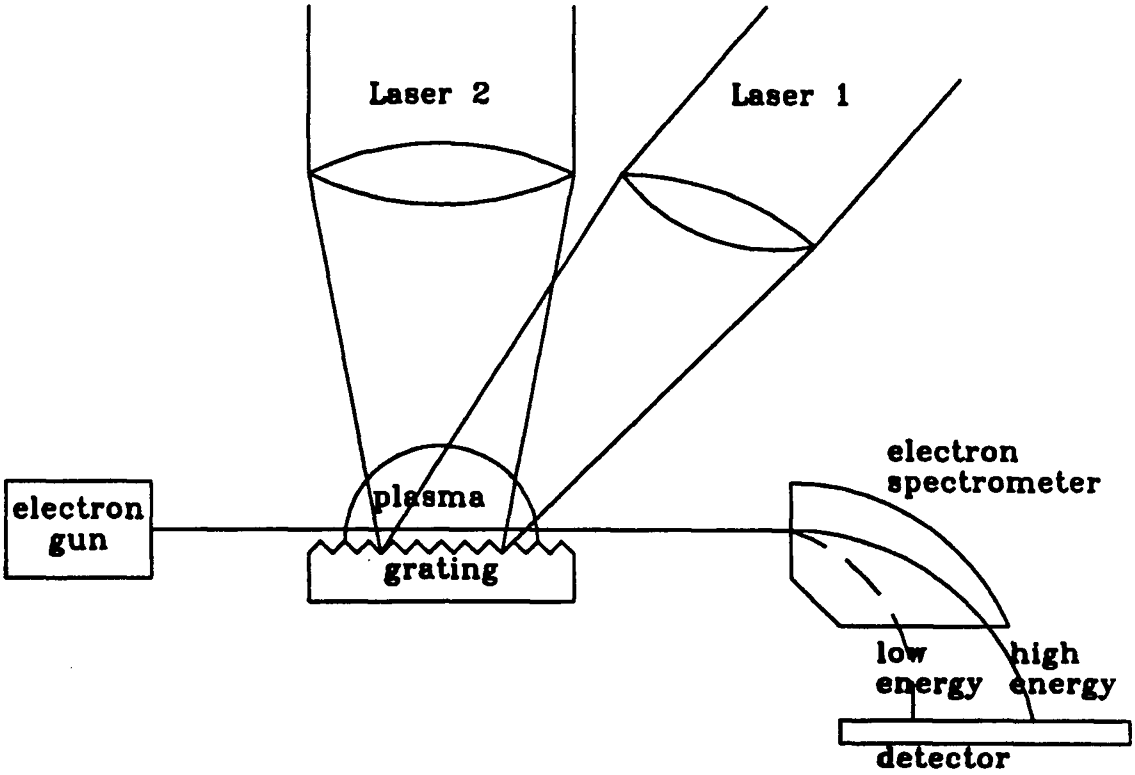

FIGURE 2.6

Proof of principle experiment.

In this experiment, laser one first irradiates the grating and produces the modulated plasma. After a suitable delay, laser two irradiates the plasma and excites the plasma wave. This wave then accelerates the electron beam from the electron gun. The spectrometer measures the gain of energy. In order to estimate this gain and decide on the value of the different parameters (grating spacing, electron gun energy, laser wavelength, etc.) we must look at the available laser systems.

CHAPTER 3

LASERS AND TARGET CHAMBER

Before presenting some experimental results, we describe some of the apparatus used. This chapter describes the lasers, the synchronization techniques developed to insure proper timing between the different lasers and the target chamber.

3.1 The CO_2 Laser

The CO_2 laser is a conventional oscillator, Pockels cell and amplifier system, built specifically for this experiment (Figure 3.1). The hybrid oscillator consists of a continuous wave low pressure section and a transversely excited three atmosphere pulsed section inside the same optical cavity. The low pressure section is filled with 20 Torrs of a gas mixture containing 70% He, 15% N_2 and 15% CO_2. A current of 10 mA produces an 80 cm glow discharge column. The high pressure discharge is generated by a LC inversion circuit (Figure 3.2) in a gas mixture of 84% He, 8% N_2 and 8% CO_2. The capacitor banks on the left and right (total capacitance $C=65$ nF) are both charged to 22 kV and no voltage appears across the laser electrodes. When the spark gap closes the left part of the circuit, the left bank discharges through the preionization rods creating a current I_1. All the resistors shown have high values and can be considered as open circuit during the laser discharge. Due to the inductance of the cables and preionization rods the current I_1 continues to flow after the left capacitors are discharged,

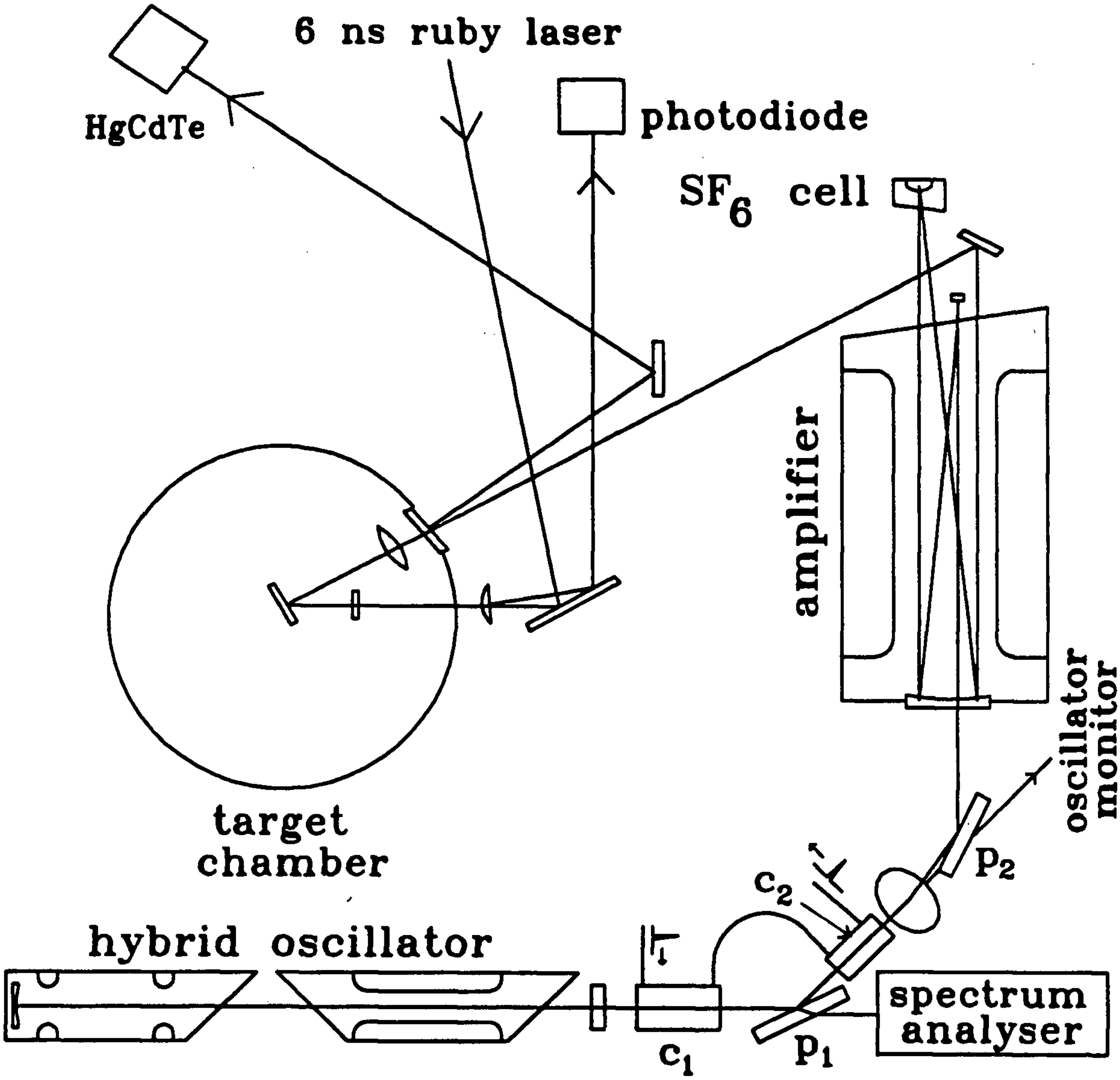

FIGURE 3.1
CO_2 laser and monitoring system
c_1, c_2 Pockels cells
p_1, p_2 Ge polarizers

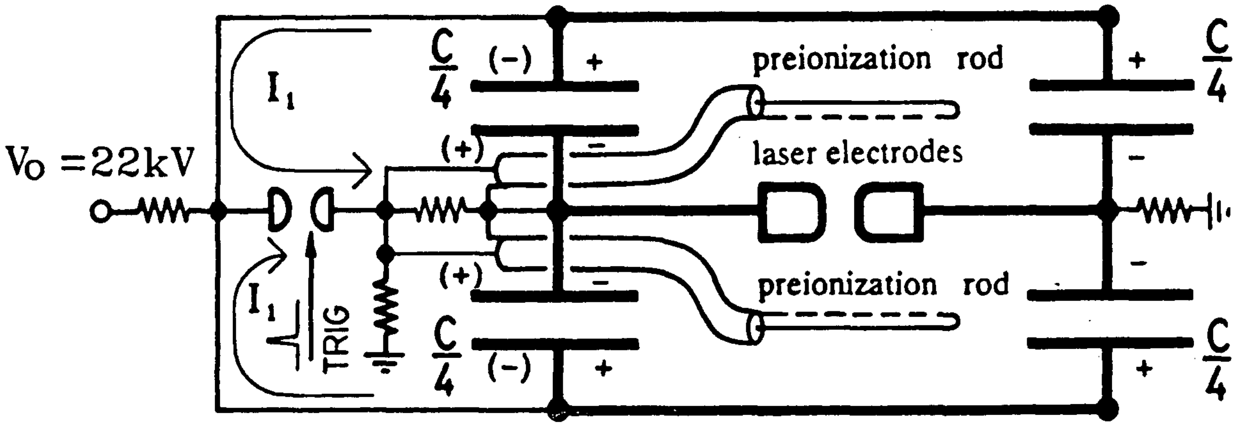

FIGURE 3.2
LC inversion circuit

so they actually recharge with the reverse polarity shown in parenthesis on the Figure (ringing). When the inversion is complete about 44 kV appear across the laser electrodes. The resulting discharge excites the gas mixture.

Because of the low pressure section, only one longitudinal mode can oscillate. But the laser can still oscillate on any of the rotational lines. The P20 line is selected by the temperature controlled Fabry Perot etalon used as an output coupler. This hybrid oscillator produces a temporally smooth 150 mJ, 60 ns pulse. In order to amplify the oscillator pulse to high power without having to use an excessive amount of energy, the pulse length must be reduced. A 1.8 ns pulse is cut out of the 60 ns oscillator output with a system of two Pockels cells in series. The contrast ratio for one cell proved to be insufficient and some pre-plasma was created on the grating before the main pulse arrived. The dimensions of the GaAs crystals used in the two cells are 7x7x80 mm^3 and 5x5x60 mm^3. Because the ratios of length over width of the two Pockels cells are almost the same, the half wave voltage $V_{1/2}$ = 12.5 kV (measured value) is very similar for both cells and we can simply connect them in series. The cable between the cells must be kept short (10 cm) because the signal in the cable travels slower (v=2c/3) than the light pulse. If the electric signal arrives at the second cell later than the laser pulse, no light will be transmitted by the double cell arrangement. The continuous wave beam goes through the first germanium Brewster angle polarizer and is sent into an Optical Engineering CO_2 spectrum analyzer to monitor the oscillator frequency. The frequency is maintained on the P20 line by adjusting the temperature of the output coupler or by changing slightly the alignment of the laser optical cavity. The signal transmitted by the second germanium polarizer is sent inside a room, shielded to reduce electromagnetic noise, to a Labimex P005 HgCdTe detector connected to a Tektronix 466 memory oscilloscope. Both the 1.8 ns pulse and the much weaker 60 ns impulsion are visible on the oscilloscope trace. We can then adjust the timing between the oscillator discharge and the Pockels cells voltage pulse to optimize the output signal. This on-line monitoring is very useful in order to keep the laser working correctly during experimental runs.

The output of the hybrid oscillator and the Pockels cells system is passed five times through the amplifier. A 1.5 cm long gas cell filled with 2 Torr SF_6 and 760 Torr Helium is placed between the third and forth pass to control parasitic oscillation and pre-pulse energy. Self lasing is a persistent problem. Great care, and a bit of luck, are needed when aligning the beam through the amplifier to avoid spurious reflection that can create parasitic oscillation. Also the target grating must be tilted to avoid reflection of the CO_2 beam back into the laser system. The amplifier has been described in reference 20. It is a 1.5 atmosphere, transversely excited discharge driven by a six stage Marx bank generator producing 6x24 kV=144 kV. Ultraviolet preionization is generated by an independent two stage Marx bank which is discharged through two preionization rods 1 μs before the main bank.

The energy on target is measured with a Gen-Tec ED-200-C Joule meter pyroelectric detector. It is 350±100 mJ, (the uncertainty reflects the shot to shot variation). The pulse length is measured with a Labimex P005 HgCdTe detector connected to a 7104 Tektronix oscilloscope (Figure 3.3).

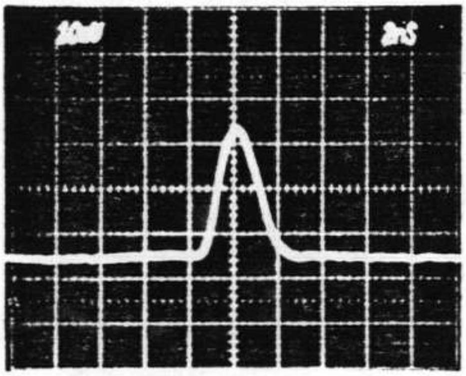

FIGURE 3.3
Temporal shape of the CO_2 laser pulse

This system has a time resolution of 0.5 ns. The FWHM (full width at half maximum) of the pulse is 1.8 ns. The peak power is thus 200 MW.

3.2 CO_2 Laser Focusing

After amplification, the 3 cm diameter beam is focused on target by a 15 cm focal length plano-convex salt lens. In some experiments we need an astigmatic focus with a long axis in the direction of the electron acceleration. This is done by tilting the lens around a vertical axis. We measured the focal spot obtained with and without tilting the lens using a diffraction technique. A metal grid is placed just in front of the focusing lens and a sheet of aluminized mylar is installed in the target plane (Figure 3.4).

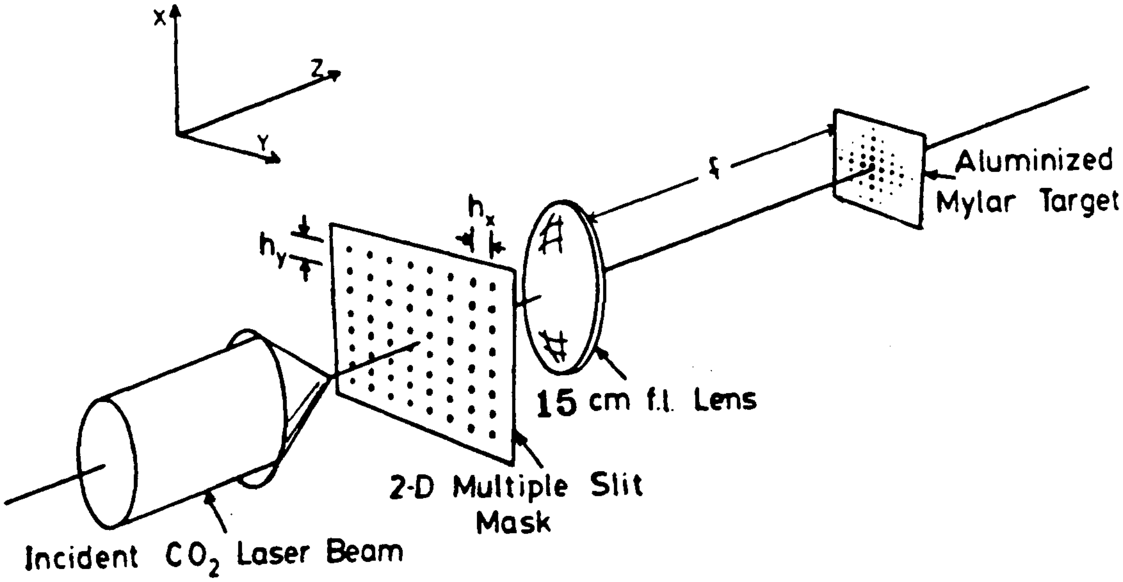

FIGURE 3.4
The experimental arrangement for measuring the intensity distribution at the focal spot

The intensity of the diffraction pattern in the focal plane is [24]:

$$I(x,y) \propto \sum_{m=-\infty}^{\infty} \sum_{n=-\infty}^{\infty} sinc^2\left(\frac{na_x}{h_x}\right) sinc^2\left(\frac{ma_y}{h_y}\right) I_0\left(x - \frac{nf\lambda}{h_x}, y - \frac{mf\lambda}{h_y}\right)$$

Where sinc(x) = sin(x)/x, $a_{x,y}$ is the width of the opening in the metal grid in the x,y direction, $h_{x,y}$ is the distance between each opening in the x,y direction, f is the focal length of the lens, λ is the wavelength of the laser and $I_0(x,y)$ is the intensity distribution in the focal plane in the absence of the grid. $I_0(x,y)$ is what we want to measure.

Each diffraction spot has the same intensity distribution as the unperturbed focal spot but is reduced by a factor $sinc^2(ma_x/h_x)$ $sinc^2(na_y/h_y)$. Because the intensity needed to burn through the aluminum coating on the mylar is constant, the edge of the burn mark traces a contour line of equal intensity for each diffraction spot. Therefore, from the burn mark on the aluminized mylar, we can reconstruct the beam profile.

The graph in Figure 3.5 represents the beam profile in the focal plane of the untilted lens. It indicates an approximately gaussian profile with a 1/e diameter of w=70±20 μm down to a relative intensity of 1/20. At lower intensities a wider profile with w=180±30 μm is inferred from the data. This wide, low intensity halo around the focal spot is due to some non uniformity in the laser beam before the focusing lens. The intensity distribution in the focal plane is the Fourier transform of the laser intensity before the lens. Thus any high spacial frequency perturbation of a perfect gaussian will be focused away from the optical axis and create the low intensity halo. The energy in the halo is 1/3 of the total energy. So only 2/3 of the power goes into the normal focal spot.

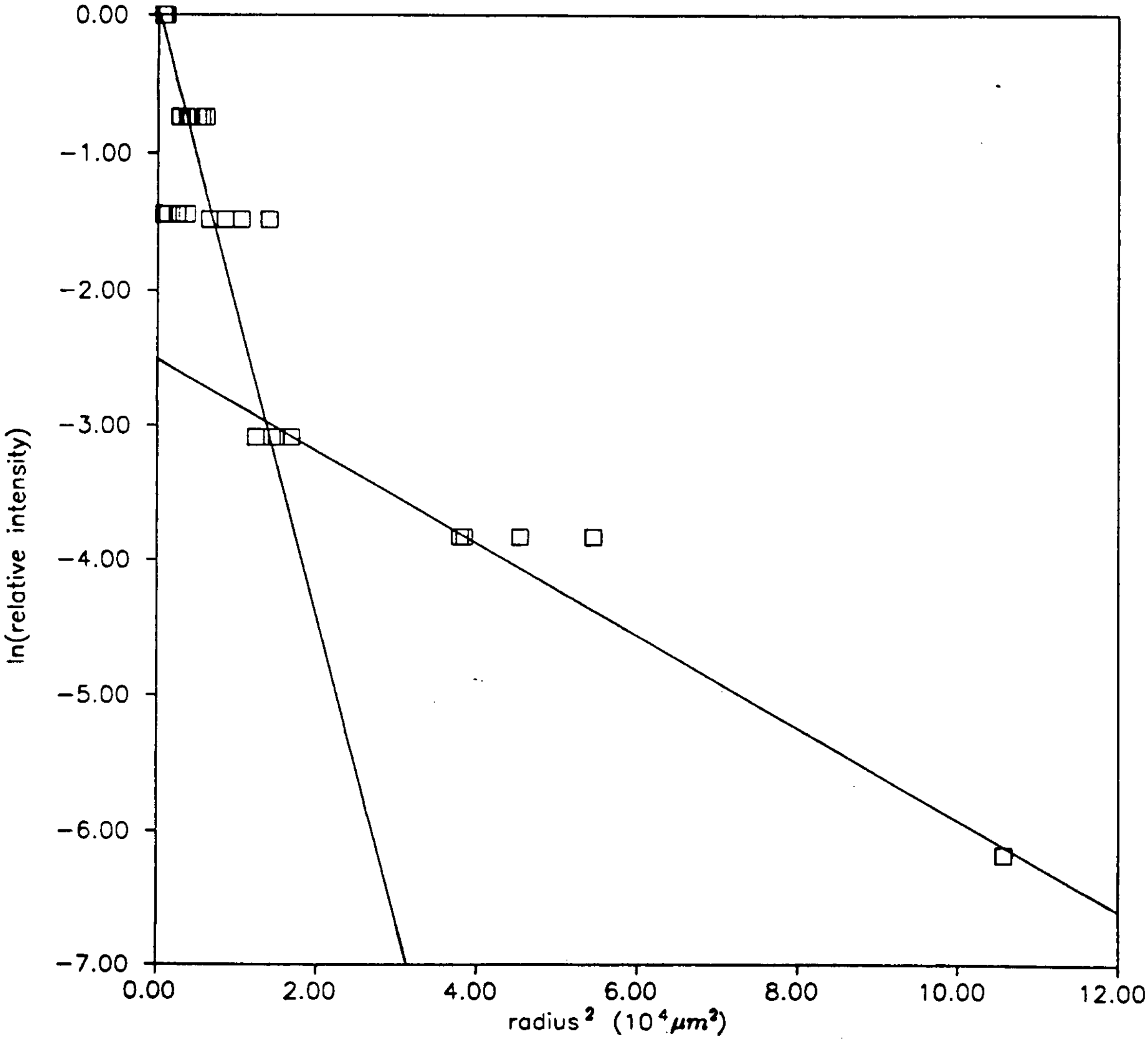

FIGURE 3.5

Intensity distribution at the focal spot

The same technique was used with the tilted lens. The burn spots were measured along their long axis (l) and short axis (s). All the results are summarized in table 3.1.

Tilt Angle (degrees)	Spot Size $(w_s x w_l)\mu m^2$	Peak Intensity W/cm^2	Peak Electric Field V/m
0^o	70 x 70	7.5×10^{11}	2.4×10^9
20^o	80 x 175	3×10^{11}	1.5×10^9

TABLE 3.1

CO_2 Laser Intensities

3.3 The 80 ps Ruby Laser

This short pulse laser is a Q-switched, mode-locked, cavity dumped oscillator of a special design (Figure 3.6) [25]. When the spark gap is triggered, a voltage step is sent along cable L_1. The Pockels cell acts as an open circuit and reflects the voltage step. At the other end of the cable, the spark gap provides a short circuit and also reflects the voltage wave, but reversing the polarity. In this way a voltage square wave is applied on the Pockels cell, initially oscillating with an amplitude of $\pm V_{1/4}$. Therefore the modulator produces a series of short reflectivity pulses when the voltage of the Pockels cell crosses zero. These pulses are recurring at integer multiples of the cable round trip time. If the cavity of the laser is adjusted to have the same round trip time, mode locking occurs. The spark gap also discharges cable L_2 into the cavity dump Pockels cell. The length of cable L_3 must be adjusted so that the cavity is dumped when the light pulse has reached maximum power.

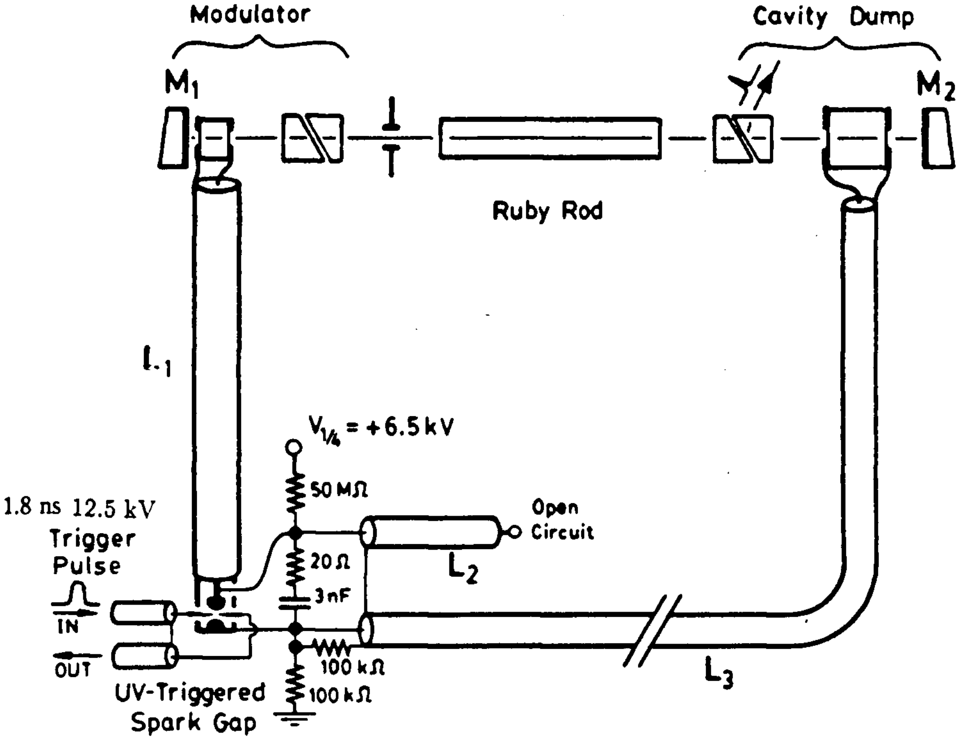

FIGURE 3.6

Schematic of the Q-switched, mode-locked and cavity-dumped ruby oscillator.

This laser is used directly, without amplifier, for diagnostic purposes. It generates a pulse of 85 mJ, 80 ps FWHM for a power of 1 GW. The laser pulse is focused with a f=150 cm plano convex lens to back light the plasma for shadowgraphy and interferometry. The f/75 focusing insures an almost parallel beam across the plasma. For shadowgraphy we image the plasma, and also the focal spot of the diagnostic laser, on a camera. The spot size of the 80 ps ruby laser was measured directly from one of these pictures. It is 1 mm FWHM.

3.4 The 6 ns Ruby Laser

This laser is a Q-switched, cavity dumped ruby oscillator followed by a spatial filter and an amplifier. The operating principle of this laser is very similar to that of the 80 ps ruby laser (Figure 3.6). The modulator cable L_1 is discharged into a 50 Ω impedance matched load. So the voltage on the Pockels cell simply falls to zero (in place of oscillating between $\pm V_{1/4}$), Q switching the laser. The cavity is dumped after a suitable delay. More information on this laser is available in reference [25]. The laser produces a 800 ±100 mJ, 6ns FWHM pulse at the exit of the amplifier. The standard deviation of 100 mJ comes from the average over many shots and indicates the shot to shot stability. Therefore the peak power is 130 MW.

This beam is then brought to the target following a complicated path. It is focused onto the target by a 30 cm plano convex lens followed by a 10 cm cylindrical lens (Figure 3.7). The losses at each optical surface (glass optics with no anti reflection coating, aluminum mirrors and a 30% beam splitter used to extract a diagnostic beam) add up, and only 150 mJ is delivered on target. The focal spot was not directly measured but the plasma produced when this laser beam strikes the grating was well diagnosed (see chapter 4). If we suppose that the size of the early plasma (less than 6 ns after the laser impact), is representative of the size of the focal spot, we find a line focus size of about 1.6 mm by 0.4 mm. This gives a peak intensity of 10^{10} W/cm^2.

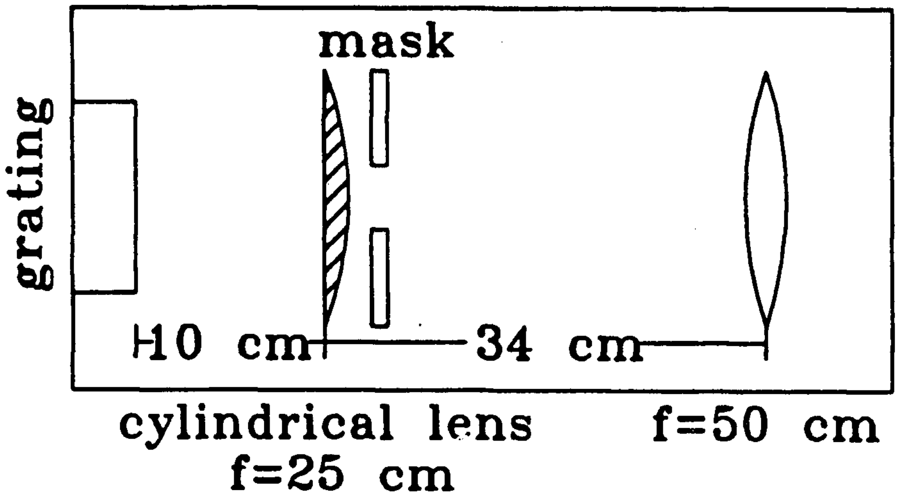

FIGURE 3.7
6 ns ruby laser focusing optic

3.5 Synchronization

In almost all the experiments carried out for this thesis, proper synchronization of the pulses produced by the CO_2 laser, 6 ns ruby laser and 80 ps ruby laser are necessary. We also have to synchronize the streak cameras, used to record the results of different experiments, with the lasers. We will now describe the system that accomplishes this function.

A 16 channel electronic adjustable delay unit is triggered with a push button by the operator when everything is ready (Figure 3.8). With suitable delays, the 40 volt signals from this unit fire the 6 ns ruby laser oscillator flashlamps (SCR 1) and amplifier flashlamps (SCR 2), the 80 ps ruby laser oscillator flashlamps (SCR 3), the CO_2 laser oscillator discharge (Krytron 4), the CO_2 amplifier preionization (Krytron 2) and main discharge (Krytron 3). The delay unit signal is stepped up to a high voltage by a silicon current rectifier (SCR) to fire the flashlamps and by a krytron unit to trigger the CO_2 oscillator and amplifier spark gaps. This can be accomplished with a timing jitter of about 10 ns between the 40 volt signal from the delay unit and the actual firing of the flashlamps and spark gaps.

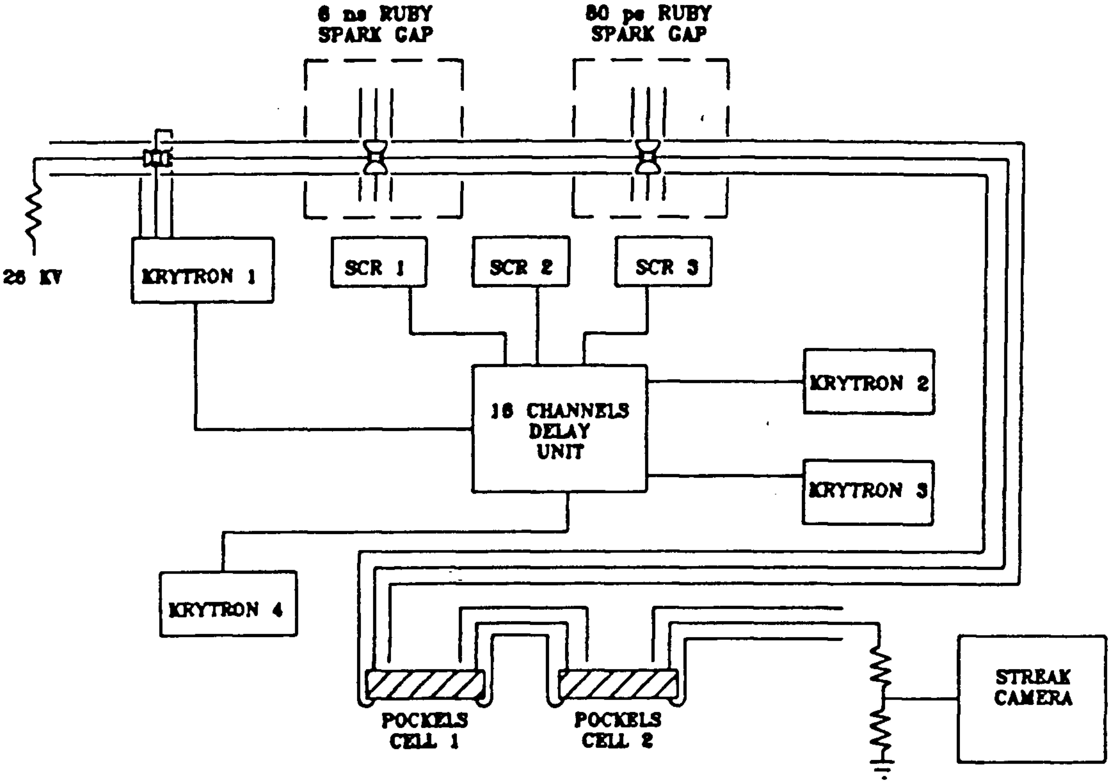

FIGURE 3.8
Laser synchronization diagram

This would be an unacceptably large imprecision but the exact time at which the different laser pulses are produced depends on the switching of the Pockels cells, not on the firing of the flashlamps or CO_2 discharges. (If the Pockels cells are switched within a relatively large timing window of 50 ns). We cannot use signals from the electronic delay unit to trigger each of the Pockels cells individually as it would produce too much jitter. To avoid excessive jitter the following system is used.

A 10 cm long 50 ohm cable is charged to 25 kV. A 40 volt signal from the delay unit, stepped up to a high voltage by Krytron 1, triggers a spark gap. This sends a 1.8 ns FWHM, 12.5 kV pulse along a RG8/U 50 ohms cable. The pulse goes through the trigger pins of the 6 ns ruby laser spark gap, then through the trigger pins of the 80 ps ruby laser spark gap, to the CO_2 laser Pockels cells and finally to the streak camera. The jitter between all the lasers is less than 0.5 ns. The delays can be adjusted by varying the length of cable between the different lasers. If one, or both, of the ruby lasers is not used, it can be disconnected out of the circuit.

3.6 Monitoring

We want to know the intensities and the relative timing of the CO_2 and 6 ns ruby lasers on-line for each experimental shot. In order to accomplish this, we used the set-up shown on Figure 3.1. The monitor beam for the 6 ns ruby laser is created by the 4% reflected from the plane surface of the plano convex lens. This beam is then focused on a fast H.P. 5082-4200 photodiode. The signal is sent to a Tektronix 466 memory oscilloscope inside the screen room. For the CO_2 laser, the monitor beam comes from the 8% reflected on the flat salt window of the target chamber. It is then focused on a fast HgCdTe detector. The signal is sent to the same oscilloscope as for the ruby laser. The optical delays before the detectors and the cable delays are adjusted to be identical. Both signals are added and displayed on the same oscilloscope trace. The relative timing and the intensities of both lasers can be read directly after firing the lasers. Calibration shots are occasionally taken. A Gen-Tec ED-200-C pyroelectric energy meter is installed just after the focusing lens of the CO_2 laser or of the ruby laser. It reads the energy delivered on target, taking into account reflection losses of the optics. The energy signal is recorded on a Tektronix 466 oscilloscope and for the same shot the HgCdTe or H.P. photodiode response is measured. This allows a good calibration of the monitoring system.

3.7 Target Chamber

The target chamber is a 24" diameter 12" high aluminum cylinder (Figure 3.9). Twenty ports are evenly distributed around the circumference, one every 18°. The four 4" diameter ports positioned every 90° and the sixteen 2 1/2" diameter ports in between allow access for laser beams, electric feedthrough, mechanic feedthrough and optic guides. The bottom of the chamber is a 2" centre to centre square array of tapped holes allowing easy mounting of different experimental apparatus anywhere on the surface. A 4" diameter Balzers diffusion pump with a water cooled cold trap backed by a mechanical pump can create a vacuum of $5x10^{-5}$ Torr.

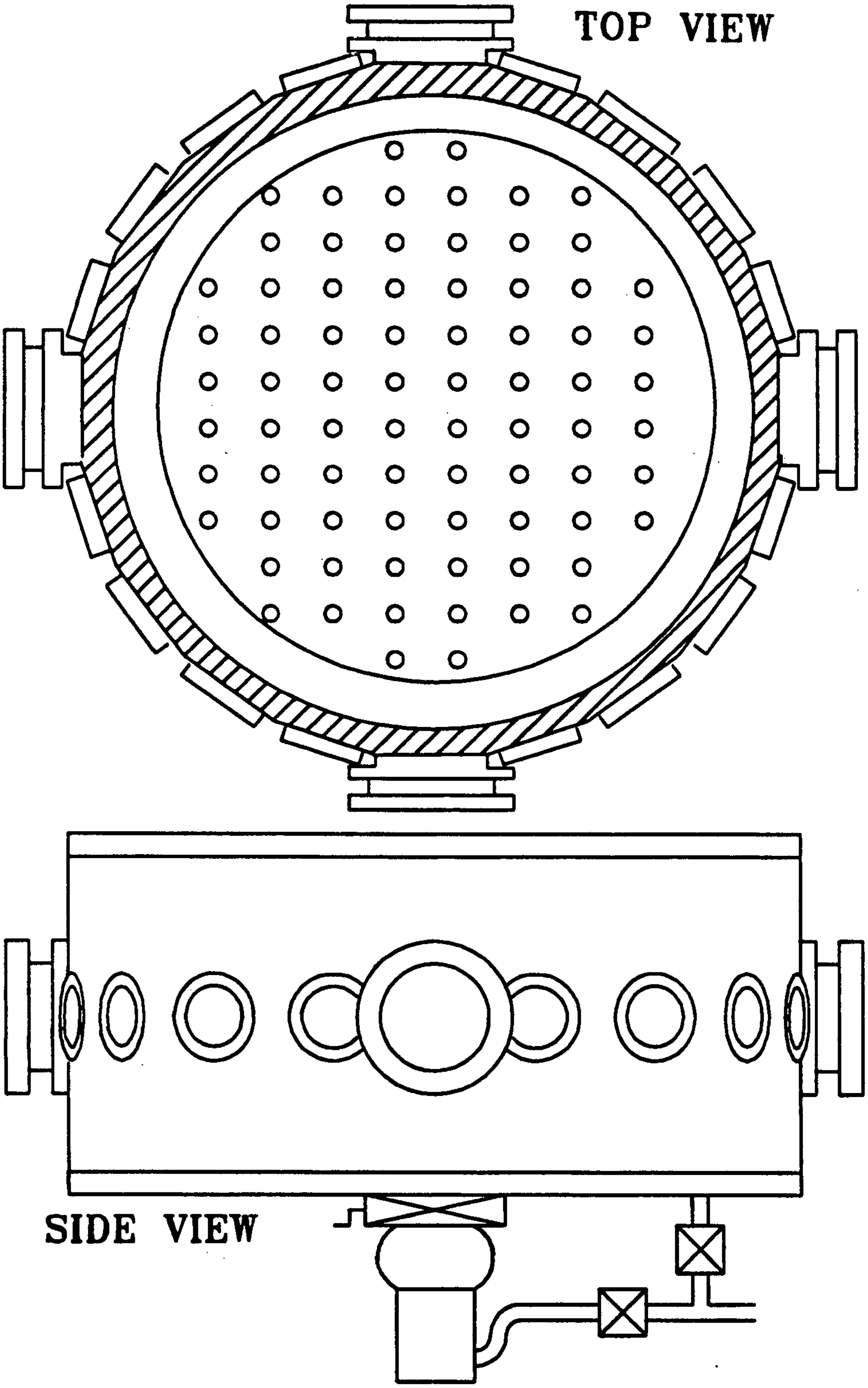

FIGURE 3.9
Target chamber

This pressure is necessary for the operation of the electron gun and electron spectrometer. For laser plasma experiments without the electron gun, only the mechanical pump is used. This pump evacuates the chamber to 20 mTorr in about 10 minutes.

Having familiarized ourselves with the target chamber and the performance of the lasers, we can now proceed to observe the modulated plasma expanding above a laser irradiated grating.

CHAPTER 4

PRODUCTION AND DIAGNOSIS OF THE MODULATED PLASMA

At the end of Chapter 2 we explained that the plasma expanding above the surface of a laser irradiated grating should be modulated with the periodicity of the grating. In this chapter we check this statement experimentally, and study the modulations to find out if they are suitable for the oscillating plasma grating accelerator.

4.1 Diffraction Order of an Expanding Plasma Grating

In order to determine if the plasma above an expanding plasma grating is modulated, we set up the preliminary test experiment shown in Figure 4.1. Only the zero order and one of the first orders are sent to the streak camera.

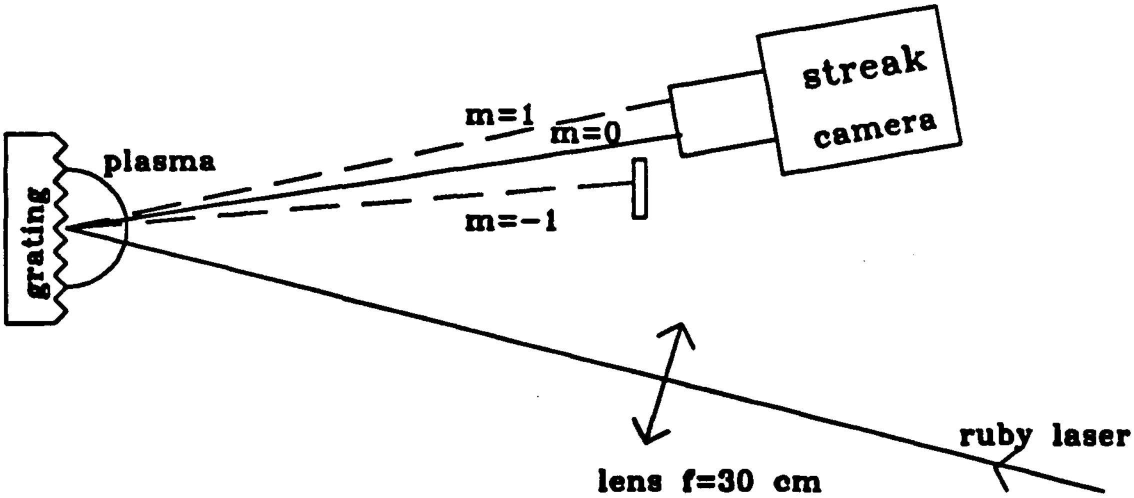

FIGURE 4.1
Set up to measure the diffraction efficiency of an exploding grating.

The streak camera observes simultaneously the zero (m=0) and first (m=1) order of diffraction of the grating irradiated by the 6 ns ruby laser. In this experiment the ruby laser was focused on the target by a 30 cm plano-convex lens to a focal spot of about 100 μm diameter (estimated from the size of the damage on the grating), giving an intensity of 6×10^{11} W/cm^2. The target is a Edmund Scientific 530 lines/mm stamped plastic grating with aluminum coating. The result of this experiment is shown in Figure 4.2.

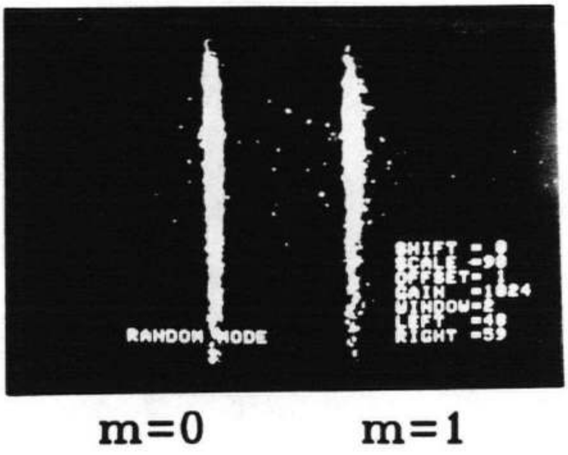

FIGURE 4.2
Streak picture of the m=0 and m=1 intensity.

We also plotted the ratio of the first order intensity over the zero order intensity as a function of time on Figure 4.3. We see that this ratio stays fairly constant for the full 6 ns of the laser pulse. This indicates that the ruby critical layer, where the laser light is reflected, is modulated for at least 6 ns after the beginning of the laser pulse and keeps diffracting light in the first order. Or alternatively, the plasma stays underdense for the full duration of the laser pulse and the diffracted beams are produced by the grating surface.

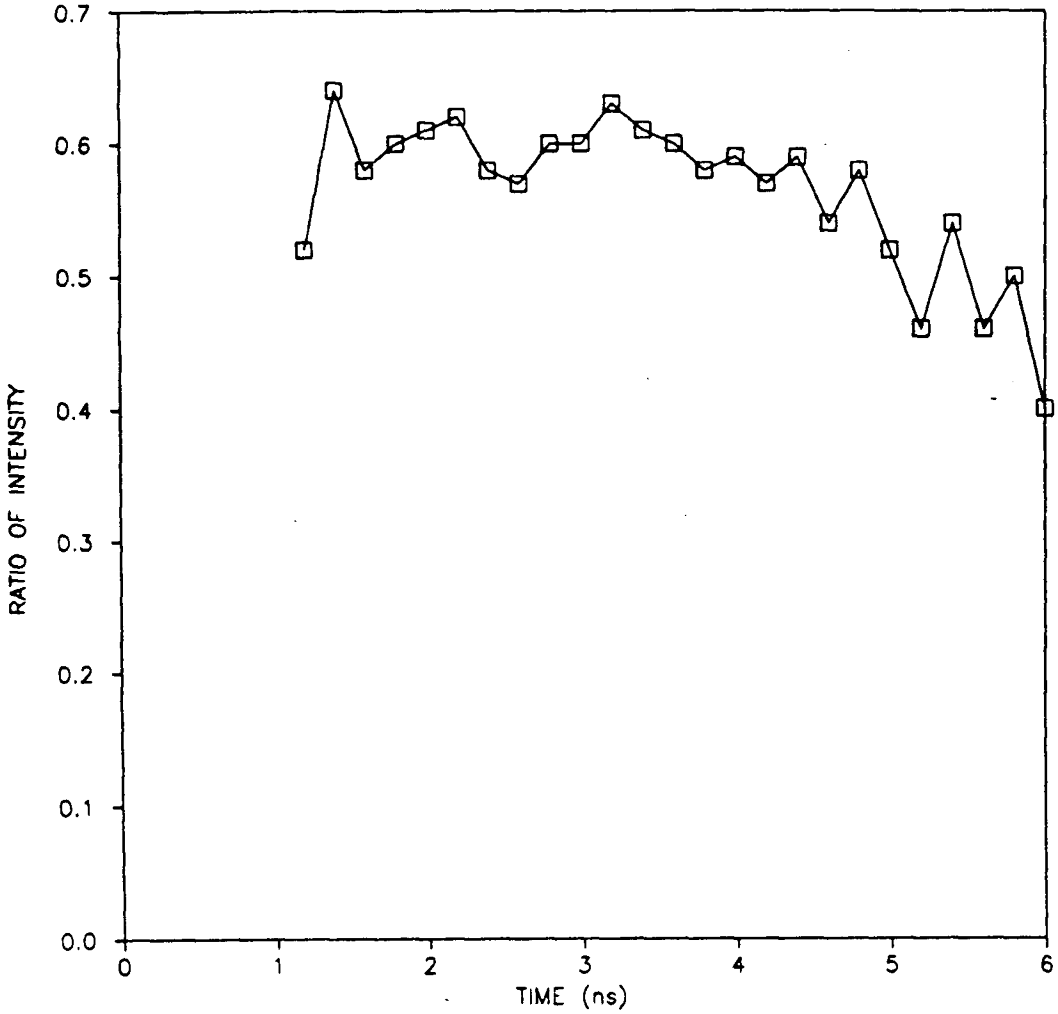

FIGURE 4.3

Ratio of I_1 over I_0 as a function of time.

The critical density n_{cr} for the ruby laser is 2×10^{20} cm^{-3} and solid density is about 10^{23} cm^{-3}. The plasma is surely overdense, but possibly only very close to the grating. This dense plasma is modulated but the plasma of interest for acceleration is the critical layer for the CO_2 laser, which at 10^{19} cm^{-3} is 20 times less dense than n_{cr} for the ruby laser. This density is reached much farther from the grating surface than the ruby critical density. The described experiment does not probe this region of the plasma. We have to observe the plasma modulation around the CO_2 critical density using a more direct method. Shadowgraphy and interferometry can directly image the plasma. Raman-Nath scattering will also be used to probe the modulation in the index of refraction of the plasma. But the spacing of 1.9 μm of the plastic grating is too small and would be very difficult to image. Also the phase speed of the plasma wave that can be created above this grating is only 0.18 c, corresponding to an electron energy of 16 keV. A larger grating spacing is necessary to accelerate electrons to a higher energy.

4.2 Gratings

We employed two types of grating. The first, a brass relief grating, (Figure 4.4a), is fabricated on a lathe by spinning a brass rod and cutting a fine thread with a sharp tool at a very low feed rate. Any spacing down to 6 μm can be generated. Because of the fabrication method, a curved surface is produced, but this is not significant since the area that the laser irradiates is much smaller than the radius of curvature of the brass rod.

The second type of grating is made of alternate lines of gold and photo-resist (Figure 4.4b). A substrate of glass is first coated with chromium, then a thick ($\sim$1 μm) layer of gold is deposited on it. The chromium undercoat ensures good adhesion of the gold layer. Then 1.3 μm of Shipley S1400 photoresist is spun on the gold coated glass. The grating lines are then produced by lithography. Any spacing down to 2 μm can be produced.

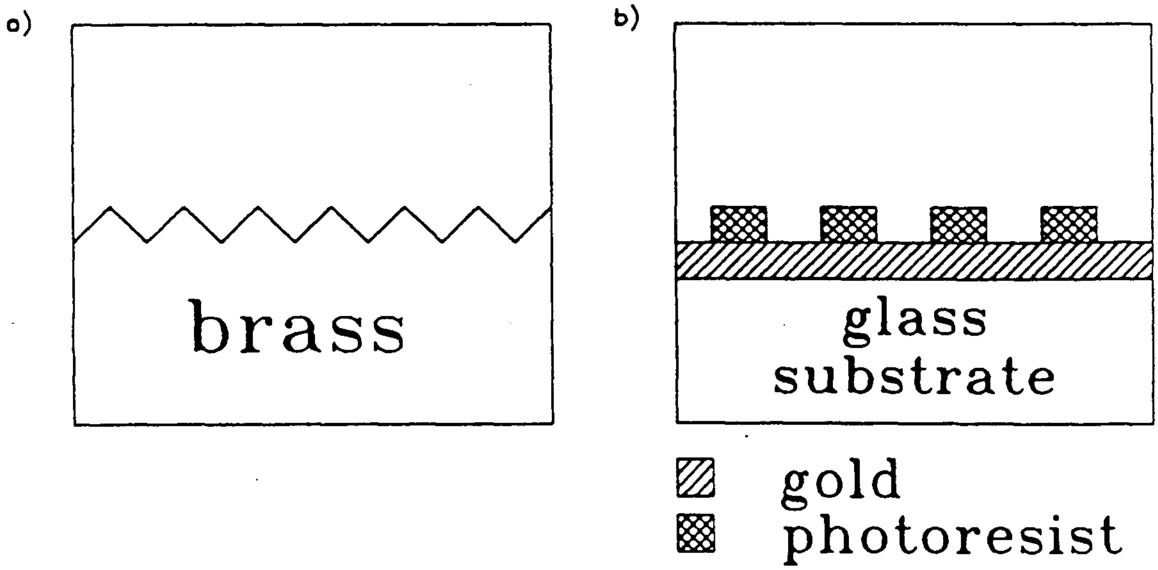

FIGURE 4.4

Details of the brass a) and lithographic b) gratings.

4.3 Experimental Set Ups

We will now irradiate these gratings with the 6 ns ruby laser and observe the plasma expanding above their surface. Three different techniques can be employed to diagnose the plasma. The first, interferometry, is the best method for obtaining information on the plasma density. It gives direct quantitative measurements of the plasma density modulation. However, we will see that it becomes impossible to detect the modulation for grating spacings smaller than 20 μm. Shadowgraphy proved to be the best method to observe the smaller modulations, but it lacks quantitative precision. Finally we will employ Raman-Nath scattering in an effort to obtain a more precise value of the amplitude of the modulation.

4.3.1 Interferometry

A Mach-Zehnder interferometer was set up to obtain interferograms of the plasma, using the 80 ps ruby laser (Figure 4.5).

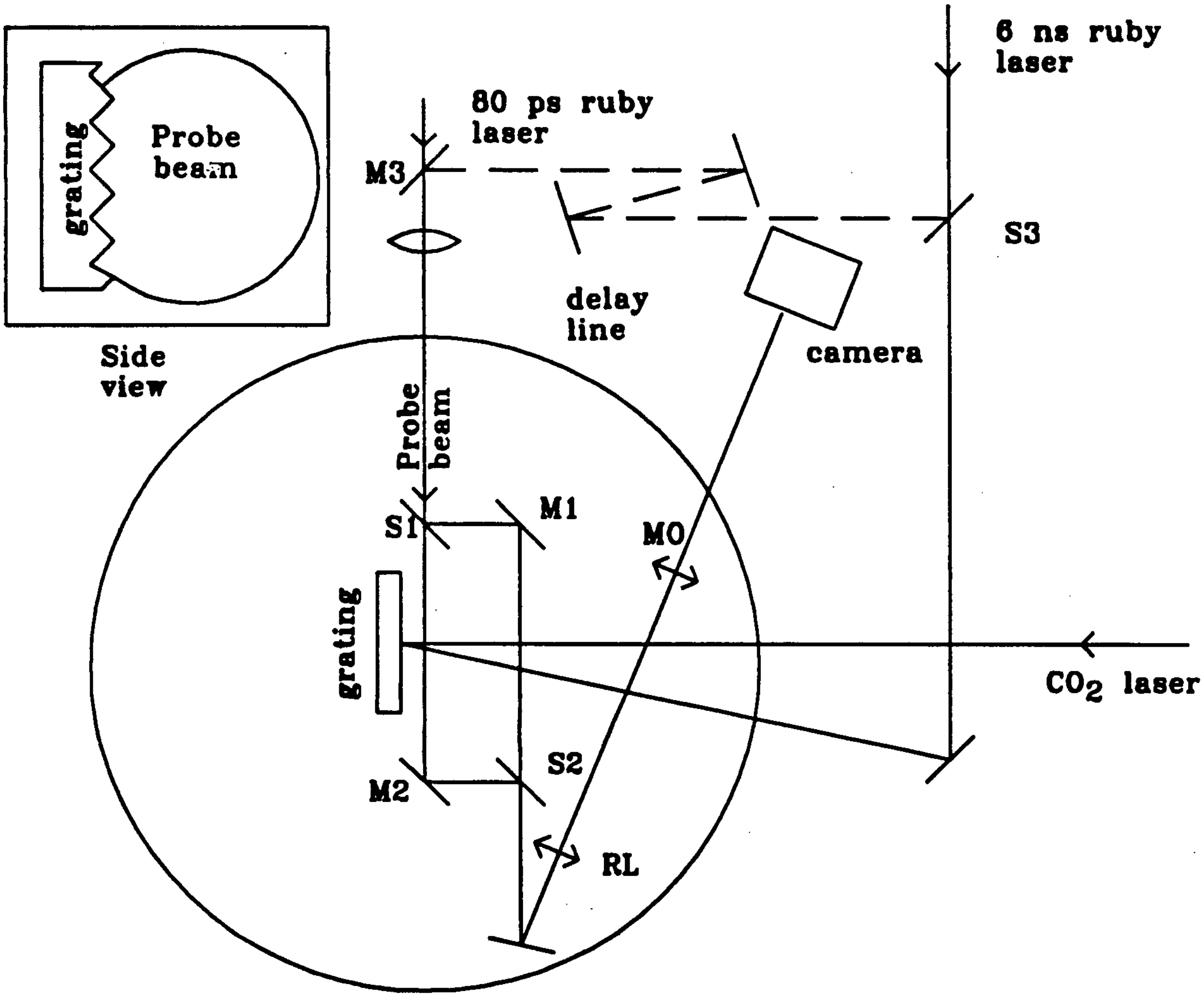

FIGURE 4.5
Set up for interferometry.

The probe beam is focused through the plasma with a lens (f=150 cm). This arrangement (f/75) produces a nearly collimated probe beam going through the plasma just above the grating. The 50% beam splitters S1, S2 and the mirrors M1, M2 form the interferometer. The relay lens RL (f=15 cm, f/2.8) images the plasma in front of the microscope objective MO (X5, .12 n.a.) which re-images the plasma onto the camera with a large magnification. The focal length of MO is too short to image the plasma directly from outside the interferometer. The 10% beam splitter S3 and the mirror M3 are only installed for time resolved interferometry. The probe beam passes through the plasma just above the grating as shown in the side view insert. We will find in section 4.5.1 that the plasma has a sound speed of $c_s=2.7\times10^4$m/s. During the 80 ps exposure, the plasma moves by only 2 μm. Any plasma feature with a scale length longer than 2 μm can therefore be observed.

In early experiments the interferograms were recorded on polaroid 667 photographic film. Later we used a Hamamatsu vidicon camera and frame memory system. This system is the image capture part of the Hamamatsu (model HTV-C1370-01/111) streak camera. This allowed us to perform direct computer analysis of the pictures.

The relative timing between the 80 ps diagnostic laser and the 6 ns main laser can be adjusted to any desired value within a jitter of ±500 ps. Thus, interferograms can be taken at different times and in principle the time evolution of the plasma can be found. However, due to the timing jitter and the variation in laser intensity from shot to shot this technique does not permit us to determine the precise time evolution of the plasma.

4.3.2 Time Resolved Interferometry

For time resolved interferometry the interferogram is generated by a probe beam split (10%) from the 6 ns main laser pulse using S3 and M3, (Figure 4.5). The main beam is focused onto the grating and produces the plasma. The probe pulse is optically delayed in a variable delay line and is focused in the plasma inside the Mach-Zehnder interferometer using a lens of 150 cm focal length. The optical system after the interferometer is the same as for the 80 ps interferometry but the camera is replaced by the streak camera. The slit of the Hamamatsu streak camera is imaged perpendicularly to the surface of the grating (as outlined in Figure 4.10). We obtain the plasma density as a function of height above the grating and time. By changing the optical delay between the probe and main beam the time evolution can be obtained in intervals of 6 ns.

Because of the poor spatial and temporal coherence of the ruby laser, great care was taken in the adjustment of the Mach-Zehnder interferometer. Both optical paths must have the same length and the two beams must be perfectly superimposed after the second beam splitter.

Interferometry gives useful information about the bulk motion of the plasma but the density modulations are difficult to see, especially for gratings with spacings $<20\ \mu m$. For the small spacing, shadowgraphy proved to be a more sensitive, though less quantitative, method.

4.3.3 Shadowgraphy

The set up shown on Figure 4.6 recorded shadowgrams.

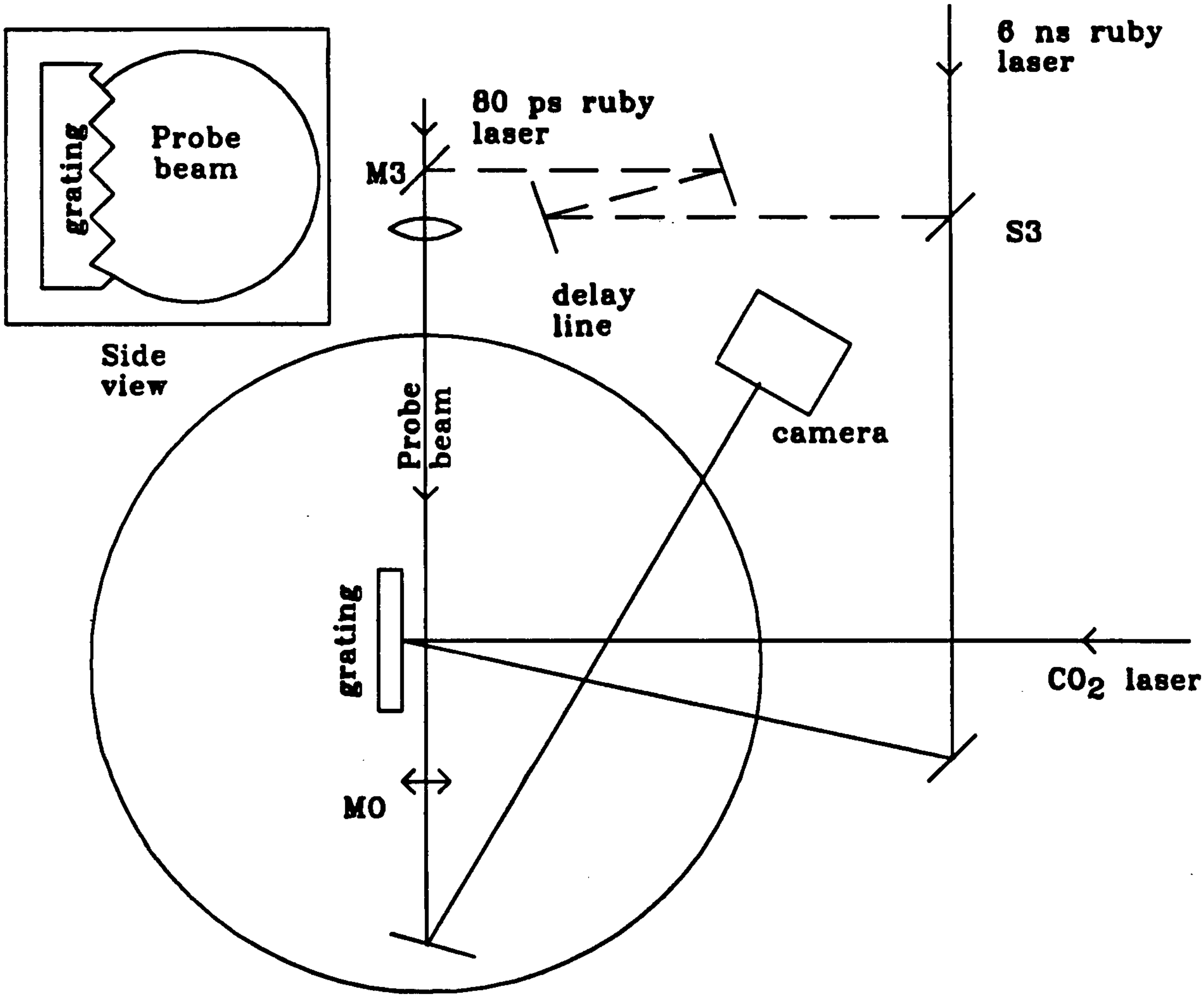

FIGURE 4.6
Set up for shadowgraphy.

The plasma is produced by the same optical system as in the interferometric experiment. The 80 ps pulse from the mode locked ruby laser (with a variable delay) is focused through the plasma using the lens of 150 cm focal length. The 5x microscope objective utilizes this light to image a plane 500 μm beyond the middle of the plasma on a 667 polaroid film. Later the vidicon camera was employed instead of the polaroid film. The relay lens was not necessary in this set up because the microscope objective could be placed close enough to the plasma. Shadowgrams with a 6 ns exposure were also taken with a probe beam split (10%) from the main beam, delayed and then focused on the plasma with the same $f=150$ cm lens.

Because most of the plasma was underdense at the ruby wavelength, only the change in the index of refraction produced the image. A modulated plasma appears on a shadowgram as light and dark bands, due to the alternate focusing and defocusing of the probe light (Figure 4.7). In order to produce shadows, a plane behind the plasma has to be imaged.

We also produced streak shadowgrams. For these experiments, we replaced the 80 ps ruby laser with 10% of the 6 ns ruby laser beam. The slit of the streak camera was imaged parallel to the surface of the grating and at different heights above it.

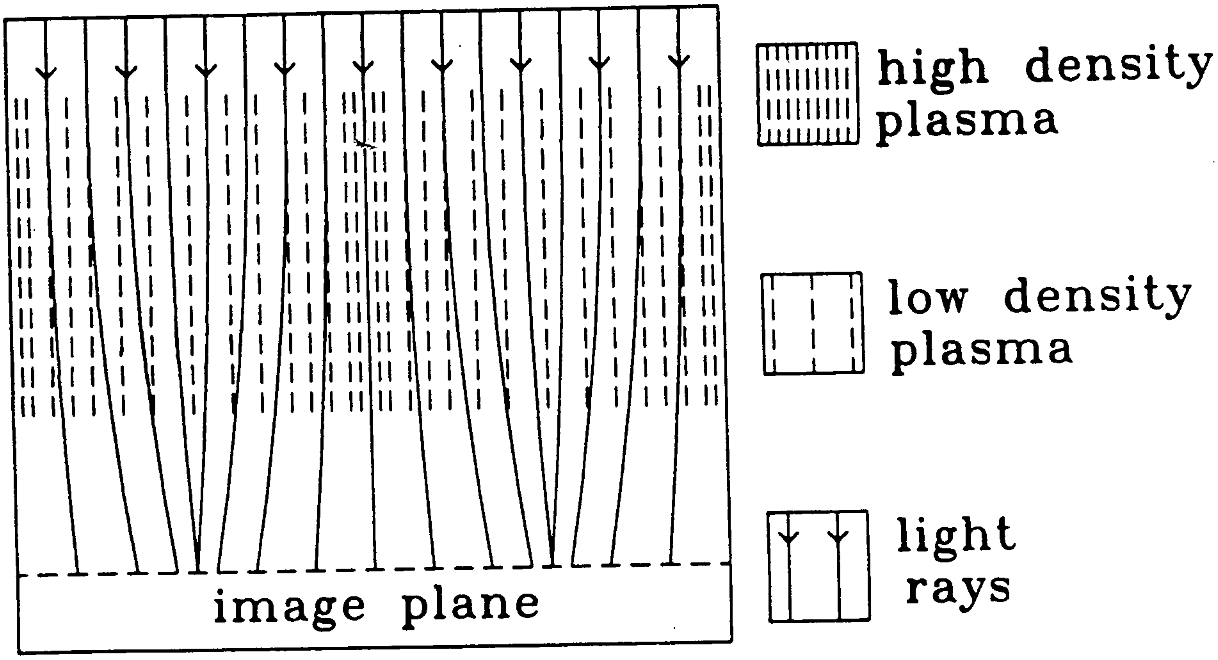

FIGURE 4.7

Shadowgram produced by an underdense modulated plasma.

4.3.4 Raman-Nath Scattering

Instead of imaging the plasma, we can observe directly the diffraction pattern produced when the probe laser beam passes through the modulated plasma (Figure 4.8). This method is called Raman-Nath scattering.

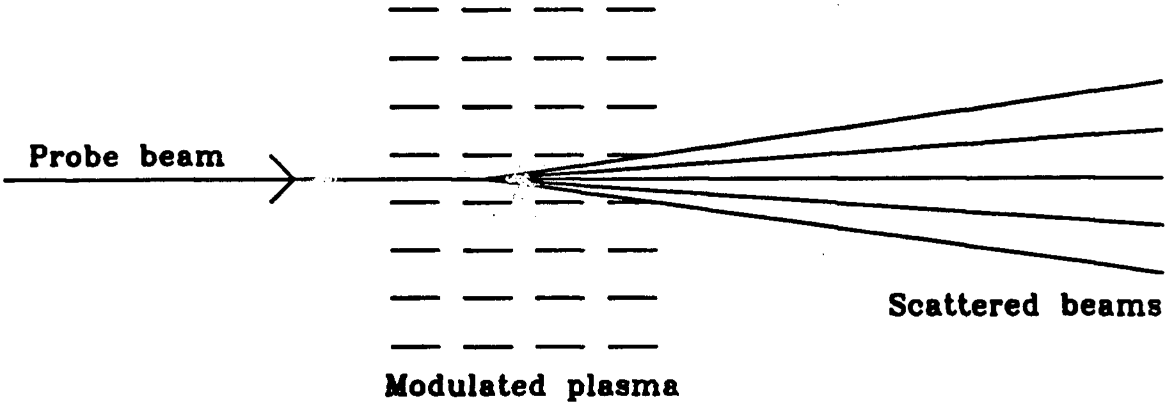

FIGURE 4.8
Raman–Nath scattering.

In order to eliminate the diffracted beam created when part of the probe beam illuminates the grating, and to increase the signal to noise ratio, a slightly more complicated arrangement was set up (Figure 4.9). The microscope objective MO1 images the shadowgram of the plasma onto the film. The beam splitter S4 produces a second image in the plane of the slit. The slit (dashed rectangle in the side view) is adjusted to reject the light coming from the grating and the light that passes too high above the surface. Only the light that has passed through the modulated plasma remains. Immediately after the slit, the light passes through the lens L1 and is focused in the plane FTP. The image formed in this plane is the Fourier Transform of the image just before the lens.

This image is the same pattern (except for a scale factor) as the far field diffraction pattern obtained by simply passing the laser beam through the modulation (as shown on Figure 4.8). This Raman-Nath image is then magnified by the microscope objective MO2 onto the film in the camera.

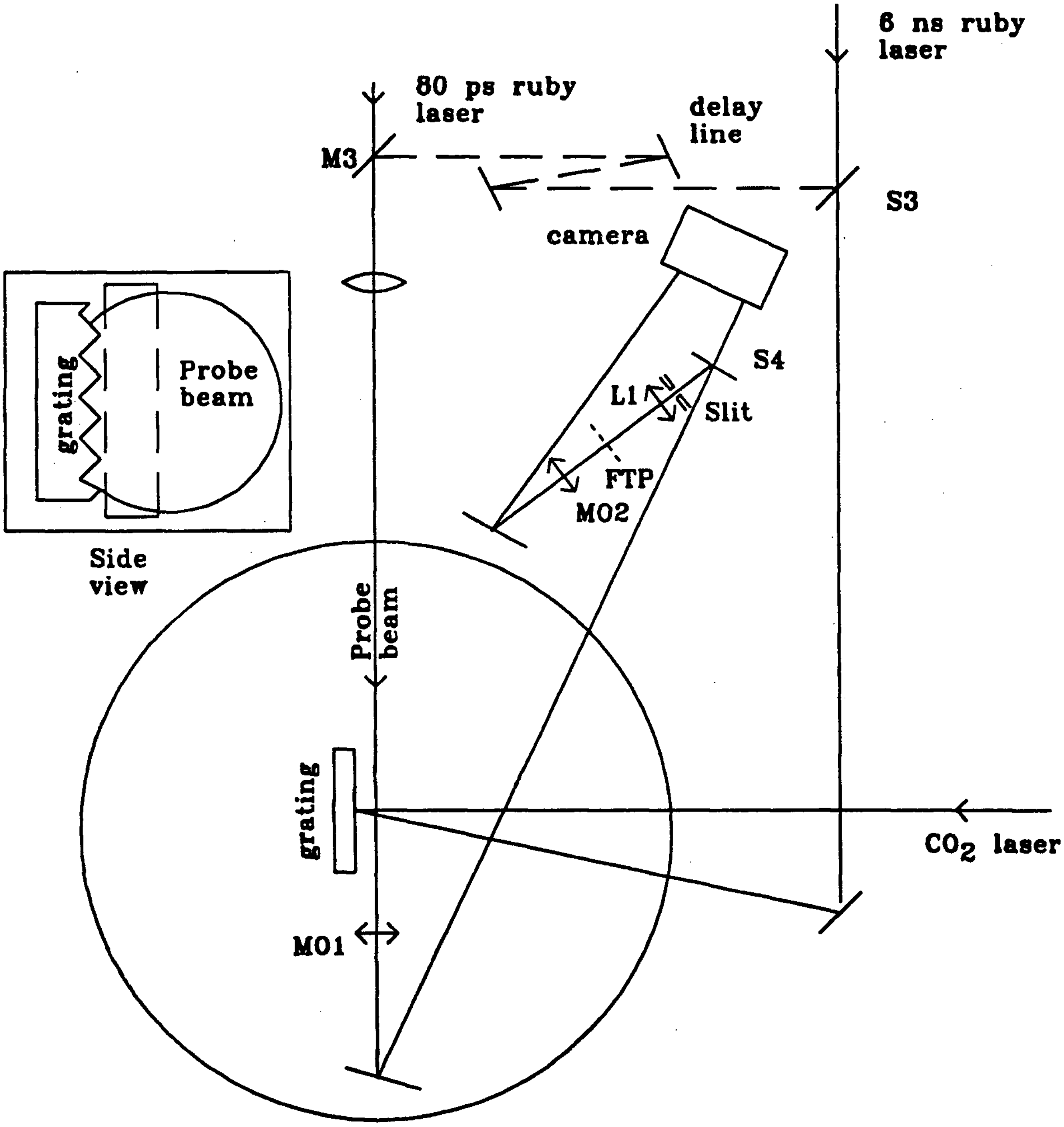

FIGURE 4.9
Set up for Raman-Nath scattering.

4.4 Results

Using interferometry we can first look at the bulk motion of the plasma. Because of the astigmatic focusing, the plasma is not cylindrically symmetrical and the Abel inversion cannot be used to find the plasma density from one interferogram. We will therefore view the elongated plasma from the side (with the probe beam crossing the plasma along its short axis) and head-on (probe beam crossing the plasma along its long axis) to find the density.

Figure 4.10 shows a side interferogram of the plasma 9 ns after its formation. The plasma is 1.6 mm long and not very uniform. This is due to the intensity variation along the line focus. Better spatial filtering of the laser beam could be used to solve this problem. The head-on view taken at the same time (Figure 4.11) indicates a bell shaped profile about 400 μm wide. If the laser focal spot has a dimension similar to the plasma, the intensity on target is 10^{10} Watt/cm^2 over an area 1.6 mm long by 0.4 mm wide.

If we assume that the relative form of the density profile is constant over the entire length of the plasma, and only modulated by a function of z, we can calculate the plasma density everywhere. We can write:

$$n(x,y,z) = r(x,y)f(z)$$

Where z is along the long axis of the plasma, y along the short axis and x is the height above the grating (Figures 4.10 and 4.11).

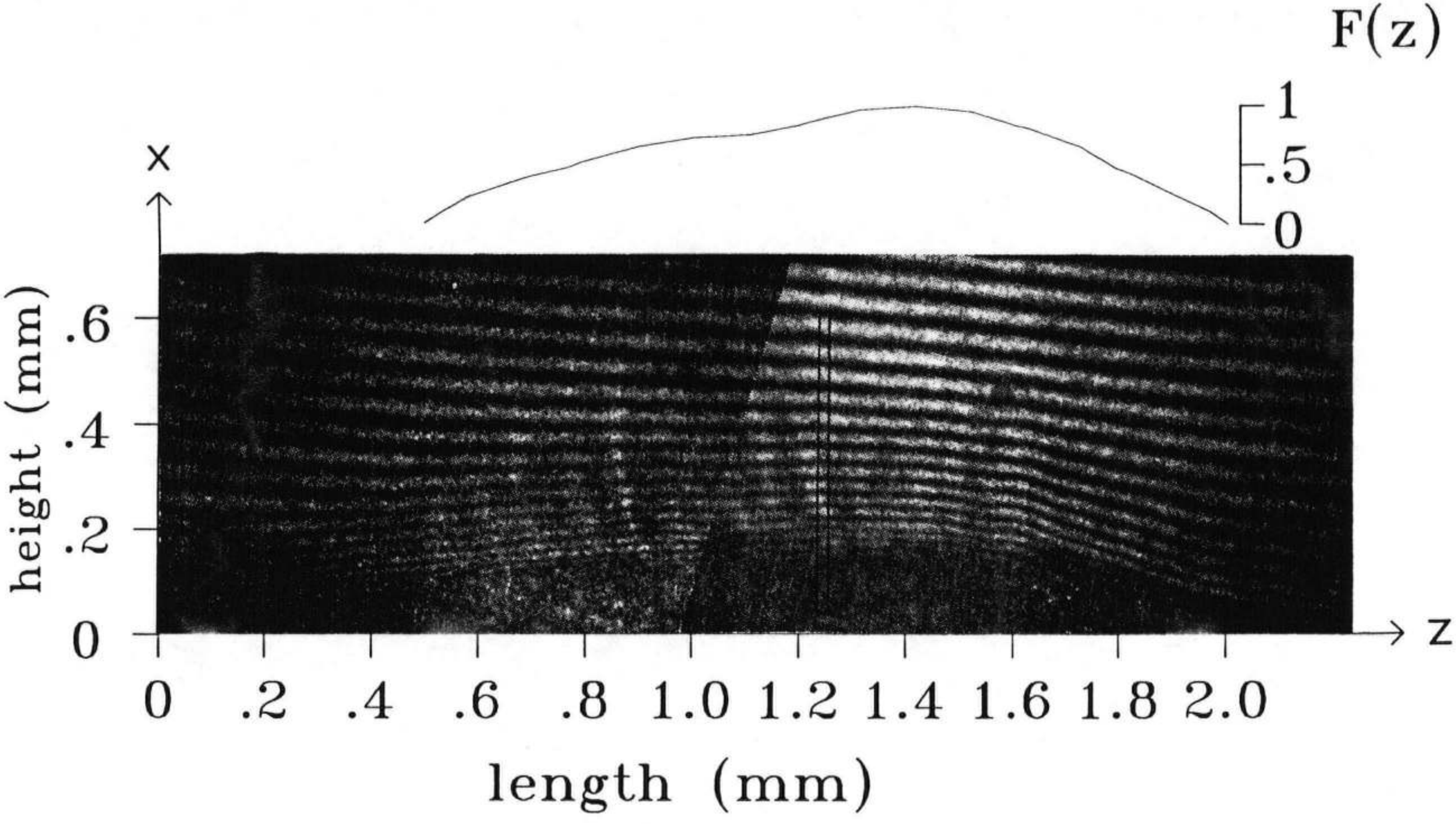

FIGURE 4.10
80 ps side view interferogram of the plasma at T=9 ns. The black rectangle is the position of the streak camera slit for streak interferometry.

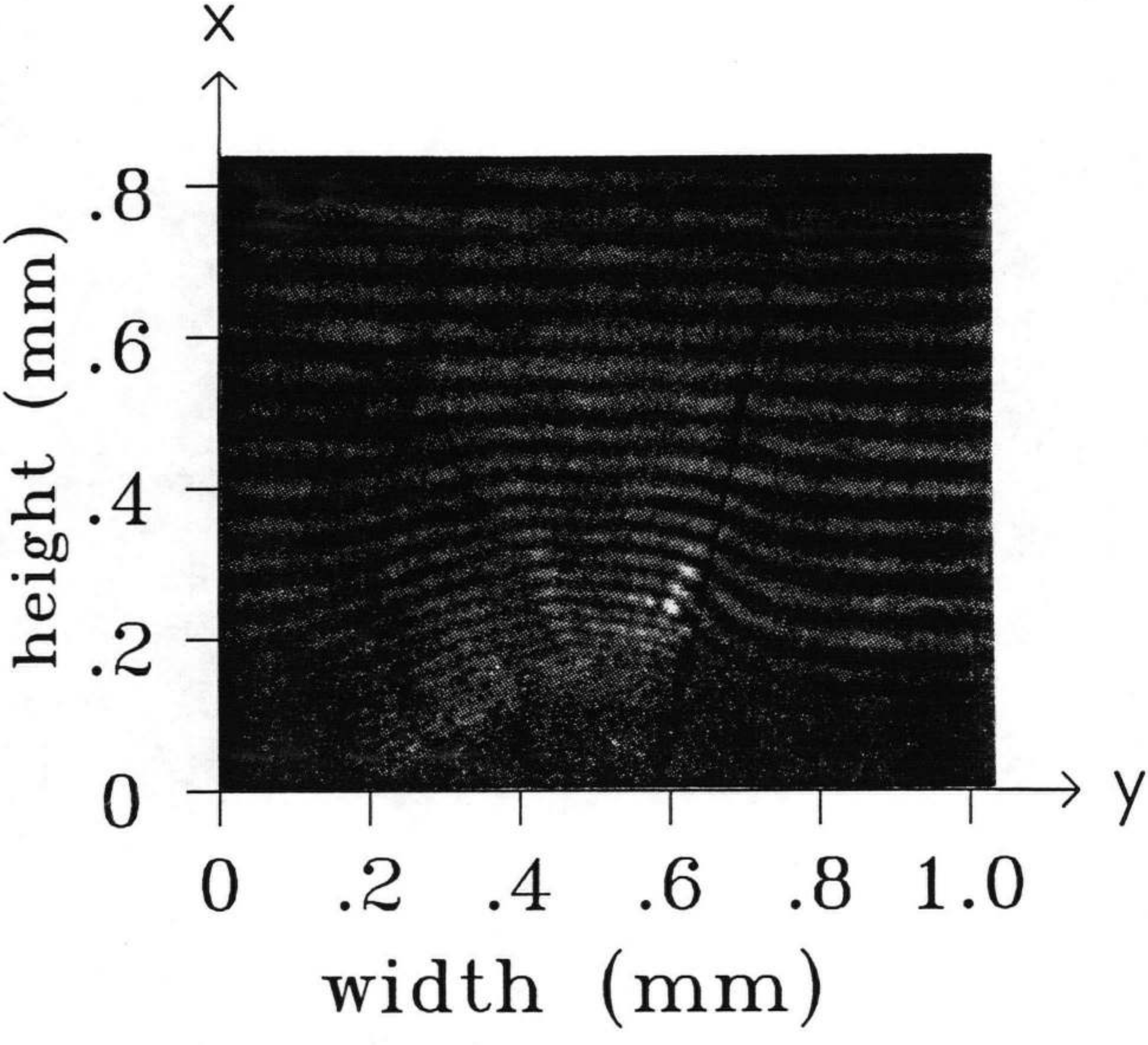

FIGURE 4.11
80 ps head-on view interferogram of the plasma at T=9 ns.

For densities much smaller than the ruby laser critical density n_{cr} the number of fringe shifts (Δ) on the interferograms are given by:

$$\Delta(x,y) = \frac{1}{2\lambda n_{cr}} \int_{-\infty}^{\infty} n(x,y,z)\,dz$$

for a head-on interferogram and

$$\Delta(x,z) = \frac{1}{2\lambda n_{cr}} \int_{-\infty}^{\infty} n(x,y,z)\,dy$$

for a side interferogram.

So: $r(x,y) = \frac{2\lambda n_{cr}\Delta(x,y)}{\int f(z)dz}$ $\qquad f(z) = \frac{\Delta(x,z)\int f(z)dz}{\int \Delta(x,y)dy}$

In these equations, λ is the wavelength of the laser ($\lambda = 0.6943$ μm). A multiplication factor can be freely exchanged between r(x,y) and f(z) without changing n(x,y,z) and we choose it so $f_{max}(z) = 1$. Figures 4.12 and 4.10 show r(x,y) and f(z) respectively. The interference fringes become indiscernible very close to the grating, so no plasma density was calculated in this region.

Streak interferometry probed the continuous time evolution of the plasma density. Imaging the slit of the streak camera into the middle of the plasma (orientation depicted on Figure 4.10) we obtain a time resolved interferogram (Figure 4.13). The rapid time variation in the brightness of the fringes is due to the mode beating of the ruby laser. Using the profile r(x,y) found previously, the plasma density from this streak interferogram is then calculated for different times. The result is shown in Figure 4.14.

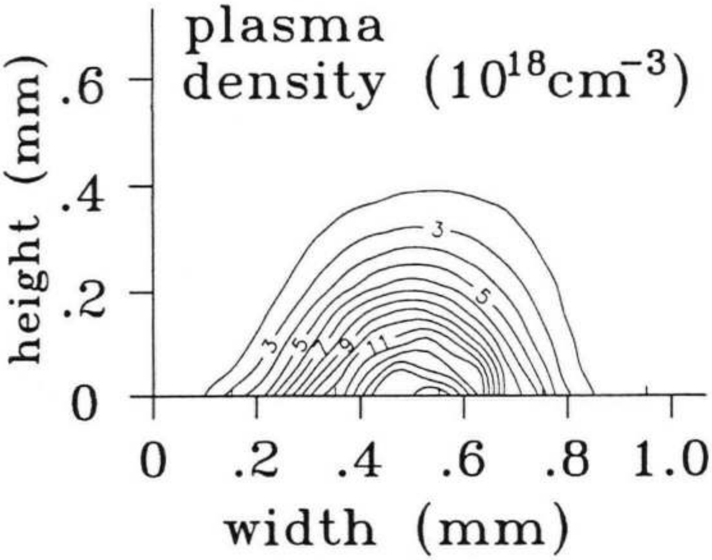

FIGURE 4.12
Density profile obtained from figures 4.10 and 4.11

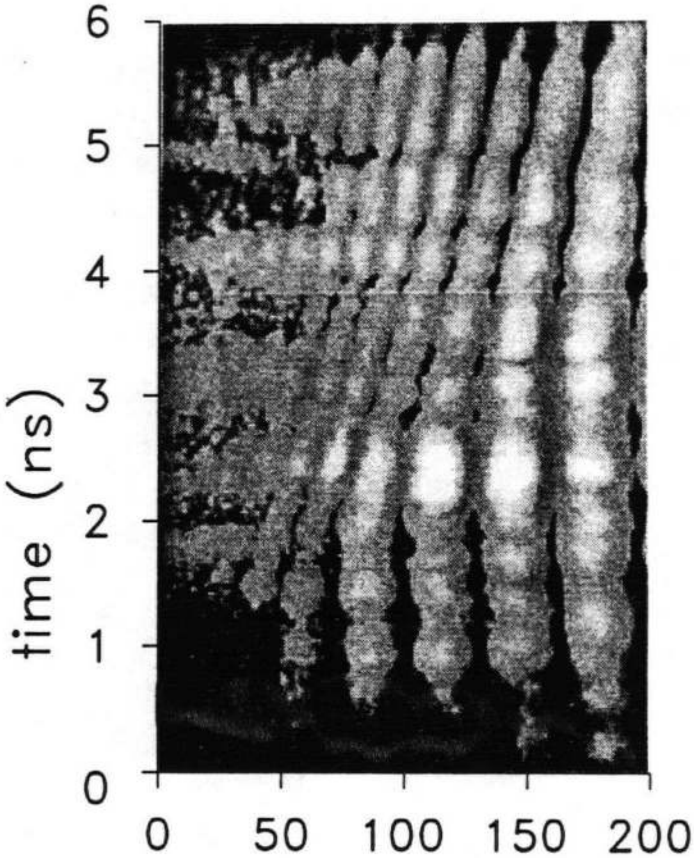

FIGURE 4.13
Streak interferogram.

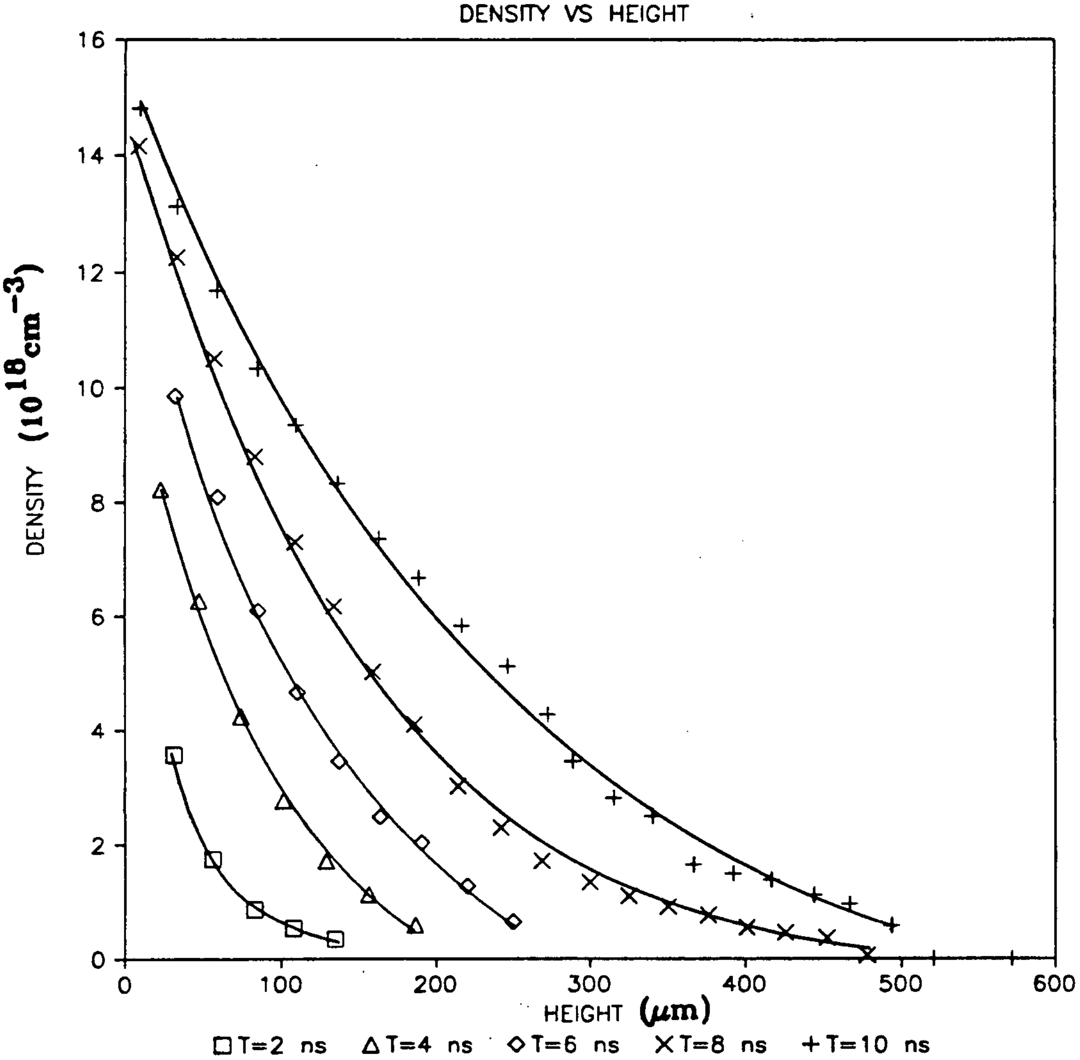

FIGURE 4.14

Density profiles at different times.

We now know the space and time evolution of the bulk of the plasma. These results are obtained by firing the laser on a flat brass surface. Experiments were also performed on gold-photoresist gratings, showing a plasma with the same dimension as on brass, but expanding at a slightly slower speed.

If we increase the magnification of the optical system and irradiate a grating, we can observe some modulation in the plasma density. An 80 ps interferogram of the plasma above a brass grating with 35 μm spacing shows ripples on the interference fringes (Figure 4.15).

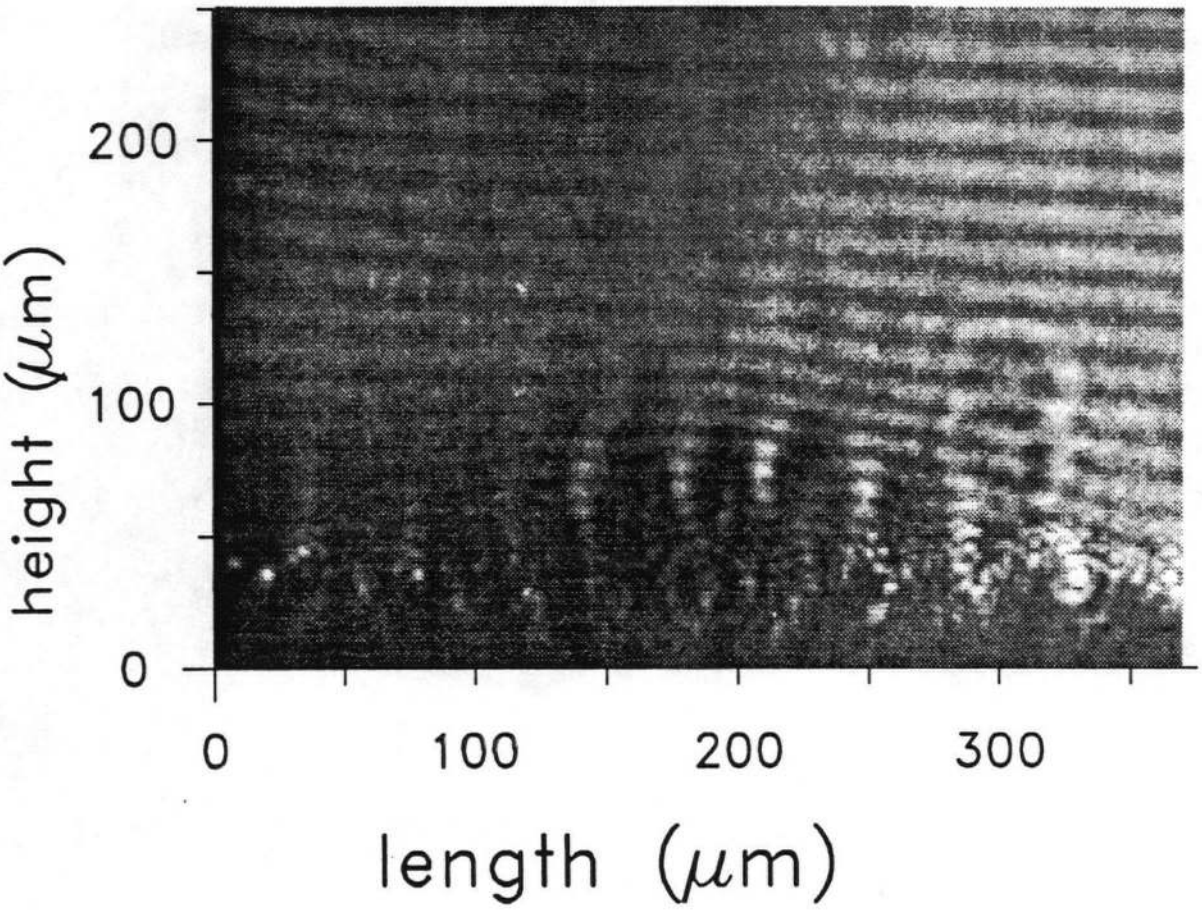

FIGURE 4.15

80 ps interferogram of the modulated plasma above a brass grating $\lambda_g = 35\,\mu$ m.

If we neglect refraction and suppose that the modulation depth $\tilde{n}/n$ is constant across the plasma, we have $\tilde{\Delta}/\Delta = \tilde{n}/n$ where $\tilde{\Delta}/\Delta$ is the modulation of the fringe defined so $\Delta(z)=\Delta(1+\frac{\tilde{\Delta}}{\Delta}\sin k_g z)$, where k_g is the grating wavenumber. The fringe shift at a height of 80 μm and a length of 180 μm on Figure 4.15, is 2.1±0.2 fringes. If we follow this fringe, we find that it oscillates with a peak to peak amplitude of 0.32±0.1 of a fringe. This is a modulation of $\tilde{\Delta}/\Delta=\tilde{n}/n=(7.6\pm2)\%$. Unfortunately, it was impossible to see modulations of shorter wavelengths using interferometry. Insufficient resolution of the optical system, reduction in the modulation of the fringe shift and plasma motion during the 80 ps exposure combined to blur any fringe oscillation.

Shadowgraphy proved to be much more sensitive for the small modulations but lacked the quantitative precision of interferometry. Figure 4.16 shows a 80 ps shadowgram of the plasma above a 10 μm spacing lithographic grating. Notice the regularity of the modulation which is important for the oscillating plasma grating accelerator. A lineout of Figure 4.16 at a height of 50 μm indicates phase fluctuations smaller than 0.6 radian (Figure 4.16 b). Modulations as small as 6 μm were observed, which is the resolution limit of the microscope objective. The contrast of the modulation shown on the shadowgrams, decreases for smaller grating spacings. For a grating spacing of 35 μm, the modulations are visible up to 20 ns after the ruby laser pulse. However, for a periodicity of 6 μm, the shadowgrams do not show any modulation for time delays longer than 6 ns.

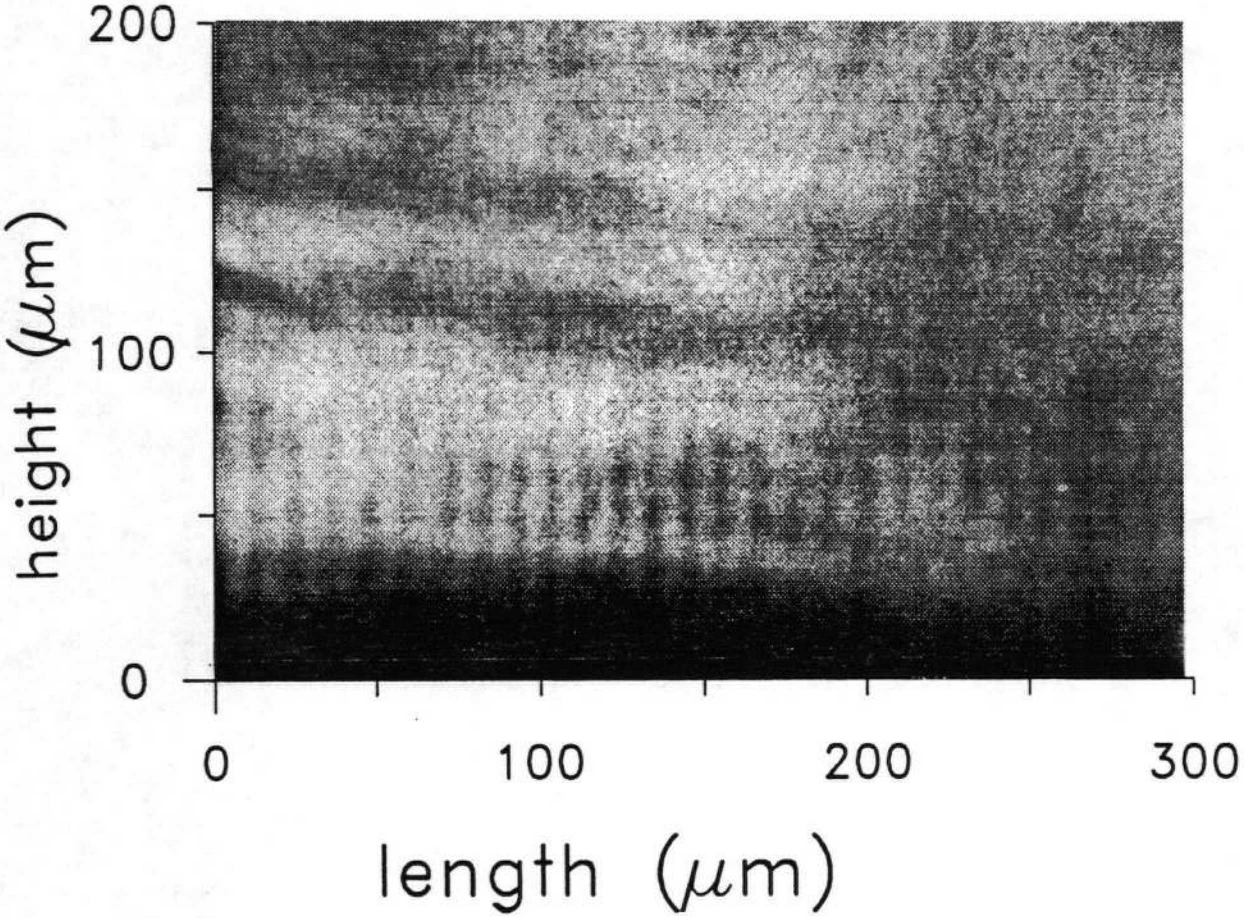

FIGURE 4.16
80 ps shadowgram of the modulated plasma above a lithographic grating $\lambda_g = 10\mu$m.

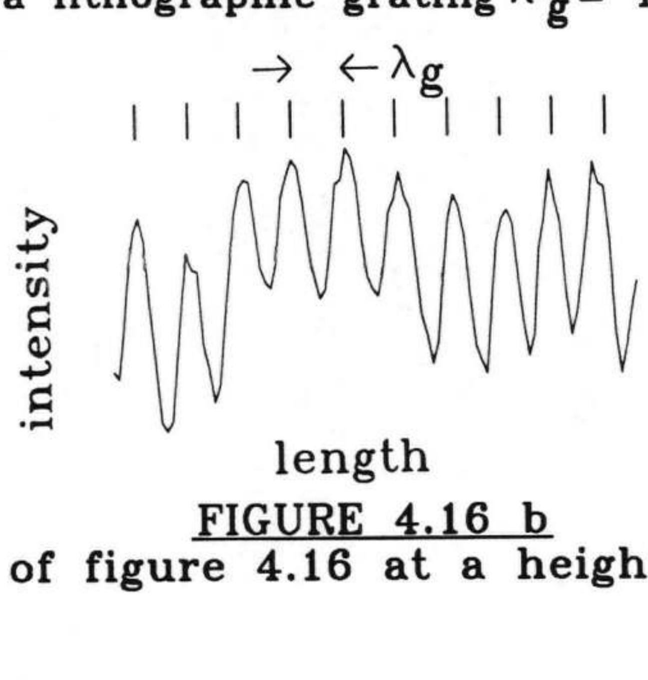

FIGURE 4.16 b
Lineout of figure 4.16 at a height of 50 μm.

Shadowgrams using a 6 ns exposure also show modulations (Figure 4.17).

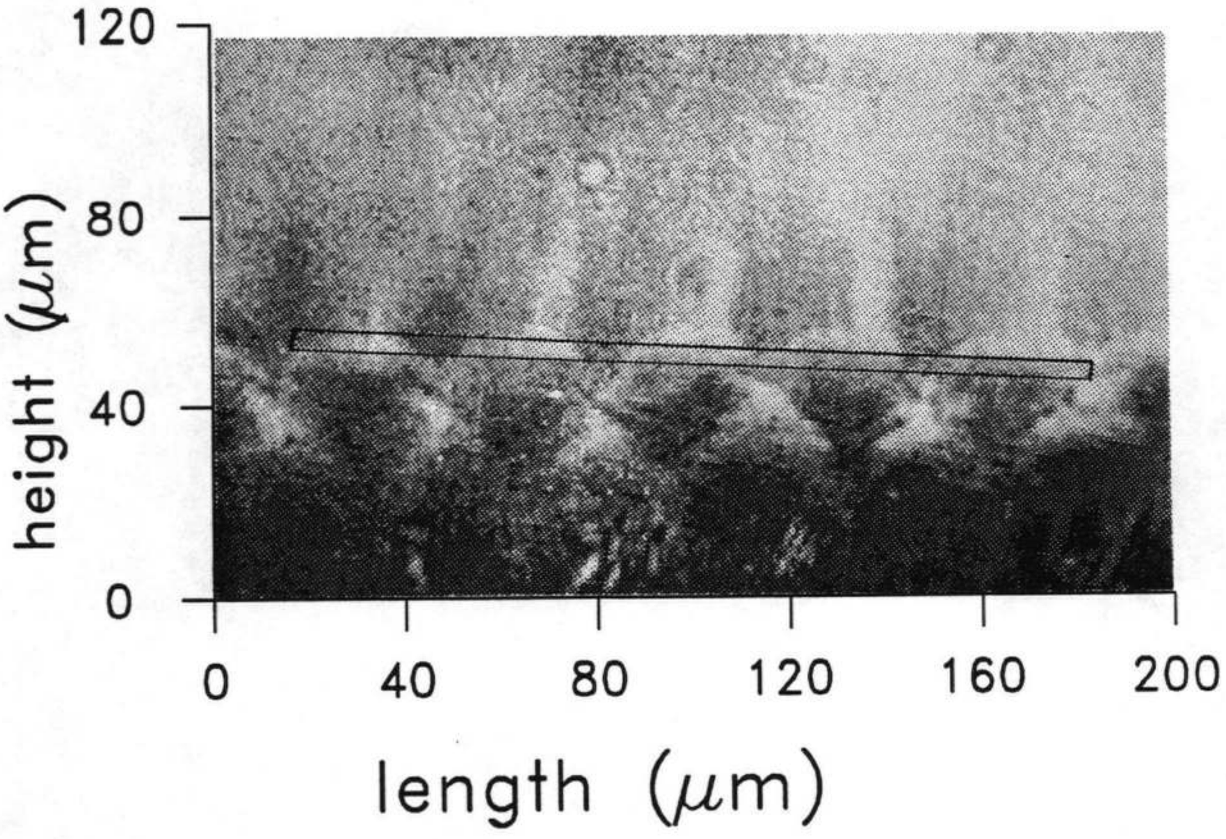

FIGURE 4.17

6 ns shadowgram of the modulated plasma above a brass grating of $\lambda g = 35\,\mu m$. The black rectangle is the position of the slit for streak shadowgraphy.

This is somewhat surprising. In these modulations there is a strong gradient of density between the high and low density regions. This drives a flow of plasma to equalize the density, but the mass of the plasma makes it overshoot the equilibrium position, and an ion acoustic oscillation results. There should be many such oscillations in a 6 ns exposure and no shadowgram should be visible. However, it is not quite as simple because these oscillations take place in a plasma which is flowing rapidly out of the grating. The plasma density at a given point above the grating increases with time so the refraction of light by the modulation also increases. Each half-cycle of the ion-acoustic oscillation therefore produces a stronger shadowgram than the one generated by the previous half-cycle. After integrating the light on the recording film or camera for a few cycles, a residual image can still be seen.

In order to see the time dependence of the modulation directly we produced streak shadowgrams. For these experiments the slit of the streak camera was imaged into the plasma as outlined in Figure 4.17. The small angle between the grating and the slit allows us to sample different heights above the grating in the same streak image. Reversals (180° phase change in the dark, light pattern) can be seen if the slit is low enough ($h<3$ grating spacings) above the grating (Figure 4.18). For $h>3$ grating spacings (not shown on the picture) no reversals are seen for the entire 6 ns duration of the streak image.

A typical Raman-Nath scattering result for a 35 μm grating is shown on Figure 4.19a. The zero order is hidden by a screen. Figure 4.19b shows the result for a 10 μm grating. The intensity of the diffracted beam is much smaller than for the 35 μm grating and only the first order is barely visible, (weak white lines above and below the zero order). For grating spacings smaller than 10 μm no diffracted beam could be seen. The ratio of the first order intensity over the zero order intensity for different grating spacings is shown on Figure 4.20. These were measured by masking the zero order beam with neutral density filters until the zero order and the first order produced the same exposure on the film.

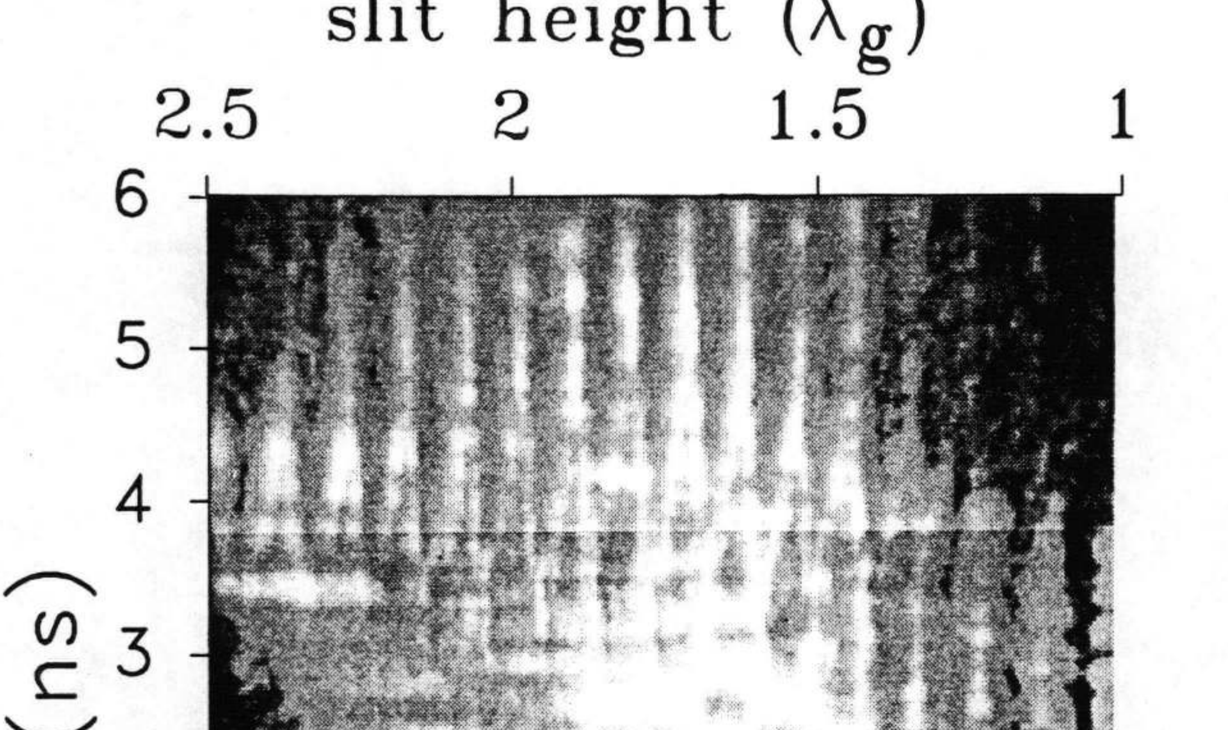

FIGURE 4.18
Streak shadowgram taken 50 μm above a brass grating λ_g= 35 μm

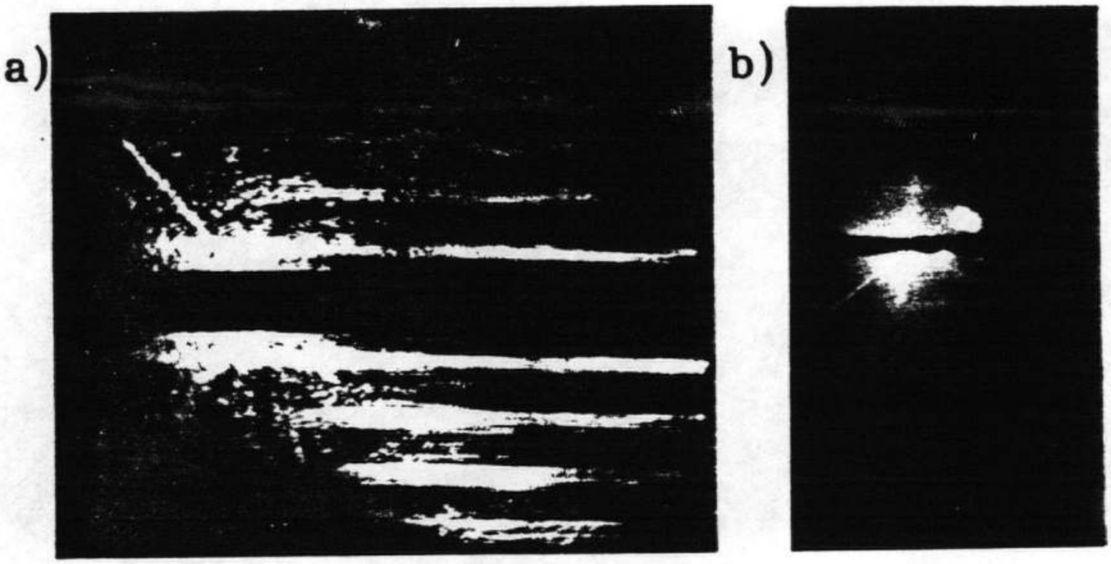

FIGURE 4.19
Raman-Nath scattering with $\lambda_g = 35\,\mu m$ a) and $\lambda_g = 10\,\mu m$ b).

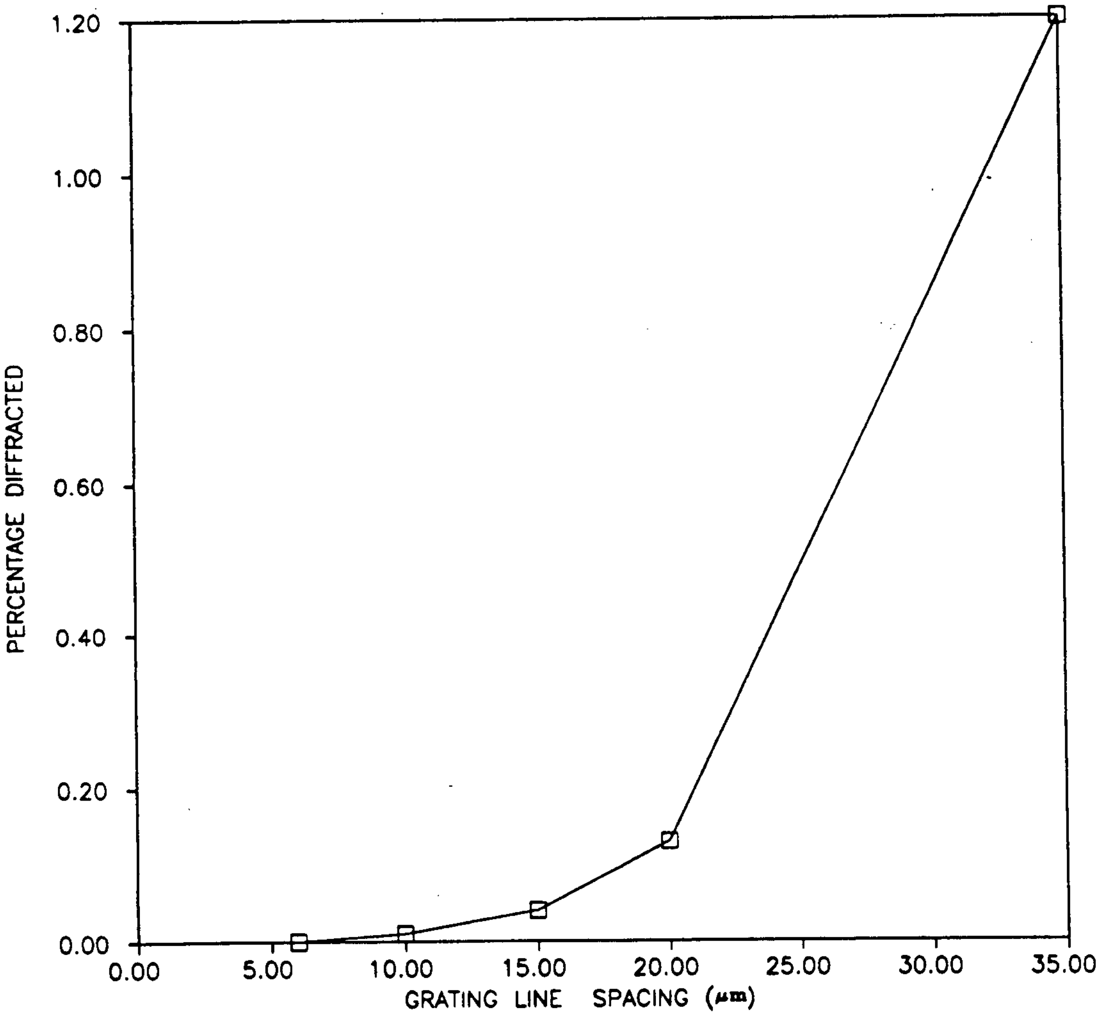

FIGURE 4.20
Percentage of light scattered for different grating spacings

4.5 Discussion

We will now discuss these results. This section is separated into two parts. In the first section, the bulk motion of the plasma is determined. In the second section we examine the plasma on a finer scale and observe the modulation of the density due to the grating lines.

4.5.1 Bulk Motion

The one dimensional hydrodynamic equations describing the plasma expanding above a flat surface are:

$$\frac{\partial n}{\partial t} + \mathrm{v}\frac{\partial n}{\partial x} + n\frac{\partial \mathrm{v}}{\partial x} = 0 \qquad \frac{\partial \mathrm{v}}{\partial t} + \mathrm{v}\frac{\partial \mathrm{v}}{\partial x} = -\frac{c_s^2}{n}\frac{\partial n}{\partial x}$$

If the expansion is isothermal, c_s is a constant and the solution is [26]:

$$n(x,t) = n_0 e^{\frac{-x}{c_s t}} \qquad (4.1)$$

$$\mathrm{v}(x,t) = \left(1 + \frac{x}{c_s t}\right) c_s \qquad (4.2)$$

Here, x is the height above the sonic surface, c_s is the speed of sound, v is the speed of plasma and n_0 is the plasma density at the sonic surface.

Assuming a one dimensional expansion in our experiment is reasonable as long as the scale length L of the plasma (defined as $1/L = \nabla n/n$) is smaller than its lateral dimension (L < plasma width). For this expanding plasma $L = c_s t$. So for small t, we can use data from streak interferometry (Figure 4.14) and plot scale length versus time (Figure 4.21) to find the speed of sound. From this data we obtain c=2,7x10^4 m/s.

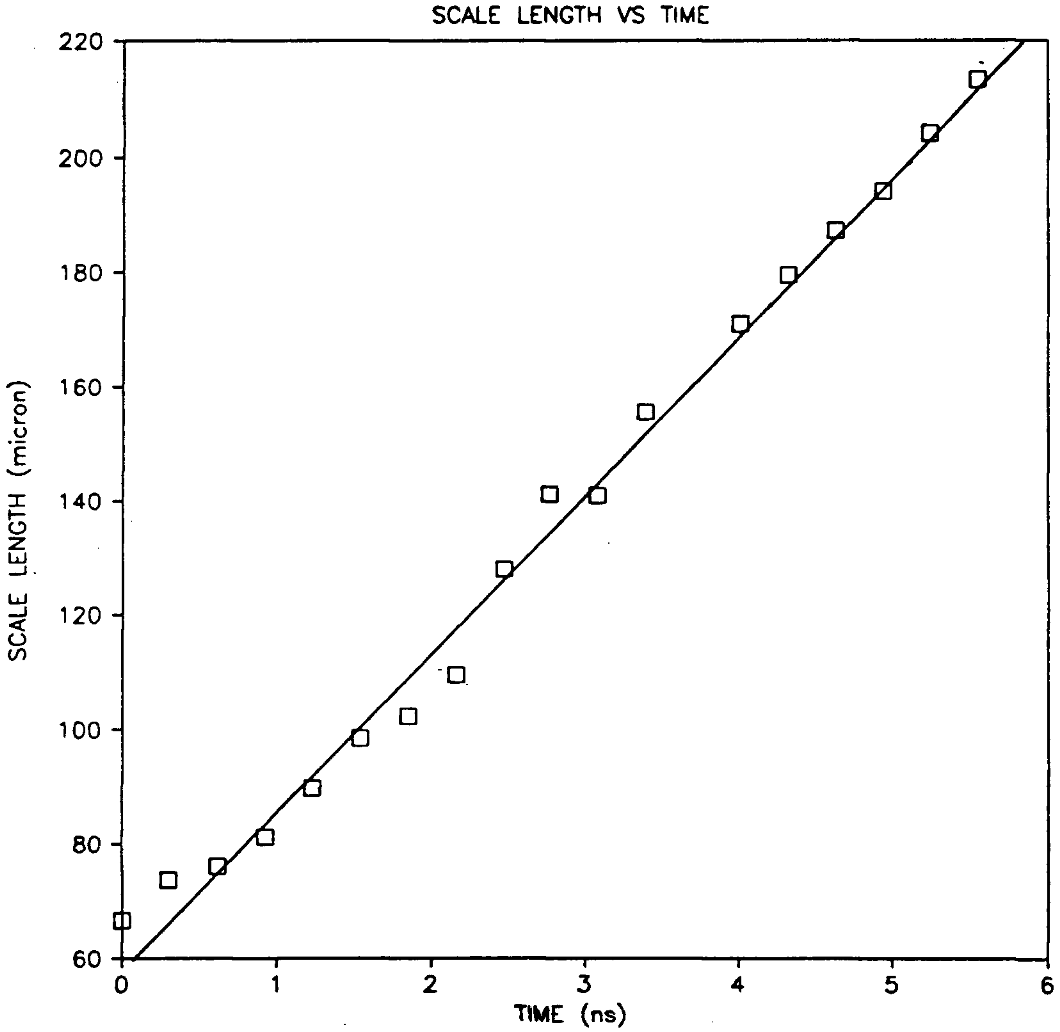

FIGURE 4.21

Scale length as a function of time.

Laser produced plasmas of this type are known to have an electron temperature (T_e) of around 50 eV (from experimental data [27] adjusted to our condition using Caruso's [28] scaling law) and a degree of ionization Z^* of approximately six [29]. This gives a speed of sound of:

$$c_s = \left(\frac{Z^* T_e}{m_i}\right)^{1/2} \approx 2.1 \times 10^4 m/s$$

This is in good agreement with our result. Therefore the approximations used would appear to be reasonable. The results described are characteristic of the bulk plasma motion.

4.5.2 Modulation

No analytical solution could be found for a modulated plasma expanding above a surface. We used a finite element computer program to solve the hydrodynamic fluid equations in two dimensions. These equations are:

$$\frac{\partial n}{\partial t} + \nabla n\mathrm{v} = 0 \qquad \frac{\partial \mathrm{v}}{\partial t} + \mathrm{v}\nabla\mathrm{v} = -c_s^2 \frac{\nabla n}{n}$$

With the initial condition:

$$\vec{\mathrm{v}}(x, y, t_0) = \left(1 + \frac{x}{c_s t_0}\right) c_s\, \hat{x} \qquad n(x, y, t_0) = n_0 \left(1 + \frac{\tilde{n}}{n} \sin(k_g y)\right) e^{\frac{-x}{c_s t}}$$

and the boundary condition on the grating.

$$\vec{\mathrm{v}}(0, y, t) = c_s\, \hat{x} \qquad n(0, y, t) = n_0 \left(1 + \frac{\tilde{n}}{n} \sin(k_g y)\right)$$

Here n is the plasma density, v is the speed of the plasma, $\hat{x}$ is the unit vector in the x direction, n_0 is the plasma density on the grating, n is the amplitude of the modulation, k_g is the wavenumber of the grating and c_s is the speed of sound.

Periodic boundary conditions in y were used. Using the experimental value for c_s ($2{,}7\text{x}10^4$ m/s), 35 μm grating and $\tilde{n}/n=8\%$ on the grating, we obtain the plasma evolution shown in Figure 4.22. Because of its importance for acceleration, we also plotted $\tilde{n}/n$ as a function of height above the grating at different times shown on Figure 4.23a. There is phase reversal close to the grating, but a fairly constant $\tilde{n}/n$ further away from the surface. The density modulation $\tilde{n}/n$ as a function of time for a constant height is presented on Figure 4.23b. It shows the expected ion-acoustic oscillation.

We can explain these results qualitatively from the computer simulation on a physical basis. From Equation (4.2) we know that the plasma expansion is supersonic, with Mach numbers increasing as we move away from the grating. As the modulation oscillates at the ion-acoustic frequency in the y direction, it is blown away from the surface at a supersonic speed. The combination of a supersonic flow in one direction and an ion-acoustic oscillation in a perpendicular direction, forms a quasi stationary wave pattern, similar to the standing waves produced by a rock in a river. But the velocity field is time dependant, and the pattern changes with time. Close to the grating the expansion speed is only slightly supersonic and phase reversal of the plasma modulation can be seen (Figure 4.17). Further away, the plasma velocity is very high and no reversal is visible.

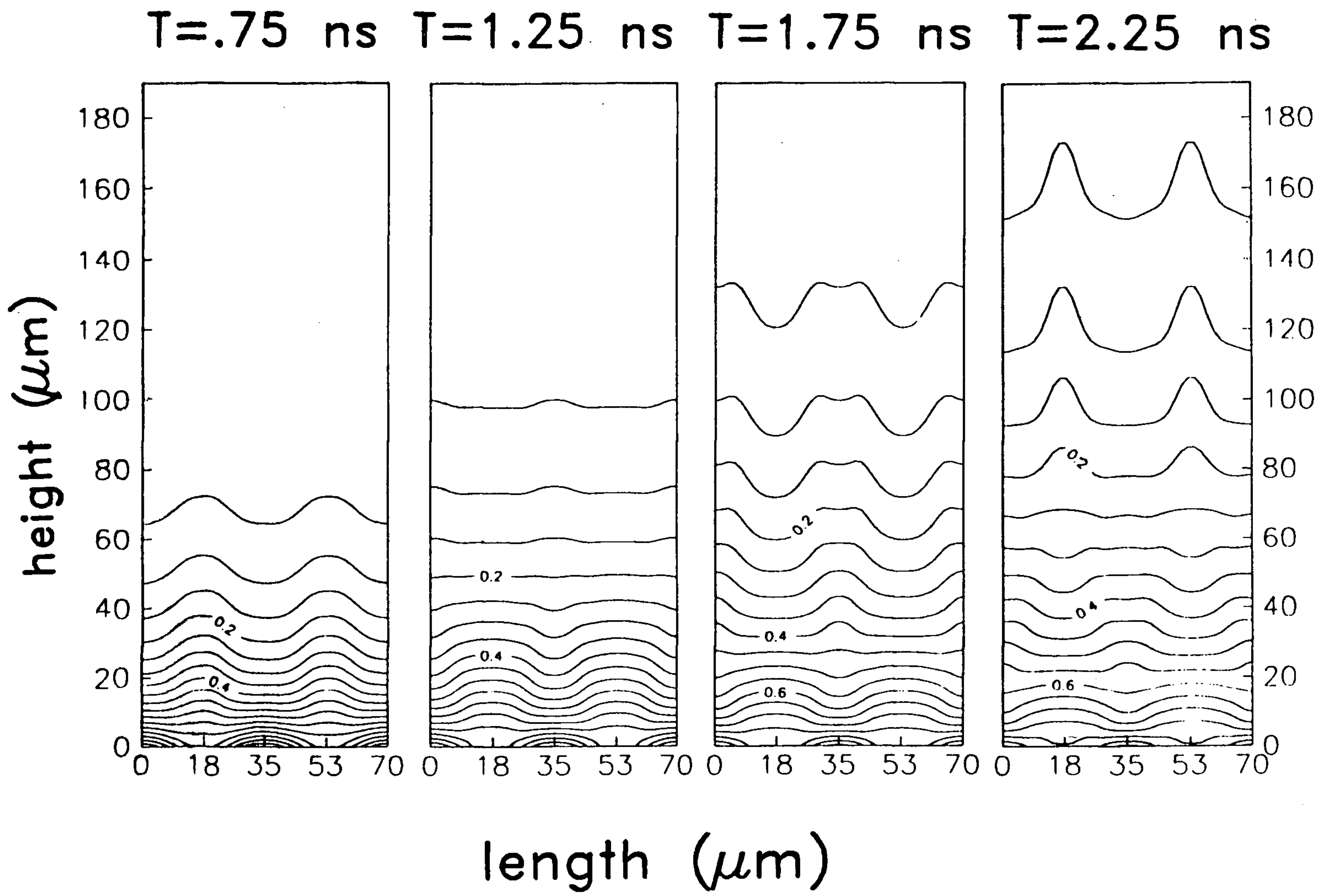

FIGURE 4.22

Plasma evolution generated by computer simulation. The plasma density is normalized to one on the grating.

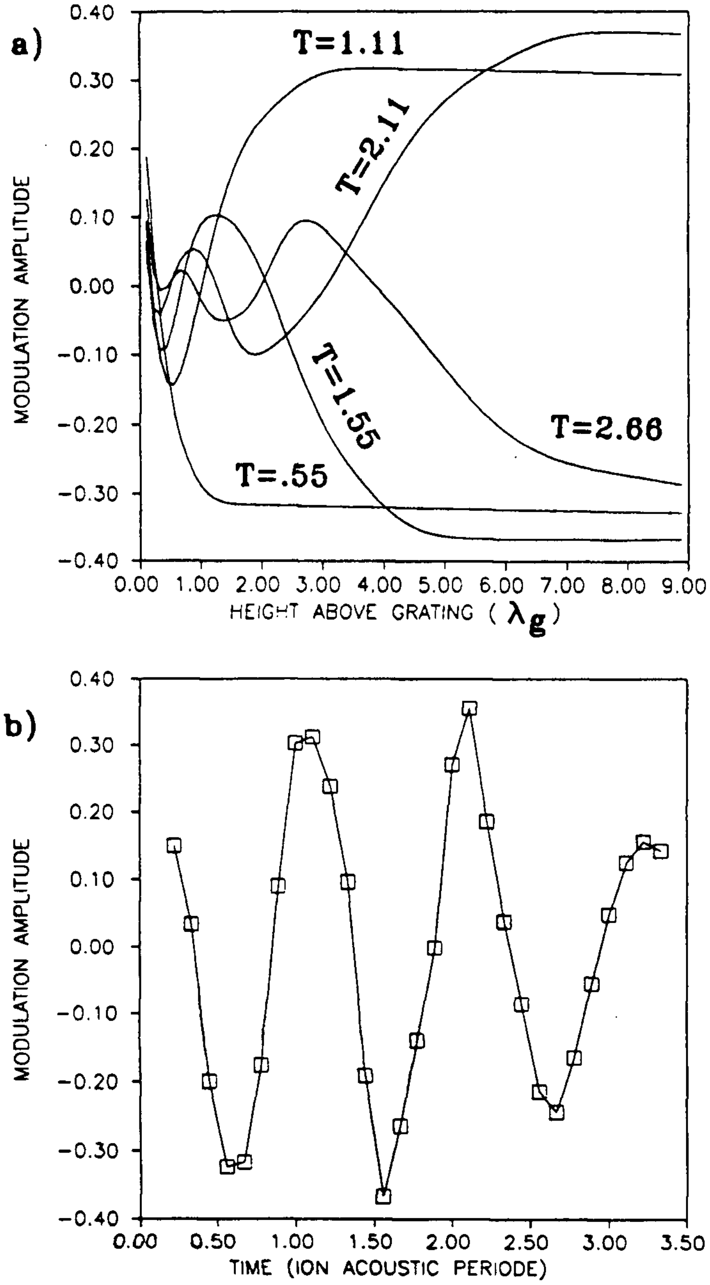

<u>**FIGURE 4.23**</u>

a) $\tilde{n}/n$ as a function of height above the grating at different times

b) $\tilde{n}/n$ as a function of time at a height of 7 grating spacings.

We compare the result of this computer solution with experimental shadowgrams using a ray tracing program. The plasma evolution found by the computer (Figure 4.22), normalized to one at the grating, is multiplied by the plasma profile (Figure 4.12). This gives a modulated plasma slab with electron density equal to the experimental value. A uniform array of light rays is refracted when passed through the modulated plasma slab. The light rays then travel to a plane 500 μm past the middle of the plasma (the value used for the shadowgraphy experiments) where their position is recorded. This procedure forms an image where the intensity is proportional to the number of rays per unit surface. The simulated shadowgram obtained by this method is shown on Figure 4.24a. It is in reasonable agreement with the experimental result (Figure 4.17). During the computer simulation it is possible to observe how the 6 ns integrated shadowgram is obtained from the summation of the instantaneous shadowgrams. The instantaneous shadowgrams change phase with every half-cycle of the ion-acoustic wave. But because their contrast increases rapidly as the plasma expands, an integrated shadowgram showing modulation is produced after the summation is completed.

We can also simulate the streak shadowgram displayed on Figure 4.18. The result is shown in Figure 4.24b.

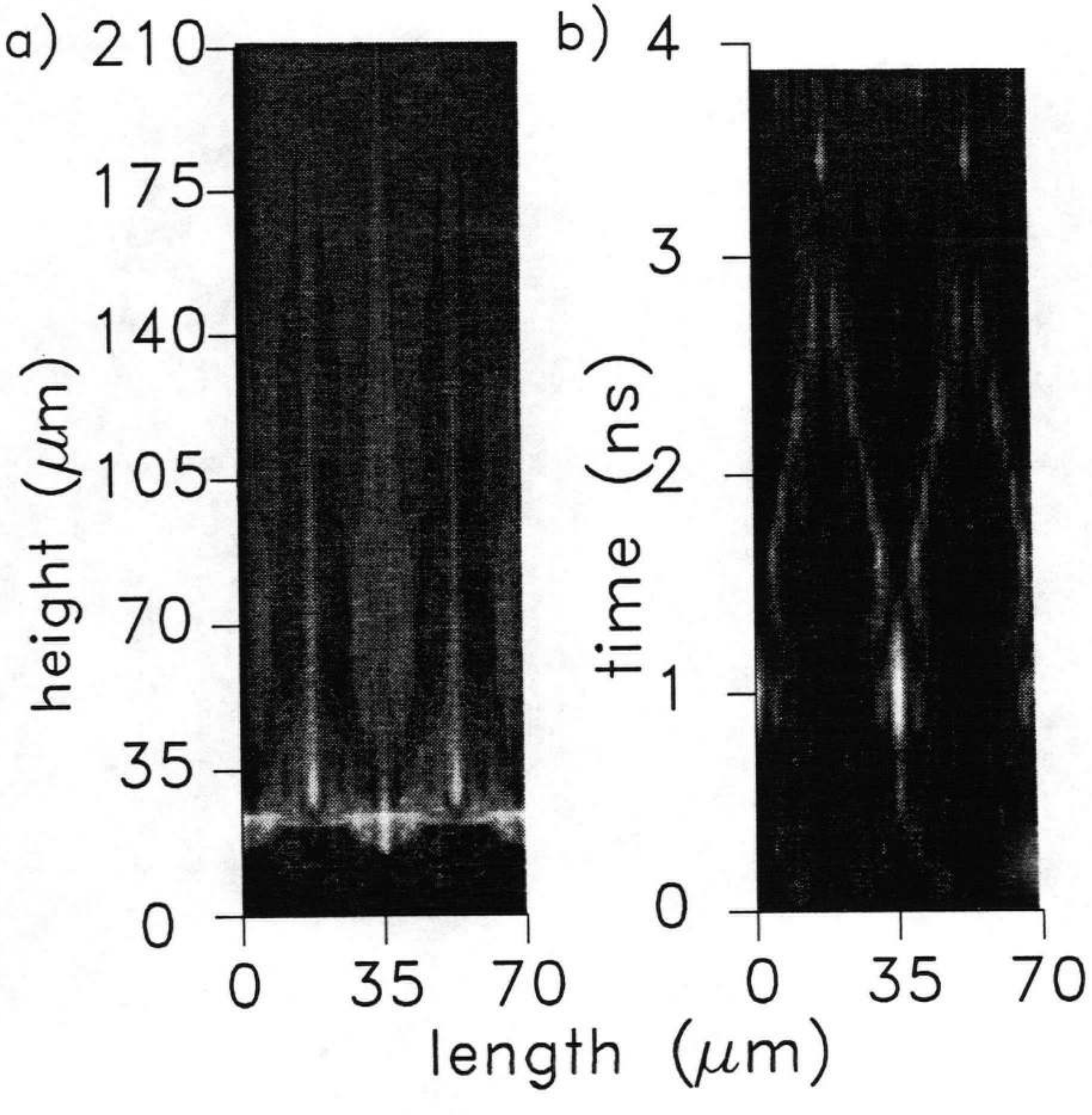

FIGURE 4.24
a) Simulated 6 ns shadowgram with λ_g =35 μm.
b) Simulated streak shadowgram with λ_g =35 μm.

Two reversals can be seen on the experimental shadowgram. The first one being barely visible in the bottom right corner of the picture (between 1 and 2 ns, around 400 μm), and the second one producing the "chevron" structure near the top (around 4 ns). This is in good agreement with the computer shadowgram that also reproduces the "chevron" structure, visible during reversal.

Given the agreement between the computer simulated shadowgram and the actual result, we can conclude that a modulation of $\tilde{n}/n \approx 8\%$ is present in the plasma expanding above a grating with λ_g as small as 6 μm, the resolution limit of the microscope objective used.

For grating spacings larger than 20 μm, $\tilde{n}/n$ can be measured directly using interferometry. For smaller spacing, modulation can be seen using shadowgraphy, but $\tilde{n}/n$ can only be estimated by comparing the shadowgram with a computer simulation.

In order to improve on this rather indirect and imprecise method, we decided to employ the Raman-Nath scattering results. To obtain qualitative information from these results, we have to calculate theoretically the percentage of light diffracted by a phase grating so that we can compare it with the experimental value (Figure 4.20).

For a simple phase grating, the index of refraction is:

$$\eta(y) = \eta + \Delta\eta \; cos(k_g y)$$

If a beam of light represented initially by $\psi = e^{ikz}$ (where k is the wavevector of the beam of light) traverses a thickness D of this grating without changing direction (we neglect refraction), the emerging beam will be:

$$\psi = e^{ikD(\eta+\Delta\eta\, cos(k_g y))}$$

In the Raman-Nath geometry (Figure 4.9) we observe the Fourier transform of this amplitude.

$$\Phi(u) = F.T.[\psi(y)] \propto \int_{-\infty}^{\infty} e^{ikD(\eta+\Delta\eta\, cos(k_g y))} e^{iyu} dy$$

$$\Phi(u) \propto \sum_{m=-\infty}^{\infty} i^m \delta(u - mk_g) J_m(\varepsilon)$$

Where $\varepsilon = kD\Delta\eta$, $\delta(u - mk_g) = 1$ for $u = mk_g$ and 0 otherwise and $J_m(\varepsilon)$ are the Bessel fonctions of order m and argument ε.

Finally the ratios of the intensities in the different diffracted orders over the intensity of the zero order are:

$$\frac{I_m}{I_0} = \frac{J_m^2(\varepsilon)}{J_0^2(\varepsilon)}$$

The limit of validity for this expression is [30]:

$$\rho\eta^2 < 1$$

and

$$\rho\varepsilon^2 < 2$$

Where $\rho = \frac{k_g^2}{\eta\Delta\eta\, k^2}$.

In our experiment we have $\varepsilon \approx 0.8$, $\eta \approx 1$ and $\rho \approx 1.5$ for $\lambda_g = 35\mu m$ to $\rho \approx 50$ for $\lambda_g = 6\mu m$. We can almost neglect refraction for the $35\mu m$ grating spacing, but certainly not for the smaller one.

Even for a case with no refraction, this simple solution does not properly represent the experimental condition. We must also take into account the large density gradient perpendicular to the grating that exists in our experiment. The index of refraction for the plasma is:

$$\eta(x,y) = \sqrt{1 - \frac{n(x,y)}{n_{cr}}}$$

Using for the plasma density the expression:

$$n(x,y) = n(x)(1 + \frac{\tilde{n}}{n}\, cos(k_g y))$$

we obtain the index of refraction

$$\eta(x,y) = \sqrt{1 - \frac{n(x)}{n_{cr}}\left(1 + \frac{\tilde{n}}{n} cos(k_g y)\right)}$$

Where the plasma density $n(x) = n_0 e^{-x/L}$, L is the scale length of the plasma and n_0 is the plasma density just above the surface of the grating.

Unfortunately $\Phi(u,v) = F.T.\left[e^{ik\eta(x,y)D}\right]$ cannot be calculated analytically with this expression for $\eta(x,y)$. A two-dimensional fast Fourier

transform program was used with the following parameters.
Distance travelled by the laser beam through the plasma: $D = 400\ \mu m$
Scale length of the plasma: $L = 100\ \mu m$
Plasma density at the surface of the grating: $n_0 = 1.6 \times 10^{19} cm^{-3}$
Grating spacing: $\lambda_g = 35\ \mu m$
These are the plasma parameters obtained by interferometry. In the Raman-Nath experiment the slit only lets the light pass through a region covering a height above the grating from 40 μm to 90 μm. This range determines the limits in the Fourier transform integral and was included in the program. The density modulation $\tilde{n}/n$ is adjusted until we obtain I_1/I_0=1.2%, the experimental value. We find that $\tilde{n}/n$ =4% gives 1.2% of diffracted light. The simulated Raman-Nath picture is shown in Figure 4.25. The zero order is attenuated by a factor of 50.

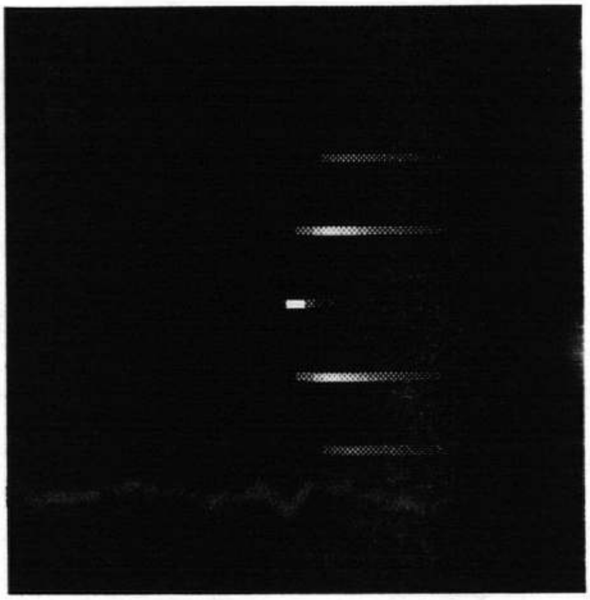

FIGURE 4.25
Simulated Raman–Nath picture.

It is in qualitative agreement with the experimental result on figure 4.19a. However the angle α between the vertical and a line passing through the maximum of the diffracted orders is not the same on both figures, and $\tilde{n}/n$=4% is too small compared to the interferometric result of $\tilde{n}/n$=8%. The angle α is found (from the Fourier transform program) to vary with D, L, n_0 and also with the position and width of the slit. The uncertainty on all these parameters adds up and it is not surprising to find a different value for both α and $\tilde{n}/n$ than the experimental values obtained from Raman-Nath scattering (α) and from interferometry ($\tilde{n}/n$).

Because of the very indirect method of estimating $\tilde{n}/n$ from Raman-Nath scattering, the direct interferometric result is the most reliable result.

However, for smaller grating spacings no interferometric results can be obtained and shadowgraphy does not provide any quantitative data. Unfortunately $\rho\eta^2 > 1$ for smaller grating spacings and we cannot neglect refraction. The complete problem including refraction and the plasma gradient is too difficult to solve. Refering to reference [30], we will examine the scattering of light from a phase grating, including refraction, but without the gradient. Useful information can be obtained from the solution of this somewhat simpler problem.

We have to solve the wave equation for the electric field with a modulated index of refraction.

$$\nabla^2\vec{E} - \frac{(\eta + \Delta\eta\, cos(k_g y))^2}{c^2}\frac{\partial^2\vec{E}}{\partial t^2} = 0$$

We know that some diffracted beams will be created at an angle $tan\ \theta = nk_g/k$. If this angle of diffraction is small enough ($k_g << k$), we can neglect the vector nature of the electric field and solve the scalar wave equation. Separating the time dependance of the field, we can write in the two dimensions relevant to this problem:

$$E(y,z,t) = \psi(y,z)e^{i\omega t}$$

The wave equation becomes:

$$\frac{\partial^2\psi}{\partial z^2} + \frac{\partial^2\psi}{\partial y^2} + \frac{\omega^2}{c^2}\left(\eta + \Delta\eta\ cos(k_g y)\right)^2\psi = 0$$

And finally, using $k = \omega/c$, we obtain the time independent scalar Helmholtz equation :

$$\frac{\partial^2\psi}{\partial z^2} + \frac{\partial^2\psi}{\partial y^2} + k^2\left(\eta + \Delta\eta\ cos(k_g y)\right)^2\psi = 0 \qquad (4.3)$$

for $\Delta\eta/\eta << 1$ we can write $(\eta + \Delta\eta cos(k_g y))^2 \cong \eta^2 + 2\eta\Delta\eta\ cos(k_g y)$ (in our experiment $\Delta\eta/\eta \cong 4 \times 10^{-5}$)
We now define:

$$\psi(y,z) \equiv e^{ik\eta z}\phi(y,z) \qquad (4.4)$$

In terms of $\phi(y,z)$ the Helmholtz equation then becomes:

$$2ik\eta\frac{\partial\phi}{\partial z} + \frac{\partial^2\phi}{\partial z^2} + \frac{\partial^2\phi}{\partial y^2} + 2k^2\eta\Delta\eta\ cos(k_g y)\phi = 0$$

Because we factorized the fast $e^{ik\eta z}$ variation of $\psi(y,z)$, $\phi(y,z)$ is slowly varying with z and $\frac{\partial^2\phi}{\partial z^2} << k\eta\frac{\partial\phi}{\partial z}$ so:

$$2ik\eta\frac{\partial\phi}{\partial z} + \frac{\partial^2\phi}{\partial y^2} + 2k^2\eta\Delta\eta\ cos(k_g y)\phi = 0$$

The solution must be periodic in y, and we can write:

$$\phi(y,z) = \sum_{m=-\infty}^{\infty} \chi_m(z) e^{mik_g y}$$

and:

$$2ik\eta\frac{\partial\chi_m(z)}{\partial z} - k_g^2 m^2 \chi_m(z) + k^2\eta\Delta\eta(\chi_{m+1}(z) + \chi_{m-1}(z)) = 0$$

finally using $\varepsilon \equiv kz\Delta\eta$

$$2i\frac{\partial\chi_m(\varepsilon)}{\partial\varepsilon} + \chi_{m+1}(\varepsilon) + \chi_{m-1}(\varepsilon) = \rho m^2 \chi_m(\varepsilon)$$

Where $\rho = \frac{k_g^2}{\eta\Delta\eta k^2}$

This is the Raman-Nath equation [31]. The intensities diffracted in each order are $I_m(\varepsilon) = \chi_m(\varepsilon)\chi_m^*(\varepsilon)$. From the experimental Raman-Nath picture shown on figure 4.19 we can see that the intensities become negligible for m>4. We can solve the truncated (χ_m=0 for m>4) Raman-Nath equation numerically with the boundary conditions $\chi_0(0) = 1$ and $\chi_{m\neq 0}(0) = 0$. The result is shown on figure 4.26 for $\rho = 1.5$ ($\lambda_g = 35\ \mu m$) and $\rho = 18$ ($\lambda_g = 10\ \mu m$).

In our experiment, the value of ε after crossing all the plasma is $\varepsilon_f \approx 0.8$. For this value of ε_f, the theory predicts that 1.5% of the light is diffracted by the 35 μm grating in the first order, in good agreement with the experimental value of 1.2%. But for higher orders the predicted intensities decrease faster than the observed ones (Figure 4.19a). This discrepency may be due to the plasma density gradient which was not included for this calculation. For the 10 μm grating we find that 0.03% of the light is

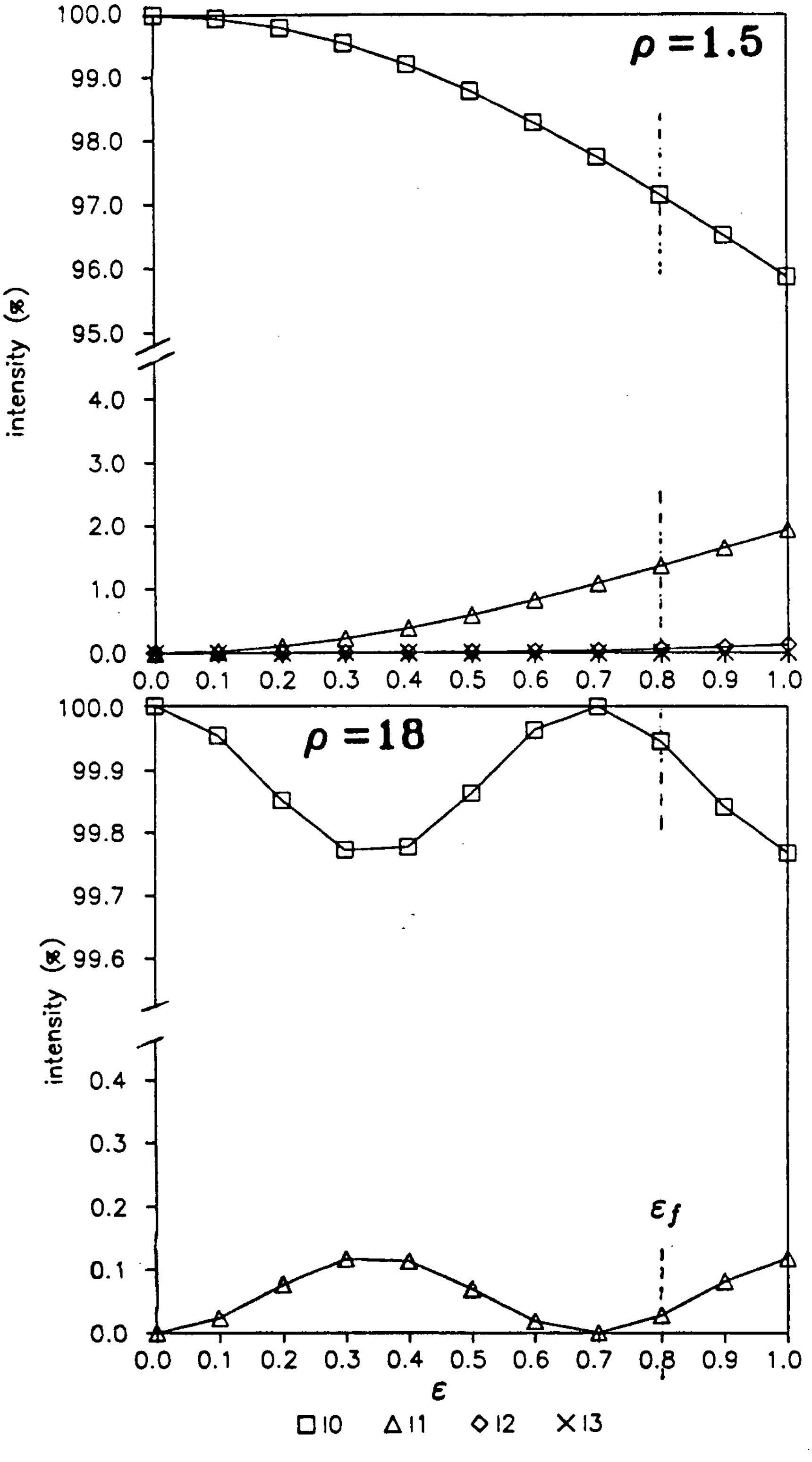

FIGURE 4.26

Intensity diffracted for $\rho = 1.5$ and $\rho = 18$.

diffracted in the first order. Again, this is in reasonable agreement with the experimental value of 0.015%. Notice that for these small grating spacings the diffracted intensity oscillates as the light propagates through the plasma and a small error in our estimate of ε_f can produce a large difference in the amount of light scattered.

The intensities diffracted decrease rapidly for increasing ρ (decreasing λ_g). For $\rho > 10$ corresponding to $\lambda_g < 14\ \mu m$, only the first order has significant intensity and I_0 is almost constant. For these conditions we can find an analytical solution. The Raman-Nath equation reduces to:

$$2i\frac{\partial \chi_1}{\partial \varepsilon} - \rho\chi_1 = -1$$

The solution is:

$$\chi_1(\varepsilon) = \frac{1}{\rho}\left(1 - e^{-i\rho\varepsilon/4}\right)$$

and

$$I_1(\varepsilon) = \frac{4}{\rho^2} sin^2(\frac{\rho\varepsilon}{4})$$

The diffracted intensity is proportionnal to $1/\rho^2$. Even if $\Delta\eta$ stays constant for smaller grating spacings, the diffracted intensity will decrease like λ_g^4. This is a very fast decrease.

Because shadowgraphy and Raman-Nath scattering are basically the same technique, in which one is the Fourier transform of the other, this drastic decrease in the diffracted intensity also explains the decrease in visibility of the modulation in shadowgrams for smaller grating spacings. It also explains why the modulation of the interference fringes could not be observed for $\lambda_g < 20\ \mu m$. Interferometry measures the difference in phase between the wavefunction (Equation 4.4), which represents the summation of the direct and diffracted beams, and the unperturbed reference wave $e^{ik\eta z}$. For increasing ρ, the diffracted terms decrease rapidly so $\phi \rightarrow 1$, and there is no phase difference . Therefore, there is no modulation in the fringes. Because the modulations in the fringes were small (i.e only 1/6 of a fringe) even for $\lambda_g = 35\ \mu m$, they rapidly become indiscernible for smaller grating spacing.

In order to determine if $\Delta\eta$ varies for smaller grating spacings, we plotted $\log(I_1/I_0)$ in function of $\ln(\lambda_g)$ on Figure 4.27. Because the slit used in the Raman-Nath scattering experiment was very large, the probe light crossing the plasma at different heights experiences a different index of refraction. The value of ε_f for different parts ot the probe beam is therefore variable. The $sin^2\varepsilon$ term in the diffracted intensity averages over the width of the probe beam and only the $1/\rho^2$ variation remain.

A slope of 4 on the graph indicates a constant $\Delta\eta$, a larger slope indicates that $\Delta\eta$ decreases for smaller λ_g. A line with a slope of 4 is drawn on Figure 4.27. The experimental results are consistent with a constant $\Delta\eta$.

From the results of all these experiments we can conclude that a plasma expanding above a grating is modulated with $\tilde{n}/n \approx 8\%$ for grating spacing in the range $\lambda_g = 6$ to $35\ \mu m$.

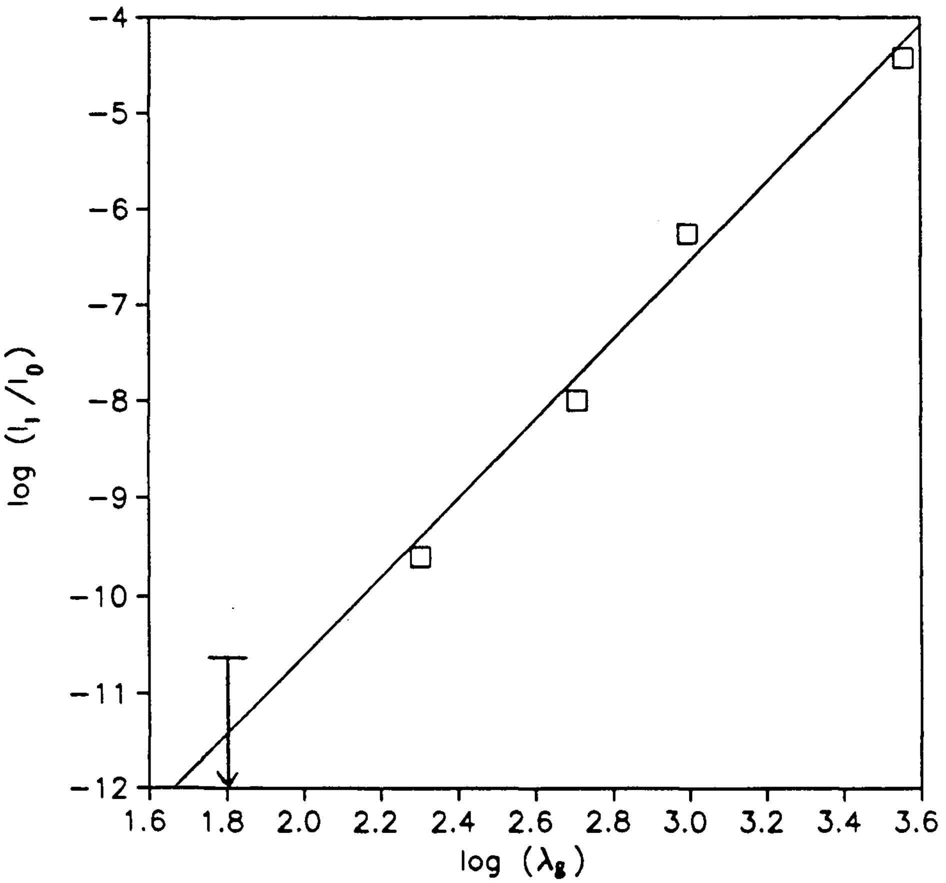

FIGURE 4.27

Log (I_1/I_0) as a function of log(λ_g)

4.6 Effect of the CO_2 Laser Beam on the Modulated Plasma

We now need to know what happens when the CO_2 laser radiation is incident on this modulated plasma. Ideally the CO_2 laser's electric field would force only the electrons to oscillate producing the desired plasma wave without disturbing the ion distribution. However, the 1.8 ns pulse used for this experiment is long enough to perturb the plasma density distribution. We observed this effect using streak interferometry. The plasma was produced with the 6 ns ruby laser and then, 6 ns after the start of the ruby pulse, the CO_2 laser irradiated this preformed plasma. The density profile of the plasma is plotted for different times (Figure 4.28).

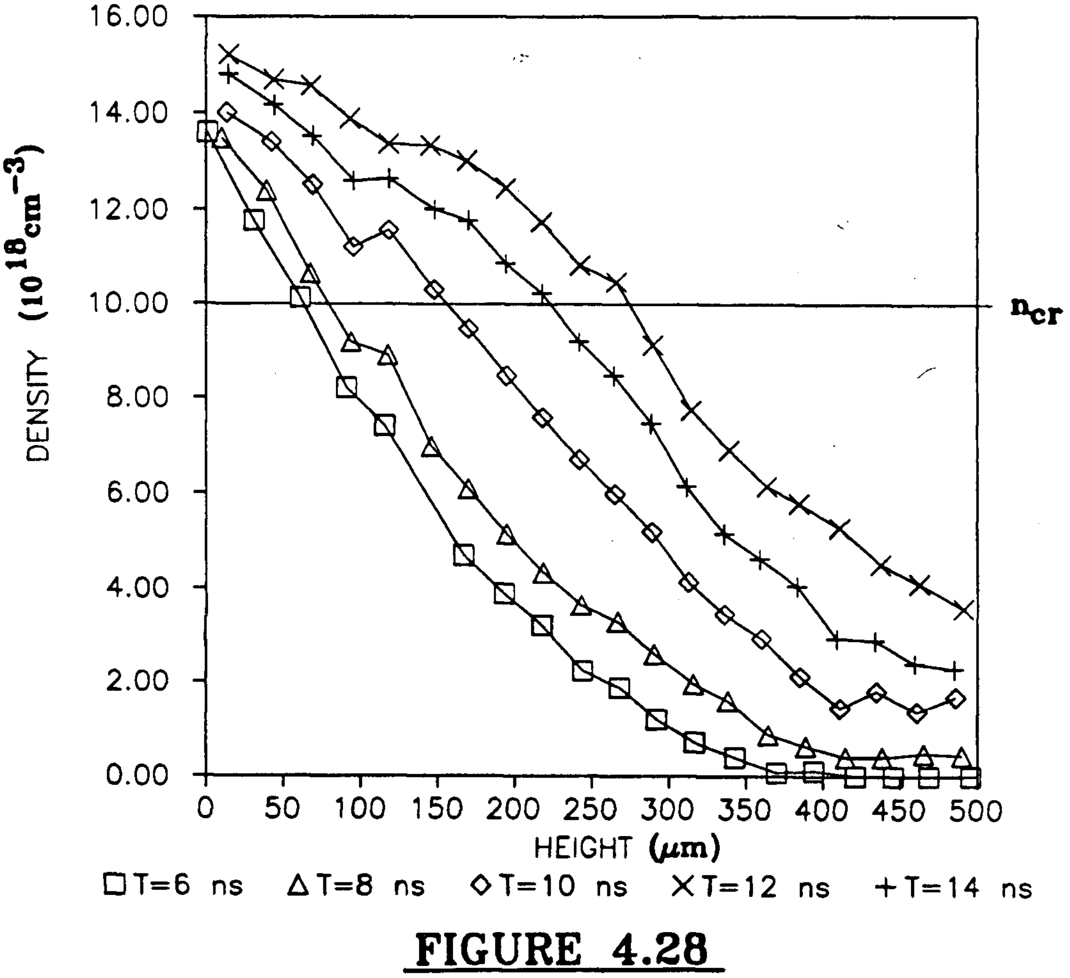

FIGURE 4.28
Density profiles at different times for a plasma irradiated by the CO_2 laser.

The CO_2 laser deposits most of its energy at a density just below the critical density, 10^{19} cm^{-3}, between t=6 ns and t=8 ns. We can see on the graph that the exponential density distribution is changed for densities around 8-9×10^{18} cm^{-3} for t=6 ns and t=8 ns. The plasma is heated and a "bump" develops in the density profile. This happens at a density slightly lower than expected and is probably due to a small error in the estimated width of the plasma. Therefore, the density inferred from the fringe shift is not exact. For t>8 ns the CO_2 laser pulse has ended and the heated region undergoes a rapid expansion making the bump grow bigger. This disturbance expands in both directions at the speed of sound. However, the plasma flows away from the grating at a speed slightly supersonic, therefore the left side of the bump (grating side) is almost stationary and the right side expands rapidly. We can estimate (imprecisely) the sound speed of this heated plasma by measuring the local scale length just past the maximum of the "bump" as a function of time, as we did previously for the expansion of the ruby laser produced plasma. We find $c=9.3\times10^4$. This sound speed is 3.5 times faster than the sound speed of the ruby produced plasma. The CO_2 laser heated plasma is therefore about 10 times hotter than the unperturbed plasma, which is 500 eV.

We also produced 6 ns shadowgrams of a CO_2 laser produced plasma above a grating. For $\lambda_g=35$ μm, they are very similar to those obtained for ruby laser produced plasmas. However, when we took shadowgrams with a smaller grating spacing, the contrast of the modulation decreased faster than with the ruby laser produced plasma. For grating spacings smaller than 10 μm, no modulation can be seen on the shadowgrams.

We have seen previously that a shadowgram is actually an integrated picture over a few cycles of the ion acoustic oscillation (section 4.4). When the CO_2 laser heats the plasma and increases the speed of sound, the ion-acoustic frequency ν_{ia} increases and there are more wave cycles during the shadowgram's exposure. This increased frequency reduces the visibility of the modulation and this effect is worse for small grating wavelengths because $\nu_{ia} = c_s/\lambda_g$. The frequency becomes too high and short wavelengths (that were already creating very low contrast on the shadowgram in a cold plasma) do not form a shadowgram with a visible modulation in a hotter plasma.

In this chapter we observed the density modulation in the plasma expanding above a laser irradiated grating. We will now examine whether this plasma is suitable for the oscillating plasma grating accelerator.

CHAPTER 5

THE TRAPPING AND ACCELERATION OF ELECTRONS BY THE PLASMA WAVE

In the previous chapter we described the production of a modulated plasma. In Chapter 2 we saw how a large electron plasma wave can be excited in such a plasma. In those calculations the plasma was modulated but otherwise uniform. Now we have a situation with a large density gradient perpendicular to the grating surface. We need to determine whether this expanding plasma is suitable for the oscillating plasma grating accelerator.

5.1 Electron Acceleration in the Expanding Plasma

It is first important to realize that a 25 keV electron (see Chapter 6 for the description of the electron system) will cross the 1.6 mm long plasma in 15 ps. The electron is accelerated by about 500 cycles of the CO_2 light and, accordingly, by about 500 oscillations of the plasma wave. In such a short time, the plasma does not move so we can neglect the expansion and study the frozen plasma at a certain time to evaluate the electron acceleration. In Chapter 2 we calculated the acceleration for an electron in a plasma modulated in the y direction but otherwise uniform. For the exploding grating the situation is more complex. There is an exponential density profile in the x direction (height above the grating). Because of the density change with height, the amplitude of the excited plasma wave will not be uniform throughout the plasma. We will now calculate the amplitude of the plasma wave as a function of the height above the plasma.

The CO_2 laser beam comes from $x=\infty$ and propagates in the underdense plasma until it reaches the critical layer where $n_{cr}=10^{19}$ cm^{-3}. It is reflected out of the plasma at this point with some loss of intensity. An evanescent wave penetrates a small distance beyond the critical layer. We can calculate the amplitude of the CO_2 laser electromagnetic (E.M.) wave at any height above the grating. For this calculation we can average over the plasma modulation because for the case of electron acceleration, the modulation must have a wavelength smaller than the wavelength λ_{CO2} of the CO_2 laser. A modulation of the plasma density, smaller than the wavelength of the laser beam, will not affect its propagation. The density is:

$$n(x)=n_0e^{-x/L}$$

Here $L=c_st$ is the scale length of the plasma. For $t>2$ ns the scale length of the plasma is much longer than λ_{C02}. If we calculate the electric field only in a region close to n_{cr} we can consider the plasma density as linear:

$$n(x)=n_{cr}(1-x/L)$$

The solution for the E.M. wave amplitude in this linear approximation is well known [21]. It is:

$$E_L(x) = 2\sqrt{\pi}\left(\frac{2\pi L}{\lambda_{CO_2}}\right)^{1/6} E_0 Ai\left(-\left(\frac{(2\pi)^2}{\lambda_{CO_2}^2 L}\right)^{1/3} x\right) \quad (5.1)$$

Where $A_i(u)$ is the Airy function (see reference [20] for example). This CO_2 laser radiation field will excite plasma waves to a saturation amplitude given by the smallest amplitude derived by Equations (2.5), (2.6) or (2.7). With our CO_2 laser intensity and our plasma temperature, the collisional damping (equation 2.5) gives the dominant saturation mechanism and the amplitude of the plasma wave electric field E_{epw} as a function of x is given by:

$$E_{epw}(x) = E_L(x)\,\frac{\tilde{n}}{n}(x)\,\frac{1}{\sqrt{\left(1-\frac{n(x)}{n_{cr}}\right)^2+(0.01)^2}}$$

In order to calculate $E_{epw}(x)$ we have to find what $\tilde{n}/n(x)$ is. We have seen (Figure 4.23) that $\tilde{n}/n$ is not constant with x but oscillates close to the grating and then stays quite constant further away. From inspection of shadowgrams like the one on Figure 4.16 we can see that phase reversal of the shadows (corresponding to oscillation of $\tilde{n}/n$) are limited to a region two to three grating spacings above the grating surface. For electron acceleration $\lambda_g < 10.6$ μm, the oscillation of $\tilde{n}/n$ extends to about 30 μm. If the CO_2 laser radiation illuminates the plasma later than 5 ns after the start of the ruby laser pulse, the CO_2 laser critical layer will be further than 30 μm from the grating. In this region $\tilde{n}/n$ is fairly constant showing no phase reversal.

$E_{epw}(x)$ and all the factors that contribute to it are plotted on Figure 5.1.

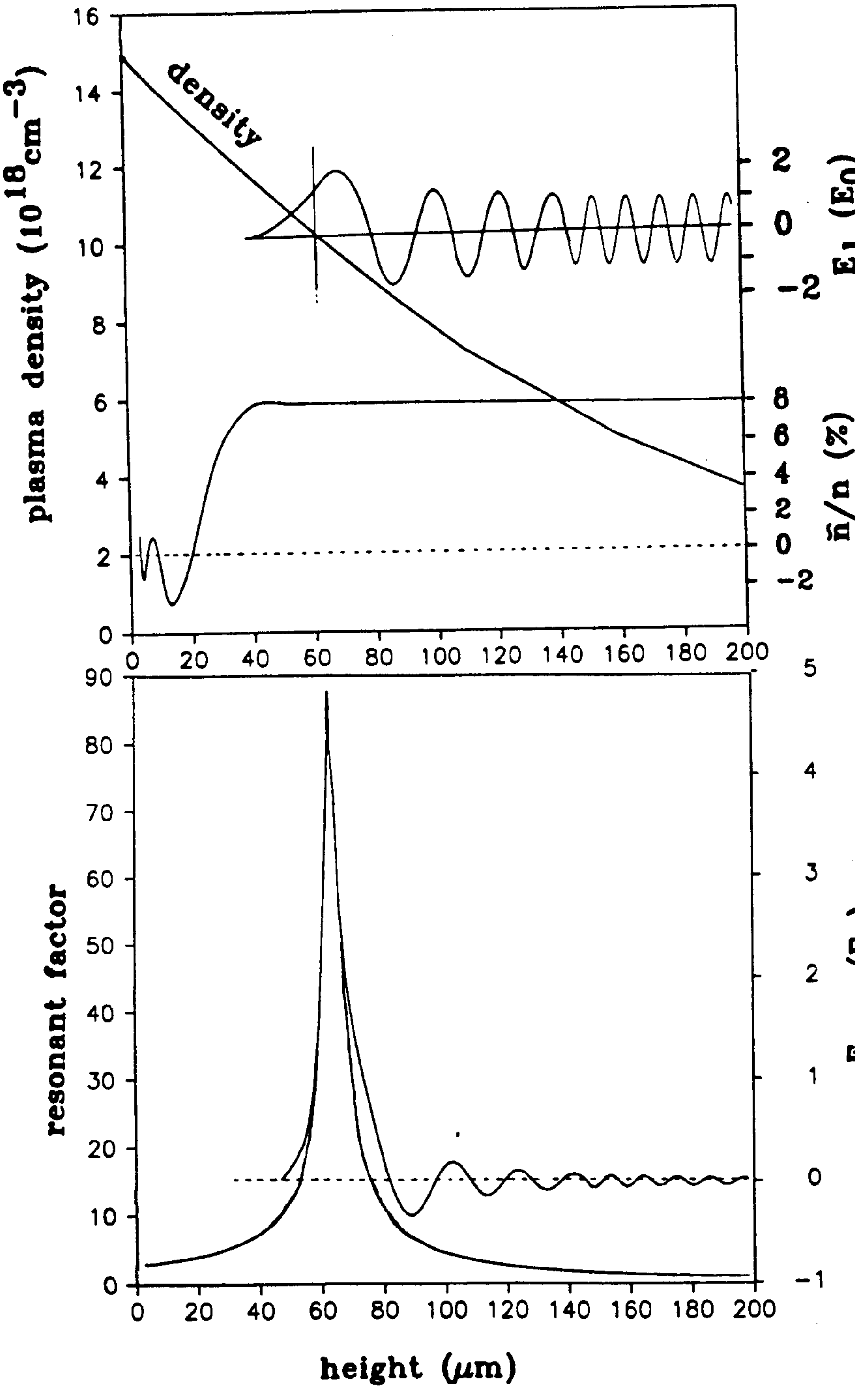

FIGURE 5.1

Density, $\tilde{n}/n$, E_L,resonant factor and E_{epw} as a function of height.

The upper graph shows the exponential density profile, the CO_2 laser electric field E_L, in unit of the incident laser electric field E_0 (this is the Airy function described by Equation (5.1)) and the plasma density modulation $\tilde{n}/n$ in percentage. The resonant factor $(1-n(x)/n_{cr})^2+0.0001)^{-1/2}$ is drawn on the lower graph which also includes the electric field of the plasma wave E_{epw} in unit of the incident CO_2 laser field E_0. All these functions are plotted versus the height above the grating. The plasma wave electric field E_{epw} has a maximum of $E_{epw}=5E_0$ at a height of 60 μm. An electron that traverses the plasma at a height of 50 μm $<x<$ 80 μm experiences a strong plasma wave electric field. But for other heights the field decreases rapidly. There is an acceleration layer around the CO_2 laser critical surface. The thickness of this layer increases with time because the scale length of the plasma ($L=c_st$) increases. In order to be accelerated the electron must stay in the accelerating layer during the time it takes to cross the plasma. However, the plasma density is not constant in the y-z plane. As a result the boundary surface of the acceleration layer looks somewhat like the surface of a rugby ball (Figure 5.2). The injected electrons will traverse the plasma in a straight line and will be in the accelerating region only for part of their trajectory (Figure 5.3a). If the time delay between the CO_2 laser pulse and the formation of the plasma is increased, the accelerating layer becomes thicker and the electrons are accelerated for a longer part of their trajectory (Figure 5.3b). In addition, the cross section area of the accelerating region onto which the injected electrons must be aimed, increases and more electrons can be accelerated. But if the time delay is too long, the plasma modulation damps away and no acceleration takes place.

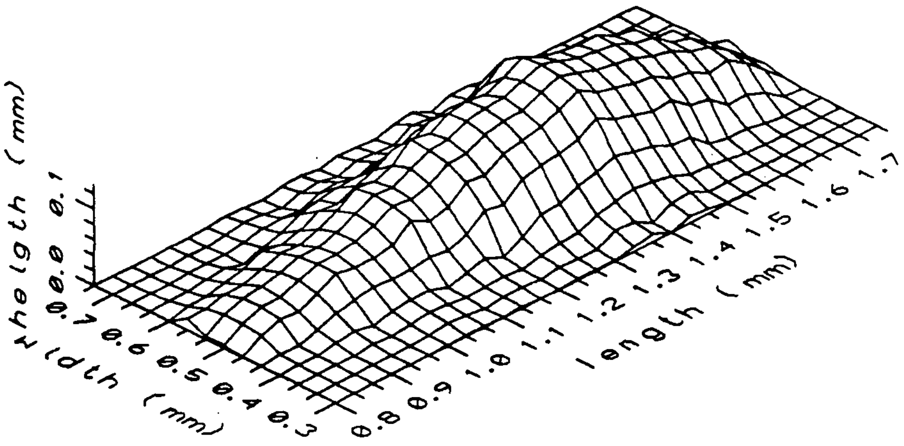

FIGURE 5.2
Critical layer. The ridges are an artifact of the digitization technique

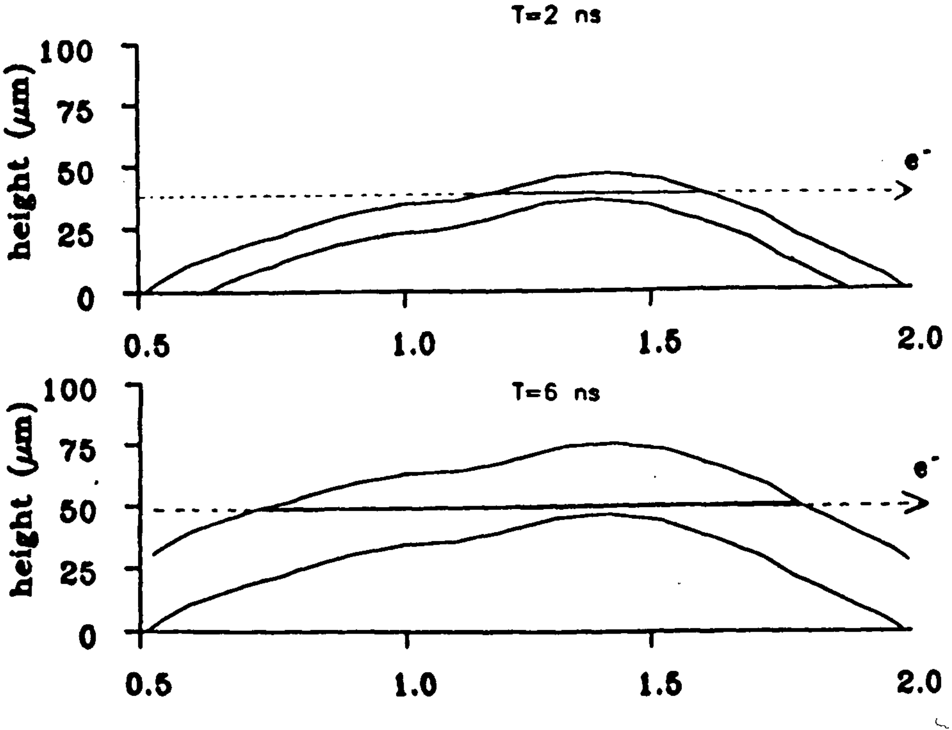

FIGURE 5.3
Trajectory of the electrons. The solid part of the straight line shows the accelerated part of the trajectory.

The formation of the plasma modulation defines a time window during which we can fire the CO_2 laser. For the smallest modulation observed (6 μm) the optimum time is 6 ns, which is as late as possible but just before the observable modulation disappears. We will vary the time delay between the CO_2 and the ruby lasers around this value during the experimental investigation.

5.2 Acceleration of the Electrons by the Plasma Wave

As seen in Chapter 2, the oscillating plasma grating technique allows very good control of the phase speed of the plasma wave and as a result we can choose a small phase speed in order to use a simple, low energy electron source for injection into the plasma. However this introduces a new problem. In other methods [11] the already highly relativistic electron beam does not change speed appreciably during the accelerating interaction with the plasma wave. For low energy electrons the speed will vary considerably and the correct accelerating phase cannot be maintained with a normal grating. The use of a chirp grating where the line spacing increases synchronously with the speed of the electrons solves this problem.

The electric field of the plasma wave produced above a chirp grating will be of the form:

$$E(z,t) = E_{epw} sin(\omega_0 t \pm k_g(z) z) \qquad (5.2)$$

Where E_{epw} is the amplitude of the electric field strength, ω_0 is the frequency of the CO_2 laser, the ± represents waves going in both directions and $k_g(z)$ is the grating wave number which is now a function of position. The phase speed of this wave will also be a function of position, and it is calculated by setting the time derivative of the argument of the sine function to zero.

$$\begin{aligned}
\frac{d}{dt}(\omega_0 t \pm k_g(z)z) &= 0 \\
\omega_0 \pm \frac{dk_g(z)}{dt}z \pm k_g(z)\frac{dz}{dt} &= 0 \\
\omega_0 \pm \frac{dz}{dt}\left(\frac{dk_g(z)}{dz}z + k_g(z)\right) &= 0 \\
\frac{dz}{dt} = \mathrm{v}_{ph}(z) = \frac{\pm\omega_0}{\frac{dk_g(z)}{dz}z + k_g(z)} & \qquad (5.3)
\end{aligned}$$

If the increase in phase speed during one cycle of the plasma wave is small compared to the actual phase speed, we can obtain the approximate equation for this slowly varying wavelength approximation:

$$\mathrm{v}_{ph}(z) \approx \frac{\omega_0}{k_g(z)} \qquad (5.4)$$

We must now determine $v_{ph}(z)$. An electron in a constant electric field increases energy according to $W(z)=W_0+m_ec^2+qE_{epw}z$, where $W(z)$ is the electron energy, W_0 is the initial kinetic energy, m_e and q are the mass and charge of the electrons respectively. If the speed of the electrons in a plasma wave is perfectly synchronized with $v_{ph}(z)$, it experiences a constant electric field E_{epw}. We therefore choose the grating chirp corresponding to a linear increase of the energy. This is a simple choice, but probably not the optimum one. More work would be needed to find the chirping rate that optimizes the trapping and acceleration of the injected electrons. But for the proof of principle experiment described in this thesis the simple linear energy increase is good enough. The increase in speed corresponding to this linear increase in energy can be found.

$$W^2(z) = m_e^2c^4 + p^2(z)c^2 \qquad p(z) = \frac{m_e \mathrm{v}_{ph}(z)}{\sqrt{1 - \frac{\mathrm{v}_{ph}^2(z)}{c^2}}}$$

Inverting this equation we find:

$$\mathrm{v}_{ph}(z) = c\sqrt{\frac{W^2(z) - m_e^2c^2}{W^2(z)}} \qquad (5.5)$$

The relativistic expression is used because the electrons can accelerate to a high energy during the experiment. Using Equations (5.5) and (5.3) gives a differential equation for $k_g(z)$.

$$\frac{dk_g(z)}{dz}z + k_g(z) = k_0\sqrt{\frac{W^2(z)}{W^2(z) - m_e^2c^4}}$$

With

$$k_0 = \frac{\omega_0}{c}$$

This equation can be solved numerically. However, for the values of the accelerating electric field E_{epw} and injection energy W_0 of our experiment, and with $\omega_0=\omega_{co2}$, the conditions for the approximate solution (5.4) are satisfied. We can therefore write:

$$k_g(z) = k_0\sqrt{\frac{W^2(z)}{W^2(z) - m_e^2c^4}} \qquad (5.6)$$

An electron trapped in the plasma wave above a grating made to satisfy this equation, will accelerate continuously if it is correctly positioned in the wave cycle and if the electric field E_{epw} is constant everywhere. This is not likely to be the case in an experimental situation. Injecting a bunch of electrons at a certain phase of the cycle is clearly impossible given a frequency of $\omega_0=\omega_{co2}=1.8\times10^{14}$ s^{-1}. Also the electric field of the plasma wave is a function of the CO_2 laser field, the plasma density and the static modulation amplitude, all of which can fluctuate considerably along the interaction region. In order to examine these effects we need to study the trajectory of the electrons in the accelerated wave produced above a chirp grating.

It is instructive to look first at the case of an electron in a wave of constant phase velocity. The electric field of the wave generates a potential:

$$\phi(z,t) = \phi_0 cos(\omega t - kz)$$

Where $\phi(z,t)$ is the potential.

We can transform this into a frame of reference moving with the wave at

$v_{ph}=\omega/k$ and integrate the equation of motion of the electron to obtain the energy-conservation equation:

$$\frac{1}{2}m_e\dot{z}'^2 - e\phi_0 \quad = 0$$

Where a dot represents the time derivative and z' is now in a reference frame moving with the wave. The solutions of this equation are elliptic integrals. The trajectories in a phase-space diagram are shown on Figure 5.4. If the difference of speed between the electron and the phase speed of the wave is small enough, i.e. $\frac{1}{2}m_e(\Delta v)^2 < e\phi_0$, the electron is trapped in the potential well of the waves where it oscillates around the potential minimum. For greater differences of speed, the electron is free and the effect of the wave is to add an oscillation around its average uniform speed.

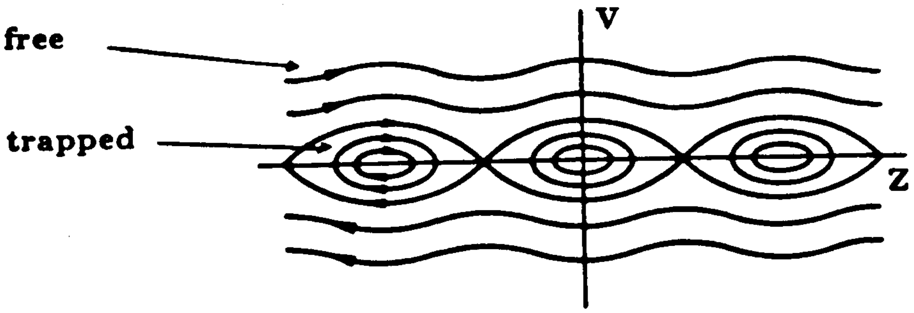

FIGURE 5.4
Electron trajectories as seen in the wave frame.

We can perform a similar analysis for an accelerated wave. In this case the potential is:

$$\phi(z,t) = \phi_{epw}(z)cos(\omega_0 t - k_g(z)z)$$

It is important to notice that not only does the wavelength of the potential wave change with distance, but the amplitude $\phi_{epw}(z)$ is also variable. This is because the potential is given by:

$$\phi(z,t) = \int E(z,t)\,dz$$
$$\phi(z,t) = \int E_{epw} sin(\omega_0 t - k_g(z)z)dz$$
$$\phi(z,t) \approx -\frac{E_{epw}}{k_g(z)} cos(\omega_0 t - k_g(z)z) + constant \qquad (5.7)$$

In the last line we use the approximation of a slowly varying grating wavelength. So for an accelerating grating, $\phi_{epw}(z)$ increases with distance. We can now transform into the reference frame of the wave. In a uniformly accelerated frame, an inertial force is introduced and therefore a linearly increasing potential adds to the potential of the wave. The left part of Figure 5.5 shows the potential of the wave at a fixed time in the wave reference frame. For zero acceleration (a), the depth (d) of the trough is large and the electrons oscillate around a minimum. For intermediate acceleration (b), the depth of the potential well decreases. The electrons can be trapped only if they oscillate with a small amplitude. If the acceleration of the plasma wave becomes too large (for $a_{pw} > a_m = qE_{epw}/m_e$), there is no more potential minimum and no electrons can be trapped. This is shown in (c). The right hand side of Figure 5.5 demonstrates this process in the laboratory reference frame. For zero acceleration, the electrons are oscillating in the propagating wave. At intermediate acceleration the electrons climb on the left side of the potential well.

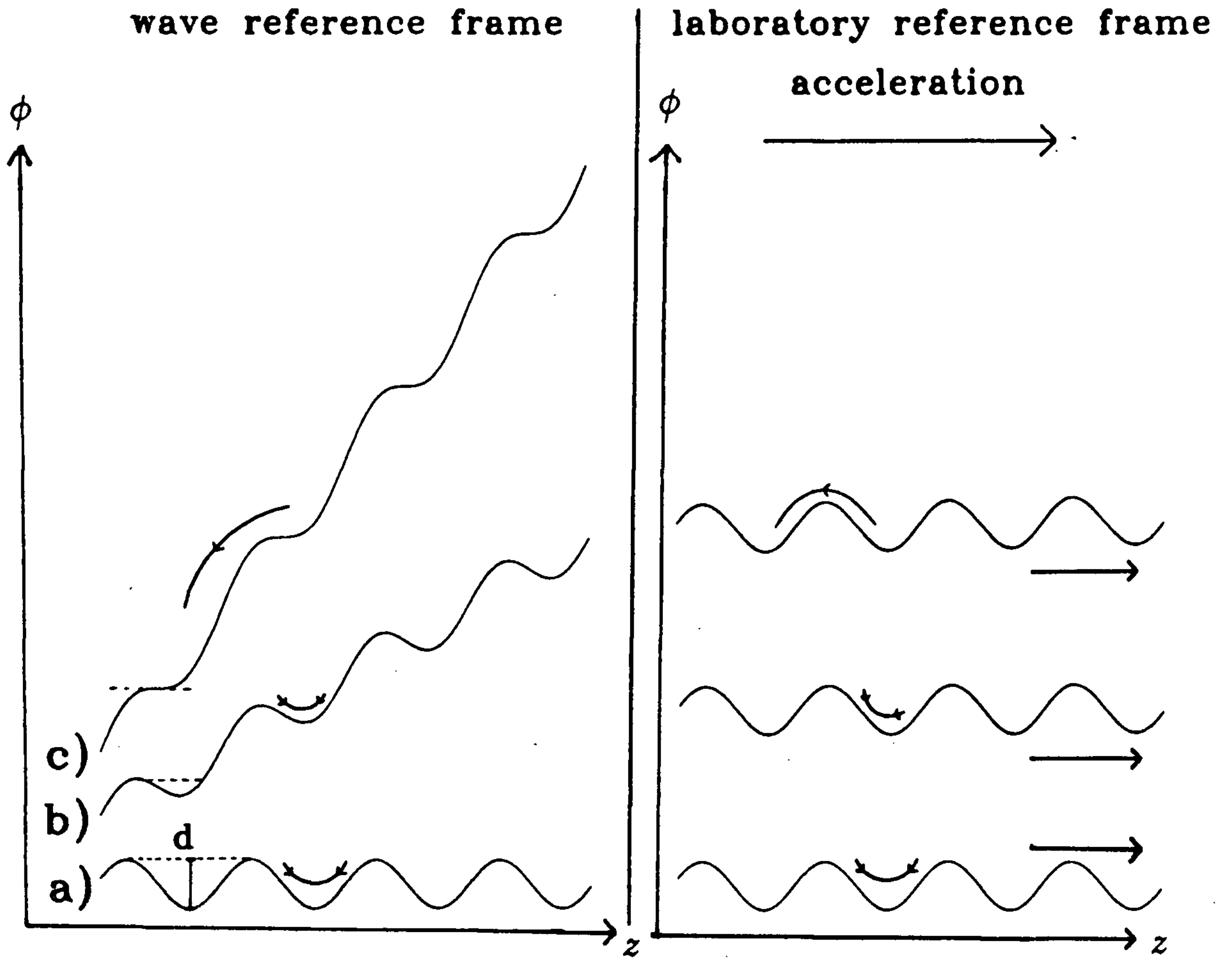

FIGURE 5.5
Potential of the accelerated wave.

Only small oscillations are possible or the electrons spill above the crest of the wave and no longer accelerate. Finally, for $a_{pw} > a_m$, all the electrons pass above the potential maximum and no acceleration is possible.

For an electron accelerator to work it is therefore necessary that $a_{pw} < a_m$. It is desirable that a_{pw} be as big as possible in order to obtain a large energy increase, but then a small number of electrons can be trapped. If it were possible to inject the electrons at a precise phase of the wave cycle, it would be possible to place many electrons in the small potential well that exists at high acceleration. However, because of the very high frequency of the wave this is not possible and the electrons arrive at a random phase of the wave cycle. Therefore, we need to calculate how many electrons can be trapped for a given acceleration.

5.3 Initial Trapping.

In order to be sure to trap the electrons, we have to inject them at a speed $v_{in} > v_{ph}(0)$, where $v_{ph}(0)$ is the phase speed of the plasma wave above the edge of the grating. As the phase speed increases along the chirp grating the electrons reach a point where $v_{in} = v_{ph}(z_{trapped})$ (Figure 5.6). To find out exactly what happened at this point, a computer program was written to solve numerically the equation of motion for the electrons in the potential of the accelerating wave.

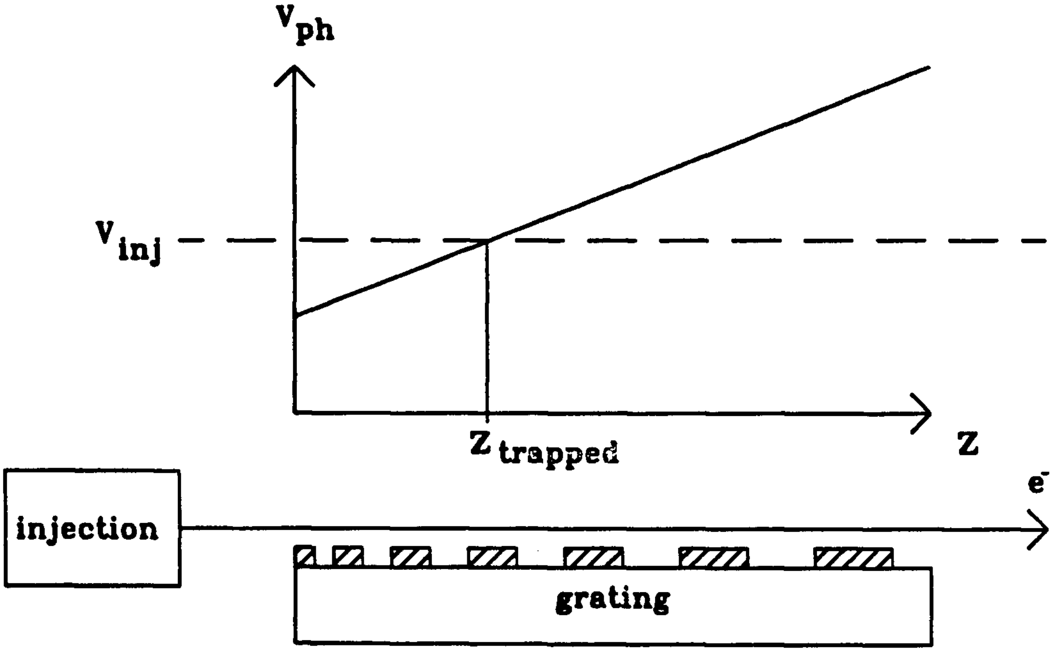

FIGURE 5.6
Injection of electrons in a wave with increasing phase speed

The equation of motion is:

$$\gamma^3 m_e \ddot{z} = eE_{epw}(z,t)$$

With $\gamma = (1-\dot{z}^2/c^2)^{-1/2}$ and $E_{epw}(z,t)$ given by Equation (5.2).

The result of this calculation was displayed on the computer screen as an animated movie showing the electron surfing the wave. It is easier to explain the motion of the electrons in the wave reference frame (Figure 5.7).

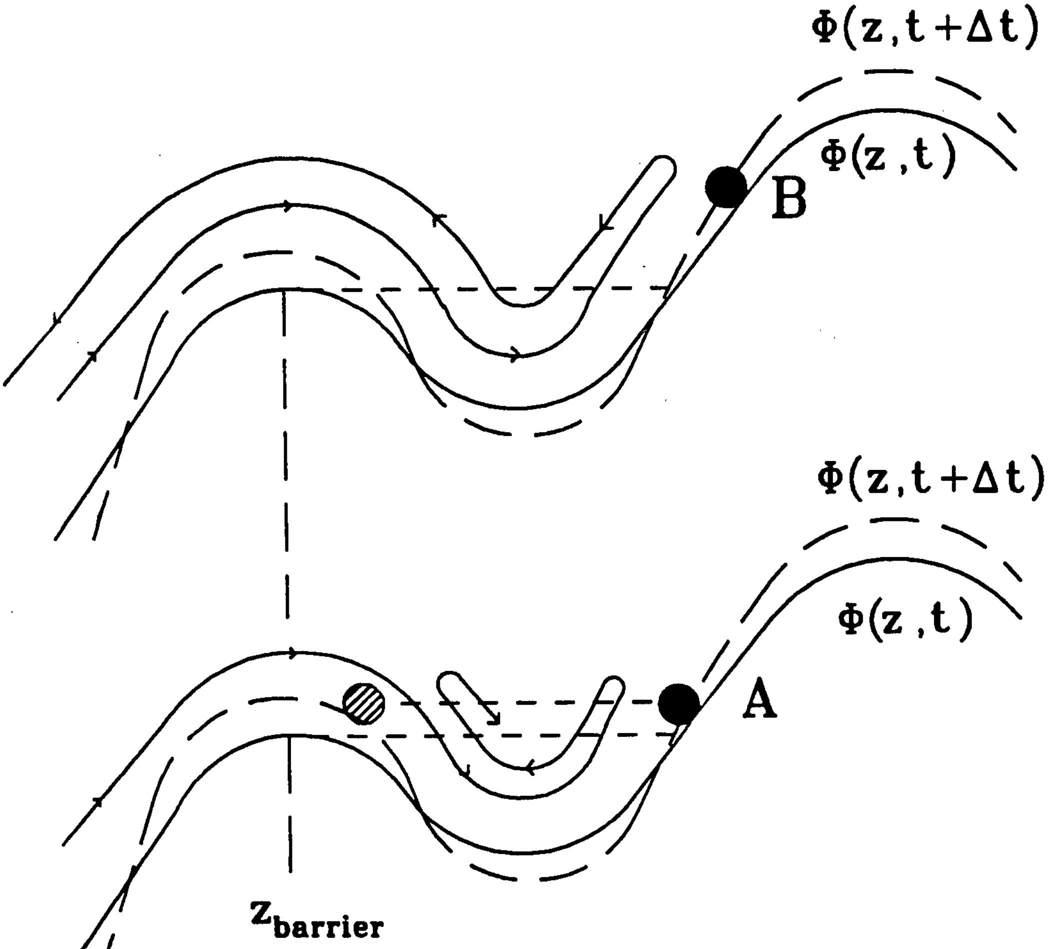

FIGURE 5.7

Detail of the electron trapping mechanism.

The electrons arrive from the left with a speed greater than the phase speed. They climb the potential hill going right through all the potential wells before their turning point. At this point the electrons stop, then reverse (as viewed in the accelerating frame, in the lab frame the electrons keep going in the same direction with only a small change of velocity) and begin going back down the potential hill. If the potential of the wave was constant, no electrons at all would be trapped. But from Equation (5.7) we know that the potential of the wave increases along the grating. Because we are in a reference frame moving with the wave this translates into a potential that increases with time. So while the electrons cross the last potential well, stop, turn around and cross the well again, the height of the potential barrier has increased slightly. This increased potential is indicated on the Figure as $\phi(z,t+\Delta t)$. After being reflected the electrons attain the bottom of the potential well with a reverse velocity v_r corresponding to a kinetic energy W_r. If $W_r<e\phi_{epw}(z_{barrier},t+\Delta t)$ the electrons will not pass the barrier and will be trapped. But for $W_r>e\phi_{epw}(z_{barrier},t+\Delta t)$ they pass above the crest of the potential and are no longer able to accelerate with the wave. The reverse velocity v_r depends on the exact turning point. If this point is just above the last potential crest (point A on Figure 5.7) the reverse velocity is low. The higher the turning point, the higher the reverse velocity until, for turning point (B), the electrons have enough speed to pass the barrier and are no longer trapped. For a given grating the turning point is a function of the injection energy and the phase of the plasma wave at the time the electrons arrive over the grating. The computer program can solve the equation of motion of the electron from the time of injection to a final time when the electrons have crossed the whole length of the plasma. Because the trapping mechanism depends critically on the exact speed of the electron at $z_{barrier}$, the small perturbation due to the counterpropagating plasma wave may be important. We therefore kept both waves in the calculation. Using a length of plasma of 100 μm, $v_{inj}=c/3$, and a grating acceleration of 500 eV/μm, the final momentum (normalized to mc) can be calculated for different injection phases. The result is plotted on Figure 5.8 for a plasma wave having an amplitude of $E_{epw}=10$ kV/μm giving $a_{pw}/a_m=5\%$ and for another wave with $E_{epw}=5$ kV/μm ($a_{pw}/a_m=10\%$). It can be seen that the final momentum is either close to the initial momentum (untrapped electron) or around 0.68, which is the momentum expected for an electron trapped and accelerated continuously by the wave. The transition between trapped and untrapped electrons is very sharp, showing that no electrons are lost along the total length of the acceleration if they are initially trapped. This is due to the increase in depth of the potential wells along the accelerator. The wavelength of the plasma wave increases and, for a constant E_{epw}, the potential well gets deeper. We can also plot the phase-space trajectory of the electrons for the different injection phases shown on Figure 5.8, in a fixed reference frame (left side of Figure 5.9), or in an accelerated reference frame following one of the potential wells (right side of Figure 5.9). Note that we are following the same well for the five different injection phases. As can be seen in the accelerated frame, the different peaks correspond to electrons trapped in different wells, except for the peaks corresponding to phases A and C that show trapping in the same well. For phase A, the electrons enter the wave close to the beginning of an acceleration cycle and gain just enough momentum to be trapped in the next well.

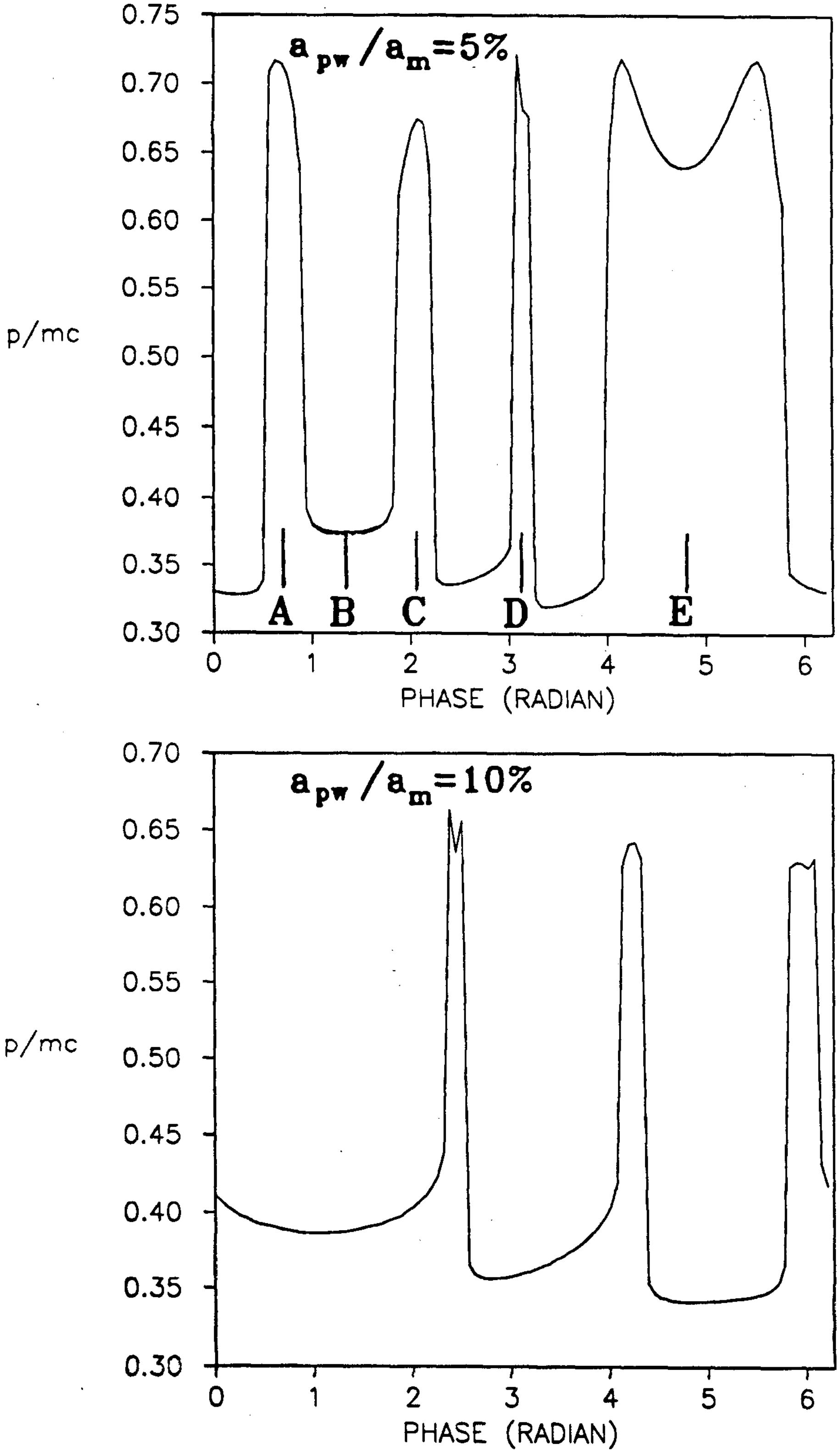

FIGURE 5.8

Final normalised momentum as a function of the initial phase

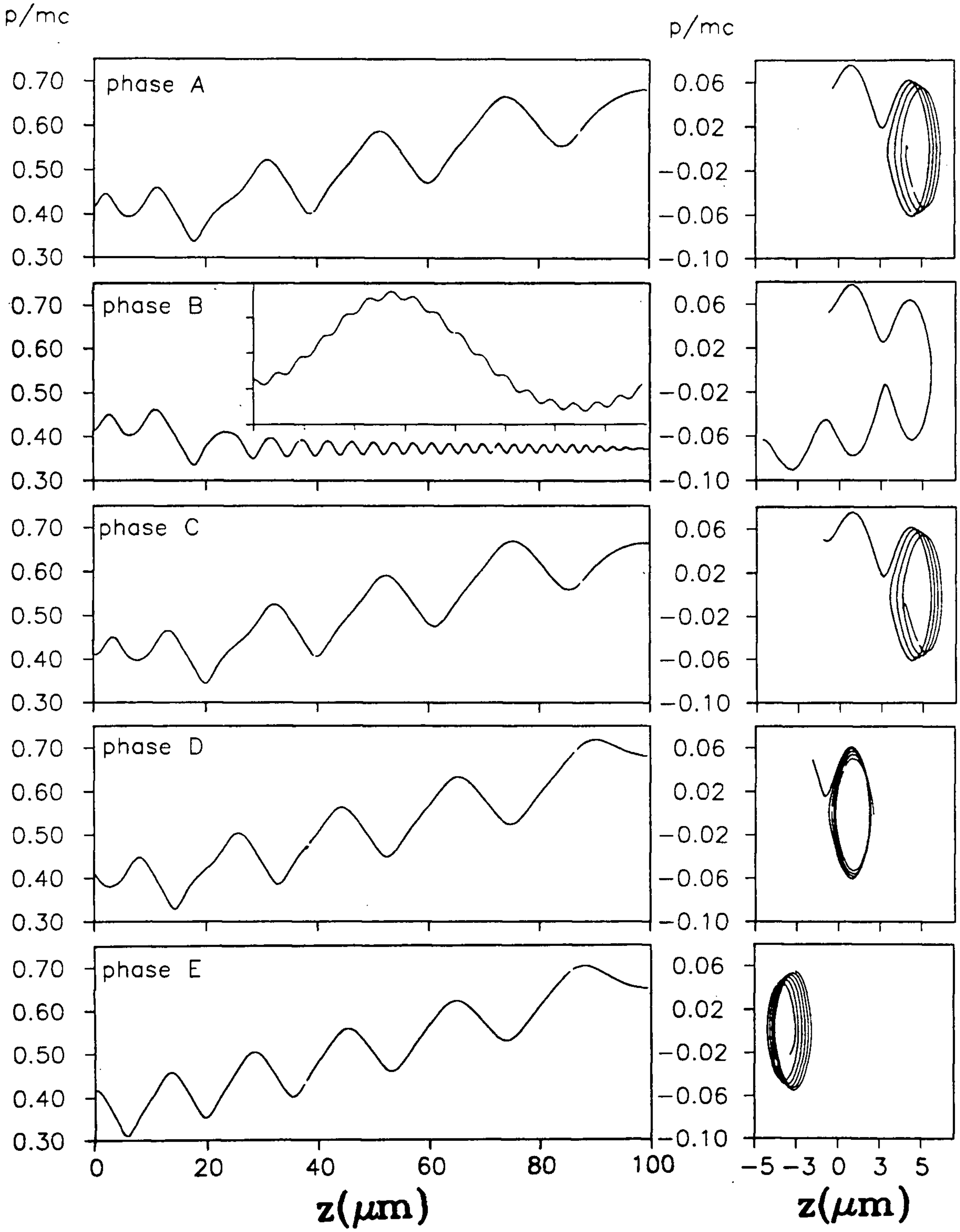

FIGURE 5.9
Phase space trajectory for different injection phases

For phase B, the electrons enter the wave at the very beginning of the acceleration cycle and gain too much momentum to be trapped in the next well, but not enough to be trapped in the following well. The electrons are therefore reflected. For phase C, the electrons enter the wave near the end of a deceleration cycle, loose some momentum and then accelerate for a full acceleration cycle. This results in an increase of momentum practically equal to the one gained in phase A and the electron is trapped. The insert in Figure 5.9 shows a magnification of the beginning of the trajectory. The small ripples are due to the counterpropagating wave. The spiral trajectories in the accelerated frame are due to the time variation of the potential well. Because the wavelength of the potential weave increases, the wells become wider with time and the oscillation of the trapped electrons is damped. This can be understood by considering a particle oscillating between two walls. If the walls are slowly moving apart, the particles will lose energy after each collision with the wall. The oscillation will therefore be damped. The movement of the centre of the spiral (to the right for phase A and to the left for phase E) is also caused by the increase in wavelength. The reference frame follows the potential minimum at $z=0$, but electrons trapped in other wells will slowly drift away from $z=0$ as the distance between each well increases.

Phase-space trajectories like Figure 5.9 clearly show the necessity for a chirp grating. Because of the very short wavelength of the plasma wave ($\lambda_g=3$ μm to 6 μm) the depth of the potential wells are rather small, $\phi_{epw}=E_{epw}/k_g=5$ to 10 kV. Electrons interacting with these waves without being trapped, experience only small momentum excursion. Only the trapped electrons accelerating with the chirp wave gain an interesting amount of energy. For a continuous beam of injected electrons only a fraction will be trapped. We ran the computer program for different values of a_{pw}/a_m and plotted the fraction of electrons that are trapped as a function of a_{pw}/a_m on Figure 5.10.

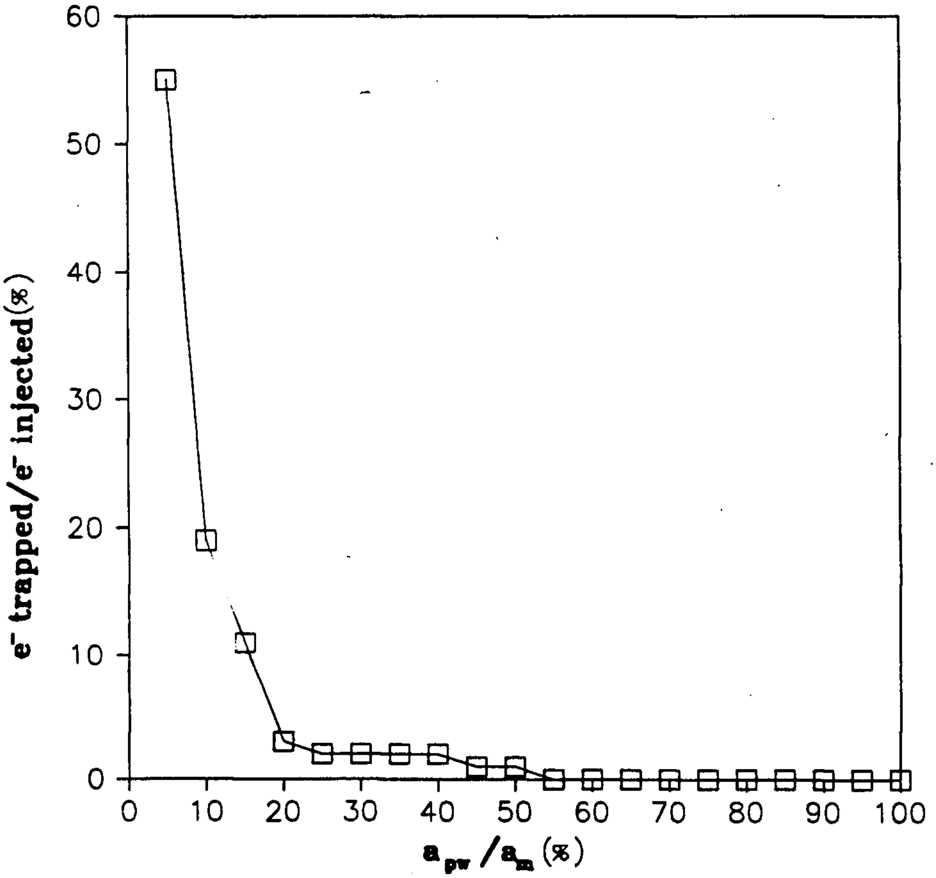

FIGURE 5.10

Percentage of electrons trapped as a function of the grating acceleration.

This fraction decreases for increasing a_{pw}/a_m. To trap more than 10% of the injected beam it is necessary that $a_{pw}<0.15\ a_m$. The phase at which the electrons are trapped depends on the injected energy. Figure 5.11 shows which combination of injection speed and phase, result in trapping the electron. The injected speed is given as a percentage of the phase speed at the beginning of the plasma wave.

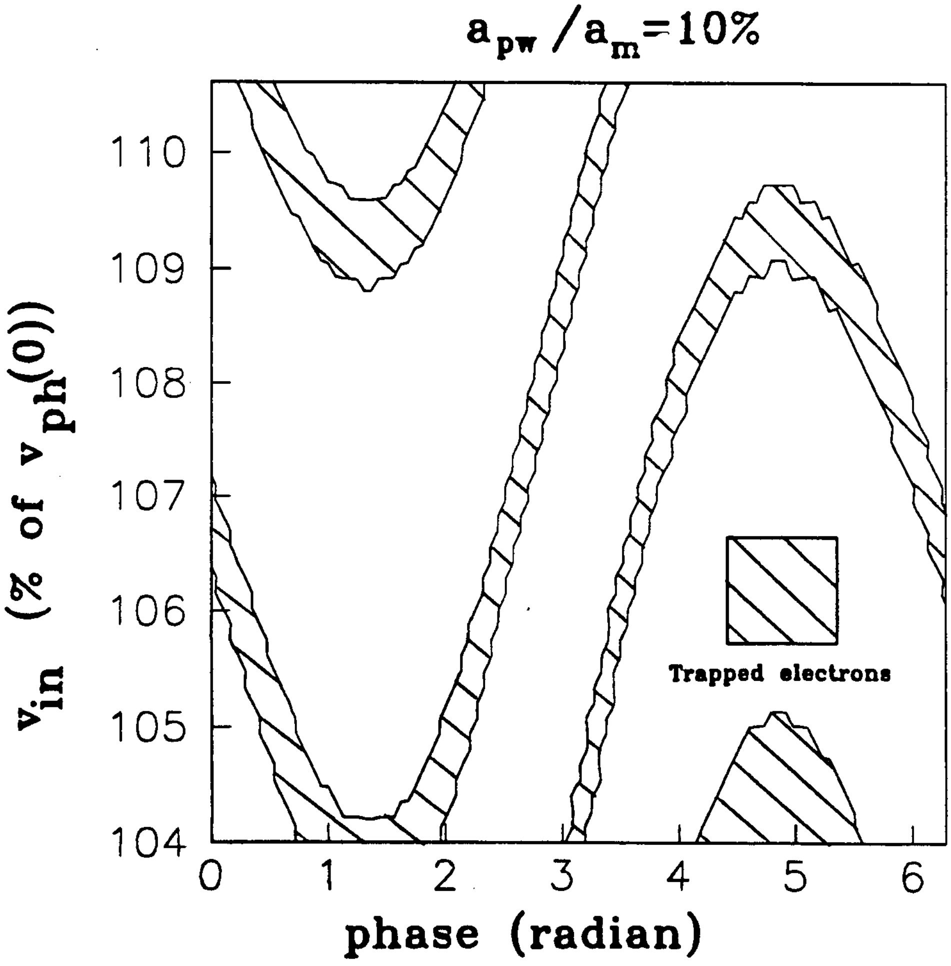

FIGURE 5.11

Trapped electron as a function of the initial speed and phase.

As the injection speed is increased the trapping phase changes. But at a certain injection speed (109% of $v_{ph}(0)$), the trapping phase becomes the same as for the lowest injection speed (104%). This happens because the electrons are then trapped exactly one potential well further along the wave. Therefore, this graph is periodic with increasing v_{inj} as the electrons are trapped in the successive potential minimum of the wave. After initial trapping the depth of the potential well increases with time. It becomes more difficult for the electrons to escape the potential minimum and they will be accelerated all the way to the end of the accelerating plasma wave.

We just saw that a certain fraction of an injected electron beam in an accelerated plasma wave will be trapped and accelerated. This was calculated for a perfect plasma wave with constant amplitude and phase. However, such a perfect wave is difficult to produce in an experimental set up. Due to misalignment and imperfection in the optical system used, the amplitude and phase of the plasma wave will not be constant. We shall now examine the effect of these unavoidable experimental fluctuations of the plasma wave on the acceleration process.

5.4. Effect of Experimental Imperfections on the Acceleration Process.

Many imperfections in the alignment and in the experimental set up can occur for the experimental implementation of the oscillating plasma grating accelerator. These imperfections will perturb the plasma wave in two ways. They can change the amplitude, or the phase, of the plasma wave. We will first look at the effect of different experimental imprecisions on the accelerating plasma wave. Then, we will examine how amplitude and phase fluctuations influence the acceleration of trapped electrons.

5.4.1 Electron Beam Misalignment

The electron beam can be misaligned such that the electron trajectories are not parallel to the grating surface. In this case, the height of the electrons above the surface will change as they travel above the grating. Since the amplitude of the plasma wave is strongly height dependant, (see Figure 5.1) the electrons will experience large changes in the amplitude of the plasma wave as a function of time.

5.4.2 Plasma Non-uniformity

We have seen in Chapter 4 that our plasma density, averaged over a few grating spacings, is not very uniform. Figure 5.3 shows a curved acceleration layer caused by the non-uniformity of the plasma. An electron following a straight trajectory will traverse this accelerating layer from the outside boundary to the inside boundary and back. The amplitude of the plasma wave is strongly peaked in the middle of the accelerating layer and decreases quickly on the edge. Therefore the electron is subjected to a strong variation of the amplitude of the plasma wave.

The phase of the plasma wave is a function of the phase of the plasma density modulation and the phase of the CO_2 laser radiation.

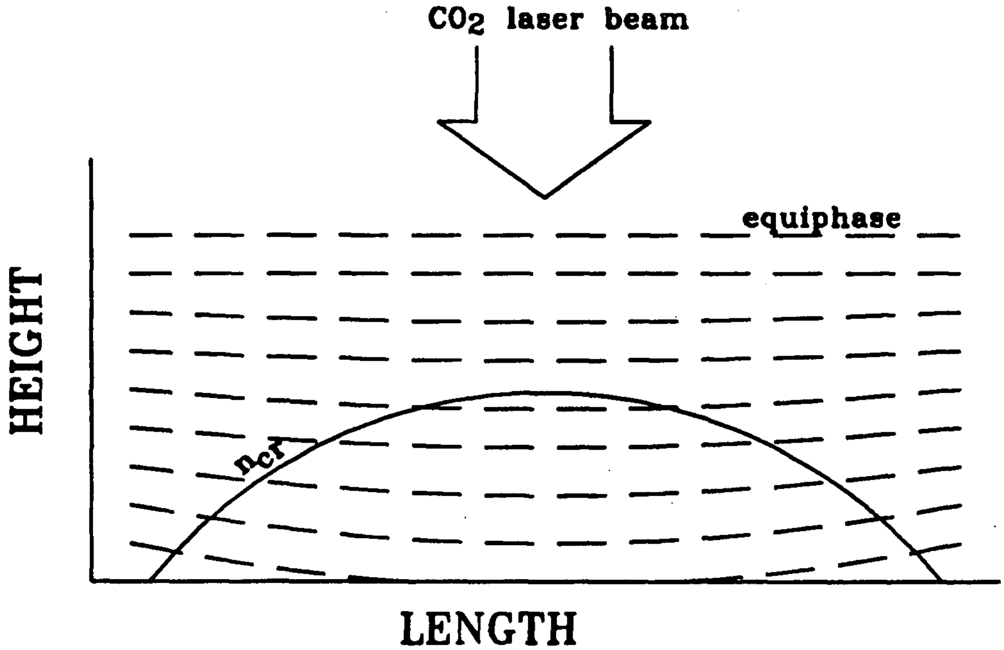

FIGURE 5.12
Phase variation due to the curvature of the critical layer.

Figure 5.12 explains the effect of a bent critical layer (labelled n_{cr}) on the phase of the CO_2 laser. If a laser beam with flat wavefronts (equiphase) is incident upon the indicated plasma, the laser beam will be defocused and the wavefront will be curved as indicated. Also, the middle of the plasma is higher above the grating surface than the edge of the plasma. Therefore, the plasma wave, excited around the critical layer by the CO_2 laser, will not have the same phase everywhere on the critical layer (n_{cr}). The phase of the edge oscillation may lag up to five cycles of the laser light (10π) behind the phase of the middle oscillation.

On a smaller scale, the amplitude of the plasma density modulation can change along the length of the grating. This is due to imperfections in the grating construction, variation in ruby laser intensity and the change of grating periodicity over distance (which is necessary for acceleration). These changes in the amplitude of the plasma density modulation will directly affect the plasma wave amplitude. We also saw in Chapter 4 that there are phase fluctuations of up to 0.6 radian in the density modulation; the plasma wave will also have these phase variations.

5.4.3. CO_2 Laser Beam Imperfection

Even in the case of a perfect beam, the intensity changes along the focal spot with more intensity in the middle of the focal spot and less on the side. This will reflect directly on the amplitude of the plasma wave. Possible phase and intensity variations in the CO_2 laser beam also create phase and amplitude variations of the plasma wave. These variations may be caused by many things: hot-spots in the focal area due to non-uniformity of the laser beam profile before focusing; diffraction patterns produced by the different apertures in the laser beam path and aberrations caused by the tilted plano-convex lens used for the final focusing.

The CO_2 beam may not be aligned perfectly perpendicular to the grating surface. This misalignment can be decomposed into two orthogonal planes. If the angle of incidence θ in the plane containing the electron trajectory is not zero, the phase speed of the accelerating wave will be changed from $v_{ph}(z)=\omega_0/k_g(z)$ to $v_{ph}(z)=\omega_0/(k_g(z)+k_{CO2}\sin\theta)$ (Figure 5.13a). In the experiment, the CO_2 beam can be aligned to $\theta<3°$, resulting in only a 5% error in the phase speed.

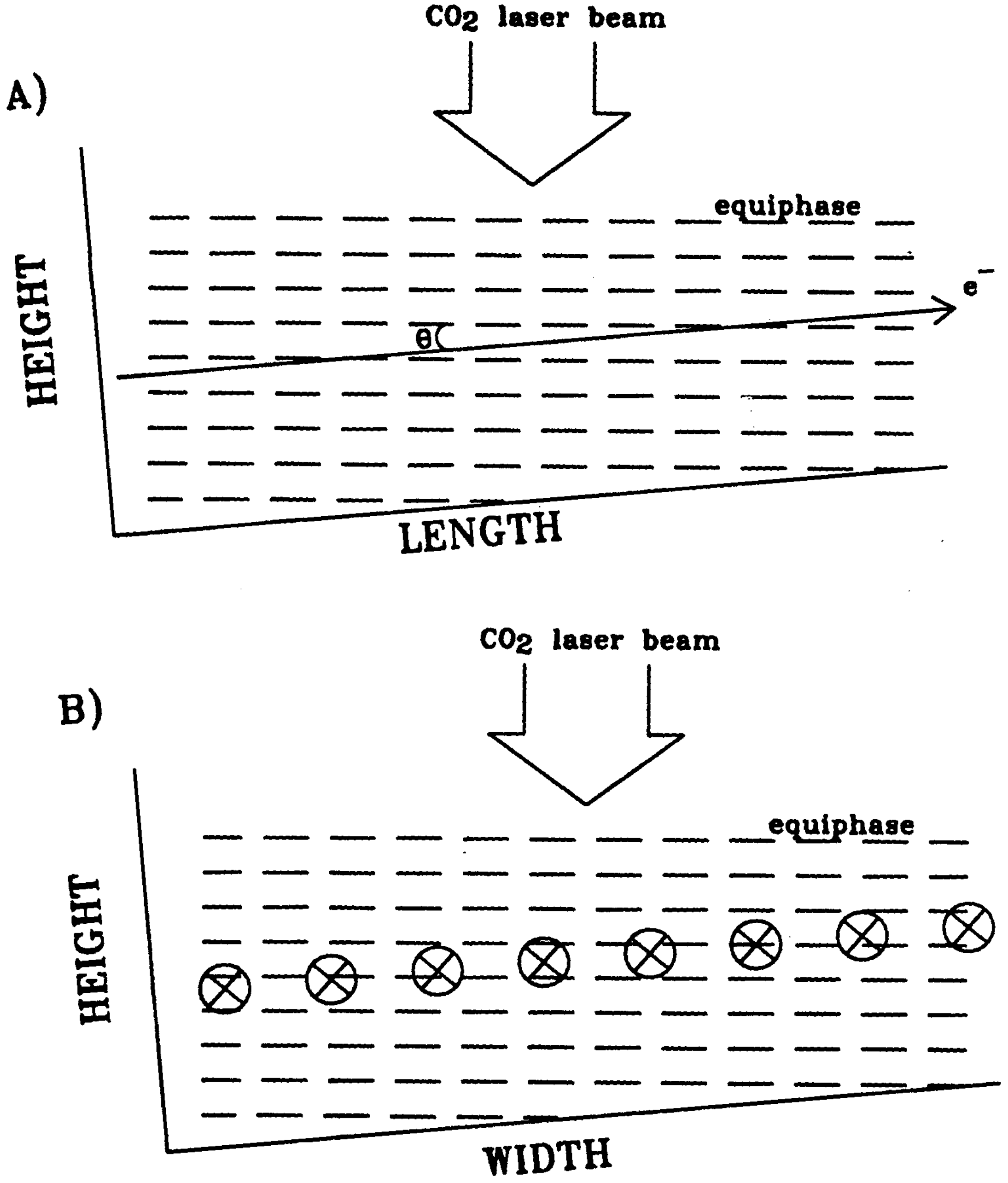

FIGURE 5.13
Change in phase speed due to a non perpendicular CO2 laser beam.

The effect of a misalignment in the plane perpendicular to the electron trajectory is not detrimental to the acceleration scheme. It simply causes electrons at different positions across the electron beam to be accelerated at a different phase of the CO_2 laser light, (Figure 5.13b).

We must now find out what effect all these phase and amplitude variations will have, and how much variation we can afford without disrupting the acceleration process.

5.5 Effect of the Amplitude Fluctuation

The fluctuations in the amplitude of the plasma wave cause $a_m(z)=qE_{pw}(z)/m_e$ to be a function of the position. This effect does not change the acceleration as long as $a_m(z)>a_{pw}$. But if $a_m(z)<a_{pw}$, the electrons escape from the accelerating potential well and stop gaining speed. Such a non-trapping situation is schematically demonstrated on Figure 5.14.

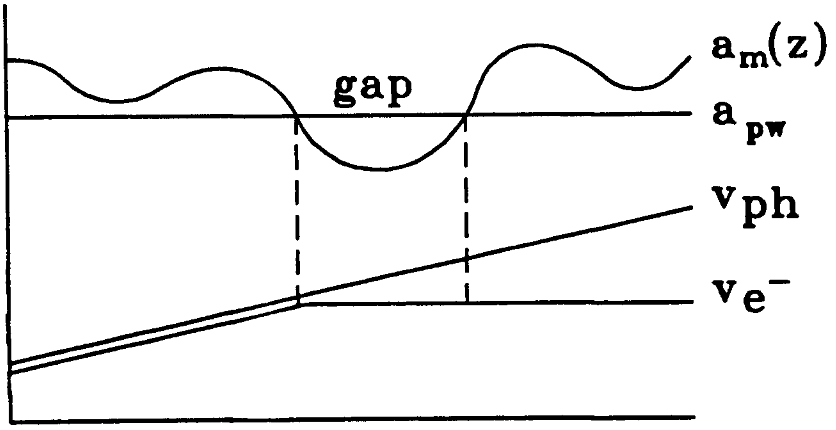

FIGURE 5.14

Loss of phase synchronization due to an amplitude fluctuation.

On this Figure, $a_m(z)$ fluctuates randomly but the speed v_e of the electrons keeps in synchronization with the phase speed v_{ph} of the plasma wave. When $a_m(z)<a_{pw}$ the electrons stop gaining speed but v_{ph} keeps increasing. Even if $a_m(z)$ becomes larger than a_{pw} again after a short distance, the electrons' speed is now too low for the electrons to be trapped by the wave and no further acceleration can take place. We must therefore have $a_{pw}<a_m(z)$ everywhere on the electron trajectory, including all amplitude fluctuations.

5.6 Effect of the Phase Fluctuation

What is the effect of the phase fluctuations? The equation of the plasma wave potential, including phase variation is:

$$\phi(z,t) = \phi_{epw}(z) cos(\omega_0 t - k_g(z)z + \alpha(z))$$

The phase speed is given by:

$$\frac{d}{dt}(\omega_0 t - k_g(z)z + \alpha(z)) = 0$$

$$v_{ph} = \frac{\omega_0}{\frac{dk_g(z)}{dz}z + k_g(z) + \frac{d\alpha(z)}{dz}}$$

Using the same approximation as in Equation (5.4), we finally get:

$$v_{ph} \approx \frac{\omega_0}{k_g(z) + \frac{d\alpha(z)}{dz}}$$

The phase variations add a term in the expression for the phase speed. The grating wavenumber, $k_g(z)$ is carefully chosen to give a constant acceleration a_{pw}. But the new term will produce fluctuations in the acceleration. Again we must have $a_{pw}(z)<a_m(z)$. Here $a_{pw}(z)$ is no longer constant, but depends

on z because of the phase changes. These phase fluctuations should be fairly small. Typically the phase error in the CO_2 wavefront should be less than 2π radian across the focal spot. For a focal spot of about 500 μm long, this phase error will give $d\alpha/dz \approx 2\pi/500\ \mu m \approx 0.013\ \mu m^{-1}$. For electron acceleration, k_g must be larger than $2\pi/10.6\ \mu m \approx 0.6\ \mu m^{-1}$. There will therefore be less than 2% fluctuation in $v_{ph}(z)$ due to the imperfection in the CO_2 laser wavefront. Similarly, the curvature of the critical layer will produce up to five wave cycles of phase change across the focal spot (Figure 5.12). So $d\alpha/dz \approx 10\pi/500\ \mu m \approx 0.06\ \mu m^{-1}$ for a 10% error in $v_{ph}(z)$. For a conservative $a_{pw}(z) << a_m(z)$ this should not be a serious problem. More problematic is the phase fluctuation of the static plasma density modulation (Figure 4.16b). Because it is not a slow phase change over many periods of the plasma wave cycle, we cannot treat it as a change in v_{ph}.

In the reference frame moving with the wave, the electrons are trapped in a potential well and oscillate around the minimum.

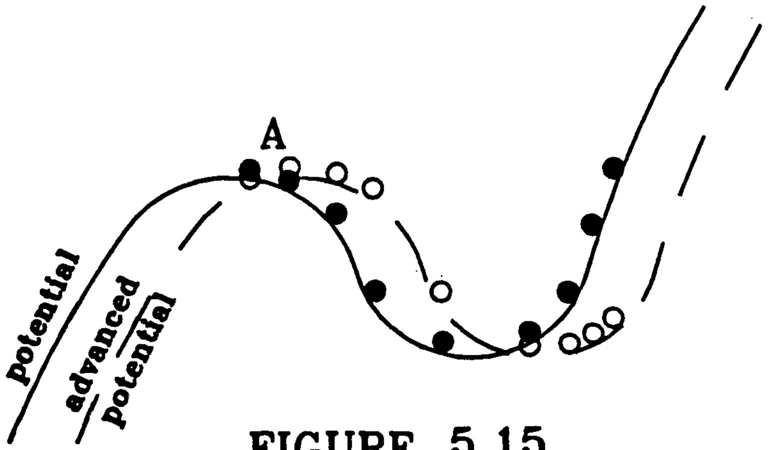

FIGURE 5.15
Effect of a sudden phase fluctuation on the trapped electrons.

Figure 5.15 shows the position of the electrons (black circle) in the wave potential (solid line) at a fixed time. Because of a phase fluctuation in the plasma density modulation, the potential well suddenly moves forwards (or backwards) by up to 0.6 radian (broken line). The relative position of the electrons in this displaced potential is shown by the white circle. The electrons that are close to the crest of the potential before the fluctuation, escape the well (A). But because the fluctuation is only 1/10 of a cycle (0.6 radian) most electrons will stay in the well and keep accelerating. Furthermore, the electrons close to the potential maximum are only there early in the accelerating process. Later, the potential well has grown considerably and the electrons only oscillate near the center of the well. Therefore, some electrons can escape during a phase fluctuation only at the beginning of the acceleration process.

This situation is in sharp contrast with the very relativistic case where a phase change of π radian across the entire accelerator will disrupt the beam. The non-relativistic acceleration is possible in the presence of the phase changes because the electrons can change speed to adjust for the phase variation. A relativistic beam goes practically at the speed of light and does not actually increase its speed when gaining energy. So a change of phase makes the electron lose energy because it cannot change speed to return to the proper phase.

5.7 Edge Effect

We can now define more precisely the concept of an accelerating layer introduced at the beginning of this chapter. It is the volume in the plasma where $qE_{epw}(z)/m_e > a_{pw}(z)$. The accelerating layer depends on the plasma density and CO_2 laser intensity distribution. Using the experimental data for these parameters we plotted the accelerating layer for different grating accelerations and for the two CO_2 focal spot lengths described in Chapter 3 (Figure 5.16).

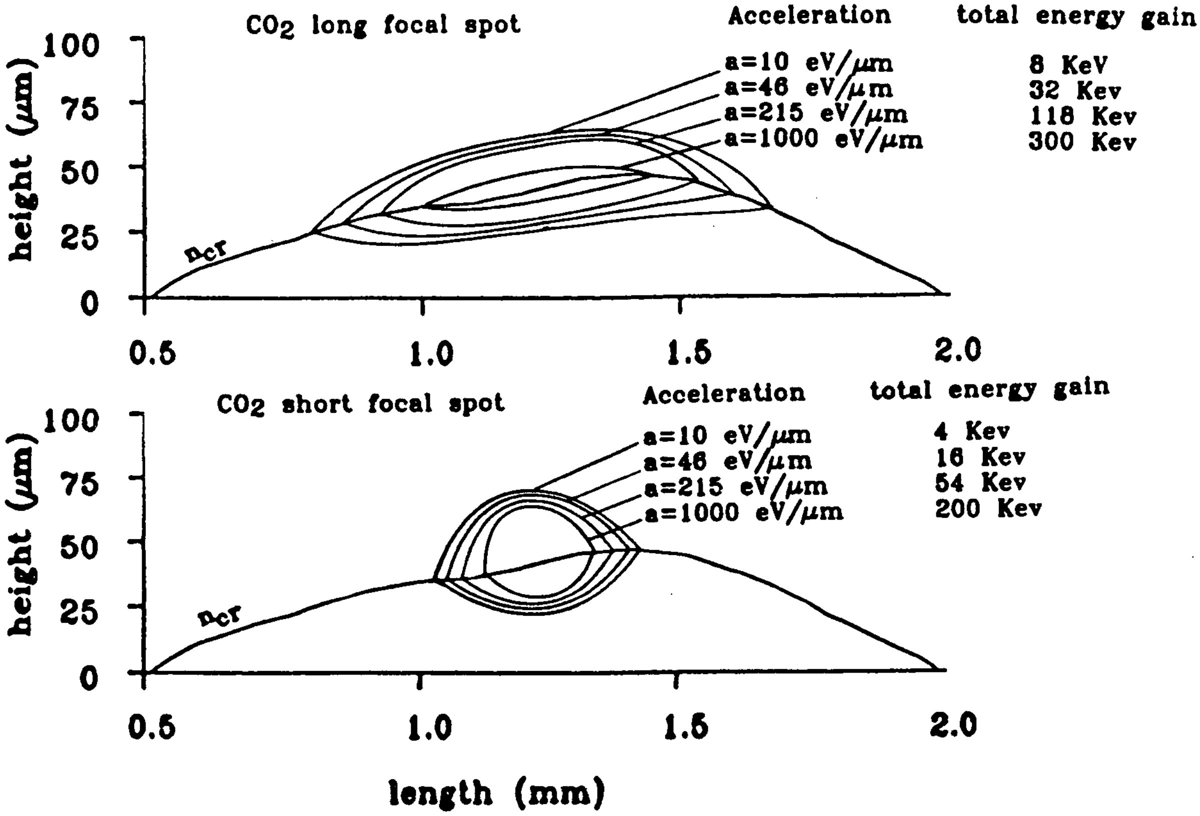

FIGURE 5.16
Accelerating layer for different values of the acceleration.

On this Figure the critical surface of the plasma produced by the ruby laser is indicated (n_{cr}). The CO_2 laser then irradiates this plasma with a long or short focal spot, shown on the upper and lower graphs respectively. The areas inside the concentric closed curve are the regions of the plasma where $a_{pw} < a_m$. Note that the length axis is compressed 20 times compared to the height axis. These accelerating layers are actually long and thin. We see that for a grating producing high acceleration, the accelerating layer is much shorter and thinner than for low acceleration. A short focal spot gives a thicker accelerating layer but, of course, the layer is shorter. We also calculated the total gain in energy for the optimum electron trajectory, (the one that stays in the accelerating layer over the longest possible distance).

In order to obtain this maximum energy gain, the relative position between the lasers and the grating must be adjusted so that the phase matching position of the grating (where $v_{inj} = v_{ph}(z)$) is just under the beginning of the accelerating layer. However, designing the experiment in this way does not tolerate any errors. If the grating position is slightly incorrect, or if the laser intensity is less than expected, the accelerating layer will start past the phase matching point. The electrons will therefore not be trapped at the point where $v_{inj} = v_{ph}$ and when they arrive in the accelerating layer the phase speed of the wave will be too large for trapping. It is much safer to position the grating so the phase matching point is close to the middle of the accelerating layer. This arrangement increases the chance of trapping the electron at the beginning of the grating (Figure 5.17).

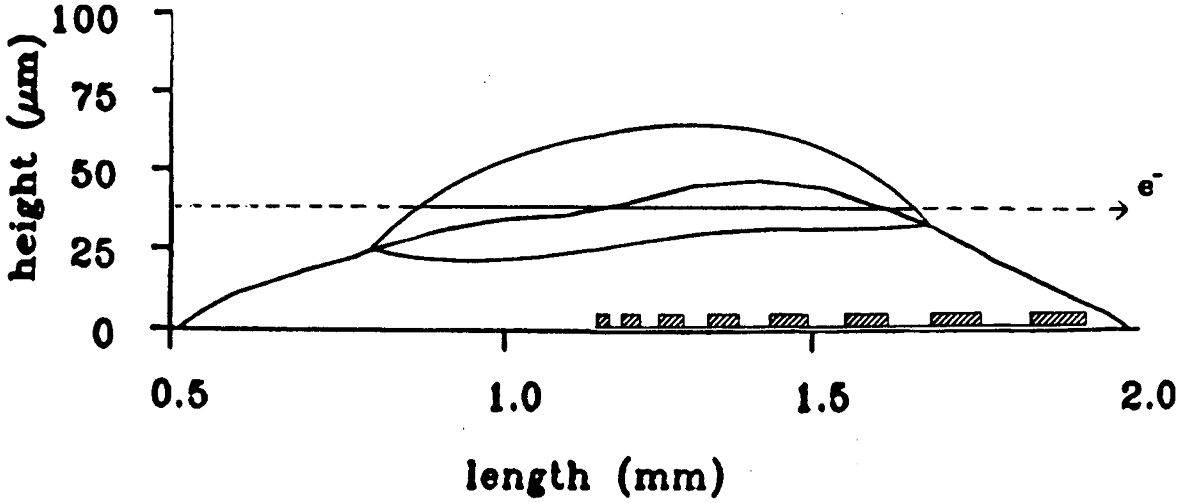

FIGURE 5.17

Relative position between the CO_2 focal spot and the grating to optimize the trapping of the electrons.

However, having the phase matching point in the middle of the accelerating layer introduces a new problem. Because of the design of the grating, the phase matching position is only a few µm after the first photoresist line of the grating. Before the photoresist lines begin, the grating surface is 100% gold. The speed of sound of the gold plasma is much less than the gold-photoresist mixed plasma above the grating lines. This produces a large plasma density step due to a differential in plasma expansion at the beginning of the lines. The interference fringes on the interferogram 5.18a clearly show this density step (the representations of the grating in Figures 5.18 and 5.19 are not to scale). The accelerating layer follows this density step and the electrons (A on Figure 5.19) that are trapped at the beginning of the grating rapidly leave the accelerating layer and gain very little energy. But the electrons (B) that go in the long, flat accelerating layer miss the beginning of the grating and cannot be trapped.

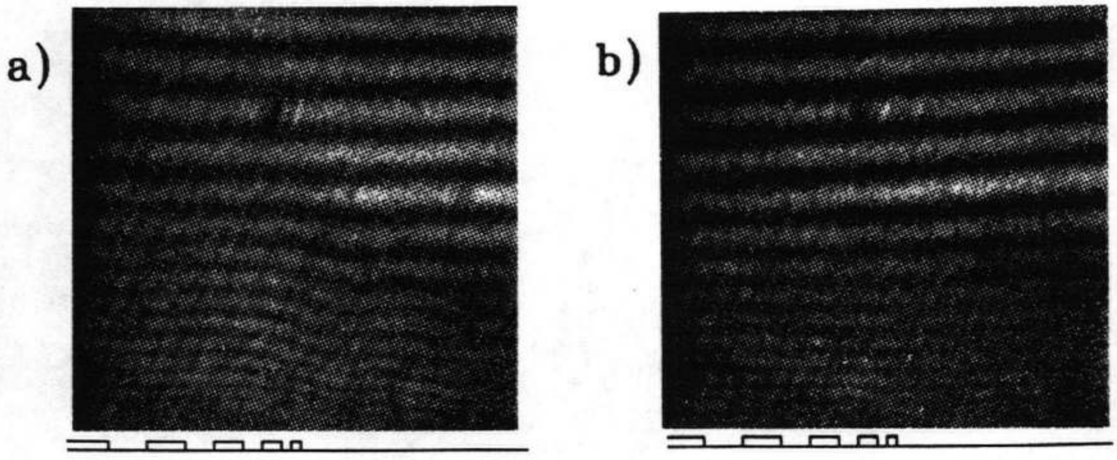

FIGURE 5.18
Interferograms of the plasma above the beginning of the grating.

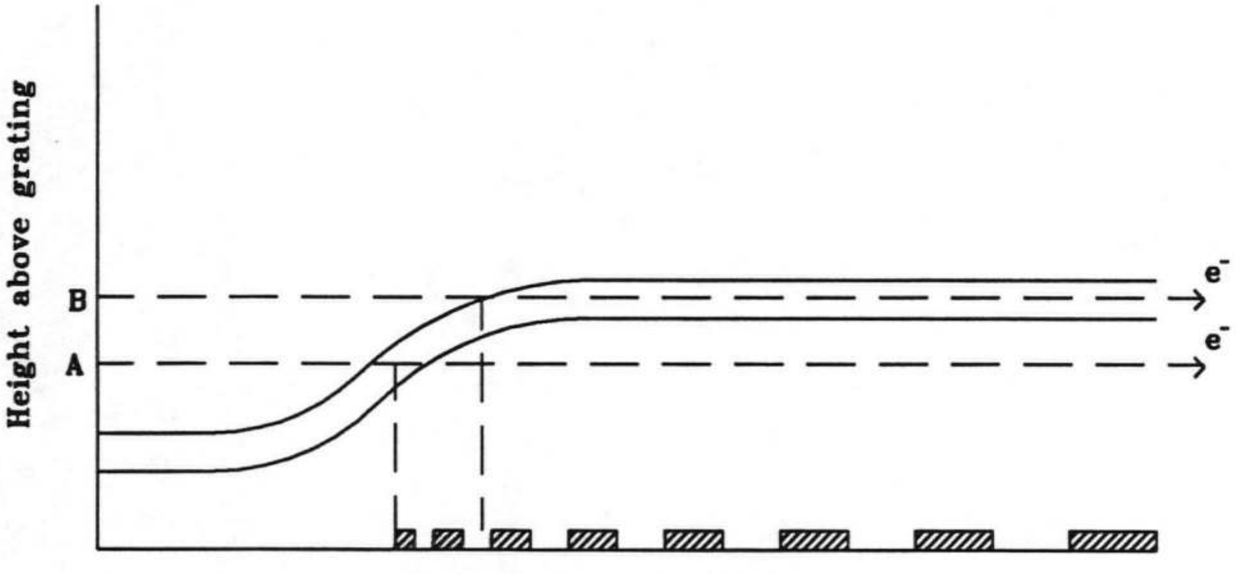

FIGURE 5.19
Influence of the edge gradient on the trapping of the electrons.

In addition, the lateral density gradient produces a side flow that changes the period of the plasma modulation above the grating (Figure 5.20a). The initial phase speed on the electron trajectory is increased, so at no point does the phase speed equal the speed of the electrons and no trapping is possible.

FIGURE 5.20
Influence of the edge gradient on the periodicity of the modulated plasma.

In order to remedy this problem we paint the gold surface in front of the grating lines with photoresist. This is carefully done under a microscope with a very fine brush. The photoresist can be deposited up to 10 μm before the first grating line. No density step is noticeable on the interferogram 5.18b. There may however, be a small step because we now have the reverse situation. The 100% photoresist plasma should expand faster than the gold-photoresist mixed plasma. However, it is less detrimental because the induced side flow shortens the period of the plasma modulations (Figure 5.20b), decreasing the phase speed. So there should still be phase matching somewhere slightly further along the grating where the electrons can be trapped.

In this chapter we found that non-relativistic electrons injected in the plasma 65 μm above a chirp grating should be accelerated. To compensate for different experimental fluctuations and uncertainty we must choose the acceleration of the grating (chirp) so that $a_{pw} << a_m$. Also the acceleration should begin close to the middle of the focal spot and not towards the edge because of the importance of the initial trapping. The injection speed must be larger than the phase speed of the plasma wave at the beginning of the grating. Finally a problem at the edge of the grating has been identified and corrected.

In the next chapter we describe our experimental attempt to demonstrate this acceleration scheme.

CHAPTER 6

ELECTRON ACCELERATION EXPERIMENTS

We saw in Chapter 4 how to produce a modulated plasma. Chapter 2 showed how a large amplitude plasma wave is produced if this modulated plasma is correctly illuminated by a CO_2 laser. Finally, we saw in Chapter 5 how a wave of this type can trap and accelerate injected electrons. It is now time to put everything together and try the experiment.

This chapter describes two electron acceleration experiments. We first inject the electrons at an energy of 25 keV. This value is chosen to be well above the energy of the fastest electron emitted by the plasma. It is then easy to distinguish the injected electrons from the plasma electrons. However, we will find that an intense electric field perpendicular to the surface of the grating is generated when the lasers produce the plasma. This field bends the trajectory of the electrons and makes them strike the grating. No accelerated electrons can be detected in these conditions. In an attempt to remedy this problem we increased the injection energy to 92 keV. Faster electrons should be less affected by the perpendicular electric field. But even at this higher energy no definitive evidence for electron acceleration could be found.

6.1 25 keV Experimental Set Up

The general set up is shown in Figure 6.1. The ruby and CO_2 lasers and the focusing system have been described previously. The rest of the set up will now be described.

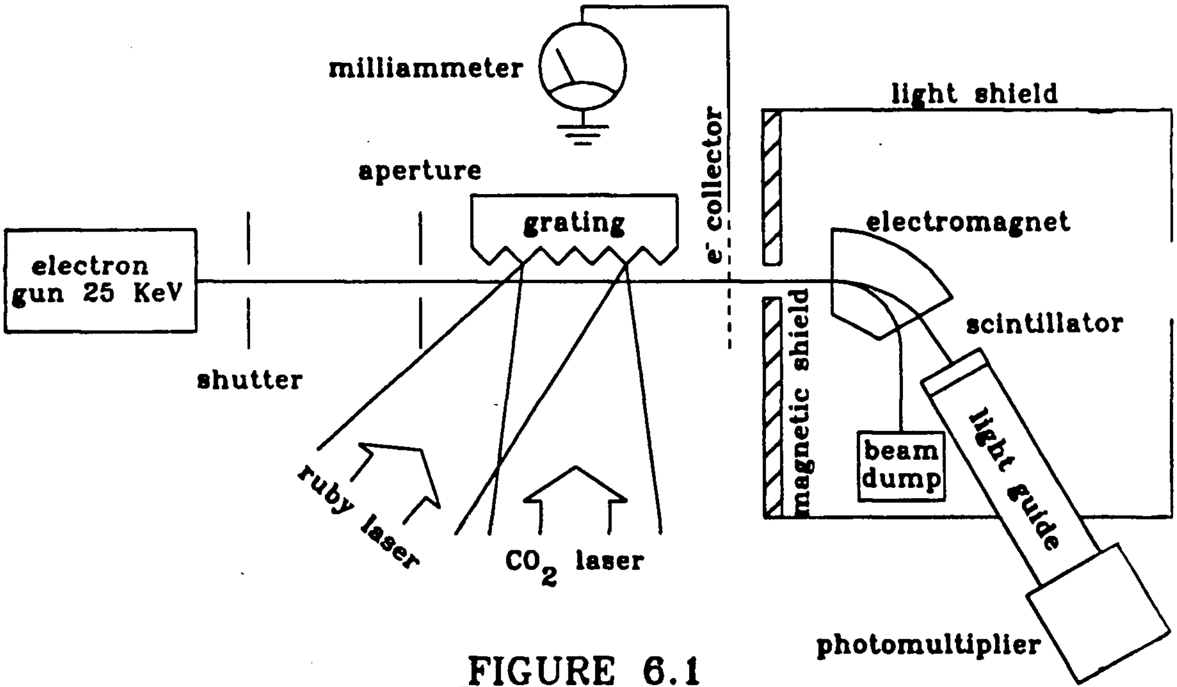

FIGURE 6.1
Experimental set up for electron acceleration

6.1.1 Electron Gun

The electrons are produced by a Nucleide Corporation EBG1 continuous current electron gun (Figure 6.2) using a home made power supply. For proper focusing, the grid must be maintained at a potential a few kilovolts lower than the filament. This is accomplished by using a 1 MΩ resistor which produces a voltage drop of 4 kV when an electron current of 4 mA is emitted by the filament. This current is adjusted by changing the temperature of the filament. The electron gun can produce a beam of up to 30 kV at one Ampere.

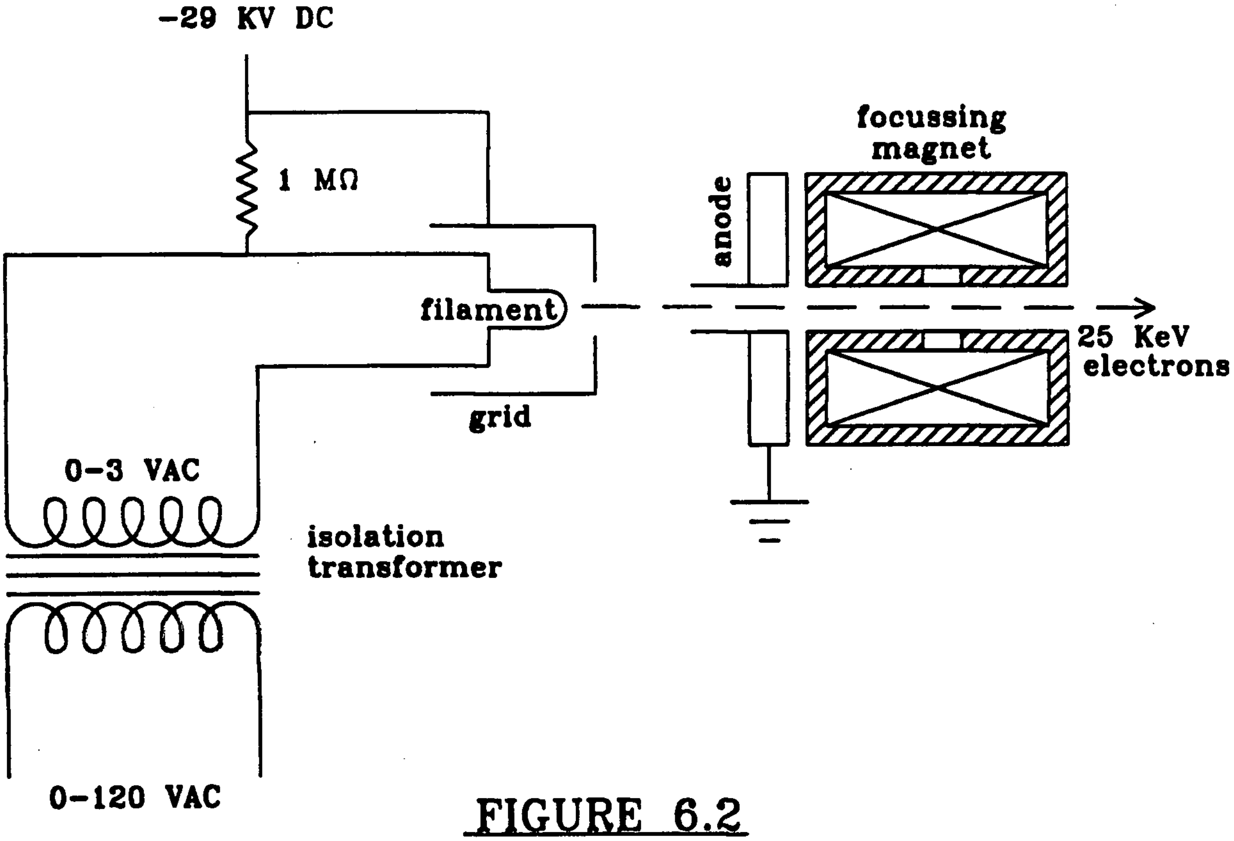

FIGURE 6.2
Detail of the electron gun

At this maximum power level of 30 KW the electron beam would melt everything in its path. Therefore we operated the gun at 25 kV and 4 mA. This still corresponds to 100 W of power, and when this beam strikes the grating for more than a second, thermal damage occurs. Obviously for a CO_2 laser pulse of 1.8 ns a very short (ns) electron pulse would be ideal. But such pulses are more difficult to produce than a continuous beam. They must be synchronized very precisely with the laser pulses. Also, alignment and focusing of the electron beam are more difficult with a pulsed beam, than with a continuous beam. For simplicity we decided to use the continuous gun with a mechanical shutter to produce a 120 ms duration electron pulse. In this time interval the energy deposited on the grating by the electrons is small enough to avoid thermal damage. Also, for such a long pulse, synchronization was not a problem and alignment and focusing of the electron beam could be easily achieved with the shutter permanently open and no grating in the grating holder.

The target at which we are aiming the electron beam is quite small. It is the region of large amplitude plasma waves produced by the lasers just above the grating. This region has a similar width to the CO_2 laser focal spot (140 - 160 μm, depending on the focusing system used) and has the thickness of the acceleration layer ($\sim$35 μm see chapter 5). Aiming directly at the plasma wave would be difficult because the height of the acceleration layer above the grating can change from shot to shot due to variation in the intensity of the ruby laser and jitters in the timing between the CO_2 and ruby lasers. To be certain to have electrons traversing the plasma wave, we used a beam of 1 mm in diameter centered at the laser focal spot and covering a region from the surface of the grating up to 1 mm above it. So instead of aiming directly at the small accelerating layer, we sent electrons everywhere in this 1 mm^2 area. Some electrons will therefore traverse the accelerating region. The electron beam cross section was produced by passing the electron beam through a square aperture placed 5 to 20 mm in front of the plasma. The electron current that passes through the aperture is measured by intercepting the electron beam before the spectrometer with an electron collector, a metal plate connected to a milliammeter. (The collector is only employed to measure the current, during the actual experiment it is removed from this position.) This method gives a minimum value for the current because secondary electrons produced by the impact of the 25 keV primary electron beam can be ejected from the plate and reduce the reading. The current measured was 0.75 mA. The actual current through the aperture is larger than 0.75 mA but smaller than the 4 mA that leaves the electron gun filament, (measured by the ammeter of the high voltage power supply). We must now calculate how many electrons we expect to accelerate with this small current. The current density is at least:

$$0.75 \text{ mA} / 1 \text{ mm}^2 = 7.5 \times 10^2 \text{ A/m}^2$$

The cross section of the plasma wave is:

$$35\ \mu\text{m} \times 150\ \mu\text{m} = 5.3 \times 10^{-9} \text{ m}^2$$

The current through the plasma wave is then 3.9 μA. If we suppose that the plasma wave lasts for the duration of the CO_2 laser pulse (1.8 ns) and that

10% of the electrons arrive with a phase suitable to be trapped (see section 5.3) we should accelerate at least 4,400 electrons.

We now need an electron spectrometer capable of detecting 4,400 or fewer electrons.

6.1.2 Electron Spectrometer

The electrons are detected by scintillations in a NE-102 plastic scintillator. For simplicity and maximum sensitivity a one channel spectrometer was built (Figure 6.1). A 60° sector magnet deflects and focuses the electrons on a 4 cm diameter and 3 mm thick scintillator held against a 4 cm diameter lucite rod. The magnetic shield, a 7 mm thick steel plate, prevents the fringe field of the magnet from extending beyond the spectrometer box. The light from the scintillator is guided inside the rod by total internal reflection and by an aluminum coated mylar sheet wrapped around the rod. A RCA-8575 photomultiplier with a 4 cm diameter photocathode terminates the light pipe. To prevent stray light from reaching the photomultipler, without cutting off the 25 keV electrons, a 0.5 μm coating of aluminum is evaporated on the scintillator. The light pipe and the mylar around it are wrapped with black electric tape for further protection against ambient light. This spectrometer is very sensitive and many precautions (described in Appendix A) must be taken to keep the noise level detected by the photomultiplier at an acceptable level.

The spectrometer in this configuration was tested to determine its sensitivity. We adjust the magnetic field such that the electrons from the gun hit the scintillator directly, instead of going into the beam dump. If we heat up the filament of the electron gun very slowly the signal from the photomultiplier shows a series of pulses. With a hotter filament the rate at which these pulses are produced increases. The filament temperature must be kept well below the normal operating temperature, otherwise the large electron current would produce too much light in the scintillator and damage the photomultipler. Each of these pulses corresponds to one electron hitting the scintillator. The average height of the pulses is 350 mV for 25 keV electrons with pulse to pulse variation of around 50%. This indicates that in absence of any background signal, single electrons can be detected. Unfortunately the background is not zero. A small signal is always present when the lasers are triggered (see Appendix A). This signal is about 1.2 Volts, corresponding to about 4 electrons. Therefore the sensitivity of the spectrometer corresponds to about 4 electrons for a signal to noise ratio of one. This should be sensitive enough, given that we expect to accelerate 4,400 electrons.

The magnetic field of the spectrometer electromagnet is calibrated using a Bell model 240 gaussmeter (Figure 6.3). The electron gun is then turned on at a given energy and at a very low current. The current in the electromagnet is varied to find the range of magnetic field for which electrons enter the scintillator and can be detected. The electron beam is detected over a large range of magnetic field because the scintillator is large (4 cm in diameter).

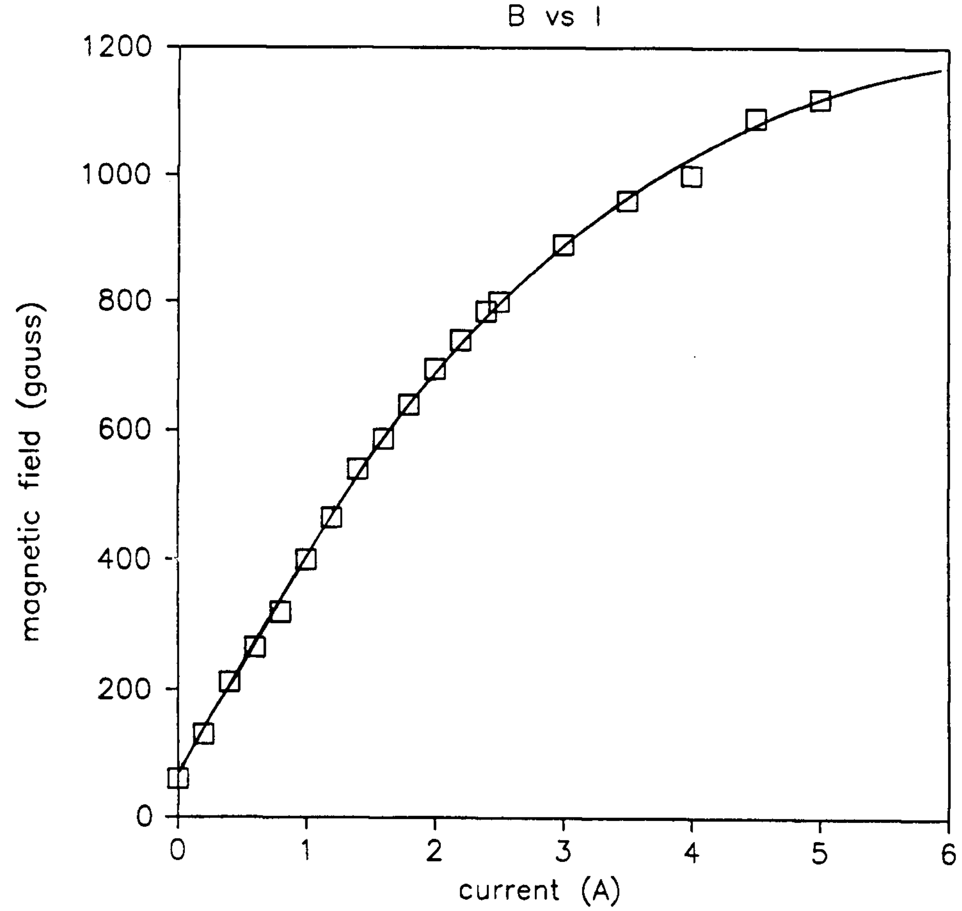

FIGURE 6.3
Calibration of the electromagnet

The non-relativistic relationship between the magnetic field and the speed of the electrons is:

$$B = \frac{m_e v}{qR}$$

Where B is the magnetic field, v is the speed of the electrons and R is the radius of curvature of the electron beam. From the graph of B vs v, shown on Figure 6.4, we can find the range of radius of curvature for which electrons are detected (hatched area on the Figure).

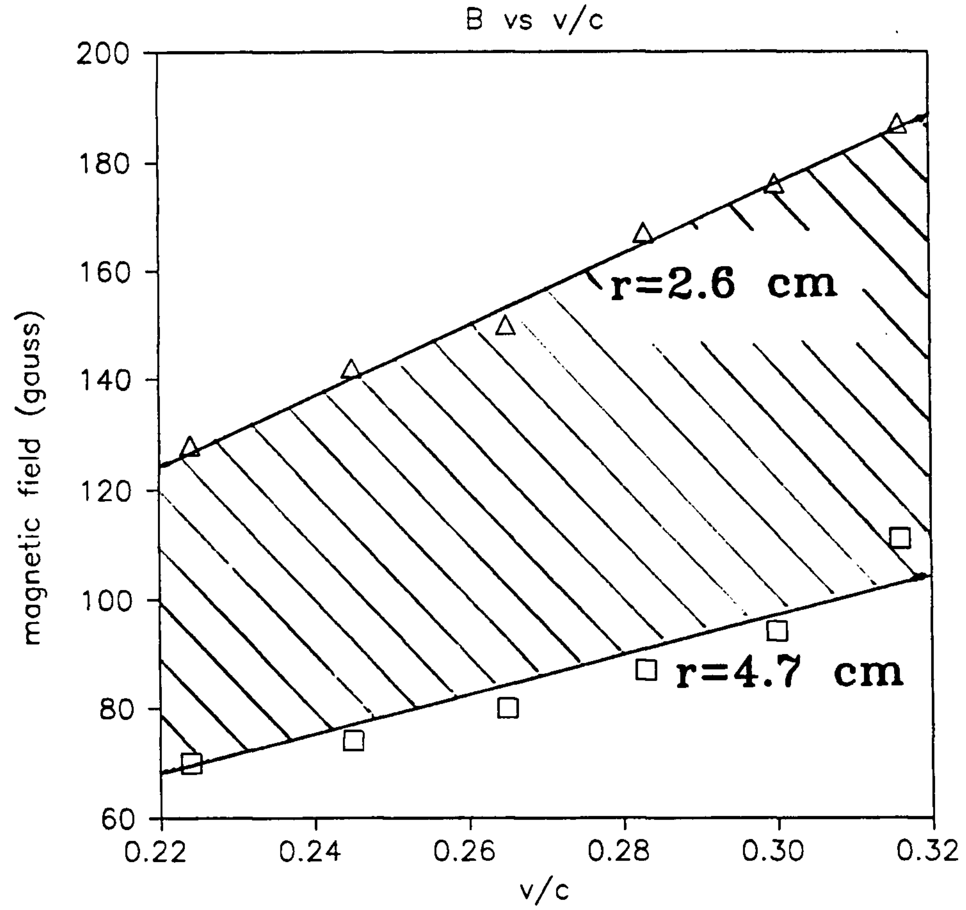

<u>FIGURE 6.4</u>
Graph of B vs v/c giving the radius of curvature of the electron beam

Using these values for the radius of curvature, and the magnetic field calibration from the gaussmeter, we can produce the calibration graph shown on Figure 6.5. This graph relates the range of energy that can be detected to the electric current passing in the spectrometer electromagnet.

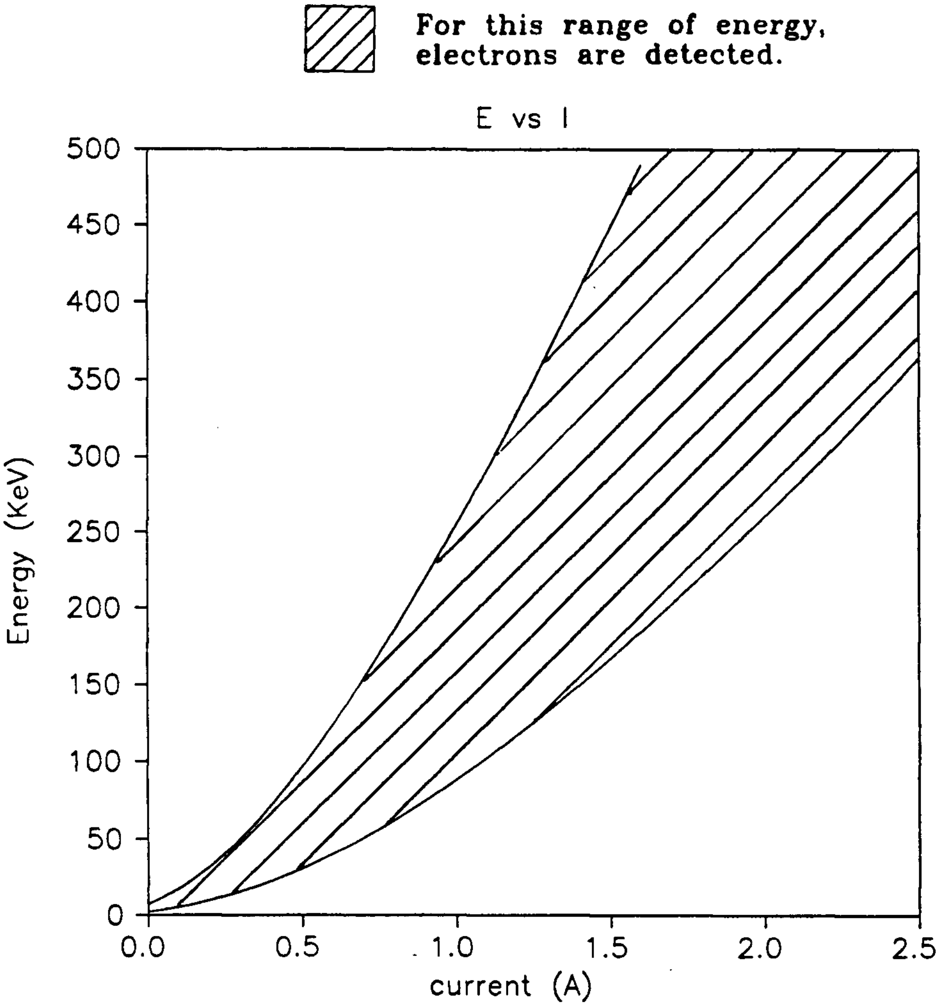

FIGURE 6.5
Calibration of the electron spectrometer

To test the spectrometer we measured the energy of the electrons emitted by the laser produced plasma. The ruby and CO_2 laser beams are sent on a flat piece of brass while we record the output of the spectrometer (Figure 6.6). Some electrons are emitted at an energy of up to 13 keV. This is less than the 25 keV of the injected electrons.

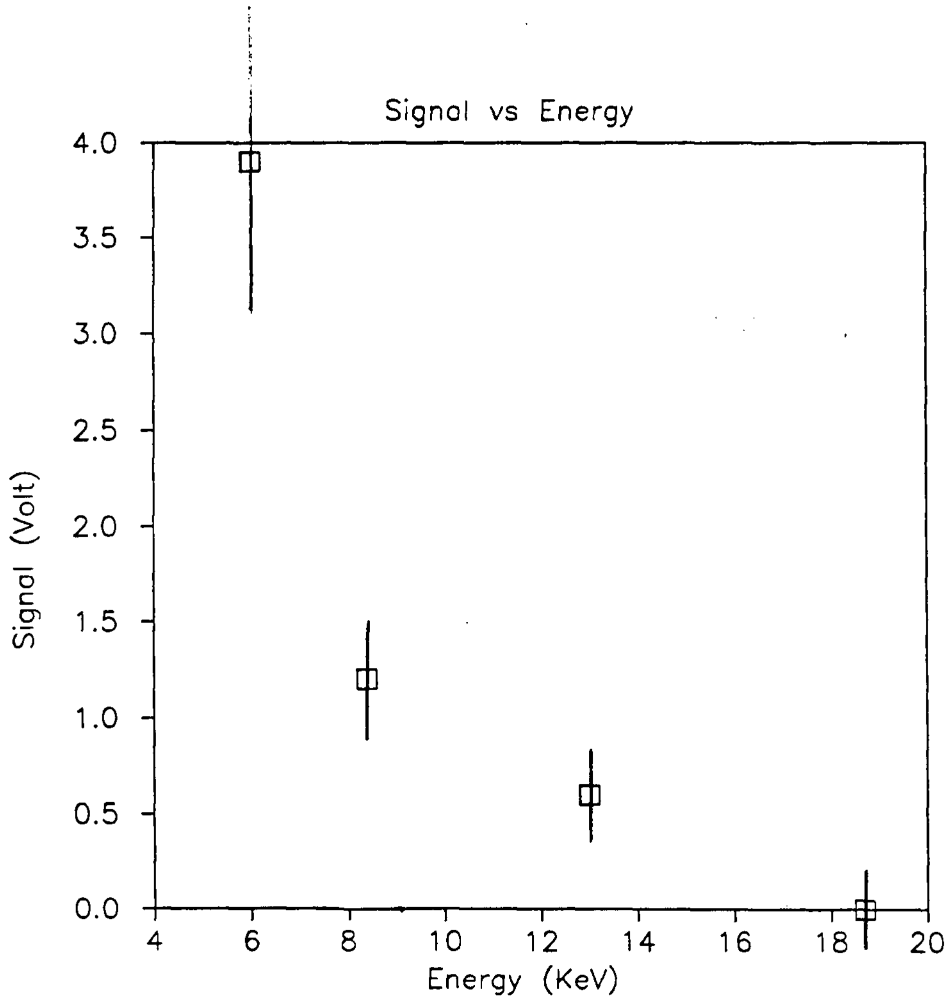

FIGURE 6.6
Fast electrons detected by the spectrometer

Therefore, if we set the spectrometer to detect accelerated electrons with an energy greater than 25 keV, no signal should be produced.

We then test the entire system. The electron gun energy is set at 25 keV and the spectrometer is adjusted to detect electrons of energies greater than 25 keV. The ruby and CO_2 laser beams are sent on a flat piece of brass. A large signal is detected at up to 52 keV (Figure 6.7)!

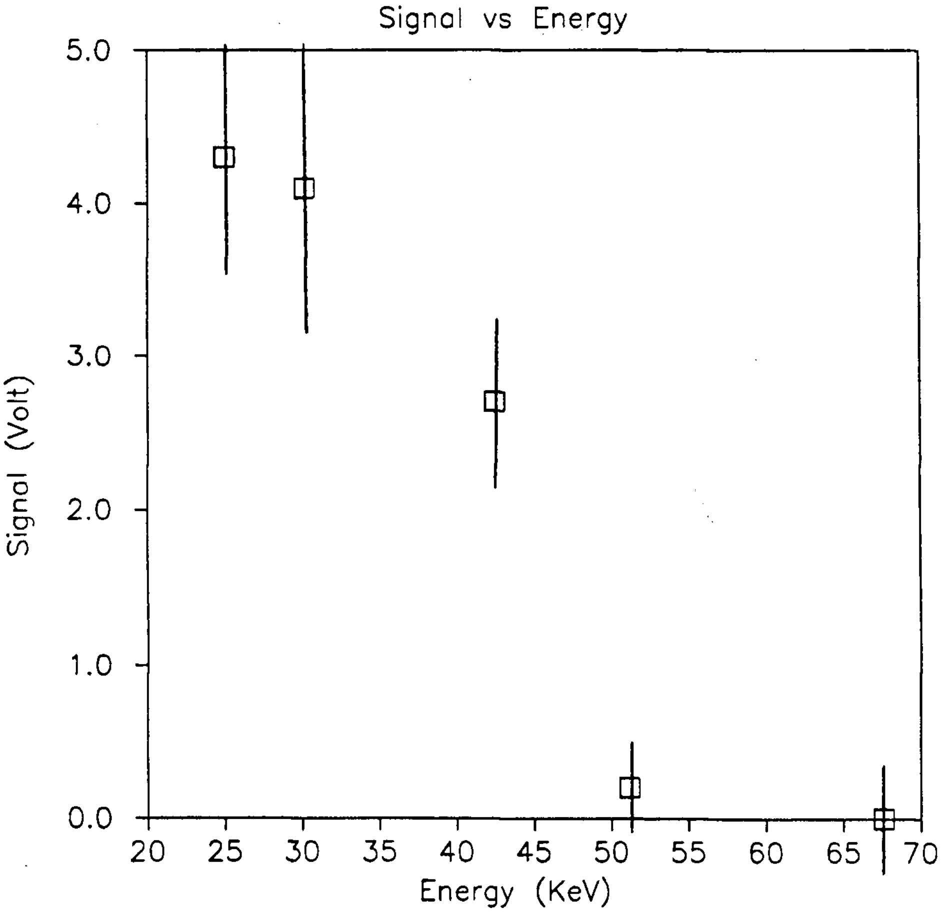

FIGURE 6.7
Electrons apparently accelerated without a grating

This is the type of signal expected if the experiment would work, but no accelerating grating is in place to generate the modulated plasma. It is very difficult to think of a reasonable process that would accelerate the electrons without the grating. A more realistic explanation is that the electrons are deflected by an electric field in the plasma and enter the spectrometer at a different angle (Figure 6.8). Such an electric field is known to occur in laser produced plasma because the fastest electrons from the plasma exit the plasma and leave it positively charged [32].

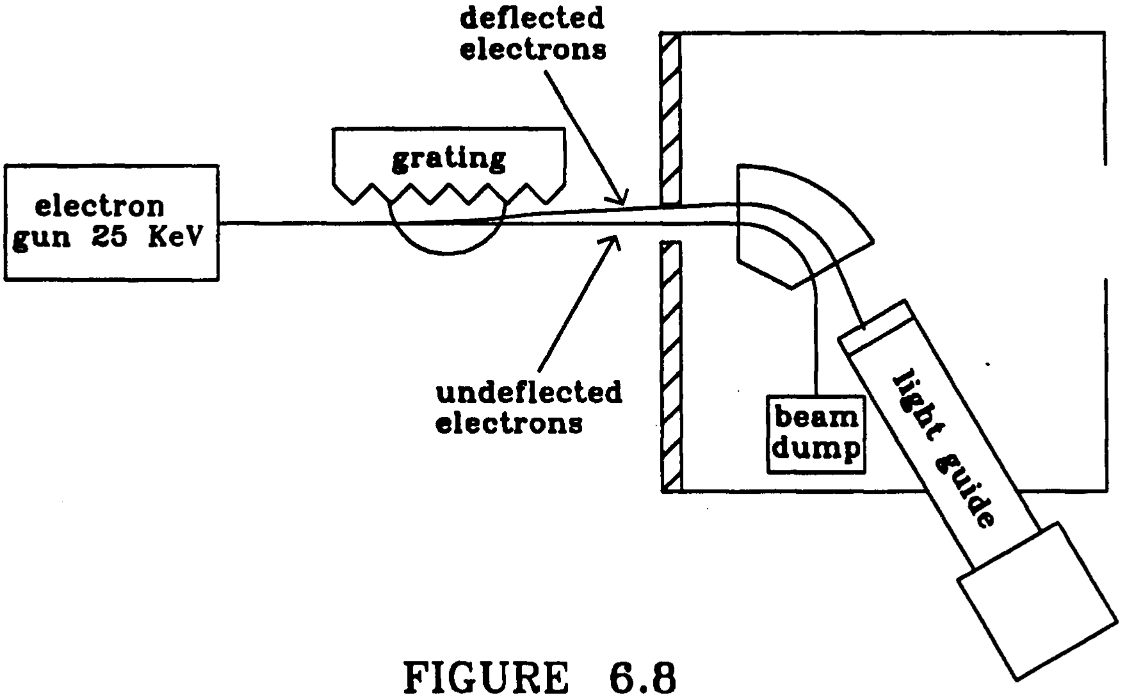

FIGURE 6.8
False signal due to deflected electrons

In theory the 60° sector magnet spectrometer is well focused and the measured energy should be independent of the entrance angle for electrons coming from the plasma. However, the fringe field of the magnet, the distortion of the field due to the magnetic shield and other stray fields, plus possible errors in the focus adjustment, can easily create a dependence of the measured energy on the entrance angle of the electron. To be certain that an electron that strikes the detector has really been accelerated we decided to put an electrostatic grid system in front of the scintillator (Figure 6.9). In system a) the electrons pass through a grounded grid and are then slowed down by a second grid charged at a slightly higher voltage (H.V.) than the electron gun filament (the difference is around 100 Volts).

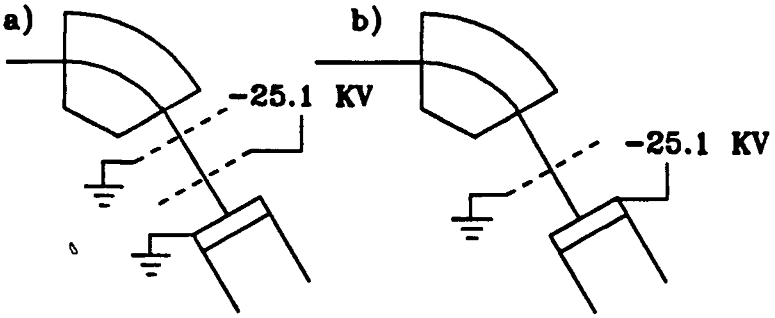

FIGURE 6.9
Electrostatic systems

No electrons from the gun can go through, but an electron accelerated by more than 100 eV passes the H.V. grid and is re-accelerated to 25 keV before hitting the detection scintillator. However, a very large signal saturated the photomultiplier when the H.V. was applied to the grid. This may have been due to electrons, emitted by the H.V. grid by field emission, or ionization of the residual gas in the vacuum chamber (corona). Both processes can produce electrons that would enter the scintillator at 25 keV. To avoid this difficulty we decided to use the system shown in Figure 6.9b). Here, the aluminum coating on the scintillator is charged to 25.1 kV. Therefore no electrons from the gun can produce a signal and any field emission or corona electrons are accelerated away from the detector. The disadvantage of this system is a lower sensitivity for slightly accelerated electrons. In the previous electrostatic system the electrons hit the scintillator with an energy of 25+ΔE keV, where ΔE is the energy gained in passing through the plasma. With system b) this energy is only ΔE keV, so electrons accelerated by less than 5 keV will not be detected because the amount of scintillation decreases for lower energies. At 5 keV a single electron gives a signal of 75±50 mV, whereas, for lower energies it becomes difficult to detect the electrons.

This spectrometer proved to work satisfactorily with a sensitivity of 15 electrons for energy gains greater than 5 keV.

6.1.3 Gratings

Chirp lithographic gratings of the geometry indicated by Equation (5.12), are manufactured by the Electrical Engineering Department. All the gratings start with a phase speed of 0.28 c corresponding to an electron energy of 20 keV, the initial grating period is therefore 3 μm. There are four different acceleration rates: 10, 46, 215 and 1000 MeV/m. This can be compared to the theoretical maximum acceleration of $E_{epw(max)} = 10$ GeV/m.

Therefore, the parameter a_{pw}/a_m varies from a conservative $a_{pw}/a_m = 0.1\%$ to a somewhat optimistic $a_{pw}/a_m = 10\%$. Each grating is 2 mm long by 750 μm wide. They are arranged in a 1 inch by 1 inch array which is partially shown in Figure 6.10. Note that the lines on the grating are not to scale. There are actually many hundreds of lines on each grating. The exact position of the n^{th} photoresist line (x_n) on the grating is given by the formula:

$$x_0 = 0$$

$$x_n = x_{n-1} + 2\pi / k_g(x_n)$$

where $k_g(x_n)$ is given by Equation (5.6).

The widths of each line is half the periodicity.

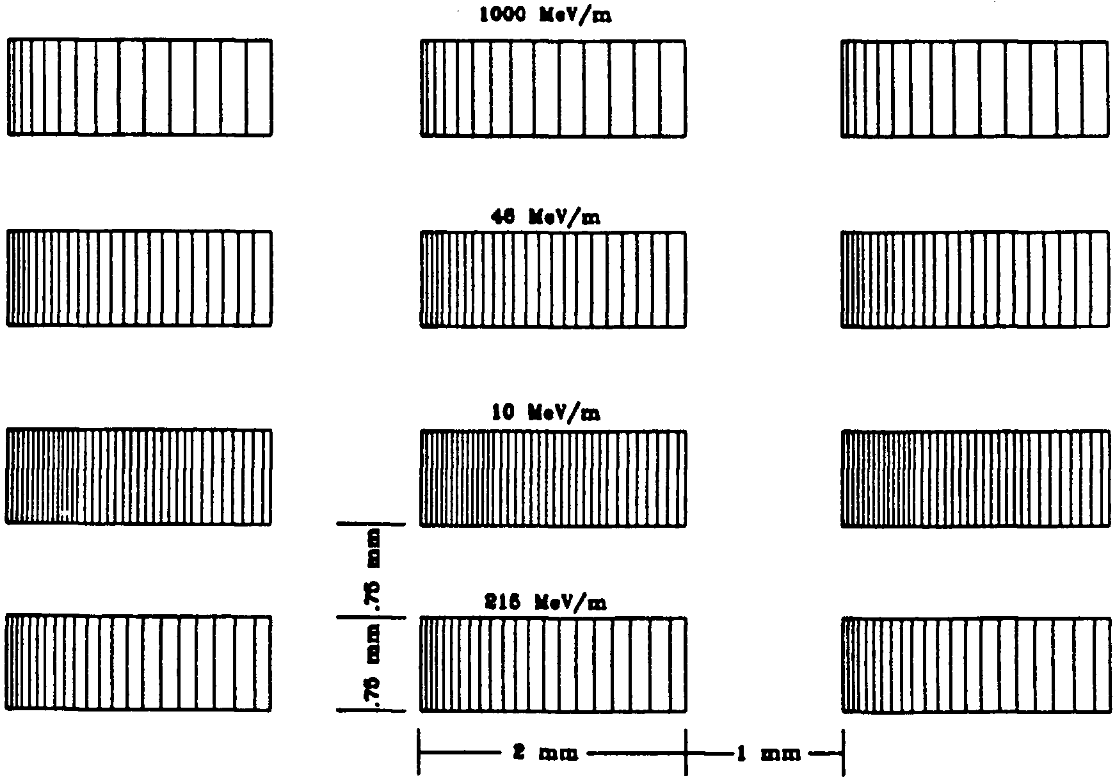

<u>FIGURE 6.10</u>
Position of individual gratings on the grating plate.

The photoresist is removed from the rest of the array and the area between the gratings is therefore a gold surface. The grating is mounted on a x-y translation stage (in the plane of the grating) by clamping it down with two spring loaded wires (Figure 6.11). This ensures a proper grounding of the gold layer to avoid electrostatic charging by the electron beam. The translation stage can be operated from outside the target chamber. This allows us to change the grating after each shot without opening the target chamber. The vertical and horizontal slits define the 1 mm^2 aperture for the electron beam. The horizontal slit is painted with fluorescent paint to help in the alignment of the electron beam.

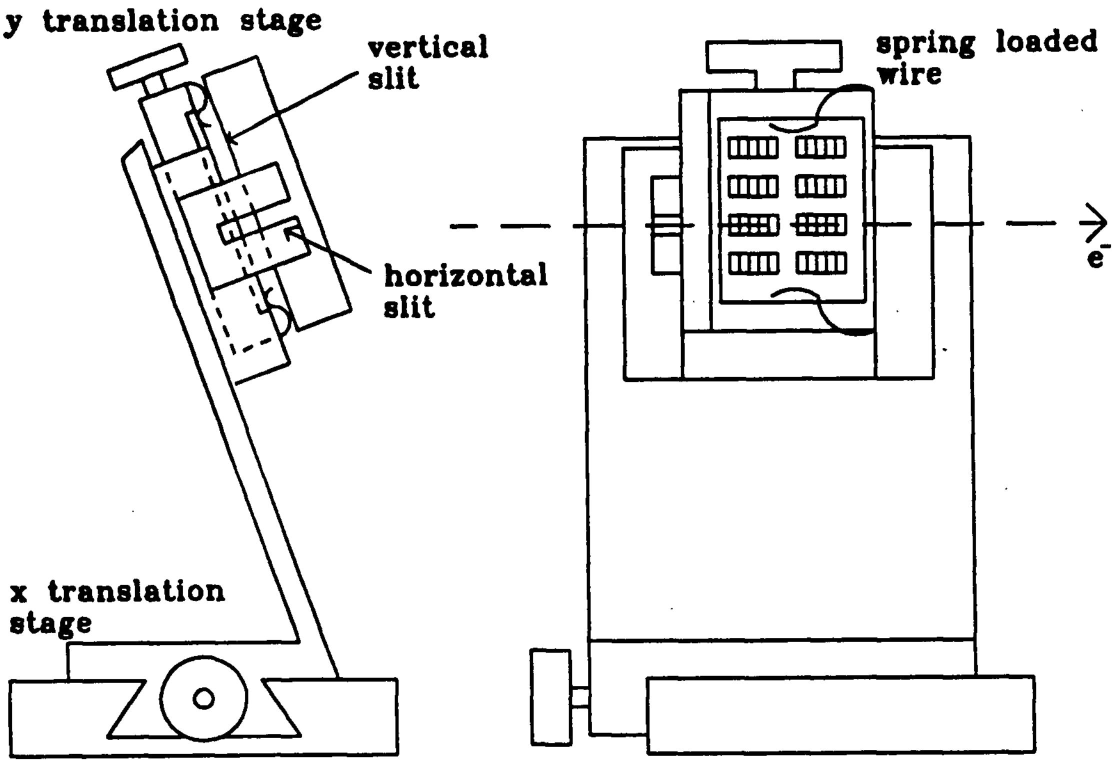

FIGURE 6.11
Detail of the grating mount

The grating plane is tilted around the electron beam axis at 20° with respect to the CO_2 laser beam direction. This arrangement was chosen to prevent the CO_2 laser light, reflected from the grating from re-entering the laser and causing parasitic oscillation (self-lasing). This tilt does not change the phase speed of the plasma wave.

6.2 Choice of Experimental Parameters

Many experimental parameters are available to us. In this section we determine which range of values of these parameters should be used for this experiment. The most important parameter of this experiment is the ratio a_{pw}/a_m. It determines the thickness of the accelerating layer and the phase acceptance window for which electrons can be trapped by the plasma wave. Initially, we want to optimize the chance of observing accelerated electrons. Acceleration to the highest possible energy is of secondary importance and can be optimized later. Therefore a small a_{pw}/a_m ratio is desirable. The electrons can be trapped more easily and stay in the accelerating layer long enough to gain a measurable amount of energy if this ratio is small. The acceleraticn, a_{pw} is defined by the chirp of the grating and is fixed by the grating construction to 10, 46, 215 or 1000 eV/μm.

The maximum possible acceleration a_m is given by:

$$a_m = qE_{epw}/m_e$$

with

$$E_{epw} = E_L \frac{\tilde{n}}{n} \frac{\omega_p}{\nu_e}$$

The maximum acceleration should be as large as possible.

The plasma density modulation, $\tilde{n}/n$, is at its maximum just after the ruby laser strikes the grating but at this early time the scale length of the plasma is very short. This short scale length plasma produces a thin accelerating layer very close to the grating surface and electrons are unlikely to remain in this layer for very long. At a later time, the scale length is longer but $\tilde{n}/n$ is smaller, particularly for small grating spacings like the line spacing of 3 μm at the edge of the grating. Since modulations of 3 μm wavelength could not be measured directly, the optimum time for acceleration is unknown but the observation of 6 μm modulation indicates an optimum delay of approximately 6 ns between the start of the ruby laser and that of the CO_2 laser. Therefore the delay was varied around this value.

The electric field E_L should be as large as possible. However, the CO_2 laser power is limited to 200 MW. At maximum laser power, we can adjust E_L by changing the focal spot dimensions. However, a change in the CO_2 laser focal spot size does not only change E_L. Many other parameters of the experiment are affected.

If we choose a short CO_2 focal spot, E_L will be as large as possible, giving a small a_{pw}/a_m. Also, the thickness of the accelerating layer will be at its maximum. The combination of a short accelerator and thick accelerating layer improves the chances of having electrons trapped and accelerated for the full length of the accelerator. This choice also has some negative effects. The total energy gained for a given grating will be smaller than for a long focal spot. A small, high intensity, focal spot will heat the plasma locally, creating a region of high temperature that will expand faster than the surrounding plasma. This effect, studied in section 4.6, will therefore bend the acceleration layer. The electrons traversing the plasma in a straight line will not stay in this curved layer for an appreciable distance. However, the expansion of the hot plasma occurs on a time scale of a few nanoseconds (see Figure 4.28) and the CO_2 laser pulse has a duration of 1.8 ns. It is therefore possible that some electrons can be accelerated before the accelerating layer becomes too bent.

It is difficult to determine which of these positive or negative effects will be dominant. We will therefore try three different focal spot lengths, the short and long focal spot described in Chapter 3, having a length of 140 μm and 350 μm, and a very long 800 μm focal spot produced by tilting the focusing lens at 30°.

In addition, we have to decide exactly where to aim the CO_2 laser and the ruby laser on the grating. The discussion in section 5.3 taught us that we increase our chances of trapping the electrons by having the maximum CO_2 laser intensity at the phase matching position where $v_{inj}=v_{ph}$. But this accelerates the electrons for only half the possible distance, since the first half of the line focus is not used. If this distance is long enough to accelerate the electrons by more that 5 keV, we will aim the CO_2 laser at the phase matching position. Otherwise, for a small a_{pw} and/or short focal spot, we will have to aim the lasers at a point further along the grating than the phase matching point (see Figure B.1 for example), so that the length of acceleration is sufficient to give a measurable energy gain. The ruby laser is always adjusted so that the middle of the CO_2 laser focal spot coincides with the middle of the ruby laser focal spot. This insures that the acceleration takes place in the most uniform region of the plasma.

The choice of injection energy for the electrons is dictated by limitations of the available equipment. High energy is desirable because the plasma modulation needed has a longer wavelength. These long wavelength modulations last longer and one can wait until the plasma has a longer scale length, resulting in a thicker accelerating layer. In addition, fast electrons are less likely to be affected by stray electric and magnetic fields. However, our electron gun is rated at 30 kV and dielectric breakdown in the high voltage connections limits the stable operating voltage at 25 kV. This will therefore be the injection energy used in the first experiment. Table 6.1 shows a resume of the parameters, their ranges and their effects.

Parameter	Range	Advantage	Disadvantage
Grating acceleration	$a = 10$ eV/μm	Small a_{pw}/a_m	Need a long acceleration for a detectable ΔE
	to		
	$a = 1000$ eV/μm	Short accelerator	Need large E_L
CO_2 laser focal length	140 μm	Produces large E_L. Plasma curvature less important on such a short distance.	Deforms the plasma distribution locally (bump)
	800 μm	More uniform plasma.	Small E_L, long accelerator.
Time Delay between the ruby and CO_2 laser	$\Delta t = 2.7$ ns	Large $\tilde{n}/n$	Small scale length acceleration layer thin & very close to the grating
	to		
	7.7 ns	Long scale length further away from the grating.	small $\tilde{n}/n$
Distance between the trapping position & the middle of the CO_2 laser focal spot	0 μm	Maximum intensity at the beginning to trap the electrons.	Uses only half the focal spot
	to		
	400 μm	Uses more of the available laser power, larger ΔE	Less intensity at the beginning

TABLE 6.1

Effect of the different experimental parameters

After selecting a set of parameters, we follow the alignment procedure described in Appendix B. We then adjust the current in the spectrometer to detect electrons in the energy range of 25.5 keV to 100 keV, a signal is therefore expected only for accelerated electrons. The complete system is finally triggered. The resulting fast sequence of events is as follows (see Figure 6.1). First the mechanical shutter of the electron gun is opened, the electron beam passes through the aperture, just above the grating and enters the spectrometer. It is then deflected by the magnet and absorbed in the beam dump and no signal is detected. About 50 ms later, while the electron beam current is at its maximum, the 6 ns ruby laser pulse strikes the grating. A modulated plasma is created and expands above the grating. After a specified time delay (which varies around 6 ns) the 1.8 ns CO_2 laser pulse irradiates this modulated plasma and creates a large amplitude plasma wave. A small portion of the electron beam crosses the plasma at the correct height above the grating and traverses the plasma wave. An even smaller fraction of the electron beam arrives in the wave at the correct phase. These electrons are trapped and then accelerated to a higher energy. Upon exiting the plasma these accelerated electrons enter the spectrometer, strike the scintillator and give a signal in the photomultiplier.

6.3 Results

Table 6.2 shows the results of the experiment. The first four columns represent the set of parameters used for the experiment.

grating	focal position	focal spot length	timing	number of shots	expected acceleration	a_{pw}/a_m	signal	noise	signal minus noise
eV/μm	μm	μm	ns		KeV	%	Volt	Volt	Volt
10	400	800	6	13	8	.33	.77±.06	.82±.07	-.05±.09
46	100	350	2.7	7	12	.76	1.0±.09	1.1±.08	-.1±.12
46	100	350	4.4	6	12	.76	.94±.1	.82±.07	.12±.12
46	100	350	6	17	12	.76	.87±.04	.86±.05	.01±.06
46	100	350	7.7	9	12	.76	1.2±.07	1.05±.08	.15±.11●
46	300	800	6	9	32	1.5	1.1±.08	1.15±.06	-.05±.1
215	50	140	4.4	8	26	1.8	.87±.05	.95±.07	-.08±.09
215	50	140	6	10	26	1.8	.98±.06	1.03±.04	-.05±.07
215	50	140	7.7	7	26	1.8	1.1±.1	.99±.07	.11±.12
215	0	140	4.4	6	15	1.8	.83±.07	.83±.05	0±.09
215	0	140	6	19	15	1.8	.97±.03	.99±.04	-.02±.05
215	0	140	7.7	8	15	1.8	.87±.07	.76±.06	-.11±.09●
215	100	350	6	9	59	3.6	1.0±.09	1.03±.08	-.03±.12
215	0	350	4.4	7	38	3.6	.87±.07	.82±.05	.05±.09
215	0	350	6	21	38	3.6	.96±.03	.91±.04	.05±.05
215	0	350	7.7	9	38	3.6	1.0±.06	1.07±.06	-.07±.08
1000	0	140	6	8	70	8	1.1±.08	1.08±.07	.02±.1

TABLE 6.2

Results with the 25 keV electron gun

Column #1 gives the accelerating gradient of the grating, column #2 is the distance between the phase matching position and the middle of the CO_2 laser focal spot, column #3 gives the length of the CO_2 laser focal spot and column #4 gives the time delay between the ruby and CO_2 laser pulses.

Column #5 gives the number of shots for which the signals have been averaged. Column #6 gives the expected acceleration and Column #7 gives a_{pw}/a_m for the given grating and CO_2 focusing. For each set of parameters the experiment is repeated many times. The signal of the photomultiplier is averaged over all these shots and appears in the column labelled "signal". The indicated uncertainty is the standard error of the mean. Before each real shot, a reference shot is fired on the end of a grating where the phase speed of the plasma wave is too fast to trap the injected electrons. Everything else is identical to a real shot, i.e. the electron gun, ruby laser, CO_2 laser and electron spectrometer. No accelerated electrons are expected. The signal obtained, labeled noise in the table, comes from X-rays, light and stray electrons. The noise is also averaged over all the shots and the standard error is calculated. The experimental runs are all performed in this manner; reference shot on the tail of a grating, real shot on the phase matching position of a grating, reference shot, real shot, etc. Shots where the CO_2 laser is not in the 350 ± 100 mJ range, or the ruby laser not in the 150 ± 30 mJ range are rejected. We also recorded the time delay between the ruby and CO_2 laser for each shot. If the delay is not as indicated (±1 ns) because of excessive jitter, the shot is rejected. We subtract the noise from the signal and write the results in the column indicated "signal minus noise". The uncertainty given is the square root of the signal and noise error squared.

6.4 Discussion

We can see in the last column of the table that only two sets of parameters produce a result that is not zero within one standard error, (these are marked by an asterix). One, 0.15±0.11, that seems to indicate electron acceleration, and the other, -0.11±0.09, showing noise larger than the signal! They only differ from zero by 1.4 and 1.2 σ respectively, which is not very significant. Also from the statistics of the 17 sets of parameters tested, we would expect to have five results different (32%) from zero by more than 1 σ even with no signal at all. We can also compare these small signal values to the expected 4,400 accelerated electrons at 350 mV of signal per electron. The photomultiplier should therefore have been totally saturated. The saturation level being 5 Volts. We must conclude that the expected acceleration process is not functioning properly.

The question then is: why is it not working? Chapter 4 shows that the plasma above the grating is modulated. When the CO_2 laser irradiates this plasma it will certainly produce plasma waves. Phase and amplitude fluctuations of those waves are unavoidable but we have seen that if we use a conservative value for the accelerating gradient the experiment should work in the presence of those imperfections.

The trajectory of the electrons must pass just above the grating at a height of less than 100 μm, over a length of 2.5 cm. This is quite difficult to achieve. It was observed in the process of developing the spectrometer (section 6.1.2) that the electron beam may be deflected while crossing the plasma. This may be due to an electric field emanating from the plasma. An electric field of this type is created when some fast electrons escape from the plasma and leave it positively charged. Such an electric field attracts the electrons towards the grating and if it is strong enough, can make them strike the grating, Figure 6.12.

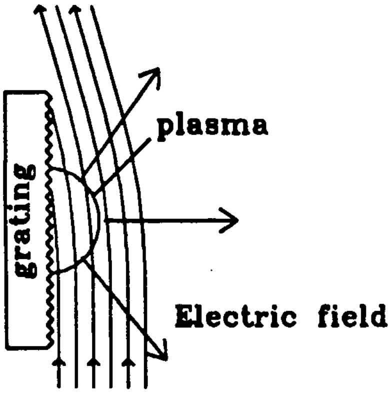

electron beam

FIGURE 6.12

Bending of the electron beam by the electric field of the plasma.

In order to study this effect we measured the electron beam current while triggering the lasers. The spectrometer magnetic field was adjusted so that the 25 keV electrons can strike the scintillator directly. The beam current must be reduced to a very small value to avoid saturating the photomultiplier. The signal from the photomultiplier produced by this low intensity electron beam, decreases to almost zero when the lasers generate the plasma on the grating. The signal recovers to its normal value after about 100 ns (Figure 6.13a). We also performed the same experiment with a piece of solid brass instead of the grating. The signal does not decrease as much and recovers more quickly, Figure 6.13b.

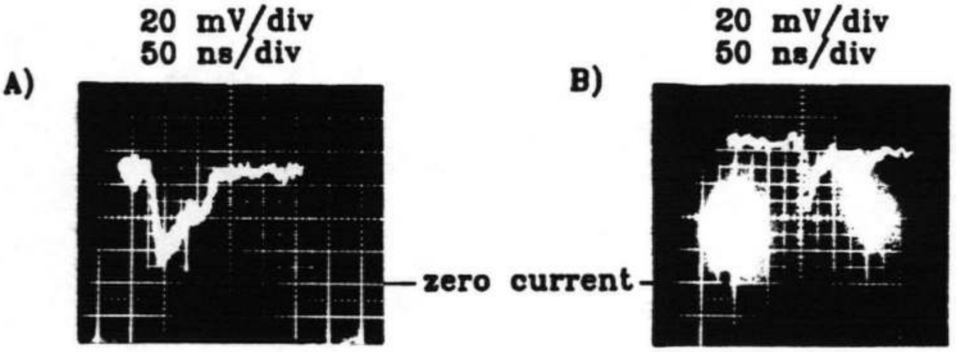

FIGURE 6.13
Interruption of the electron beam by the plasma

These results can be explained as follows. The gold layer of the grating is grounded by two spring loaded metal wires connected to the x-y translation stage which is grounded to the target chamber. When the lasers are fired, fast electrons leave the plasma so it becomes positively charged in less than 1.8 ns. The grounded gold layer of the grating tries to cancel this charge, but because of the inductance of the system (thin gold layer and springs), the electric current from the ground to the plasma does not increase fast enough and an electric field is generated attracting the electron beam toward the grating. The electrons strike the grating so the signal on the photomultiplier is strongly reduced. After the laser pulse, the plasma cools down so that no more electrons are ejected and the charge is cancelled by electrons from the gold layer with a time constant $\sqrt{LC}$, where L is the inductance of the gold layer spring system and C is the capacitance of the plasma cloud. The signal on the photomultipler therefore recovers after the laser pulse with the same $\sqrt{LC}$ time constant. The solid pieces of brass have less inductance than the springs gold layer system, and cancel the charge more quickly. The beam does not totally disappear and recovers faster after the laser pulse.

With this grating, the electron current is reduced to about 13% of its original value. This should still be enough to see accelerated electrons given the sensitivity of the detector. However, we must consider the response time of the detector. For a signal of this type (interruption of a continuous signal) it is not the rise time which is important but the decay time. The RCA 8575 signal decays to 1/e of its maximum in 20 ns. Therefore, even if the intensity of the electron beam that enters the scintillator decreases to zero for 1.8 ns, the signal of the photomultipler would not reduce to zero. Because of the response time of the photomultiplier, it is impossible to know if the electron beam current decreases to zero during the 1.8 ns CO_2 laser impulsion. However, we know that the current is strongly reduced.

If the electron beam is deflected towards the grating, the electrons that are close to the surface will be the first to strike the grating. These are the electrons that would be accelerated by the plasma wave (see Figure 6.12). Even if all the electrons closer than 100 μm from the grating, strike the surface, 90% of the electron beam can still pass above the grating. This is because the electron beam aperture is 1 mm wide. However, those electrons will not show any acceleration because they pass above the plasma wave.

In order to observe electron acceleration, the signal of the photomultiplier must not decrease by more than 10%. However, we just saw that less than

13% of the beam passes through the plasma during the CO_2 laser pulse. This explains the negative result of the experiment.

6.5 Origin of the Electric Field

We can first calculate the electric field caused by the thermal electrons. In a plasma the electrons have a much larger thermal velocity than the ions. If there is a density gradient, the electrons will move towards the low density faster than the ions. A space charge electric field will therefore be created and this prevents the electrons from moving too fast towards the low density. The electrons then attract the ions because of the electric field. The fluid equation for the electron acceleration is:

$$m_e n_e \left(\frac{\partial \vec{v}_e}{\partial t} + \vec{v}_e \nabla \vec{v}_e\right) = -k_B T \nabla n_e - q\vec{E} n_e$$

And for the ions:

$$m_i n_i \left(\frac{\partial \vec{v}_i}{\partial t} + \vec{v}_i \nabla \vec{v}_i\right) = -k_B T \nabla n_i + qZ^* \vec{E} n_i$$

Because the expansion is a slow process involving ion motion we can use the quasi-neutrality approximation $n_e \approx Z^* n_i$ and therefore:

$$\left(\frac{\partial \vec{v}_e}{\partial t} + \vec{v}_e \nabla \vec{v}_e\right) \approx \left(\frac{\partial \vec{v}_i}{\partial t} + \vec{v}_i \nabla \vec{v}_i\right)$$

(i.e. the acceleration of the electrons is almost the same as the acceleration of the ions, otherwise large charge separation would occur).

Solving the equations for E we find:

$$E = \frac{-k_B T}{qL}$$

Where $L = \frac{n_e}{\nabla n_e} \approx \frac{n_i}{\nabla n_i}$ is the scale length.

In our experiment the temperature is around 100 eV and the scale length is about 150 μm. This gives an electric field due to the thermal electrons of:

$$E = 6.6\times10^5 \text{ V/m}$$

An injected electron beam moving perpendicularly to this field will be deflected by an angle of:

$$\theta = \frac{qE}{m_e}\frac{d}{\mathrm{v}_{inj}^2} \approx 2.3 \text{ mrad}$$

Where d is the length of plasma that the electrons have to traverse and $\mathrm{v}_{\mathrm{inj}}$ is the injection speed.

After they cross the plasma, the electrons have to continue above the grating for up to 20 mm. If they are deflected by $\theta = 2.3$ mrad, they will approach the grating by $\theta \times 25$ mm$=50$ μm. Given that the accelerating layer is at a height of about 75 μm, the accelerated electrons will not strike the grating due to this field. The electrons avoid the grating, but not by very much. However, this calculation is for the worst case geometry. The plasma is produced at the very beginning of the grating plate and, after being deflected, the electrons have to travel the full length of the plate (25 mm). Having recognized this fact, we only used the two last gratings before the end of the grating plate. For this geometry the electrons will approach the grating by less than $\theta \times 4$ mm = 9 μm, a more comfortable margin.

We can calculate the electric field necessary to reduce the detected electron beam current by 87% (Figure 6.13A). Because the electron beam is 1 mm wide, we know that it was deflected by 870 μm. The distance between the edge of the grating plate and the plasma was 4 mm. The electron beam was therefore bent by 870 μm/4 mm=218 mrad. If we suppose that the electric field exists only in the plasma, we calculate a deflecting electric field of 6×10^7 V/m. This field is 100 times larger than our estimate of the ambipolar field. We also saw that the intensity of the deflecting electric field changes with the inductance of the target, a result inconsistent with the ambipolar field that depends only on the scale length and plasma temperature. Clearly, some other source of electric field is present in this experiment.

It is well known that an intense laser pulse irradiating a plasma will produce high energy supra-thermal electrons. These electrons are accelerated by plasma waves produced predominantly by two types of instability, the stimulated Raman [33] and the two plasmon decay instabilities [34]. Because of their high energy the electrons can escape the plasma even against a large electric field and leave it highly charged [32]. Of these two instabilities, the two plasmon decay instability has the lower threshold. The linear theory of this instability predicts a threshold of:

$$L(\mu m)\lambda_{laser}(\mu m)I_{laser}(10^{14}W/cm^2)/T(keV) > 61.25$$

For $T_e = 100$ eV and $L = 150$ μm the threshold is 4×10^{11} W/cm². This is an intensity similar to the one used in our experiment. However, this is the threshold of the instability, electron trapping will occur only when the plasma waves have grown to a large amplitude. Fast electrons are observed for an intensity larger than 3×10^{13} W/cm² in a plasma having a scale length of 50 μm [34]. Because the threshold decreases for a longer scale length (in our experiment $L\approx150$ μm), fast electrons should be produced only for intensities larger than 10^{13} W/cm². We intentionally chose the intensity of the CO_2 laser in our experiment to be far less than this value in order to avoid these problems. ($I = 7.5\times10^{11}$ W/cm² for the smallest focal spot used.) Therefore no instability should be excited to a level sufficient to produce supra-thermal electrons.

Nevertheless we observed some electrons with energy up to 13 keV (Figure 6.6), and an electric field intense enough to disrupt the electron beam. Previous observation of supra-thermal electrons has been done at intensities relevant to laser-fusion experiments. Large amounts of hot electrons and target charging was observed. However, the low intensities range was not thoroughly studied and these effects may still be generated at a level insufficient to be of concern for fusion (pre-heating of the core, energy balance) but nevertheless very damaging for a laser accelerator. If target charging is the cause of the electron beam deflection, it causes an electric field over a region much larger than the focal spot of the laser. For this case our estimate for the perpendicular electric field of 6×10^7 V/m from the deflection of the electron beam is an upper limit because a weaker field over a larger region could create the same deflection. Whatever the exact reason for the creation of the electric field, it deflects the electron beam and prevents the accelerated electrons from being detected.

6.6 The Grounded Metal Channel

We first tried to remedy this problem using a grounded metal channel just above the grating (Figure 6.14).

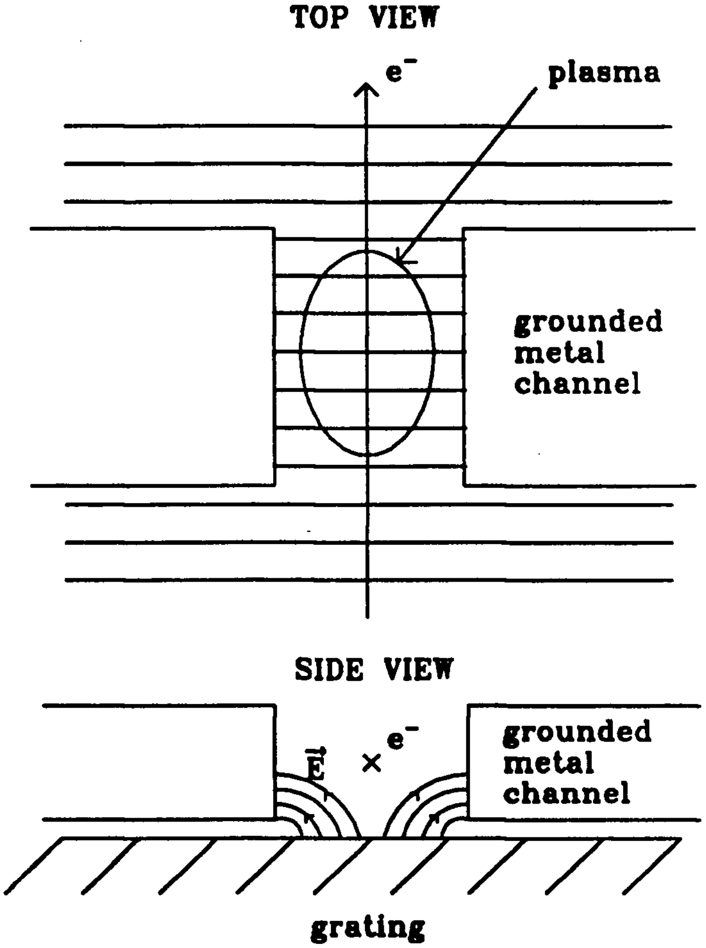

FIGURE 6.14
Detail of the metal channel used to reduce the electric field

The field lines from the charged plasma are expected to terminate at the grounded metal and produce a relatively field free zone inside the channel. With the metal channel in place, the electron beam current detected by the photomultiplier is reduced by only 25% when the lasers are triggered. This is an improvement over the plain grating (87% reduction), but there is still some loss. We tried the experiment with the metal channel in place. The results are shown on table 6.3.

grating	focal position	focal spot length	timing	number of shots	expected acceleration	a_{pw}/a_m	signal	noise	signal minus noise
eV/μm	μm	μm	ns		KeV	%	Volt	Volt	Volt
46	100	350	4.4	8	12	.76	1.1±.07	1.01±.06	.09±.09
46	100	350	6	11	12	.76	.97±.04	1.02±.05	-.05±.06
46	100	350	7.7	6	12	.76	.89±.07	.87±.06	.02±.09
215	0	350	4.4	5	38	3.6	.93±.08	.90±.07	.03±.11
215	0	350	6	11	38	3.6	1.0±.05	1.08±.04	-.08±.06
215	0	350	7.7	6	38	3.6	.97±.06	.96±.05	.01±.08

TABLE 6.3

Results with the 25 keV electron gun and the metal channel

No accelerated electrons are detected. Again, even if the dip in electron current during the lasers' pulse is small, the important low trajectory electrons strike the grating and are no longer able to be detected.

Electrons injected at a faster speed would be deflected much less for a given deflecting electric field. In addition, we can use a larger grating spacing and the plasma could be modulated higher above the grating so more deflection can be accommodated before the electrons touch the surface. The scale length of the plasma could also be increased allowing more electrons to be in the thicker accelerating layer. We therefore decided to build a new electron source and spectrometer which could operate at a higher voltage.

6.7 High Voltage Electron Gun

The insulation of the 25 keV electron gun cannot hold more than 30 kV. Also for higher voltages and the same current, the power in a continuous beam becomes prohibitive. Because of these limitations a pulsed electron gun of 92 keV was designed and built (Appendix C). This gun can deliver 0.5 A in a 25 ns long pulse. This is 125 times more current than the 25 keV and should therefore be enough to obtain a detectable signal if the acceleration process occurs.

6.8 Five channel electron spectrometer

The very sensitive one channel spectrometer used with the 25 keV gun was designed to detect the few electrons expected to be accelerated. The new pulsed source should produce 125 times more accelerated electrons each with about 4 times more energy, relaxing considerably the sensitivity constraint. Unfortunately the background noise will also increase dramatically and the increased number of stray electrons will produce a large signal from the photomultiplier. In addition, the 92 keV X-rays produced by the impact of the electrons on the beam dump can penetrate light aluminum shielding and enter the scintillator. Our experience with the very sensitive one channel spectrometer indicates that it would be impossible to operate with this electron source without having a very large background signal saturating the photomultiplier.

Fortunately a less sensitive five channels electron spectrometer was available from previous work by L. Legault [35]. It was modified to meet our requirements. The design is shown on Figure 6.15.

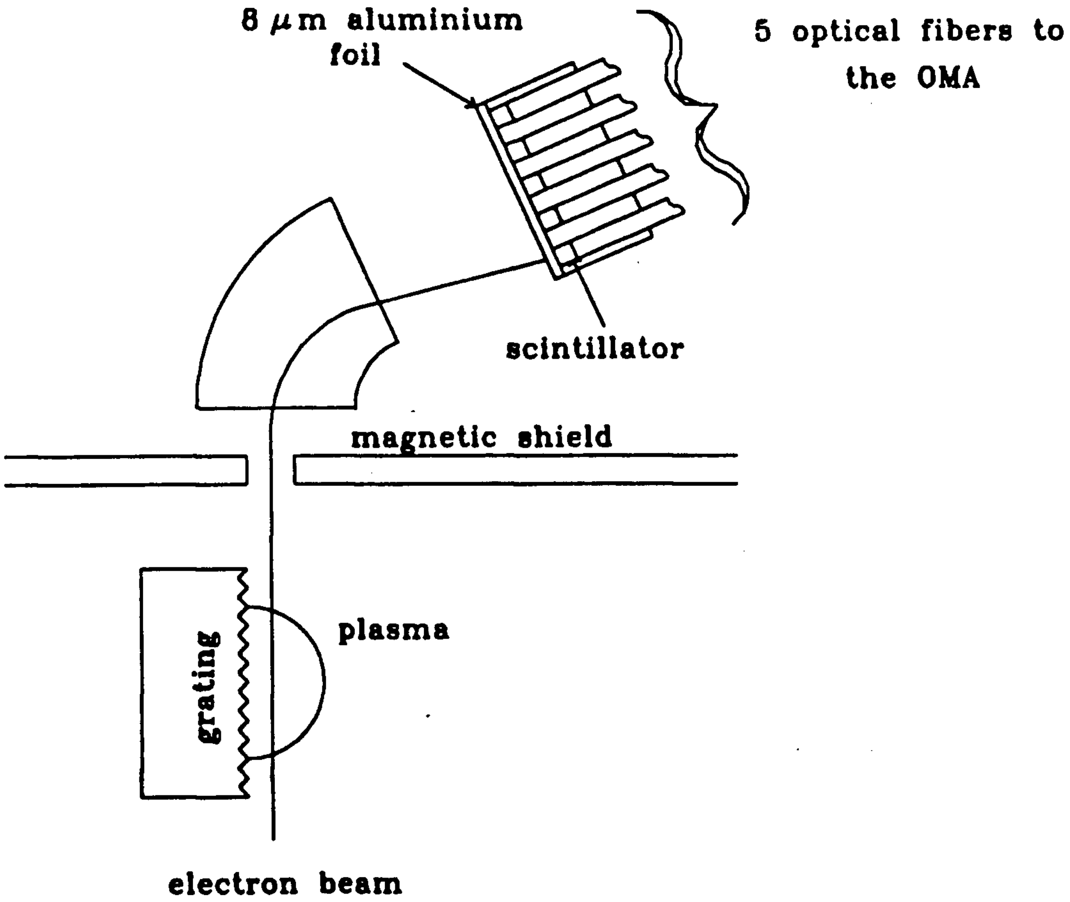

FIGURE 6.15
Design of the 5 channel spectrometer

Five Ne-102 plastic scintillators are coupled via 5 optical fibres to a Princeton instrument optical multichannel analyzer (OMA). Because of the increased energy we can cover the scintillator with 8 μm thick, pin hole free aluminum foil in place of evaporating a thin coating on the scintillator (see Figure A.1 for electron range in aluminum).

We calibrated the new electron spectrometer using the 92 kV electron pulses, and varying the magnetic field of the deflecting electromagnet, until all the signals appear in only one channel. Of course the channel is then completely saturated and we cannot estimate the sensitivity of the spectrometer with this method. This procedure is repeated for each of the 5 channels. The calibration result is shown on Figure 6.16. Because single electrons could not be detected by this system, it is difficult to find the absolute sensitivity of the spectrometer. We will have to rely on a rough theoretical estimate.

For a conversion efficiency of about 10% [36] between the electron energy and the light produced, there will be 5,000 photons generated for each 100 keV electron. About 50% (estimate) of the light is coupled to the fiber which then transmits only 15% [35] of this light to the OMA. The coupling between the fiber and the OMA is about 50% and the OMA sensitivity is 100 photons/count. The total sensitivity will therefore be 2 counts/100 keV electron. The background signal due to light leakage, X-rays and dark current of the OMA, is about 300 counts per channel. This detector can therefore detect 150 electrons, which is a suitable sensitivity.

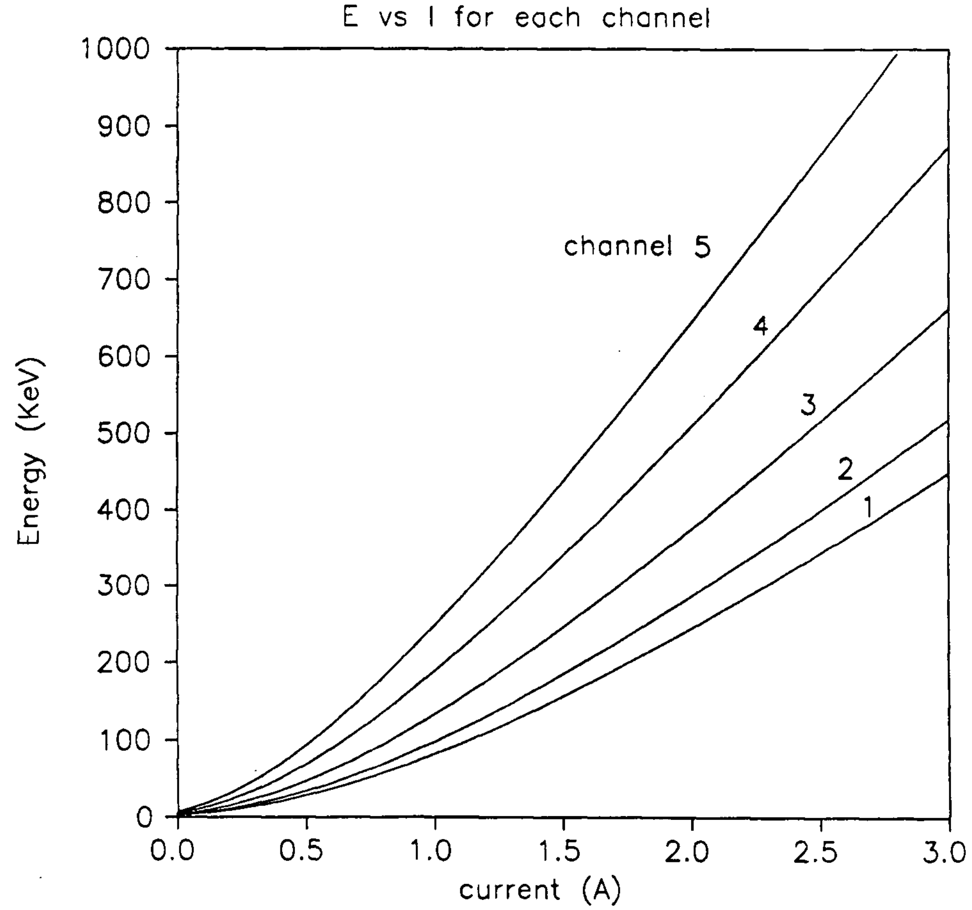

FIGURE 6.16

Calibration of the 5 channel spectrometer

We can calibrate the relative sensitivity of the 5 channels using the X-rays produced by the electron pulse. If we adjust the magnetic field of the spectrometer electromagnet to a very high value, the electrons are deflected with a short radius of curvature. In place of entering the beam dump, the electron beam strikes the magnetic shield close the spectrometer entrance and produces X-rays. At the position of the 5 scintillators, the X-ray flux is fairly uniform and we obtain the relative signal in each channel shown on table 6.4. We can compare this signal with the old calibration obtained by L. Legault [35].

Channel Number	L. Legault Calibration	New Calibration
1	1.00	0.03
2	0.89	1.00
3	0.69	0.75
4	0.63	0.71
5	0.28	0.31

TABLE 6.4

Relative sensitivity of each channel of the spectrometer.

We see that the sensitivity of channel #1 is greatly reduced. This may be due to a broken optical fibre or a weak coupling between the scintillator and the fibre or between the fibre and the OMA. We did not use channel #1 to detect accelerated electrons. The magnetic field of the spectrometer is adjusted so that the direct, non-accelerated electron beam hits the scintillator of channel #1. Because of the decreased sensitivity, channel #1 is not saturated and the signal could be used to obtain the relative (shot to shot) intensity of the injected electron beam. Any accelerated electrons can be detected in channel #'s 2, 3, 4 and 5.

6.9 Result with the High Energy Electron Gun

The experiment is repeated with the same procedures and parameters as in section 6.3. However, we now have five signals from the five channels of the electron spectrometer. So in place of a table, a graph will be plotted for each parameter set (Figure 6.17). The points for each channel are the mean of the signal, the mean of the noise and finally the signal minus noise. For clarity, the error bars are indicated only for the signal minus noise points. They represent the standard error of the mean. The magnetic field of the spectrometer is adjusted so the different channels detect electrons at the energy shown on Table 6.5.

Channel #1	Energy (keV)
1	92
2	100
3	138
4	189
5	250

TABLE 6.5

Energy of the electrons detected by each channel of the spectrometer.

The direct, non-accelerated, electron beam strikes channel #1 which is therefore used to monitor the electron beam intensity. The actual counts in channel #1 are 100 times those indicated on the graph. The square on the graph represents the average of the electron beam intensity for the proper shots and the triangle represents the average for the reference shots. No signal minus noise points are plotted for channel #1. We also used the grounded metal channel on a few shots in an attempt to reduce the deflecting electric field. The results are show on Figure 6.17.

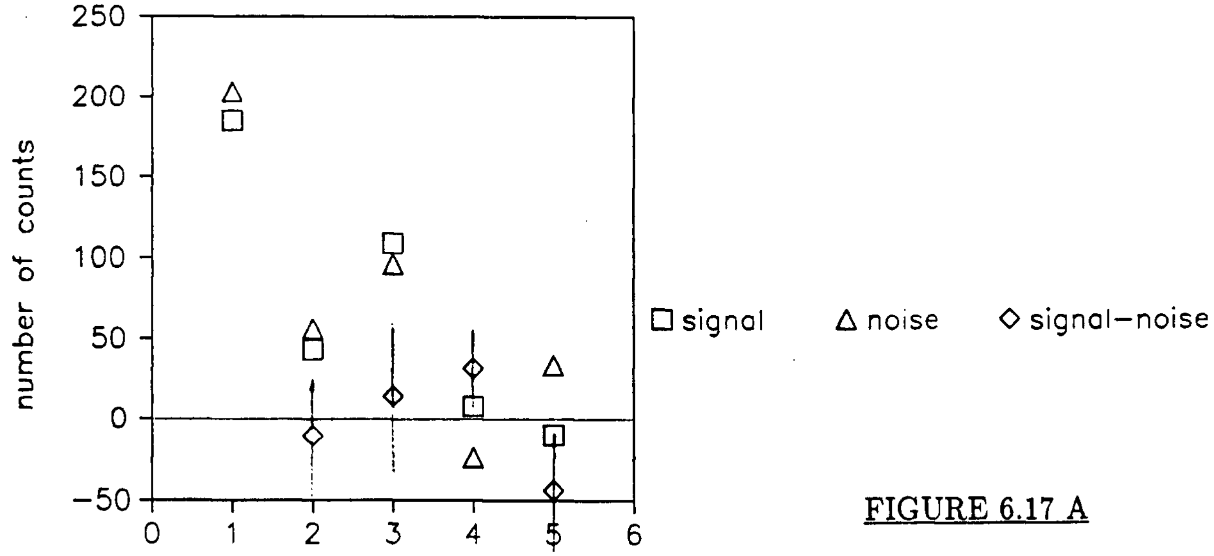

FIGURE 6.17 A

focal spot length: 800 μm grating chirp: 10 eV/μm

time delay between the CO_2 and ruby lasers: 6 ns a_{pw}/a_m=0.33%

distance between the trapping point and the center of the CO_2 focal spot: 400 μm

injection energy: 92 KeV expected energy gain: 8KeV

number of shots averaged: 6

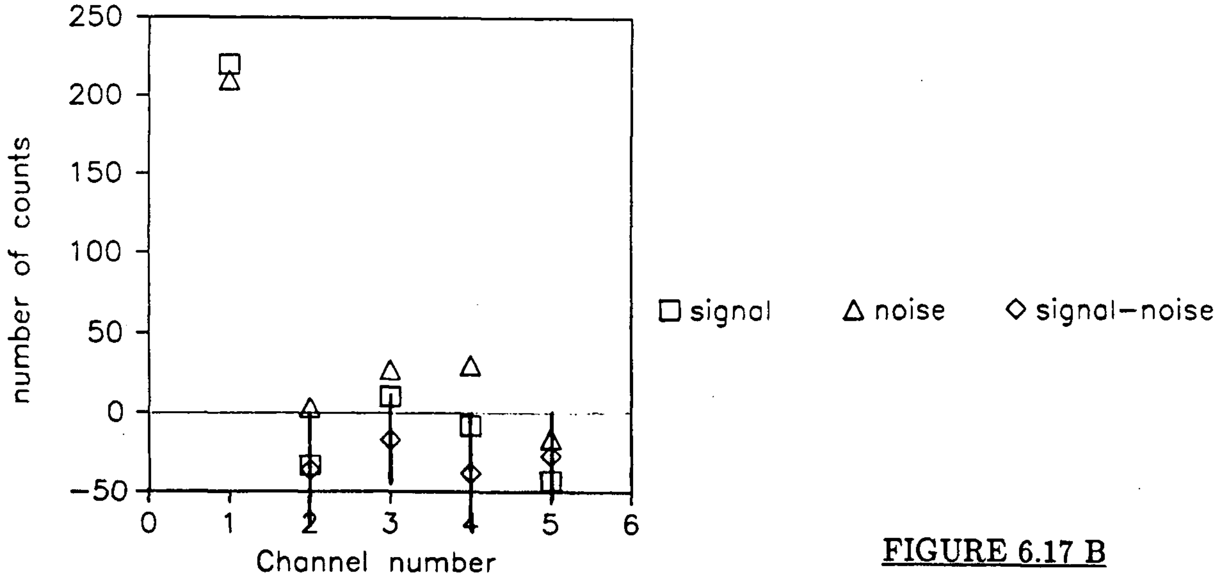

FIGURE 6.17 B

focal spot length: 350 μm grating chirp: 46 eV/μm

time delay between the CO_2 and ruby lasers: 3 ns a_{pw}/a_m=0.76%

distance between the trapping point and the center of the CO_2 focal spot: 100 μm

injection energy: 92 KeV expected energy gain: 12KeV

number of shots averaged: 8

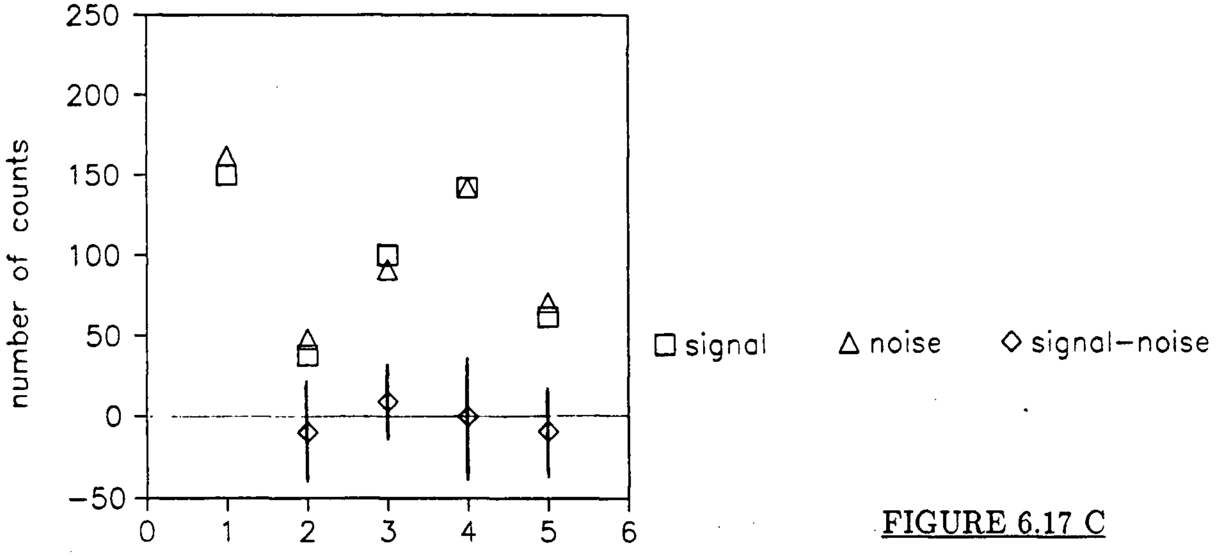

FIGURE 6.17 C

focal spot length: 350 μm grating chirp: 46 eV/μm

time delay between the CO_2 and ruby lasers: 6 ns a_{pw}/a_m=0.76%

distance between the trapping point and the center of the CO_2 focal spot: 100 μm

injection energy: 92 KeV expected energy gain: 12KeV

number of shots averaged: 7

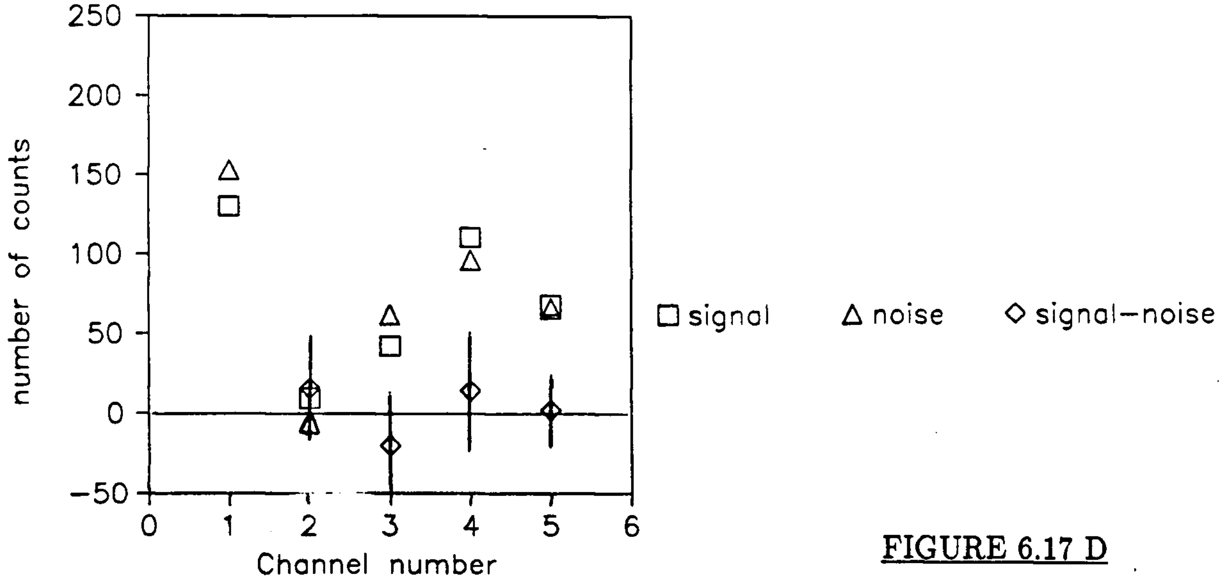

FIGURE 6.17 D

focal spot length: 350 μm grating chirp: 46 eV/μm

time delay between the CO_2 and ruby lasers: 9 ns a_{pw}/a_m=0.76%

distance between the trapping point and the center of the CO_2 focal spot: 100 μm

injection energy: 92 KeV expected energy gain: 12KeV

number of shots averaged: 7

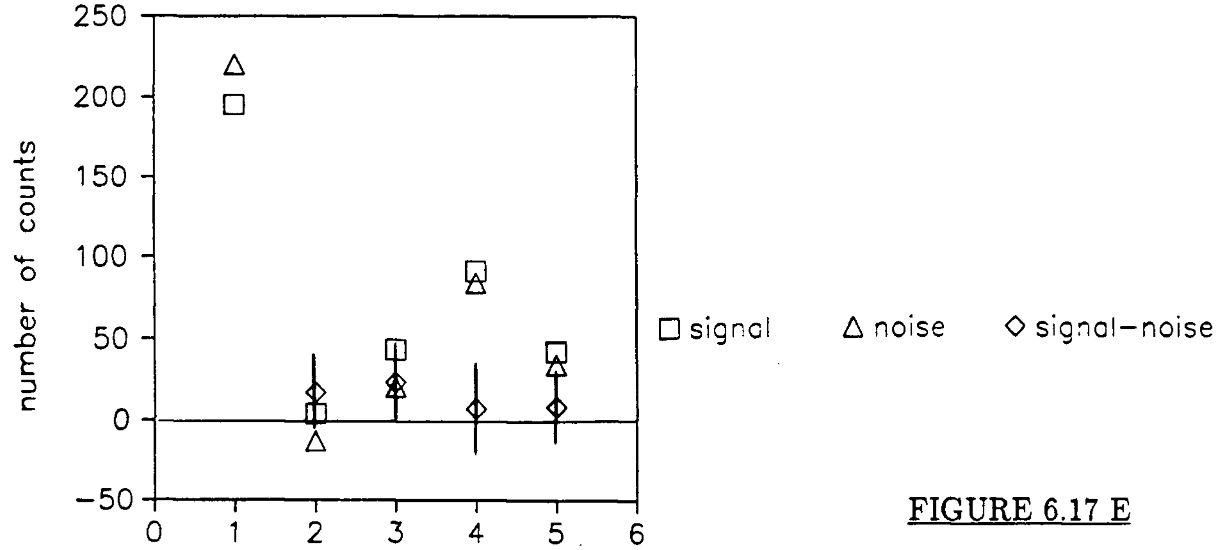

FIGURE 6.17 E

focal spot length: 800 μm

grating chirp: 46 eV/μm

time delay between the CO_2 and ruby lasers: 6 ns

a_{pw}/a_m=1.5%

distance between the trapping point and the center of the CO_2 focal spot: 0 μm

injection energy: 92 KeV

expected energy gain: 18KeV

number of shots averaged: 7

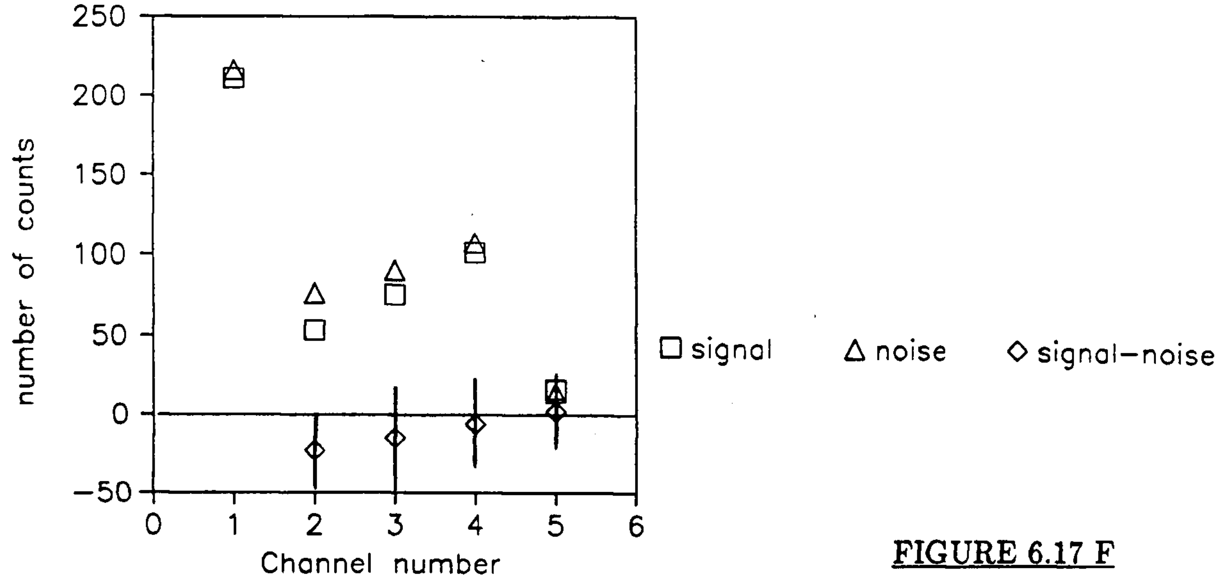

FIGURE 6.17 F

focal spot length: 140 μm

grating chirp: 215 eV/μm

time delay between the CO_2 and ruby lasers: 3 ns

a_{pw}/a_m=1.8%

distance between the trapping point and the center of the CO_2 focal spot: 0 μm

injection energy: 92 KeV

expected energy gain: 15KeV

number of shots averaged: 6

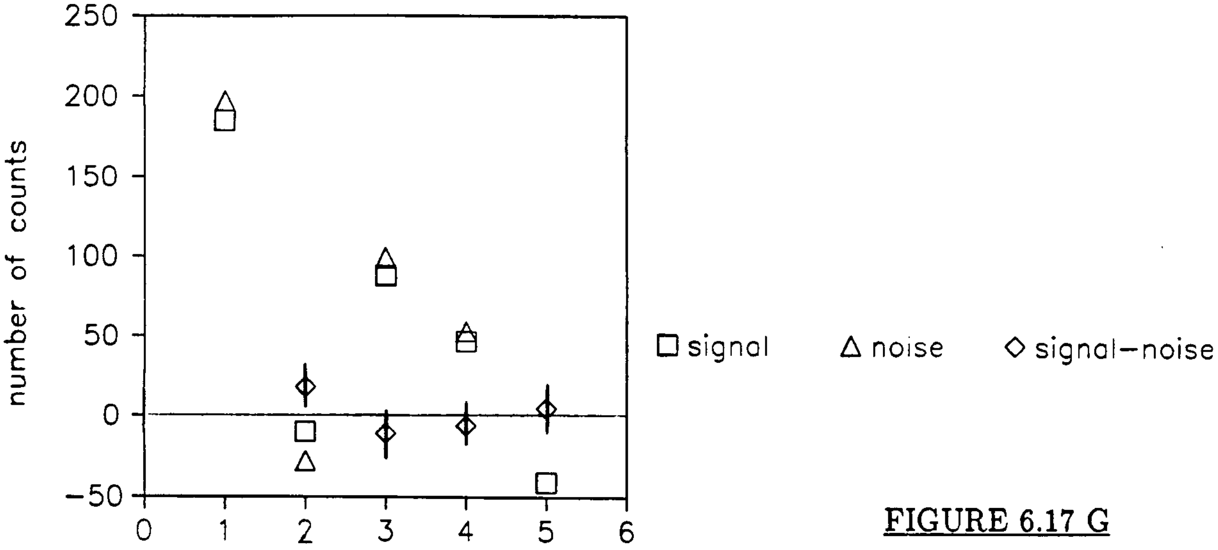

FIGURE 6.17 G

focal spot length: 140 μm grating chirp: 215 eV/μm

time delay between the CO_2 and ruby lasers: 6 ns a_{pw}/a_m=1.8%

distance between the trapping point and the center of the CO_2 focal spot: 0 μm

injection energy: 92 KeV expected energy gain: 15KeV

number of shots averaged: 17

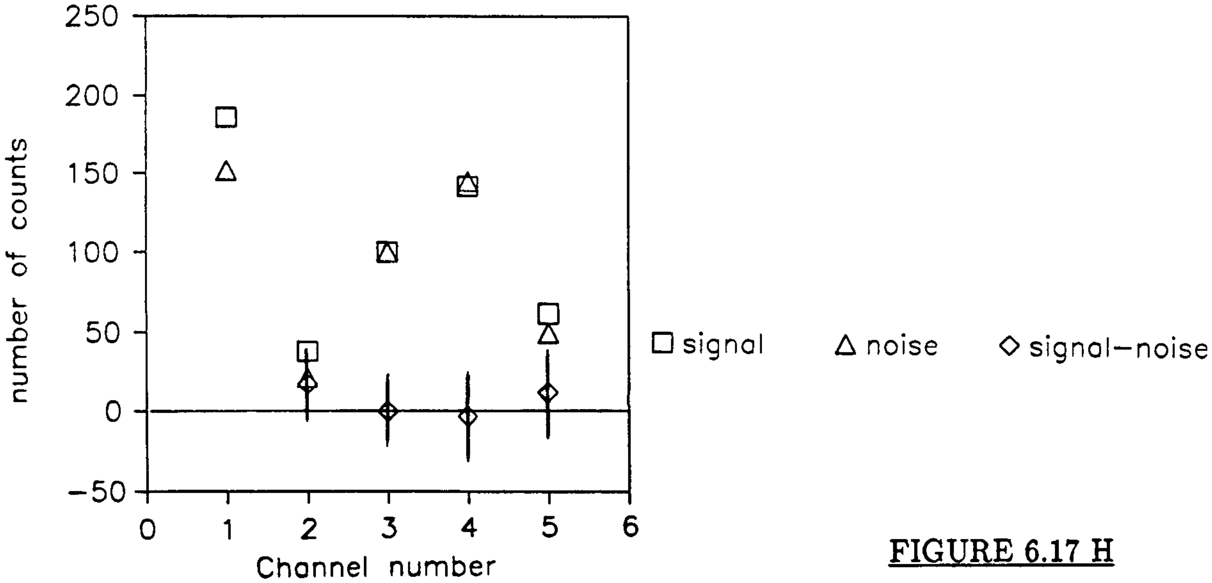

FIGURE 6.17 H

focal spot length: 140 μm grating chirp: 215 eV/μm

time delay between the CO_2 and ruby lasers: 9 ns a_{pw}/a_m=1.8%

distance between the trapping point and the center of the CO_2 focal spot: 0 μm

injection energy: 92 KeV expected energy gain: 15KeV

number of shots averaged: 8

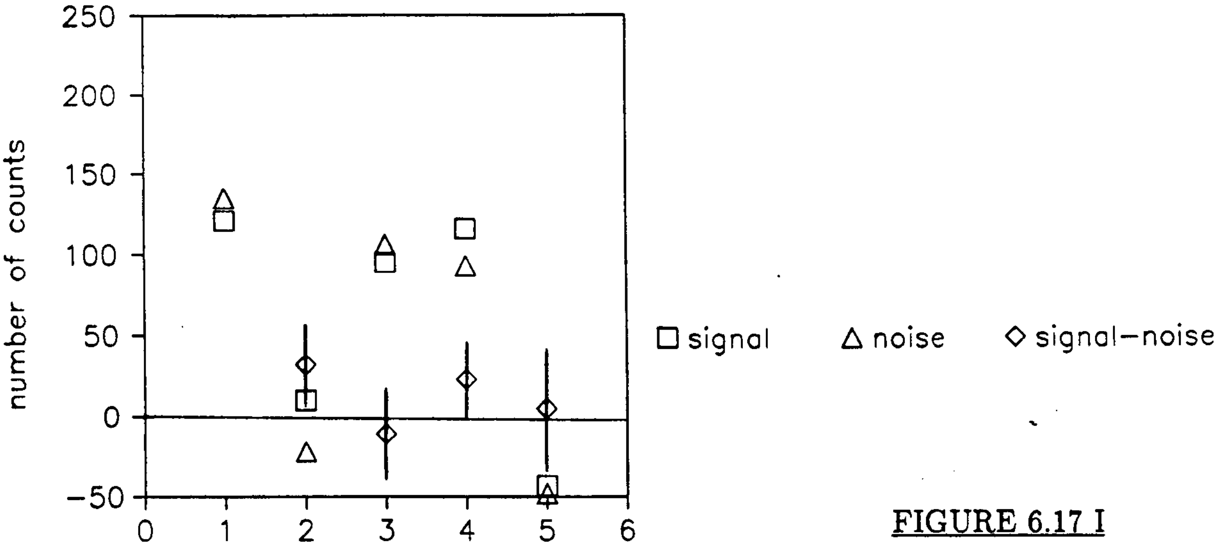

FIGURE 6.17 I

focal spot length: 140 μm grating chirp: 215 eV/μm

time delay between the CO_2 and ruby lasers: 12 ns $_{pw}a/a_m$=1.8%

distance between the trapping point and the center of the CO_2 focal spot: 0 μm

injection energy: 92 KeV expected energy gain: 15KeV

number of shots averaged: 6

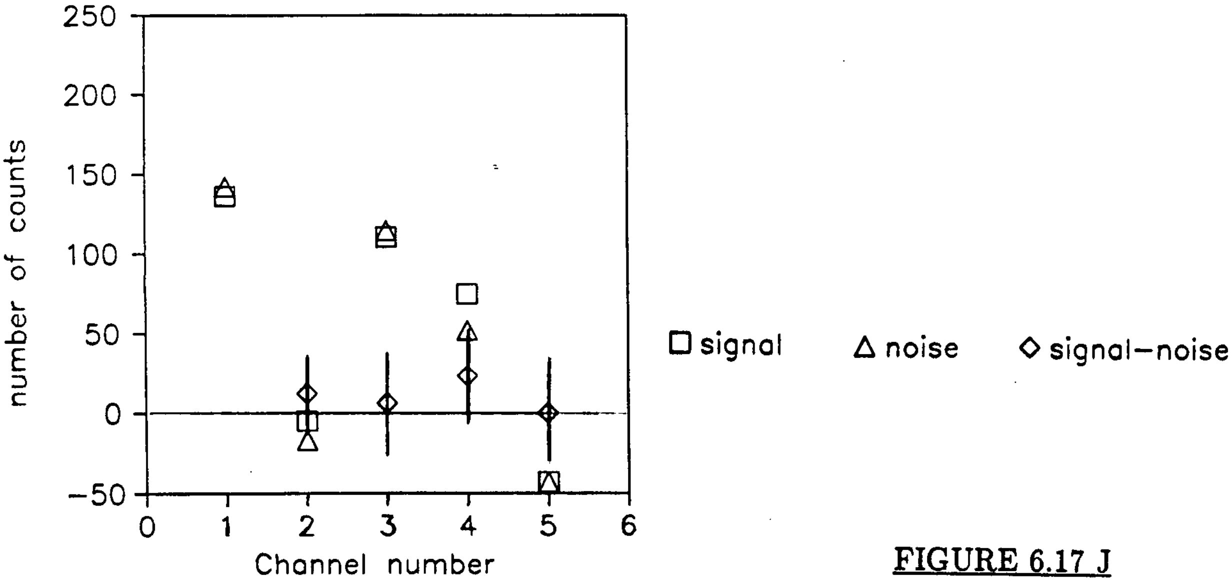

FIGURE 6.17 J

focal spot length: 140 μm **grating chirp: 215 eV/μm**

time delay between the CO_2 and ruby lasers: 6 ns **a_{pw}/a_m=1.8%**

distance between the trapping point and the center of the CO_2 focal spot: 0 μm

injection energy: 92 KeV **expected energy gain: 15KeV**

number of shots averaged: 5 **with metal channel**

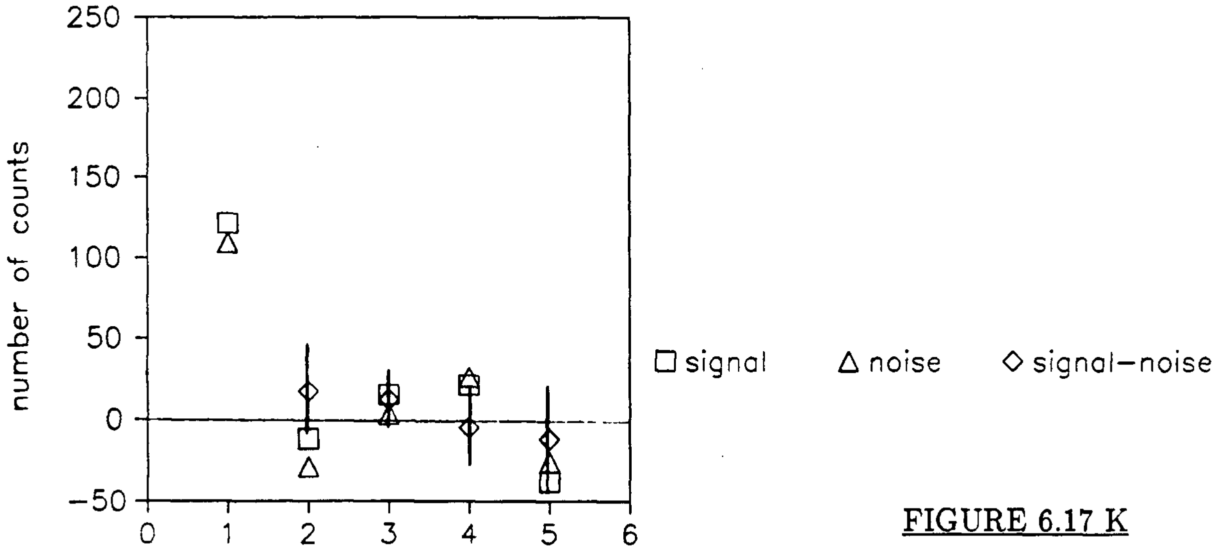

FIGURE 6.17 K

focal spot length: 350 μm grating chirp: 215 eV/μm

time delay between the CO_2 and ruby lasers: 3 ns a_{pw}/a_m=3.6%

distance between the trapping point and the center of the CO_2 focal spot: 0 μm

injection energy: 92 KeV expected energy gain: 37KeV

number of shots averaged: 7

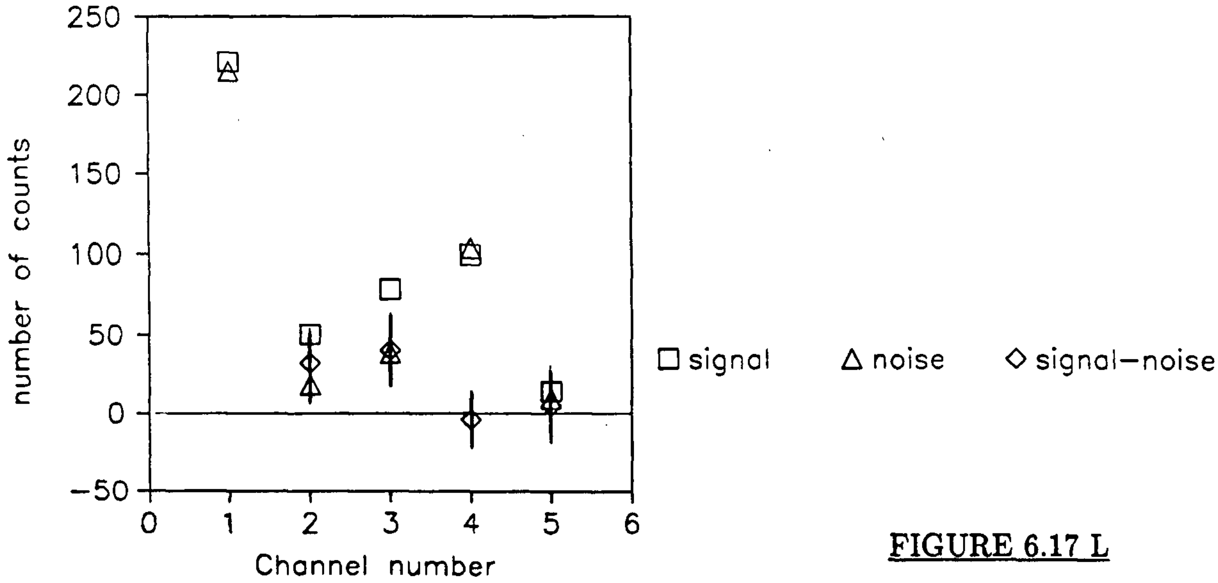

FIGURE 6.17 L

focal spot length: 350 μm grating chirp: 215 eV/μm

time delay between the CO_2 and ruby lasers: 6 ns a_{pw}/a_m=3.6%

distance between the trapping point and the center of the CO_2 focal spot: 0 μm

injection energy: 92 KeV expected energy gain: 37KeV

number of shots averaged: 13

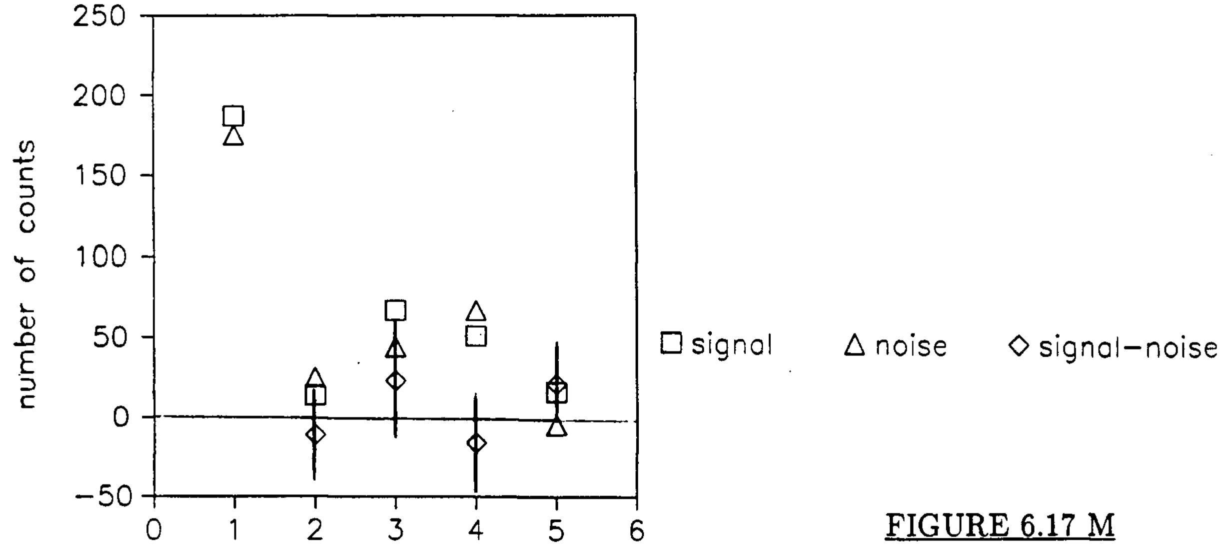

FIGURE 6.17 M

focal spot length: 350 μm grating chirp: 215 eV/μm

time delay between the CO_2 and ruby lasers: 9 ns a_{pw}/a_m=3.6%

distance between the trapping point and the center of the CO_2 focal spot: 0 μm

injection energy: 92 KeV expected energy gain: 37KeV

number of shots averaged: 8

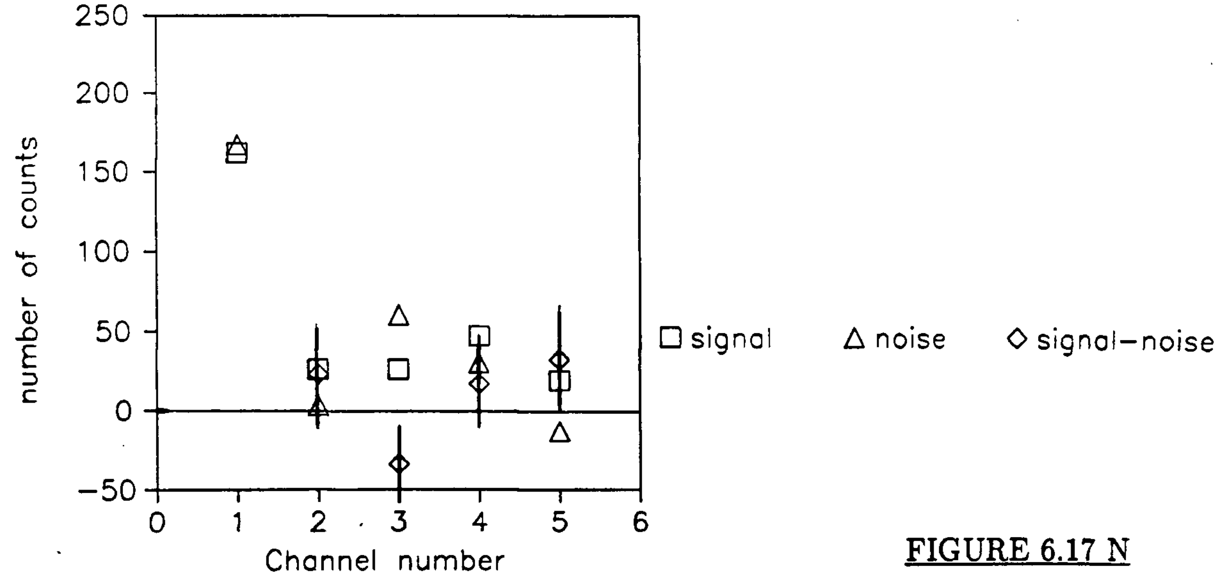

FIGURE 6.17 N

focal spot length: 350 μm grating chirp: 215 eV/μm

time delay between the CO_2 and ruby lasers: 6 ns a_{pw}/a_m=3.6%

distance between the trapping point and the center of the CO_2 focal spot: 0 μm

injection energy: 92 KeV expected energy gain: 37KeV

number of shots averaged: 4 with metal channel

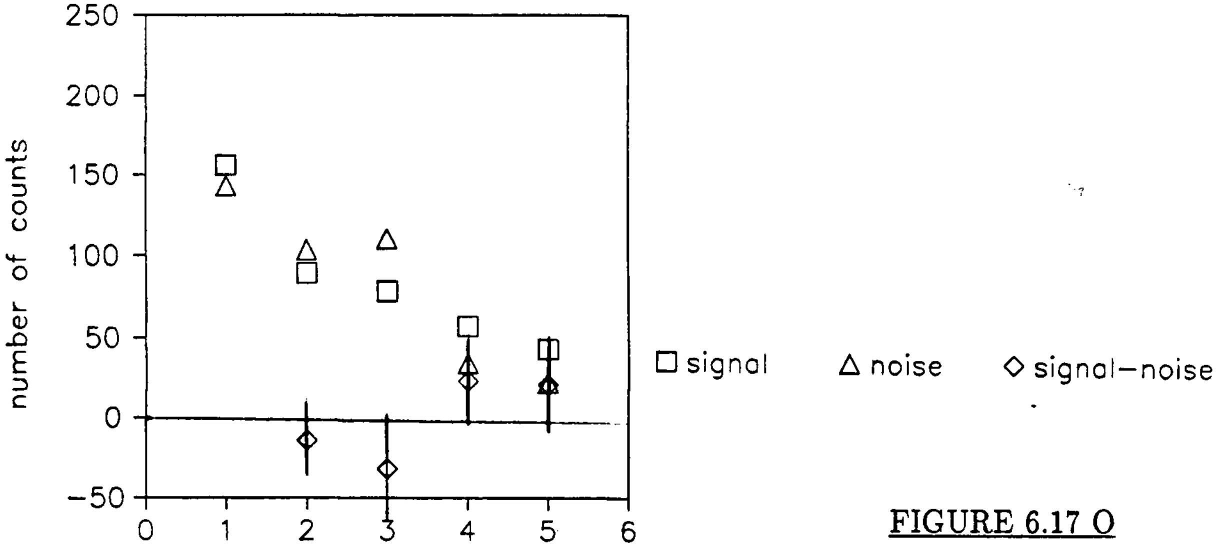

FIGURE 6.17 O

focal spot length: 140 μm grating chirp: 1000 eV/μm

time delay between the CO_2 and ruby lasers: 6 ns a_{pw}/a_m=8%

distance between the trapping point and the center of the CO_2 focal spot: 0 μm

injection energy: 92 KeV expected energy gain: 70KeV

number of shots averaged: 6

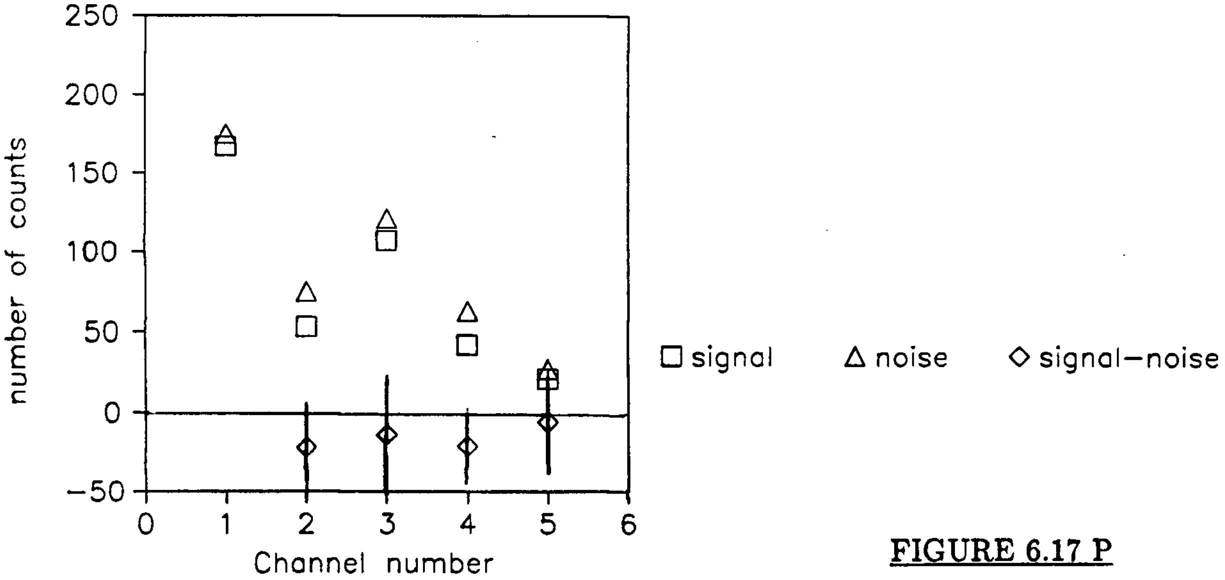

FIGURE 6.17 P

focal spot length: 350 μm grating chirp: 1000 eV/μm

time delay between the CO_2 and ruby lasers: 6 ns a_{pw}/a_m=16%

distance between the trapping point and the center of the CO_2 focal spot: 0 μm

injection energy: 92 KeV expected energy gain: 175KeV

number of shots averaged: 7

6.10 Discussion of the High Energy Electron Gun Results

Again, most points are zero within the standard error. However the graphs on Figures 6.17 G and I show a number of counts in channel #2, slightly (1.3 σ) above zero. The expected acceleration is 15 keV so channel #2 is the one that is expected to have an excess count. In the graph on Figure 6.17 L, channel #'s 2 and 3 have excess counts. The expected acceleration is 37 keV and the signal should be in channel #3. However the trajectory of trapped electrons can exit the acceleration layer before the full length of the CO_2 focal spot is traversed. So electrons accelerated by less than the expected energy can be produced and can generate a signal in channel #2. Graph 6.17 O shows an excess number of counts almost outside the standard error for channel #'s 4 and 5. The expected acceleration is 70 keV which should be detected by channel #4. On Figure 6.17 A, the number of counts in channel #4 is not zero. But the expected acceleration is only 8 keV, making this point very suspicious. Of course there are also a few points with negative signal minus noise (Figure 6.17 A and N). Out of the 64 points recorded there should be (statistically) 20 non zero points (32%), even with no signal at all. Therefore, the few points slightly above zero could be explained only by statistical variations. We can also compare the very small number of counts observed to the 10^6 counts expected theoretically.

In the light of these very unconvincing statistics we cannot conclude definitively that the expected acceleration is taking place.

The most likely explanation for the failure to detect the expected signal is, once again, the deflection of the electron beam by the electric field in the plasma. We have observed this effect with the 25 keV gun and increased the injected energy to 92 keV in an attempt to remedy this problem. However, even this higher energy is insufficient to prevent the electron from striking the grating. Unfortunately the 5 channel spectrometer does not have a sufficient time resolution (because of the OMA used) to look for a fast interruption of the electron beam when the lasers are triggered. Some experimental evidence for deflection of the 92 keV beam comes from visual observation of the spectrometer entrance hole while firing the lasers. For alignment purposes, the entrance hole is painted with fluorescent paint. When the lasers and the electron pulse are fired, the grating side of the hole emits a flash of light (Figure 6.18).

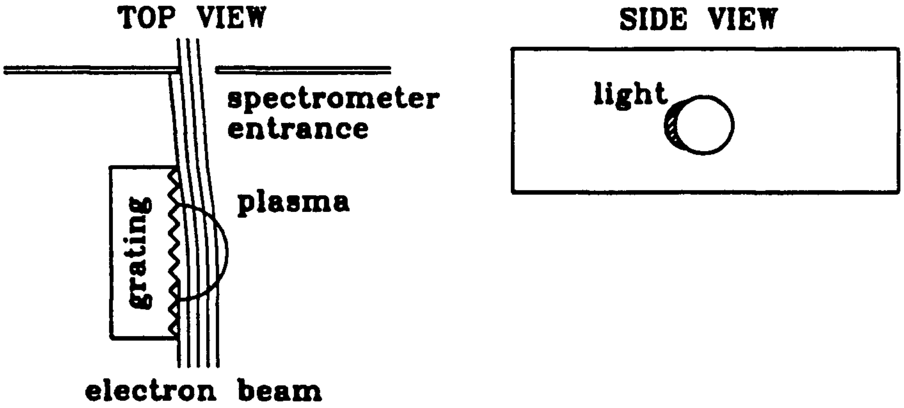

FIGURE 6.18

Experimental evidence showing deflection of the high voltage electron beam

When the electrons only, or the lasers only, are triggered, no such flash is visible. This observation is explained if the 92 keV beam is deflected by the electric field of the plasma and hits the side of the hole. The deflection is small but, again, the important electrons are the ones passing within 100 μm of the grating and those are the first to strike the grating even for a small deflection. The electric field generated by the plasma is sufficient to deflect the electrons close to the surface and make them strike the grating, even with the more energetic 92 keV electron beam. Therefore no accelerated electrons can be detected by the spectrometer.

CONCLUSION

In this thesis we tried to demonstrate experimentally the laser acceleration technique proposed by Katsouleas et al.

We first described the theory of this method: a laser irradiating a modulated plasma creates plasma waves. We then observed the plasma expanding above a grating illuminated by a ruby laser at an intensity of 10^{10} W/cm^2. We found that this plasma is modulated with $\tilde{n}/n = 8\%$ for grating wavelengths between 6 and 35 μm. The modulation extends up to 100 μm above the grating. This new method of producing a plasma with a precisely controllable density modulation could also be used for other purposes. For example, it could be used in the study of the Rayleigh-Taylor instability; or in filamentation and other effects influenced by non uniformities in a plasma.

We then showed that non relativistic electrons injected into the plasma wave above a chirp grating should be accelerated. This acceleration should occur, if the acceleration given by the chirp is smaller than qE_{epw}/m_e, where E_{epw} is the amplitude of the electric field of the plasma wave. Finally we tried to accelerate electrons injected at 25 keV in the plasma wave created by a CO_2 laser of 7×10^{11} W/cm^2. No accelerated electrons could be detected. We found that the injected electrons were deflected by a positively charged plasma and struck the grating. The presence of detrimental electric or magnetic fields in the plasma is a serious problem. These fields have also caused difficulties in another plasma wave electron acceleration experiment at U.C.L.A. [37]. In an attempt to remedy this problem, we increased the energy of the electron gun to 92 keV. But even at this higher energy no clear evidence for accelerated electrons could be obtained. Unfortunately, the obvious solution of going to still higher injected energies, 1 MeV or more, is impractical in the frame of this thesis due to budget and time constraints.

The method of formation of the plasma must be carefully chosen to minimize the stray electric or magnetic fields. We propose a number of suggestions to control these fields. We could, for example, use a very thin self supporting grating and irradiate it with two lasers, one on each side of the grating. This is similar to an exploding foil experiment [38]. The plasma expansion and any electric field produced, would be symmetrical on each side of the grating. The electrons travelling in the plane of the grating would not be deflected and any off axis electrons would be focused back into the symmetry plane.

Alternatively, the self-supporting grating could be replaced by a series of liquid droplets (Figure CO.1a), a series of very fine nozzles expelling a solid (extruding fibers), a liquid (fine liquid jets) or a gas (Laval nozzles), or any method capable of producing a similar self-standing grating (Figure CO.1b). We could also use a modulated laser striking a uniform target instead of a uniform laser irradiating a modulated target. In the former method, two laser beams intersecting each other at an angle θ on the surface of a thin foil should generate a modulated plasma with $\lambda_\theta = \lambda_{laser}/\sin\theta$, and a symmetrical expansion for sufficiently thin foil. We could also aim two beams at a gas target (Laval nozzle) to produce the same effect.

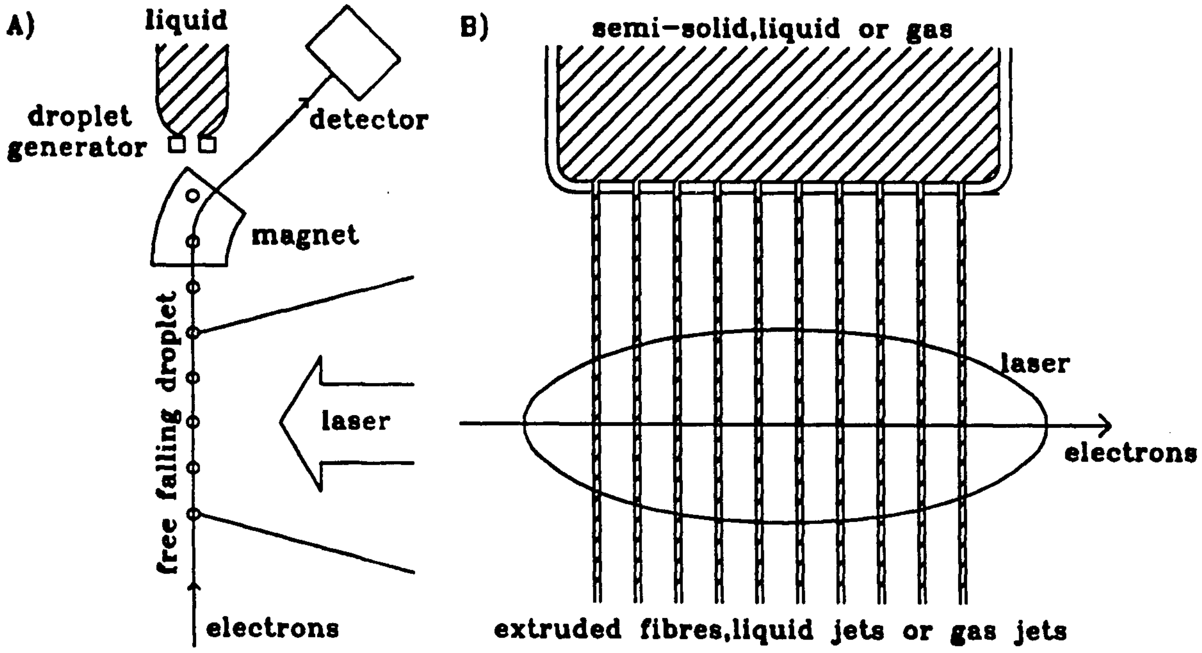

FIGURE CO.1
New grating concepts

BIBLIOGRAPHY

1. Shimoda, K., Appl. Opt. 1, 33 (1962)

2. Katsouleas, T., Dawson, J.M., Sultana, D., and Yan, Y.T., IEEE Transactions on Nuclear Science, Vol. NS-32, 3554 (1985)

3. Laser acceleration of particles, AIP Conference Proceeding No. 91, New-York, Paul J. Channell, 2 (1982)

4. Palmer, R.B., Particle Accelerators 11, 81 (1980)

5. Kheifets, S.A., 8th Conf. on High Energy Acc., CERN, 597 (1971)

6. Csonka, P.L., Particle Accelerators 5, 129 (1973)

7. Kroll, N.M., Morton, P.L., and Rosenbluth, M.N., IEEE Journal of Quantum Electronics QE-17m, 1436 (1981)

8. Pantell, R.H., and Smith, T.H., Appl Phys. Lett. 40 , 735 (1981)

9. Piestrup, M.A., Rothbort, G.B., Fleming, R.N., and Pantell, R.H., Jour. Appl. Phys. 46, 132 (1975)

10. Fontana, J.R., and Pantell, R.H., J. Appl. Phys. 54 , 4285 (1983)

11. Tajima, T., and Dawson J.M., Phys. Rev. Lett. 43, 267 (1979)

12. Chen, P., Dawson, J.M., Huff R.W., and Katsouleas, T., Phys. Rev. Lett. 54, 693 (1985)

13. Edighoffer, J.A., Kimura, W.D., Pantell, R.H., Piestrup, M.A., and Wang, D.Y., Phys. Rev. A 23, 1848 (1981)

14. Clayton, C.E., Joshi, C., Darrow C., and Umstadter, D., Phys. Rev. Lett. 54, 2343 (1985)

15. Ebrahim, N.A., Lavigne, P., and Aithal, S., IEEE Trans. Nucl. Sci. NS-32, 3539 (1985)

16. Rosenzweig, J.B., Cline, D.B., Cole, B., Figueroa, H., Gai, W., Konecny, R., Norem, J., Schoessow, P., and Simpson, J., Phys. Rev. Lett. 61, 98 (1988)

17. Rosenbluth, M.N., and Liu, C.S., Phys. Rev. Lett., 29, 701 (1972)

18. Ginzburg, V.L., Propagation of Electromagnetic Waves in a Plasma, Pergamon, New York, (1970)

19. Piliya, A.D., Sov. Phys.-Tech. Phys. 11, 609 (1966)

20. Abramowitz, M., and Stegun, I.A., Handbook of Mathematical Functions, Dover Publications Inc., New York, 475 (1965)

21. Kruer, W.L., The Physics of Laser Plasma Interactions, Addison-Wesley Inc., New York (1988)

22. Perkins, F.W., Flick, J., Phys. of Fluid, 14, 2012 (1971)

23. Walsh, C.J., Baldis, H.A., and Evans, R.G., Phys. of Fluid, 25, 2326, (1982)

24. J.E. Bernard, Ph.D. Thesis, University of British Columbia (1985)

25. Houtman, H., and Meyer, J., J. Appl. Phys. 57, 4892 (1985)

26. Schmalz, R.F., and Eidmann, K., Phys. Fluids 29, 3483 (1986)

27. Baldis, H.A., Samson, J.C., and Corkum, P.B., Phys. Rev. Lett. 41, 1719 (1978)

28. Caruso, A., and Gratten, R., Plasma Phys. 10, 867 (1969)

29. Banfi, G.P., Gobbi, P.G., Morosi, S., and Reali, G.C., Appl. Phys. Lett. 37, 23 (1980)

30. M.V. Berry, The Diffraction of Light by Ultrasound, Academic Press, New York (1966)

31. Raman, C.V., and Nath, N.S.N., Proc. Indian Acad. Sci. 3, 119 (1936)

32. Pearlman, J.S., and Dahlbacka, G.H., Appl. Phys. Lett. 31, 414 (1977)

33. Sullivan, D.J., and Godfrey, B.B., IEEE Trans. Nuc. Sci. NS-28, 3395 (1981)

34. Meyer, J., and Houtman, H., Phys. Fluids 28, 1549 (1985)

35. Legault, L.E., M.Sc. Thesis, University of British Columbia (1987)

36. Prescott, J.R., and Rabual, A.S., Can. J. Phys. 39, 221 (1961)

37. Clayton, C., Joshi, C., Leemans, W., Marsh, K., and Williams, R., AIP conference proceedings No. 113, Advanced Acceleration Concepts, 37 (1989)

38. Pert, G.J., Laser and Particle Beams, 5, 643 (1967)

39. Dyson, N.A., X-Rays in Atomic and Nuclear Physics, Longman Group Limited, London (1973)

APPENDIX A

SPECTROMETER SHIELDING

This appendix describes the measures taken to prevent background signals from being detected by the photomultiplier.

The thin aluminum coating deposited on the surface of the scintillator is difficult to produce. Any dust particles on the surface of the scintillator when it is in the vacuum deposition vessel prevent the aluminum from sticking to the substrate. This produces small pinholes in the coating. The ruby laser produces a large amount of visible light that is scattered inside the target chamber. Any small pinholes transmit enough light to the photomultipler to produce a very large signal that can hide the electron signal. Due to the relatively low electron energy we cannot use a self supporting aluminum foil that can be bought pinhole free. These aluminum foils have a minimum thickness of around 5 μm, thick enough to stop the 25 keV electrons [39]. (See electron range on Figure A.1). Satisfactory results are obtained by applying the coating in two stages and blowing compressed air on the scintillator between the two stages. This dislodges the dust particles and the probability of having a new particle at the same place as a previous one is very remote. In addition, sophisticated light shieldings and baffles empirically developed are necessary to bring the level of stray light to an acceptable level.

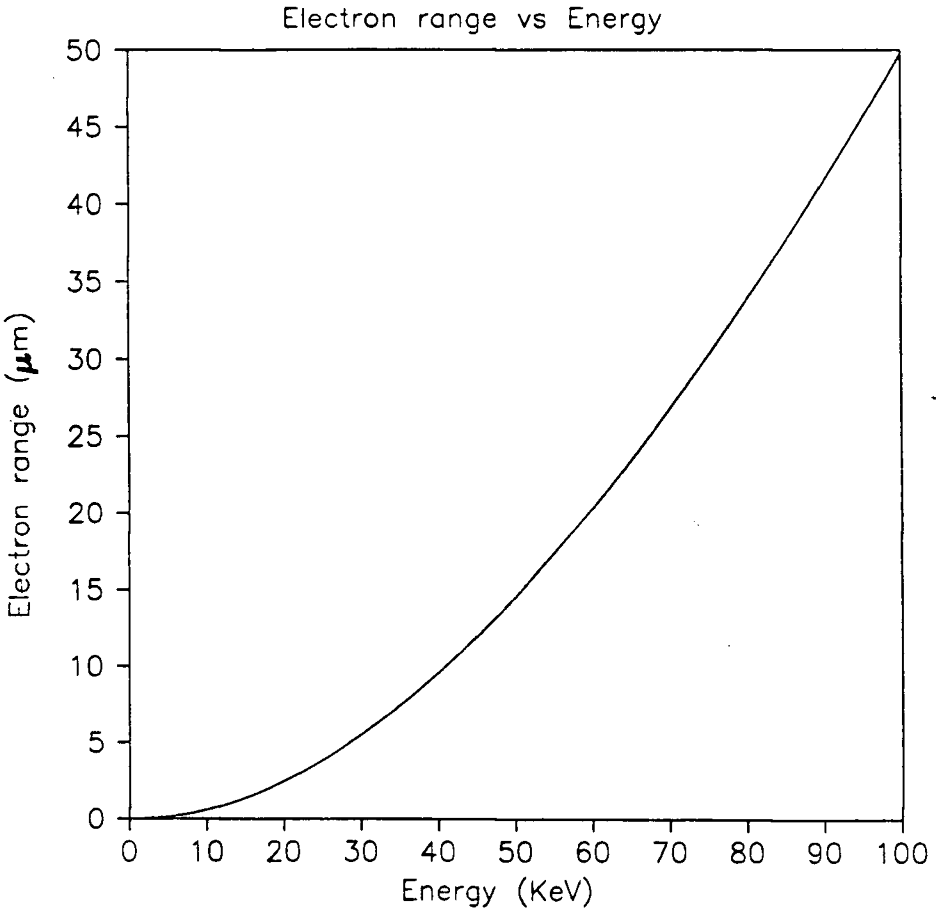

FIGURE A.1
Electron range in aluminium

Another source of noise signals were X-rays generated by the laser produced plasma. The aluminum in front of the scintillator is not thick enough to prevent X-rays from entering the scintillator and producing scintillation. Again the resultant large signal would cover a genuine accelerated electron signal. This problem can be reduced, but not completely eliminated, by using shieldings and baffles. Nothing must intrude into the X-ray cone defined by the plasma and the opening in the spectrometer light shielding box (Figure A.2), otherwise scattered X-rays can hit the scintillator and produce a large signal.

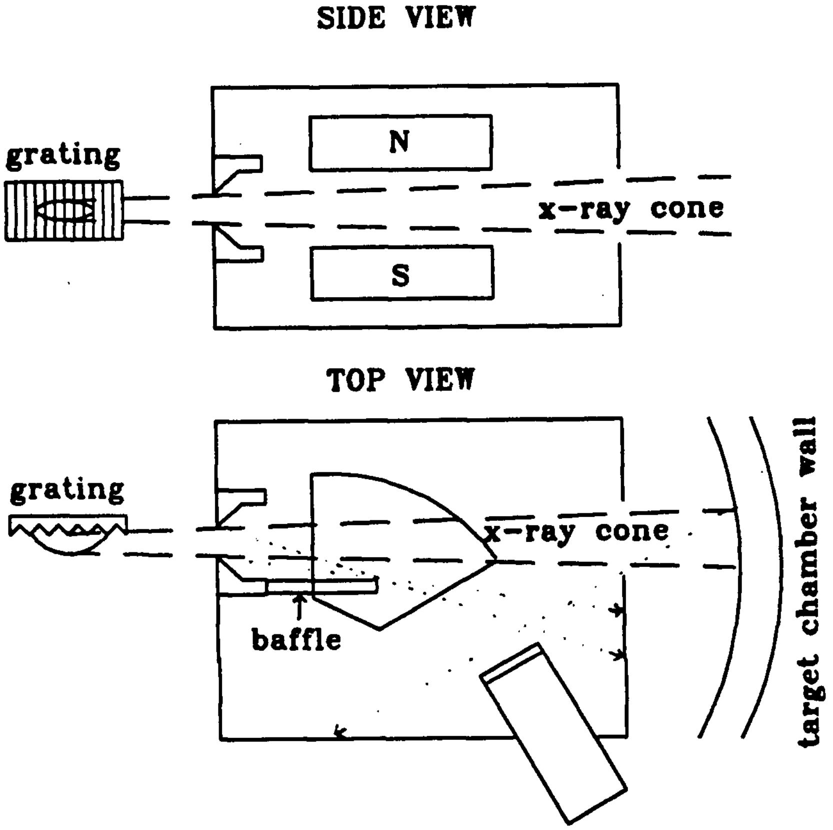

FIGURE A.2
Detail of x-ray shielding

In particular the pole pieces of the sector magnet have to be separated by a large enough distance to avoid intercepting the X-ray cone, and a large hole was drilled in the back of the light shield box to allow the X-rays to exit. A baffle is installed between the scintillator and the spectrometer entrance to prevent X-rays scattered from the rim of the entrance hole from reaching the scintillator. (The scattered X-rays are indicated by dots on the Figure). Also, the geometry must be arranged such that the scintillator is shielded from the X-rays scattered by the wall of the target chamber which is illuminated by the X-ray cone, otherwise a large signal is produced.

Careful design of the electron beam dump is necessary to keep the background counting rate of the photomultiplier at a low level. Electrons from the beam can rebound off the beam dump or generate secondary electrons. These electrons can then enter the scintillator and produce a background signal. Also a large number of X-rays are generated when the electrons bombard the beam dump. The relative position of the beam dump and the scintillator must be such that these X-rays cannot reach the scintillator. Figure A.3 shows the beam dump design. It is made out of a block of graphite to keep the X-ray production low (X-ray generation is less for low Z material than for heavier elements). The fins are machined in the block in an attempt to trap the electrons and minimize rebound and secondary productions.

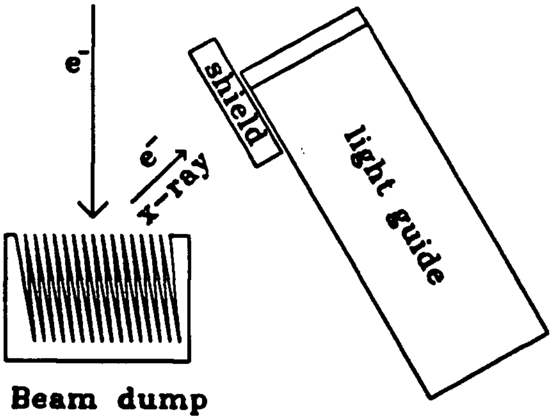

FIGURE A.3
Electron beam dump design

APPENDIX B

ALIGNMENT PROCEDURE

In order to produce the modulated plasma, excite the plasma wave and accelerate electrons, the laser beams, electron beam and grating position must be properly adjusted. This appendix describes the procedure used to insure proper alignment.

We first align the CO_2 laser beam to intersect the grating at the same height as the electron spectrometer aperture (see Figure 6.1). We then line up a Helium-Neon (He-Ne) laser beam through the spectrometer at $90^{\circ}\pm3^{\circ}$ with respect to the CO_2 beam direction. This beam is adjusted to follow the trajectory of the electron beam, but in the reverse direction. It enters the spectrometer by the large hole at the back of the light shield box, passes between the pole piece of the electromagnet and exits by the spectrometer entrance aperture. After passing just above the grating, this alignment beam finally illuminates the filament of the electron gun. The grating is then turned on a vertical axis until the alignment He-Ne laser beam passes exactly parallel to its surface. If the grating is positioned at a small angle with respect to the He-Ne laser beam, part of the light illuminates the grating and is reflected from the gold surface. Two spots become visible on a white screen installed about one meter away, (the reflected part of the beam and the direct one). We adjust the grating until the two spots converge to the same point. This can be done with a precision of ~ 1 mm on the screen. The He-Ne laser beam is then parallel to the grating within an angular precision of 0.5 mrad. It is very important to have the He-Ne laser beam precisely parallel to the grating surface since we want to pass the electrons 75 μm above the grating surface over a distance of 25 mm. Therefore the He-Ne laser beam needs to be parallel to the grating to within 75 μm/25 mm = 3 mrad, which can be achieved.

A thin flat piece of glass is then fixed at the end of the electron gun, perpendicularly to the electron beam axis. We adjust the position and orientation of the gun until the He-Ne laser beam hits the filament and the reflection from the glass goes back in the direction of the incident He-Ne laser beam . We adjust the horizontal slit (see Figure 6.11), so that the He-Ne laser beam passes through its center. The glass in front of the gun is removed and the grating replaced by a piece of brass to avoid thermal damage due to the next alignment step. The chamber is evacuated. The gun is turned on with the shutter permanently open. Because we painted the horizontal slit with fluorescent paint we can now see where the electron beam strikes. It should be perfectly aligned on the aperture, but because of stray magnetic fields (especially the earth's field) the electron beam is about a millimeter off alignment. The electron collector is positioned just in front of the spectrometer entrance hole. The gun's focus and position are adjusted to optimize the current that passes through the electron beam aperture. The electron beam is now passing just above the grating surface and parallel to it within ±0.5 mrad.

We then fire the CO_2 laser and produce a small footprint on the grating. A second He-Ne laser beam, collinear with the CO_2 laser, is adjusted on this burn mark. In order to do this adjustment with sufficient precision we observe the grating through a telescope with a large magnification. With the target chamber open we adjust the height of the CO_2 laser focusing lens until the CO_2 alignment He-Ne laser beam marking the position of the CO_2 laser focal spot intersects the electron beam alignment laser. This is only a small adjustment because the CO_2 laser was adjusted to be at the same height as the spectrometer entrance. The large magnification of the telescope allows us to adjust the intersection of the two He-Ne beams to within ±50 μm. The electron beam is 1 mm wide, providing more than enough precision to insure that electrons pass through the CO_2 laser focal spot.

Because of the CO_2 laser focusing lens, the ruby laser cannot irradiate the grating at an angle of incidence of 0°, we therefore used an angle of incidence of 18°. This angle is acceptable because the ruby laser only generates the modulated plasma and an angle of incidence of 18^0 will not affect the period or phase of the plasma density modulation produced. The ruby laser is focused on the grating and the exact position of irradiation can be adjusted with the last turning mirror before the beam enters the vacuum chamber (see Figure 3.1). A third alignment He-Ne laser beam is adjusted to be collinear with the ruby laser. This alignment laser beam passes through the ruby laser focusing system and produces a visible elongated focal spot on the grating. We then adjust the position of this focal spot until it is centered on the CO_2 alignment laser beam to within ±50 μm (Figure B.1). Again this is sufficiently precise, given that the ruby laser focal spot is 400 μm wide, to be sure that the CO_2 laser focal spot is in the modulated plasma produced by the ruby laser. The final item to line-up is the grating array.

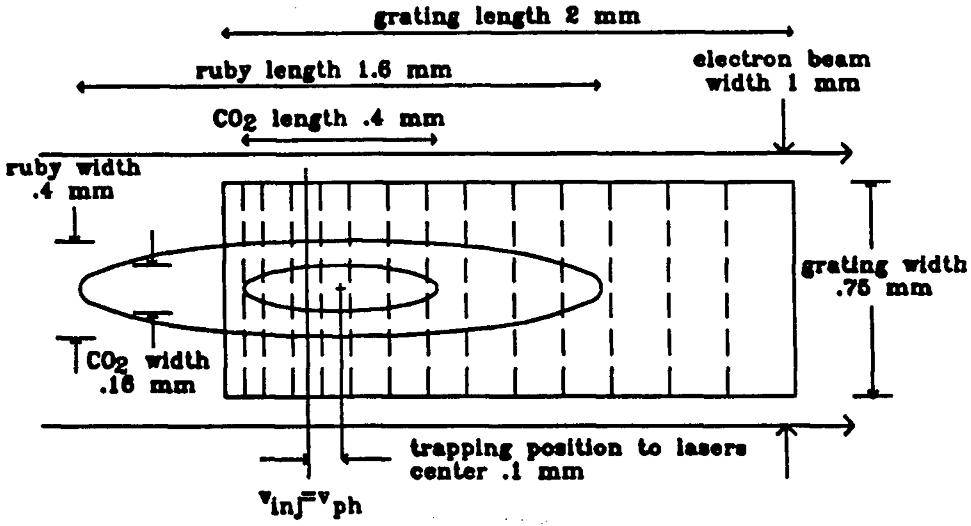

FIGURE B.1
Detail of the alignment of the lasers

It is moved with the x-y translation stage while looking through the telescope. The grating array is moved vertically until the CO_2 focal spot is positioned in the middle of the chosen grating to within ±50 μm. This precision is sufficient because each grating is 750 μm wide. In the horizontal direction, it is first necessary to decide the distance between the phase matching position and the middle of the CO_2 laser focal spot (see section 6.2). The grating array is then moved until the CO_2 focal spot is positioned at this determined distance from the phase matching point. The precision at which this can be done is ±50 μm. Because of the size of the CO_2 laser focal spot length (from 140 to 800 μm) this is precise enough to be sure that the phase matching point is irradiated by the CO_2 laser. After each shot this last step is repeated with a new grating but the rest of the alignment procedure is executed only once in the morning except if a laser realignment is needed during the day. We see that all the components of the experiment can be aligned to within acceptable tolerances.

APPENDIX C

92 keV ELECTRON GUN

The design of the 92 keV electron gun is shown in Figure C.1.

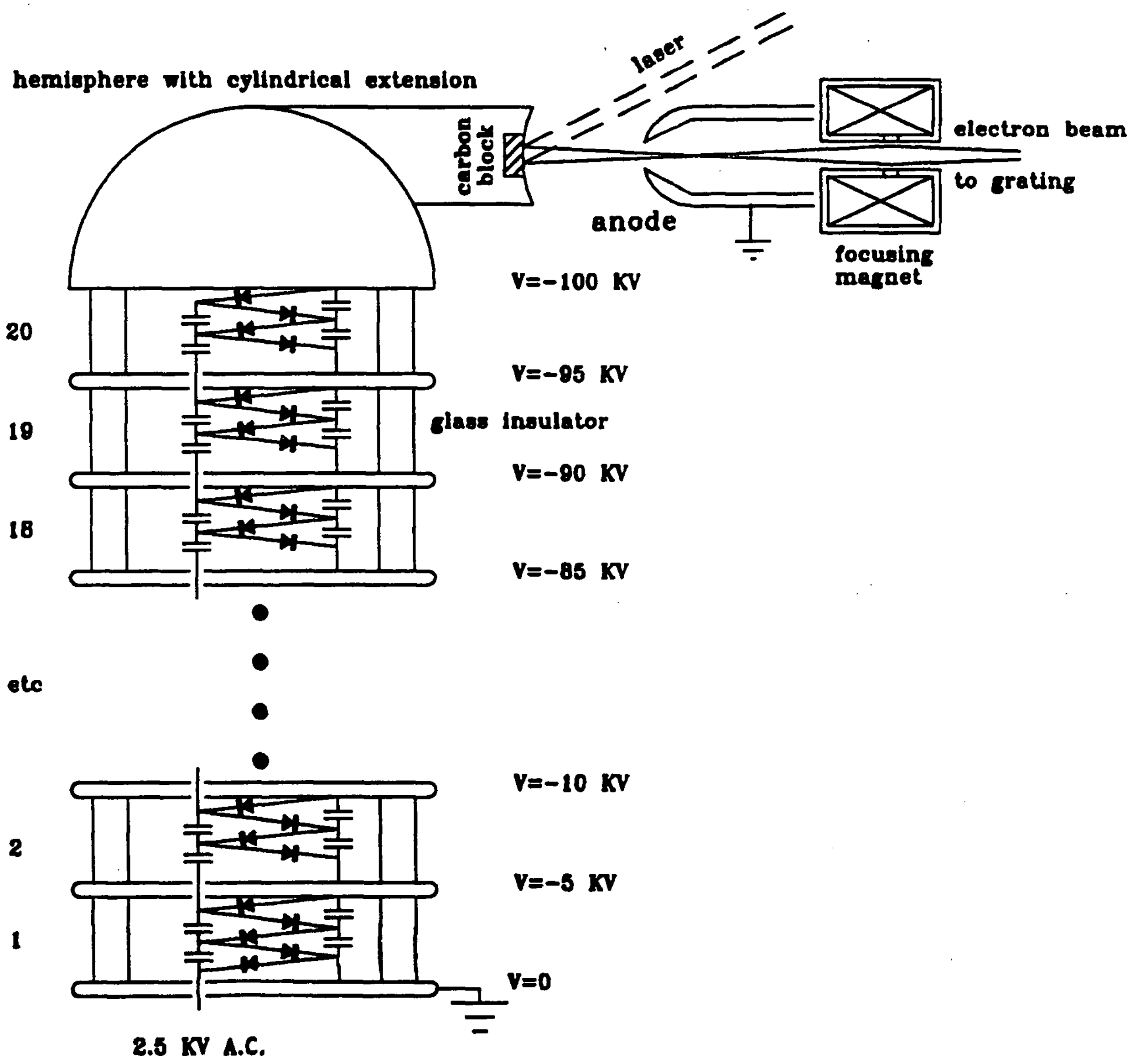

FIGURE C.1
Design of the high voltage electron gun

The electrons are extracted from a laser produced plasma on a carbon cathode held at -92 kV D.C. We used 8% of the 6 ns ruby laser to produce this plasma. Synchronization of the electron pulse with the laser pulse involves adjusting the optical delay between the 8% that generates the electron pulse and the rest of the ruby laser beam that produces the modulated plasma. A 40 stages Cockroft-Walton voltage multiplier charges the cathode to -92 kV. Each diode on Figure C.1 actually consists of 6 diodes in series, each of them being able to support one kV. The capacitors are 4.7 nF, 6 kV ceramic disc capacitors. The necessary 6 kV A.C. for the voltage multiplier is supplied by a 100 Volts, 5 KHz frequency generator feeding a 60 to 1 step up, air core transformer. The original design was for 200 kV, including a safety margin below the theoretical limit of the components (240 kV). But electric breakdown of the residual gas in the target chamber (5×10^{-5} Torr) limits the voltage to 92 kV. The concave cathode and convex anode with a hole in the middle produce a focusing electric field configuration. After the anode the electrons pass through the magnetic lens of the 25 kV gun and are focused at the position of the grating.

Since the beam is pulsed, alignment and focusing are more difficult than with a continuous beam. For the focusing procedure the high voltage is turned on and the ruby laser is fired. The electron pulse produces a fast bright flash on the fluorescent paint of the horizontal slit. Focus and alignment are adjusted accordingly. The process is repeated until a perfectly focused spot appears on the horizontal slit. The electrons from the carbon cathode are imaged on the horizontal slit plane, consequently adjusting the point where the ruby laser irradiates the cathode moves the point where the electrons strike the horizontal slit. It is therefore possible to steer the electron beam, from outside the evacuated chamber, by moving the ruby laser beam.

The current is measured using the electron collector connected to a 50 ohms terminator on a Tektronix 466 oscilloscope. The capacitance of the electron collector and cables is measured to be 15 pF, giving an RC time of 0.75 ns which is faster than the 5 ns response time of the oscilloscope. Again, the current measured is a minimum value because the 92 keV electrons can bounce off the metal plate or produce secondary electrons. The current pulse is shown on Figure C.2.

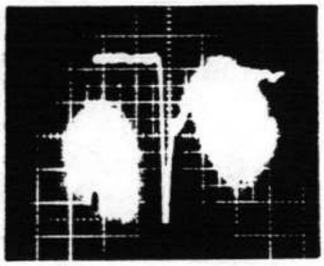

5 V/div 2 μs/div

FIGURE C.2
Current pulse of the high voltage electron gun

The rise time is ~8 ns (measured on a faster time scale). The decay time to half of maximum value, is ~1 μs. The electron pulse is therefore ~1 μs long. Because the electron pulse is long compared to the 1.8 ns laser pulse, synchronization will not be difficult to accomplish. The measured current maximum is 0.5 A through the 1 mm^2 aperture. This is a current density 125 times larger than with the 25 kV gun. We should now be able to accelerate at least 10^6 electrons (see section 6.1.1).

The voltage of the cathode is measured with a 11 GΩ voltage divider. It is important to have a high impedance for the measurement to avoid discharging the electron gun cathode because the Cockroft Walton voltage multiplier can only provide a very small current. The voltage divider is built of 11, 1 GΩ resistors in series. The voltage is measured across the 1 MΩ internal resistance of a digital multimeter connected in series with the 11 GΩ resistor chain. The maximum stable (no breakdown) voltage was 92 kV. We operated at this value.

We would appear to have a 1 μs window in which to synchronize the electron pulse. However, we need to examine this synchronization window more closely. It takes a few seconds for the Cockroft-Walton generator to charge the cathode hemisphere to 92 kV. During the 1 μs electron pulse, a current is drawn from the terminal by the electron beam, but almost no new charges are brought in to compensate for this loss of charge. As a result the voltage of the hemisphere drops. This can actually be seen on the voltmeter. Only the beginning of the electron pulse has an energy of 92 keV. We need to establish at what rate this energy decreases. The rising time of the electron pulse is measured to be 8 ns. Because of their inductance, the 80 capacitors of the Cockroft-Walton generator will not have time to supply new charges to the cathode in such a short time. The only available charges are therefore the ones stored on the hemisphere. The capacitance of the hemisphere is approximiately half the capacitance of a sphere, $C=2\pi R\varepsilon_0=2.8$ pF, where R is the radius of the hemisphere (5 cm) and ε_0 is the permitivity of free space. The time to lose 5% of the voltage is only $T=0.05\ CV/I=25$ ns. This is the timing window. We adjusted the optical path so that 8% of the ruby beam strikes the cathode 15 ns before the rest of the beam strikes the grating. This insures that the electron pulse has time to increase to its maximum current but does not have time to drop in energy.

Note on Alignment with the 92 kV Electron Gun

With the 25 keV electron gun the edge of the grating and the phase matching position where $v_{ph} = v_{inj}$ were almost the same. When aligning the CO_2 and ruby lasers, we could see the edge of the grating and aim properly. But for the 92 keV this is not the case, the phase matching condition does not occur close to the edge. The position of the phase matching point can be calculated using Equation (5.6).

Grating (eV/μm)	Phase Matching Position (from the edge of the grating in μm)
10	1246
46	632
215	228
1000	120

TABLE C.1

Phase matching position for the different gratings.

The laser can be adjusted to strike these points by first aiming at the front edge of the grating and then turning the micrometer of the translation stage to the desired value. The correct position can also be checked by an independent measurement. We have seen in appendix B that the CO_2 laser is aligned on the grating using a collinear He-Ne laser. Because of the small wavelength of the alignment He-Ne laser, its focal spot is quite small (~20 μm). The He-Ne laser light is diffracted by the grating lines of this small surface. By measuring the angle of diffraction we can calculate the local grating spacing and check that we are using the part of the grating with the suitable phase speed. Those two independent methods agree with each other and convince us that we are using the correct grating phase speed.